

Experimentation and analysis of the Vaporising Liquid Micro-resistojet

J.J.A. Vaes



Experimentation and analysis of the Vaporising Liquid Micro-resistojet

by

J.J.A. Vaes

to obtain the degree of Master of Science
at the Delft University of Technology,
to be defended publicly on December 19th, 2024 at 13:00.

Student number: 5879388
Project Duration: March 18, 2024 - December 19, 2024
Thesis committee: Dr. J. Guo TU Delft, Chair
Ir. J.A. Melkert TU Delft
Ir. B.T.C. Zandbergen TU Delft, Supervisor

An electronic version of this thesis is available at <https://repository.tudelft.nl/>.



Preface

This work marks the end of a long and winding student career. This journey began over seven years ago with the Bachelor Industrial Design at the TU/e. I quickly discovered that this was not the study for me, so I started looking further. Unfortunately, my gaze did not reach far enough, which is why I settled for Mechanical Engineering. Although I noticed something was missing, I did not fully understand what. It was not after seeing the *Apollo 11* documentary that I understood my true passion. From that point onwards I knew I had to pursue space. After finishing my bachelor's and completing several other side quests in Eindhoven, it was time for me to take my next small step.

I was fortunate enough to be admitted to the Aerospace Engineering program at TU Delft. From the moment I set foot in the AE hall, I knew I was in the right place. The last two years have been one of the most challenging ones so far, but I never felt out of place. I look back with great pleasure to these short but rewarding years and cherish the lessons learned here.

Lastly, I would like to extend my gratitude to a number of people. I would like to thank my supervisor Barry Zandbergen for accepting to guide me and for sharing your wise and enthusiastic counsel. I also want to thank Şevket Uludağ and the other TU Delft staff that has helped and supported me throughout my brief stay at this university. Naturally, I would not have been here without the incredible support of my homebase in the deep south of the Netherlands (Limburg). Merci. Finally, I want to thank all the friends made throughout this adventure for their company, support, humour, motivational speeches, free coffee, and so much more. Without you I would not be able to reach for the stars. Thank you all. Adieje.

*Jules Vaes
Delft, December 2024*

Abstract

A recent trend in the Aerospace industry is the miniaturisation of spacecraft. Historically these could not be controlled actively, limiting their operations and lifespan. TU Delft has already committed numerous research towards the development of miniaturised propulsion system using different technologies. This thesis continues work on the Vaporising Liquid Micro-resistojet (VLM) developed by Versteeg. Already three other master students have worked with this thruster and encountered several issues. Water tests had been attempted before but were unsuccessful due to the used feed system. Moreover, the latest experiments showed a significant degradation in terms of nozzle geometry and leak rate, which likely led to a decreased thruster performance. Lastly, the change to the TB-50m thrust bench resulted in unexpected drift behaviour.

This thesis addresses these challenges by implementing changes to the thruster en test set-up. The thruster's sealing surface has been restored to its original state using a CNC-machine. This was done to counter degradation of the nozzle geometry and reduce the VLM's leak rate. Additionally, a sealing gasket was developed for the same reason. Unfortunately, its implementation resulted in an undesirable deviation of the nozzle's geometry and was thus left out. A new water feed system is developed, based on the use of a pressurised tank. This reduced unwanted effects, such as bubble formation, that were encountered with the previously used syringe-based feed system. With the implementation of a liquid mass flow meter, the flow rate can be measured more accurately, thus reducing uncertainty in the VLM's performance. While these improvements proved to be successful initially, several issues encountered during the work have resulted in a worse overall performance. The nozzle geometry already showed signs of deformation after just two months. Furthermore, a major leak was identified which could not be addressed on time. Despite this, tests were executed with chamber temperatures up to 400 °C using both nitrogen and water as propellants. For nitrogen, the measured thrust varied between 4.1 and 8.6 mN for a throat Reynolds range of 1250 to 3300. The specific impulse increased from 34 to 37 s, while the specific impulse efficiency increased from 0.33 to 0.52. Discharge coefficients between 0.66 and 0.72 were measured. Although the errors are comparable ($\pm 15\%$ at most), this performance is significantly worse compared to earlier results. The water experiments were not successful due to an uncontrollable thruster operation. Regardless of this, the obtained test results showed an equally degraded thruster performance. These were executed at chamber pressures of ~ 0.85 bar and at various chamber temperatures. Thrust and specific impulse levels of 4.2 mN and 67 s were achieved, with errors as large as $\pm 34\%$. The corresponding specific impulse efficiency and discharge coefficient were 0.56 and 0.39, respectively. The throat Reynolds number decreased from 1550 to 1000. Because of these unsuccessful tests, the VLM performance could not be verified against earlier results, let alone used for validating the developed analytical model. Recommendations are provided to address the encountered issues and improve the thruster's performance. This should enable successful nitrogen and water tests in the future.

Contents

Preface	i
Abstract	ii
Contents	v
List of Figures	vii
List of Tables	ix
Nomenclature	x
1 Introduction	1
2 Contextual Background	4
2.1 Micropropulsion research at TU Delft	4
2.2 EDM-based VLMs	4
2.2.1 VLM-HV1 & VLM-HV2	5
2.2.2 VLM-RH	6
2.2.3 VLM-LC	7
2.3 Conclusion	10
3 Design Modifications	11
3.1 VLM Improvements	11
3.1.1 VLM Disassembly	11
3.1.2 Thruster body improvements	11
3.1.3 VLM Assembly	19
3.2 Test set-up Improvements	21
3.2.1 Test bench improvements	21
3.2.2 Water feed system	22
3.3 Expenditures	26
4 Analytical Model	27
4.1 Ideal Rocket Theory	27
4.1.1 Characteristic Parameters and Quality Factors	28
4.2 Modified Rocket Theory	29
4.2.1 Modified Discharge Coefficient	30
4.2.2 Modified Thrust Coefficient	30
4.2.3 Modified Rocket Theory	32
4.3 Model validation	32
4.4 Test predictions	33
4.4.1 Nitrogen tests	33
4.4.2 Water tests	34
5 Experimental Set-up	37
5.1 Test equipment	37
5.1.1 Thrust bench	37
5.1.2 Feed system	38
5.1.3 Sensors	39
5.1.4 Actuators	40
5.1.5 Data Acquisition Devices	40
5.1.6 Power supplies	41
5.1.7 Software	41

5.2	Calibrations	42
5.2.1	Load cell calibration	42
5.2.2	Thrust bench calibration	44
5.2.3	SLI-1000 calibration	48
5.3	Error Propagation	49
6	Preliminary Tests	51
6.1	Optical Characterisations	51
6.1.1	VLM-LC2	52
6.1.2	VLM-JV1	54
6.1.3	VLM-JV2	56
6.2	Leak tests	59
6.2.1	Leak test plan	59
6.2.2	VLM-LC2	60
6.2.3	VLM-JV1	61
6.2.4	VLM-JV2	65
6.2.5	Effects of leaks on the results	66
6.3	Discussion	67
7	Nitrogen Tests	68
7.1	Test plan	68
7.2	Test results	70
7.2.1	Drift correction	70
7.2.2	Results processing	71
7.2.3	Acceptance criteria	72
7.3	Test discussion	73
8	Water Tests	75
8.1	Test plan	75
8.1.1	Test procedures	77
8.2	Test results	77
8.2.1	Acceptance criteria	78
8.3	Test discussion	79
9	Validation & Verification	81
9.1	Validation of the Analytical Model	81
9.2	Verification of the test results	83
9.2.1	Nitrogen tests	83
9.2.2	Water tests	85
10	Conclusion	87
11	Recommendations	89
11.1	Vaporising Liquid Micro-resistojet	89
11.2	Experimental set-up	90
	Bibliography	92
A	Experimental Set-up	96
A.1	Equipment overview	96
A.2	Component inventory	97
A.3	Feed systems	98
A.4	Electrical Diagram	99
B	Test Data	101
B.1	Calibrations	101
B.2	Optical Characterisation	104
B.3	Leak Tests	106
B.4	Nitrogen Tests	107
B.5	Water Tests	113
B.6	Validation & Verification	118

B.6.1	Validation of the Analytical Model	118
B.6.2	Verification of the test results	120
C	Datasheets	121
C.1	Sealing gasket	121
C.1.1	Sigraflex® APX pure graphite foil	121
C.1.2	Technical drawing sealing gasket	123
C.2	Futek LSB200	124
C.3	Scaime CPJ Amplifier	125
D	Procedures	126
D.1	Disassembly Procedure	126
D.1.1	Required equipment	126
D.1.2	Disassembly procedure	127
D.2	Assembly Procedure	127
D.2.1	Required equipment	127
D.2.2	Assembly procedure	128
D.3	Water test procedures	128
D.3.1	Required equipment	129
D.3.2	Preparation	129
D.3.3	Environment set-up	132
D.3.4	Thrust testing	132
D.3.5	Shutdown	133
E	MATLAB Resistojet Performance Tool	135

List of Figures

2.1	The iterations of the Vaporising Liquid Micro-resistojet.	5
2.2	The original Vaporising Liquid Micro-resistojet as developed by Versteeg [81].	6
2.3	Comparison of C_d and ξ_{Isp} as a function of Re_t with (nitrogen) experimental results of Versteeg [81], Hutten [28], and Bayt [3] and modelled output of the RPT [28].	7
2.4	The pendulum (left) and torsional (right) test benches used throughout different works.	8
2.5	The pendulum (left) and torsional (right) interfaces as designed and manufactured by Versteeg [81] and Cramer [15], respectively.	9
2.6	Overview (left) and detailed view (right) of the Vaporising Liquid Micro-resistojet (VML-LC) used by Cramer [15].	10
3.1	Thruster body after polishing of the sealing surface [15].	12
3.2	Nozzle exit after assembly and tightening by Cramer [15]. The deformation of the once-rectangular nozzle exit is clearly visible.	13
3.3	Design of a graphite sealing gasket.	14
3.4	Two designs for the copper sealing ring.	15
3.5	Design of a nozzle cover.	16
3.6	Bottom copper block before (left) and after (right) polishing.	19
3.7	The realised graphite gasket (left) and its effect on the nozzle area (right).	19
3.8	The modified graphite gasket (left) and its effect on the nozzle area (right).	20
3.9	The improved test bench showing the added bull's eye level and the new load cell location closer to the rotation point.	22
3.10	Schematic overview of the water feed system used by Hutten.	23
3.11	Overview of the new water feed system (excluding the mass flow meter).	24
3.12	Schematic overview of the new water feed system.	25
5.1	The nitrogen feed system.	39
5.2	The Sensirion Sensor Viewer used to measure the liquid mass flow [58].	41
5.3	The two TB-50m test bench states used for the calibration campaign.	45
5.4	Drift compensation process for the TB-50m thrust bench calibrations in vacuum and with a full test bench at 200 °C (CAL-111a). Top shows the original load and fitted linear function. Bottom shows the corrected load.	46
5.5	Results of the TB-50m thrust bench calibrations in vacuum and with a full test bench at 200 °C (CAL-111a). The left graphs show the original loads, while the right graphs show the loads with drift compensation.	47
6.1	The nozzle throat can be made visible by increasing the picture's brightness (VLM-LC2).	52
6.2	Illustration of the nozzle exit area (A_e) measurement process (VLM-LC2).	53
6.3	The Vaporising Liquid Micro-resistojet nozzle, after improvements (VLM-JV1).	54
6.4	Zoomed out views of the VLM nozzle areas before (VLM-JV1, left) and after (VLM-JV2, right) testing.	57
6.5	The Vaporising Liquid Micro-resistojet nozzle after testing (VLM-JV2).	58
6.6	Measured leak rate of the Vaporising Liquid Micro-resistojet, before improvements (VLM-LC2).	61
6.7	The leakage locations identified on VLM-JV0. The leaks occur at the interfaces between two component.	62
6.8	The implementation of the 062 MINSTAC Safety Screen in the aluminium interface (VLM-JV1).	63
6.9	Measured leak rate of the Vaporising Liquid Micro-resistojet, after improvements (VLM-JV1).	64

6.10 Observation of a major leak and soot formation on the Vaporising Liquid Micro-resistojet, after testing (VLM-JV2).	65
6.11 Measured leak rate of the Vaporising Liquid Micro-resistojet, after testing (VLM-JV2). . .	66
7.1 Observation of 'sticky friction' in the measured load (nitrogen test at 300 °C and 1.0 bar). .	71
7.2 Drift compensation process for the nitrogen test at 300 °C and 1.0 bar (N2-10-300). . .	71
7.3 Measured parameters of the nitrogen test at 300 °C and 1.0 bar (N2-10-300).	73
8.1 Measured parameters of the water test at 300 °C and 1.5 bar (H2O-15-300).	78
9.1 Comparison of the modelled and test performance for the different nitrogen tests.	82
9.2 Comparison of the test performance for the nitrogen tests with different authors.	85
9.3 Comparison of the test performance for the water tests with different authors.	85
A.1 The nitrogen feed system used during the final nitrogen test campaign.	98
A.2 The water feed system used during the final water test campaign.	99
A.3 An electrical diagram of the experimental set-up used for this thesis.	100
B.1 Results of the TB-50m thrust bench calibrations with an empty test bench (CAL-000). The left graphs show the original loads, while the right graphs show the loads with drift compensation.	101
B.2 Results of the TB-50m thrust bench calibrations in vacuum and with an empty test bench (CAL-100). The left graphs show the original loads, while the right graphs show the loads with drift compensation.	102
B.3 Results of the TB-50m thrust bench calibrations with a full test bench (CAL-010). The left graphs show the original loads, while the right graphs show the loads with drift compensation.	102
B.4 Results of the TB-50m thrust bench calibrations in vacuum and with a full test bench (CAL-110). The left graphs show the original loads, while the right graphs show the loads with drift compensation.	103
B.5 Results of the TB-50m thrust bench calibrations in vacuum and with a full test bench at 200 °C (CAL-111a). The left graphs show the original loads, while the right graphs show the loads with drift compensation.	103
B.6 Results of the TB-50m thrust bench calibrations in vacuum and with a full test bench at 300 °C (CAL-111b). The left graphs show the original loads, while the right graphs show the loads with drift compensation.	104
B.7 Total overview of the measured nozzle parameters of the Vaporising Liquid Micro-resistojet.	105
B.8 Total overview of the measured leak rates of the Vaporising Liquid Micro-resistojet. . . .	106
B.9 Total overview of the measured leak rates of the Vaporising Liquid Micro-resistojet. . . .	107
B.10 Measured parameters of the nitrogen test at 20 °C and 1.0 bar (N2-10-020).	108
B.11 Measured parameters of the nitrogen test at 200 °C and 1.0 bar (N2-10-200).	109
B.12 Measured parameters of the nitrogen test at 200 °C and 1.5 bar (N2-15-200).	110
B.13 Measured parameters of the nitrogen test at 300 °C and 1.0 bar (N2-10-300).	111
B.14 Measured parameters of the nitrogen test at 400 °C and 1.0 bar (N2-10-400).	112
B.15 Measured parameters of the water test at 200 °C and 1.0 bar (H2O-10-200).	114
B.16 Measured parameters of the water test at 300 °C and 1.5 bar (H2O-15-300).	115
B.17 Measured parameters of the water test at 400 °C and 1.5 bar (H2O-15-400).	116
B.18 Measured parameters of the water test at 400 °C and 1.5 bar (H2O-15-400).	117
D.1 The water feed system required for the water tests.	131

List of Tables

3.1	Overview and trade-off of the different concepts for decreasing the leakage rate. Green (+) means it is the best option, while red (-) means it is the worst option of that row. Orange (/) is in between.	17
3.2	Overview of the expenditures of this work, including VAT and shipping costs.	26
4.1	Validation of the Resistojet Performance Tool (RPT) developed by Hutten [28] and the M-RPT developed in this work. The errors are absolute values.	33
4.2	Overview of the nitrogen test campaign.	34
4.3	Input and output of the Resistojet Performance Tool (RPT) showing the predicted parameters of the planned nitrogen test campaign.	34
4.4	Overview of the water test campaign.	35
4.5	Input and output of the Resistojet Performance Tool (RPT) showing the predicted parameters of the planned water test campaign.	36
5.1	Measured mass, weight, and voltage for the load cell calibration.	43
5.2	Measured weight and voltage including the determined linear relationship.	43
5.3	Overview of the TB-50m thrust bench calibration campaign.	44
5.4	Overview of the TB-50m thrust bench calibration results.	48
5.5	Measured volumetric flow rates for the SLI-1000 calibration.	49
5.6	Top view of the SLI-1000 calibration set-up.	49
5.7	The confidence bounds of the test equipment [15].	50
6.1	Measured nozzle parameters of the Vaporising Liquid Micro-resistojet, before improvements (VLM-LC2).	54
6.2	Measured nozzle parameters of the Vaporising Liquid Micro-resistojet, after improvements (VLM-JV1).	55
6.3	Comparison of the measured nozzle parameters of VLM-RH and VLM-JV1.	56
6.4	Measured nozzle parameters of the Vaporising Liquid Micro-resistojet, after testing (VLM-JV2).	57
6.5	Comparison of the measured nozzle parameters of VLM-RH and VLM-JV2.	58
6.6	Acceptance criteria for the leak tests.	59
6.7	Measured leak rate of the Vaporising Liquid Micro-resistojet, before improvements (VLM-LC2).	60
6.8	Internal volume of Vaporising Liquid Micro-resistojet.	62
6.9	Measured leak rate of the Vaporising Liquid Micro-resistojet, after improvements (VLM-JV1).	64
6.10	Measured leak rate of the Vaporising Liquid Micro-resistojet, after testing (VLM-JV2).	66
6.11	Estimated leak rates (and % of predicted flows) for the different test conditions and resulting corrected mass flow rates.	67
7.1	Overview of the nitrogen test campaign.	68
7.2	Overview of the measurement parameters for the nitrogen tests.	69
7.3	Acceptance criteria for the nitrogen tests.	69
7.4	Averaged results and measurement errors of the nitrogen tests.	70
7.5	Averaged results and total errors of the nitrogen tests.	72
7.6	Quality factors of the nitrogen tests.	72
7.7	Estimated leak rates (and % of measured flows) and resulting corrected mass flow rates for the different tests.	74
8.1	Overview of the water test campaign.	75

8.2	Overview of the measurement parameters for the water tests.	76
8.3	Acceptance criteria for the water tests.	76
8.4	Averaged results and total errors of the water tests.	77
8.5	Quality factors of the water tests.	78
8.6	Calculated leak rates (and % of measured flows) and resulting corrected mass flow rates for the different tests.	79
9.1	Comparison of the modelled and measured parameters for the nitrogen test at 300 °C and 1.0 bar (N2-10-300).	82
9.2	Comparison of the modelled and measured parameters for the water test at 300 °C and 1.5 bar (H2O-15-300).	82
9.3	Comparison of the corrected mass flow rates of the model ($\dot{m}_{MRT,corr}$) and measurements ($\dot{m}_{meas,corr}$).	83
9.4	Comparison of the results for N2-15-200 with different authors.	84
9.5	Comparison of results for H2O-15-300.	86
A.1	Overview of the various components that contribute to the experimental set-up.	97
A.2	Inventory of the project's designated box. This excludes the equipment used during testing. Note that this list is not complete and subject to changes. The box is marked with the author's name and situated in the cleanroom workshop.	98
B.1	Total overview of the measured nozzle parameters of the Vaporising Liquid Micro-resistojet.	104
B.2	Total overview of the measured leak rates of the Vaporising Liquid Micro-resistojet.	106
B.3	Averaged results and absolute errors of the nitrogen tests.	107
B.4	Quality factors of the nitrogen tests.	108
B.5	Averaged results and measurement errors of the water tests.	113
B.6	Averaged results and total errors of the water tests.	113
B.7	Quality factors of the water tests.	113
B.8	Comparison of the modelled and measured parameters for the nitrogen test at 20 °C and 1.0 bar (N2-10-020).	118
B.9	Comparison of the modelled and measured parameters for the nitrogen test at 200 °C and 1.0 bar (N2-10-200).	118
B.10	Comparison of the modelled and measured parameters for the nitrogen test at 200 °C and 1.5 bar (N2-15-200).	118
B.11	Comparison of the modelled and measured parameters for the nitrogen test at 300 °C and 1.0 bar (N2-10-300).	119
B.12	Comparison of the modelled and measured parameters for the nitrogen test at 400 °C and 1.0 bar (N2-10-400).	119
B.13	Comparison of the modelled and measured parameters for the water test at 200 °C and 1.0 bar (H2O-10-200).	119
B.14	Comparison of the modelled and measured parameters for the water test at 300 °C and 1.5 bar (H2O-15-300).	119
B.15	Comparison of the modelled and measured parameters for the water test at 400 °C and 1.5 bar (H2O-15-400).	120
B.16	Comparison of the results for N2-10-020 with different authors.	120
D.1	Actions to undertake during the water thrust measurements.	133

Nomenclature

Abbreviations

Abbreviation	Definition
AE	Aerospace Engineering
COTS	Commercial off-the-shelf
CNC	Computer numerical control
DAQ	Data Acquisition
DEMO	Dienst Elektronische en Mechanische Ontwikkeling
EDM	Electric Discharge Machining
IRT	Ideal Rocket Theory
LPM	Low-Pressure Micro-resistojet
MEMS	Micro-Electro-Machanical System
M-RPT	MATLAB Resistojet Performance Tool
MRT	Modified Rocket Theory
NI	National Instruments
RMS	Root mean square
RO	Rated output
RPT	Resistojet Performance Tool
SCCM	Standard cubic centimetre per minute
VLM	Vaporising Liquid Micro-resistojet
VTDC	Varying Turn-Density Coil

Symbols

Symbol	Definition	Unit
A_e	Nozzle exit area	[m ²]
A_L	Leak area	[m ²]
A_t	Nozzle throat area	[m ²]
C_d	Discharge coefficient	[-]
C_p	Specific heat at constant pressure	[J/kg·K]
C_F	Thrust coefficient	[-]
C_v	Specific heat at constant volume	[J/kg·K]
$C_{\theta,div}$	Divergence loss	[-]
c^*	Characteristic velocity	[m/s]
D_{ht}	Throat hydraulic diameter	[m]
d	Distance	[m]
F	Thrust force	[N]
g_0	Gravitational acceleration	[m/s ²]
H_e	Nozzle exit height	[m]

Symbol	Definition	Unit
H_t	Nozzle throat height	[m]
h	Specific enthalpy	[J/kg]
I_{heat}	Heater current	[A]
I_{sp}	Specific impulse	[s]
M	Molar mass	[kg/mol]
m	Mass	[kg]
\dot{m}	Mass flow rate	[kg/s]
\dot{m}_L	Leak flow rate	[kg/s]
P_a	Ambient pressure	[Pa or N/m ²]
\dot{P}_c	Chamber pressure drop	[Pa/s or N/m ² ·s]
P_c	Chamber pressure	[Pa or N/m ²]
P_e	Nozzle exit pressure	[Pa or N/m ²]
P_p	Pressurant pressure	[Pa or N/m ²]
P_{heat}	Heater power	[W]
q_L	Leak rate	[mbar·L/s]
R_A	Universal gas constant	[J/K·mol]
R	Specific gas constant	[J/kg·K]
r_c	Radius of curvature at the nozzle throat	[m]
r_t	Nozzle throat radius	[m]
Re	Reynolds number	[-]
Re_t	Throat Reynolds number	[-]
T_c	Chamber temperature	[K]
T_t	Throat temperature	[K]
U_e	Exhaust flow velocity	[m/s]
V	Volume	[m ³ or L]
V_{heat}	Heater voltage	[V]
W_e	Nozzle exit width	[m]
W_t	Nozzle throat width	[m]
Γ	Vandenkerckhove function	[-]
γ	Specific heat ratio	[-]
ϵ	Nozzle expansion area ratio (A_e/A_t)	[-]
η_{heat}	Heating efficiency	[-]
θ_{div}	Nozzle divergence half angle	[rad or °]
μ	Viscosity	[Pa·s]
ξ_c	Combustion quality	[-]
ξ_F	Thrust quality	[-]
ξ_{Isp}	Specific impulse quality	[-]
ξ_n	Nozzle quality	[-]
ρ	Density	[kg/m ³]
σ	Standard deviation	[-]
τ	Torque	[Nm]

1

Introduction

A notable trend in the space industry is the growing trend of miniaturised spacecraft in the last couple of years [68]. Where satellites traditionally were the size of small cars and weighed over several tons, nowadays they commonly come in CubeSat formats [37]. This format was first introduced by Puig-Suari, Turner, and Twiggs [53] in an effort to standardise and simplify the development of satellites. A CubeSat, as the name suggests, has a cubic shape with dimensions of $10 \times 10 \times 10 \text{ cm}^3$ (1U) and a mass up to 2 kg [10], which can be extended by stacking multiples cubes together. Smaller dimensions also exist such as cubes of $5 \times 5 \times 5 \text{ cm}^3$, called PocketQubes. They have a mass of 250 g per unit at most [1].

Such smaller spacecraft have several benefits over their larger counterparts. For example, a reduced size also means a reduced development and production time. In turn, this increases the cost-effectiveness and allows for an increased deployment rate [68]. Another benefit is that more satellites can be launched simultaneously, as opposed to launching a single large satellite at a time. This leads to an increased redundancy and lowers the risk of a critical mission failure in case a satellite fails [43].

However, the reduction in dimensions also introduces new challenges, among which the extreme volume and mass constraints are the most pronounced. This also makes it difficult to integrate a dedicated propulsion system in the satellite. Consequently, these are often left out, limiting the lifespan of the spacecraft severely [45]. A lot of effort has already been put into developing miniaturised propulsion systems that can be implemented into CubeSats and PocketQubes, and some have already been demonstrated in orbit [37]. The technology has still more room to mature though, which is what some research at the TU Delft is focused on [13].

Micropropulsion systems still allow for attitude control and orbital manoeuvres, while reducing costs and mass [49]. The Aerospace faculty of TU Delft has dedicated considerable research towards developing such miniaturised propulsion systems. They are based on several unique working principles and fabrication techniques [14]. Among these, the micro-resistojet concept has been researched extensively at TU Delft. Micro-resistojets heat a liquid or gaseous propellant and expel it into space. Two main types of resistojets can be identified; the Vaporising Liquid Micro-resistojet (VLM) and the Low-Pressure Micro-resistojet (LPM). The former of which is of interest in this work. A VLM uses a de Laval (converging-diverging) nozzle to accelerate a propellant and produce thrust [16]. The propellant can either be a liquid (usually water) or gas (usually nitrogen), based on the needs of the specific project. Using liquid water has several advantages over gaseous nitrogen. For example, the higher density of water makes it more volume efficient. Moreover, it provides an excellent velocity increment per volume of propellant and is safe and easy to work with [26]. A LPM thruster uses low pressures (below 1000 Pa) and a heater chip to accelerate gas to space. The most recent work on this concept has been carried out by Singh [62]. LPM thrusters will not be investigated further in this work.

The VLM on the other hand, will be discussed in detail. Most notably, the Vaporising Liquid Micro-resistojet made using Micro-Electro-Mechanical Systems (MEMS) techniques has been researched extensively at the university (De Athayde Costa e Silva [16], Makhan [42], among others). This technique integrates mechanical and electrical parts into a single device using specialised equipment [17]. Resistive heaters and fluidic channels are made on the same chip, for example. However, this technique also has its drawbacks; it has long lead times and high batch prices. Therefore, Versteeg [81] developed a VLM using the less costly wire Electric Discharge Machining (EDM) technique. The VLM Versteeg originally manufactured forms the centre of attention of this thesis.

Versteeg verified his thruster's functioning and leak-tightness using nitrogen gas as propellant. Nitrogen gas was chosen, instead of liquid water, as it is easy to use and readily available. However, it is not as efficient as water, because of its low storage density [26]. So, a year later Hutten [28] adapted the propulsion system to use liquid water instead. As stated earlier, water has several advantages over gaseous nitrogen (easy to store, high storage density, good performance, and relatively safe to use).

Hutten repeated Versteeg's experiments and verified the nitrogen results. However, the tests he performed with water provided some new challenges, such as an unstable mass flow and chaotic thrust measurements. Furthermore, the syringe-based feed system did not allow for an accurate estimate of the mass flow [28]. This resulted in a less accurate thruster performance. Cramer [15] continued the work of Versteeg and Hutten and changed the test setup to remove its dependency on the centre of gravity. She also performed extensive preliminary tests, such as an optical characterisation and leak tests. This revealed that the thruster had degraded over time (e.g. increased leak rate and altered nozzle geometry) and required some maintenance. The thruster has also been tested using nitrogen gas and a significant decrease in thrust performance was noticed [15]. while the exact cause of this degraded performance is debatable, it likely arises from a combination of several factors, such as the leak rate, nozzle geometry and altered test set-up.

This thesis will build upon the aforementioned work by first replicating Cramer's experiments. In this way, the author gains experience in conducting the experiments and performing a data analysis, which will be essential for tests planned in this work. After these initial experiments, an attempt is made to decrease the leakage rate to acceptable levels, whilst avoiding permanent deformation of the thruster. This will be done by first disassembling the thruster, after which improvements can be made. These include ideas like resurfacing the thruster, implementing a sealing gasket, or manufacturing an entirely novel thruster. The aim of these improvements is to restore the VLM to a similar state to the one used by Versteeg and Hutten. This process is detailed in [chapter 3](#).

The feed system will be converted to allow for a more stable water mass flow rate without bubble formation in the feed lines. Instead of using a syringe, a tank filled with water and pressurised with nitrogen can be used to feed the propellant to the thruster. The nitrogen gas is used to push the water through the feed lines and remove any leftover liquids at the end of the test. A (liquid) mass flow meter will be implemented to measure the mass flow rate inside the system, which allows for more accurate results and hopefully less error in the quality factors; C_d (discharge coefficient) and ξ_{Isp} (specific impulse quality). The changes to the (water) feed system are also detailed in [chapter 3](#). Moreover, an improved way to measure the nozzle throat will be developed to reduce the inaccuracies in these measurements. The VLM's leak-tightness will be tested extensively as well ([chapter 6](#)).

After these preliminary tests, a thorough test campaign is executed using both nitrogen and water ([chapter 7](#) and [chapter 8](#)). These tests help characterise the thruster behaviour and shed light on the effectiveness of the changes implemented throughout the work. Lastly, this thesis will analyse the previously obtained thruster data and compare the different tests ([chapter 9](#)). This will lead to a better understanding of the VLM and improved insights into its performance. In short, this thesis aims to test the thrust system using both gaseous nitrogen and liquid water as propellants and draw meaningful conclusions on the thruster's performance. The discussion and reasoning above can be summarised with the following research objective:

To adapt the thruster and test set-up to allow for improved results using gaseous nitrogen and liquid water as propellants and to analyse the VLM performance by comparison to previous experiments.

In the context of the nitrogen tests, improved results are defined as test results closer resembling those found by Versteeg and Hutten, instead of the decreased performance found by Cramer. In the context of the water tests, this means a measured and stable liquid flow rate and a more extensive test campaign. The research objective will be achieved by means of a brief background study, design modifications, experiments, and data analysis. To meet the research objective, the thesis will aim to answer the following research questions:

- **RQ-1:** How can the thruster be adapted to allow for improved thrust test results?
- **RQ-2:** How can the experimental set-up be adapted to allow for improved thrust test results?
- **RQ-3:** How does the VLM performance compare to that found by Versteeg [81], Hutten [28], and Cramer [15]?
 - **RQ-3a:** What is the measurement accuracy of the test results?
 - **RQ-3b:** How do the quality factors compare to those found by the previous works?

Since this thesis directly builds upon the works of many previous students, some context is required to provide the reader with an understandable and readable thesis. More importantly, this contextual background introduces the main issues addressed in this work. This necessary context will be established in [chapter 2](#). Once this groundwork is laid out, the first two research questions (**RQ-1** and **RQ-2**) will be addressed by focusing on improving the thruster and experimental set-up ([chapter 3](#)). Problems like the leakage rate will be handled to allow for more accurate thrust tests. The design and implementation of the new water feed system is also described here. After improving the thruster and test set-up, an analytical model is developed and elaborated upon in [chapter 4](#). This model is used to validate an earlier model, which is then used to predict the VLM's performance. The updated experimental set-up as well as the required calibrations are described in [chapter 5](#).

Before performing the thrust tests, some preliminary tests will be executed ([chapter 6](#)). These are mainly focused on characterising the nozzle geometry and the leak rate. Once these checks are completed, the testing phase can commence. In [chapter 7](#), the VLM is tested with nitrogen to verify its functioning and determine the effects of the improvements. Afterwards, the resistojet is tested using water ([chapter 8](#)). These tests should result in improved results that are in close agreement with those of Versteeg and Hutten. These results will be analysed thoroughly in the final chapter, [chapter 9](#). **RQ-3** is dealt with in this chapter as well. The thesis will end with a conclusion on the established research objective by answering the research questions ([chapter 10](#)). The final chapter ([chapter 11](#)) will provide recommendations for future studies.

2

Contextual Background

This chapter will discuss the current state-of-the-art regarding micropropulsion research. The focus will be on research conducted at the Delft University of Technology as this thesis is a direct continuation of previous efforts on this topic. More specifically, the works of Versteeg [81], Hutten [28], and Cramer [15] will receive the most attention, as the same thruster used by these works will be investigated in this thesis. Issues encountered by these authors are identified and analysed to lay the foundation for the work done in this work.

2.1. Micropropulsion research at TU Delft

A notable amount of research at TU Delft is focused on the development and characterisation of micro-resistojets. This research effort can generally be divided into two categories, based mainly on their manufacturing techniques: micro-electromechanical systems (MEMS) and Electric Discharge Machining (EDM). As explained before, MEMS thrusters are made using specialised equipment that is also used in the production of silicon microelectronics [16]. Mechanical and electrical parts are integrated into a single device. MEMS engines can be manufactured with high accuracies and on very small scales but at the cost of long lead times and high batch prices [14]. Moreover, they are often limited to relatively low operating temperatures because of the used materials. This limits their efficiency as well. The EDM thrusters on the other hand are made using (relatively) readily available and cheap components and offer extended temperature ranges. Both techniques have been employed to manufacture micro-resistojets at TU Delft. A significant portion of these micro-resistojets employ the Vaporising Liquid Micro-resistojet (VLM) working principle. As explained in the introduction, a VLM resistively heats a propellant (usually liquid water) and accelerates it in its nozzle to generate thrust. This working principle forms the foundation for the work presented here.

2.2. EDM-based VLMs

The thruster that is at the centre of attention in this work, has been developed and manufactured by Versteeg [81] in 2020 (see Figure 2.2). It is a Vaporising Liquid Micro-resistojet made using wire-EDM. In this work, it will further be referred to as the VLM or thruster in general. Over the five years of the VLM's existence, some notable changes were made regarding its design. To help distinguish between the different versions of the thruster, a simple naming-system is introduced. When referring to a specific thruster, the author who made the changes is added as a suffix. For example, Hutten's thruster will be referred to as VLM-RH. Moreover, Versteeg distinguishes two versions (cold and hot) in his work. These are referred to as VLM-HV1 for the cold version, and VLM-HV2 for the hot version. The subsections below will briefly introduce the preceding works and highlight the challenges encountered during them. These challenges form the foundation for the work done in this thesis. Figure 2.1 illustrates the different iterations of the VLM, including some of the most important changes made between them.

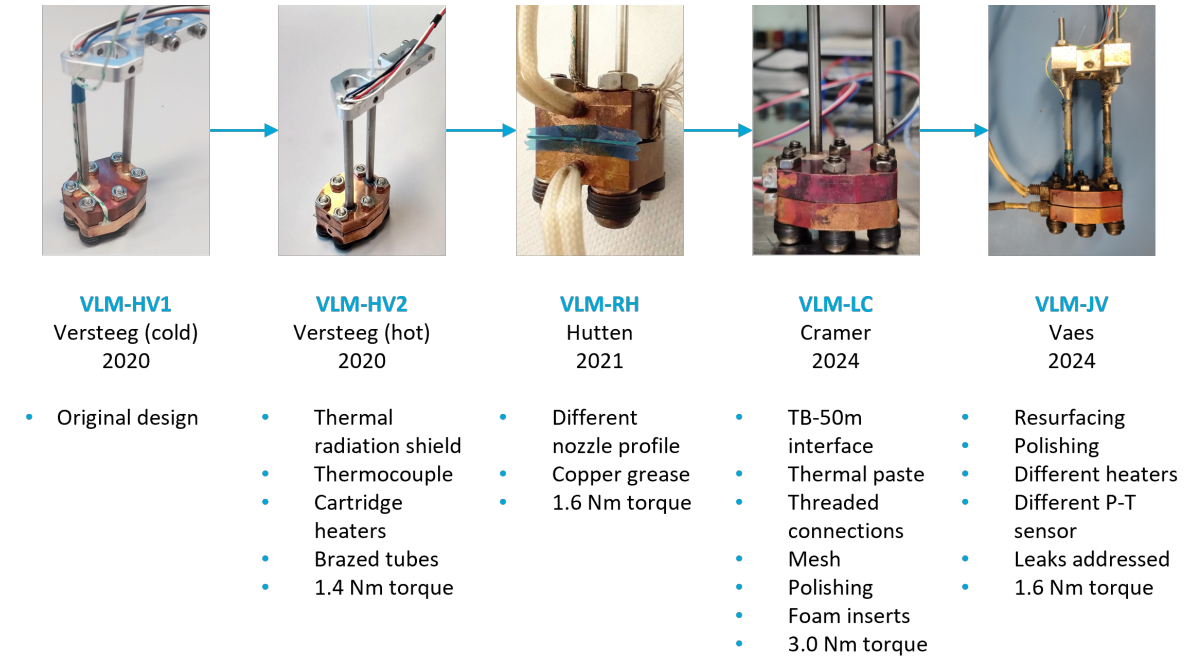


Figure 2.1: The iterations of the Vaporising Liquid Micro-resistojet.

2.2.1. VLM-HV1 & VLM-HV2

The original intent of this work was to develop a thruster that was both faster and cheaper to produce compared to MEMS-based thrusters. Versteeg opted for a wire EDM-based design to achieve this goal. The wire electric discharge machining technique uses a thin electrode wire to cut through a material by generating electric sparks. In this way, a relatively quick and cheap stainless steel nozzle profile could be cut while still maintaining a high accuracy. Furthermore, the VLM consists of two copper blocks that press into the nozzle profile. Six bolts should produce sufficient clamping force to create a leak tight seal by deformation of the softer copper. The construction forms a two-dimensional conical nozzle with an ideal throat width and height of $130\ \mu\text{m}$ and $500\ \mu\text{m}$, respectively. The nozzle exit has the same height, but an (ideal) exit width of $1072.5\ \mu\text{m}$. Note that these are the designed values, which do not represent the final measured values. These difference arise because of manufacturing tolerances and deformations due to wear and tear. The actual nozzle dimensions will be discussed in a later chapter (6).

The top copper block is connected via two stainless steel tubes to an aluminium interface. One tube guides the propellant, which enters from the top of the interface, towards the heating chamber. The other tube, the one closest to the nozzle exit, houses the P - T sensor and ensures this sensor measures the chamber pressure. Both tubes contain metal foam to aid in transferring the heat in the chamber. This has an opposite purpose for both steel tubes. For the P - T sensor tube, the foam helps distribute the heat from the chamber to the tube, protecting the sensor from possibly damaging temperatures ($>85\ ^\circ\text{C}$, [71]). For the propellant tube, the foam helps pre-heat the propellant with the heat from the chamber, so that it achieves the desired temperature faster. This addition was done later by Cramer [15]. The aluminium interface has been designed specifically to attach to the pendulum-based test bench (TB-5m). This TB-5m test bench uses a pendulum structure and a low-friction pivot to measure the thrust [6]. It is affected by a changing centre of gravity, which negatively influences the thrust measurements. Two cartridge heaters inside the copper blocks provide the necessary heat to achieve the desired chamber temperature. A rectangular metal foam block inside the chamber acts as a heat exchanger between the copper and the propellant due to its high surface area. Originally, the heaters were inserted loosely inside the blocks without any form of thermal paste. Next iterations iterated on this design.

Versteeg successfully tested the VLM with nitrogen up to a temperature of 400 °C for brief periods. These tests were conducted with the TB-5m and only lasted 15-seconds. A leak rate of approximately 0.122 mg/s was measured for the VLM-HV2. This equates to 0.7% of the expected full mass flow rate of 17.5 mg/s. His results agreed with those of a comparable micro-thruster, verifying the VLM's performance.



Figure 2.2: The original Vaporising Liquid Micro-resistojet as developed by Versteeg [81].

2.2.2. VLM-RH

Hutten [28] continued the work of Versteeg by repeating the thrust tests and testing the VLM using water as propellant. He found similar results as his predecessor, thus verifying both results. The leak rate was found to have increased to 0.240 mg/s (1.4%), after reassembly of the thruster. Indicating that the sealing method degrades over time. The leak rate was deemed acceptable since it was still below 5%. Furthermore, Hutten successfully carried out water experiments at 300 °C. The water flow was controlled using a syringe pump, which expelled a constant volumetric flow. This introduced some difficulties with maintaining a constant chamber pressure and accurately predicting the actual mass flow. Bubble formation inside the (flexible) propellant lines resulted in sudden pressure bursts and chaotic thrust production (see chapter 6 of Hutten's work). Moreover, the dependence of the TB-5m on the centre of gravity, introduced additional uncertainty in the measured thrust.

Since the work presented here will also perform experiments with water, Hutten will be used as a main reference point for areas of improvement and performance comparisons. Based on his recommendation, a liquid mass flow meter will be implemented to directly measure the water flow, thus reducing some uncertainty. Moreover, a feed system based on the use of a pressurised tank, will be developed as suggested by Cramer (see chapter 3). A similar system has been used previously by Krusharev [36] and Stohr [64], although they use it in a blow-down configuration. By placing this tank inside the vacuum chamber and venting the air from it, bubble formation will hopefully be prevented.

Like Versteeg, Hutten also established an analytical tool to estimate the VLM's performance, which is described in depth in the second chapter of his thesis. This tool, called the Resistojet Performance Tool (RPT), is hosted publicly on GitHub¹. Hutten introduced changes to Versteeg's model by correcting small errors and improving some definitions and assumptions. Afterwards, he verified that both models showed a similar output with a maximum deviation of 2% from each other. Earlier Versteeg validated his model for the experimental thrust (F), mass flow (\dot{m}) and specific impulse (I_{sp}), as the difference between the predicted and measured values were within 10%. However, the differences between the modelled and actual discharge coefficient (C_d) and specific impulse efficiency ($\xi_{I_{sp}}$) were more

¹The link to Hutten's Resistojet Performance Tool: <https://github.com/RickHutten/ResistojetPerformanceTool>

significant. The discharge coefficient was overestimated with 5 to 10%, while the specific impulse efficiency was underestimated with 10 to 15%, depending on the throat Reynolds number (Re_t). This Reynolds number ranged from 1100 to 2500. Hutten's results showed a similar discrepancy for C_d and ξ_{Isp} , indicating that the model could be improved in this area. This will not be the focus of this work, however. Figure 2.3 shows a comparison of the experimental results of Versteeg, Hutten, and Bayt [3] with the predicted values of the RPT. Bayt also developed and tested a micro-propulsion system, which Versteeg used as a reference for his VLM design. Bayt's results were analysed by Versteeg to see how well the thrusters compare and to verify his test results.

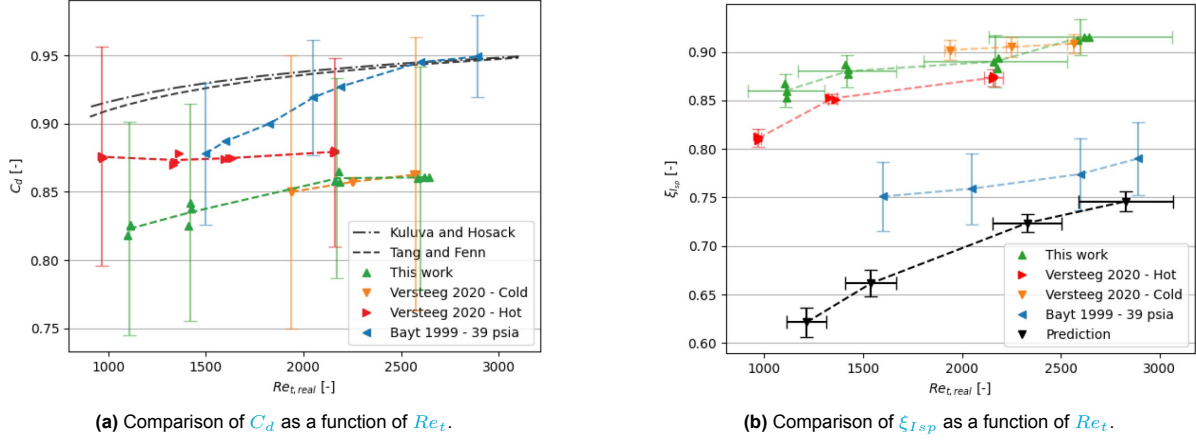


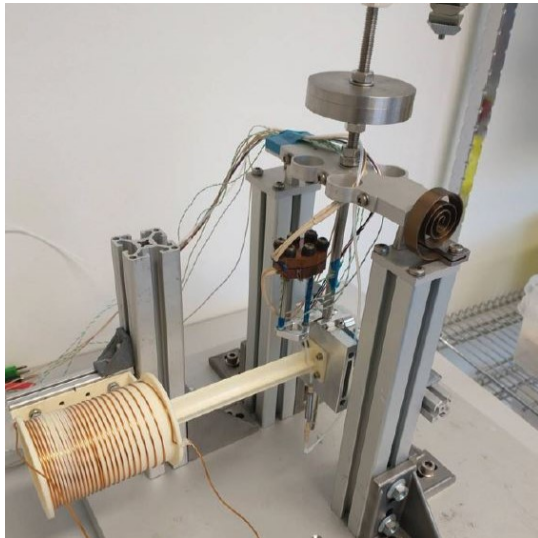
Figure 2.3: Comparison of C_d and ξ_{Isp} as a function of Re_t with (nitrogen) experimental results of Versteeg [81], Hutten [28], and Bayt [3] and modelled output of the RPT [28].

To determine the validity of Hutten's model, an independent model will be developed in chapter 4. This model is used to check the previous one and simplify its use. The output of the analytical model will be used to predict the VLM's behaviour, which aids in the development of the test set-up and plan (chapter 5). A later comparison (chapter 9) will determine whether the model output agrees with the measured results or that the differences have increased.

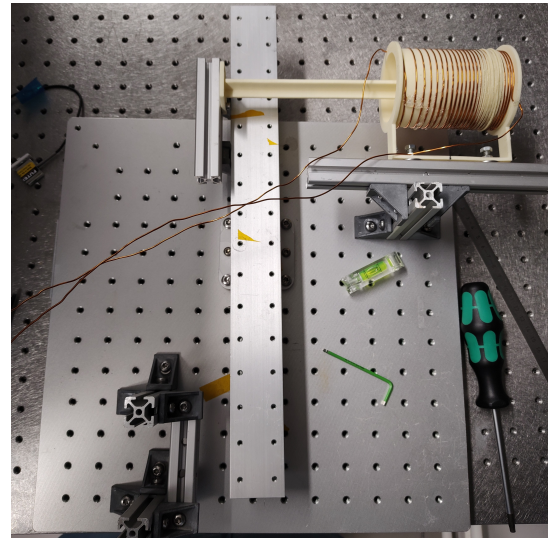
2.2.3. VLM-LC

Directly preceding this work, Cramer [15] introduced several major changes to the VLM (Figure 2.6a) and test set-up. Due to a changing centre of gravity of the thruster during operation, the TB-5m introduced some uncertainties in the measurements. Therefore, Cramer decided to switch to the torsional test bench, the TB-50m (see Figure 2.4 for a visual of both test benches). It is a torsional test bench, which was developed by Janssens [30] and calibrated again by Takken [69]. It consists of a horizontal beam, suspended on a low friction bearing. The thruster is placed on one end of the beam, while a load cell is placed on the opposite side. When the VLM produces thrust, it causes a rotation, which is distributed through the beam to the load cell. This sensor subsequently registers the rotation with a change in voltage. Cramer used the Futek LRF400 load cell for her experiments. Unfortunately, this sensor broke during another thesis, so the Futek LSB200 will be used as a replacement in this work. More on the workings of this sensor (and others) is described in chapter 5. The thrust bench has a calibrated range from 0 - 12.3 mN with an uncertainty of $\pm 1.43\%$. This is sufficient for the expected produced thrust between 5 and 15 mN.

Besides being independent on the centre of gravity, the TB-50m has another advantage over the TB-5m. Since the horizontal beam has a lot of threaded M3 holes, it is relatively simple to alter the position of components. In this way, it is easy to play with the moment arm and thus the force acting on the load cell. This property will be exploited to artificially enhance the force measured by the load cell (see chapter 5).



(a) The TB-5m thrust bench [28].



(b) The TB-50m thrust bench.

Figure 2.4: The pendulum (left) and torsional (right) test benches used throughout different works.

Besides its advantages, the introduction TB-50m also brings forth an important drawback. Cramer namely describes a noticeable amount of drift in the thrust signal (see chapter 6 of her work). She believed this drift could be attributed to the test set-up. The drift is especially noticeable during her calibration campaign when the test bench is fully loaded with all necessary equipment and exposed to testing conditions (vacuum and heaters on). Cramer mentioned several factors that could cause the signal drift, such as: wire stiffness, an uneven floor (test bench not level and wobbly), environmental influences (humidity and temperature), and friction in the test bench's bearing. This work will perform an extensive test bench calibration campaign to gain more insight in this drift behaviour (see [chapter 5](#)). During the thrust tests, the drift can be compensated for relatively easily as shown in chapter 7 of Cramer [15], which will also be illustrated in [chapter 5](#) and [7](#) of this work.

The changing of the used test bench also affects the thruster design directly. The interface Versteeg developed was designed specifically to fit the TB-5m. So, Cramer designed a new interface that is compatible with the TB-50m thrust bench. This is done with four M3 holes to allow for a bolted connection to the thrust bench. [Figure 2.5](#) shows the old and new interface side by side. The new interface was found to have some problems with leakage, which will be described in [chapter 6](#).

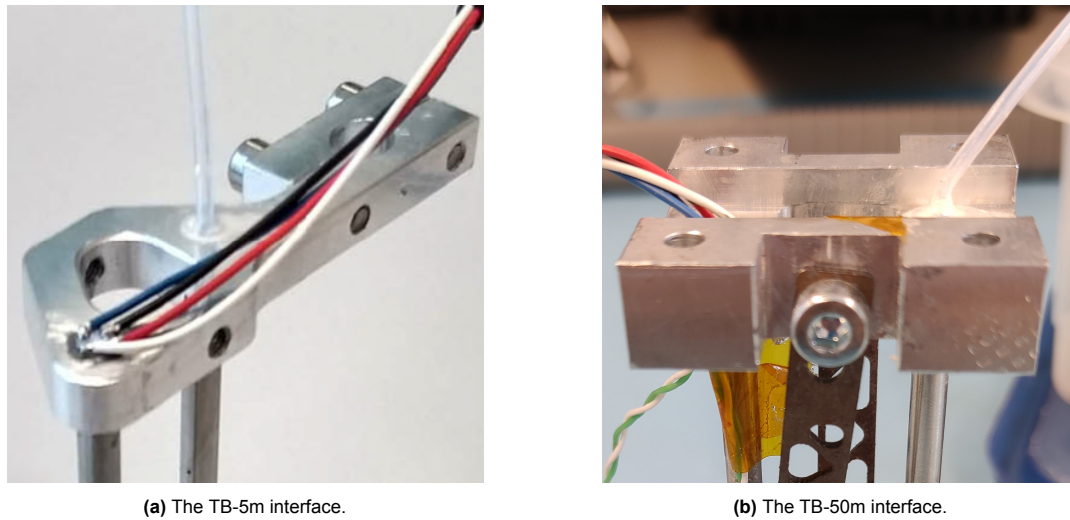
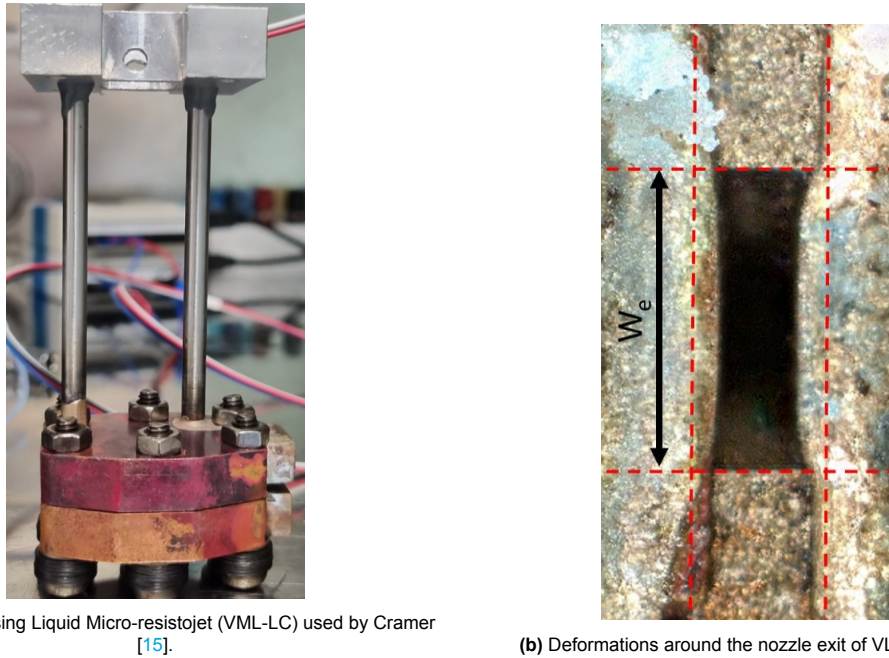


Figure 2.5: The pendulum (left) and torsional (right) interfaces as designed and manufactured by Versteeg [81] and Cramer [15], respectively.

As alluded to before, the heating components of the original VLM also have seen some changes. Earlier works indicated that the heaters were at risk of popping out of the copper blocks during operation. Moreover, the cartridge heaters could overheat and break due to their loose fit and thus lack of conduction inside the blocks. Cramer successfully tackled these issues by attaching threaded blocks to the copper blocks via brazing and threaded sleeves to the heaters using thermal sealant. In this way, the cartridge heaters are held in place via a threaded connection. A thermal paste consisting of a gallium-indium-tin alloy is used to conduct the heat towards the copper. Although these improvements solved the problems they were designed for, they also introduced new challenges. For example, the addition of the threaded blocks makes it even harder to image the nozzle geometry, as will be explained in [chapter 6](#). Moreover, the threaded sleeves were hard to remove from the heaters, as explained in the next chapter (3).

Since the resistojets have microscopic dimensions, small deformations, especially near the nozzle throat, may have significant effects on the thruster's performance. It is therefore important that the nozzle area is rectangular. Unfortunately, Cramer already noticed drastic deformations around the nozzle exit due to an excessive clamping force (see [Figure 2.6b](#)). This likely has a negative influence on boundary layer forming and thus on the VLM's performance. The enhanced clamping force (3.0 Nm) was deemed necessary to reduce the leak rate to an acceptable level (0.22 mg/s or 1.3%). This is a direct effect of the reassembly of the thruster. After some time, the sealing capacity of the copper diminishes thus requiring a higher clamping force. An alternative way of achieving a satisfactory leak rate is to restore the sealing surface to its original state, which can be done by resurfacing the copper blocks. This and other options will be explored to alleviate the leaking issue and prevent leaks for future iterations. See [chapter 3](#) for a complete description.

Cramer performed several measurements using nitrogen. The subsequent data analysis revealed a significant deviation from the results obtained by Versteeg and Hutten. Not only the nozzle geometry had deteriorated a lot, also the measured thrust and specific impulse were nearly 50% lower than previously found. The discharge coefficient and specific impulse efficiency decreased with roughly 20% and 40%. Cramer hypothesised that this degradation in thruster performance could be attributed to the changed experimental set-up and deteriorated VLM. However, more data is necessary to determine the exact cause of the altered VLM performance. This thesis will partially focus on replicating Cramer's test campaign to determine whether the changes made throughout the work, have resulted in an improved thruster.



(a) The Vaporising Liquid Micro-resistojet (VML-LC) used by Cramer [15].

(b) Deformations around the nozzle exit of VML-LC [15].

Figure 2.6: Overview (left) and detailed view (right) of the Vaporising Liquid Micro-resistojet (VML-LC) used by Cramer [15].

2.3. Conclusion

This chapter focused on three works specifically, those of Versteeg [81], Hutten [28], and Cramer [15]. These authors have worked with and experimented on the same vaporising liquid micro-resistojet as the author of this work. The VLM and test set-up under investigation have seen some significant changes throughout the years. Each iteration had its own set of advantages and disadvantages, as described above. This thesis will address some of the challenges encountered by others in an attempt to answer the research questions posed in the previous chapter.

The most important lessons to this work are taken from both Hutten and Cramer. Hutten is the only predecessor who worked with water as propellant. Based on his experiences, a different feed system will be envisioned, and a liquid mass flow meter will be implemented (chapter 3). Cramer noted a significant deviation in VLM performance and load signal drift, which both could not be explained entirely. To restore the thruster to its earlier state and simultaneously reduce the leak rate, several options will be explored (chapter 3) and their effects will be measured (chapter 6). An independent analytical model will be developed in chapter 4 to validate Hutten's RPT and to predict the thruster's behaviour. The test bench will be calibrated again to increase the understanding of the measured thrust signal drift (chapter 5). Lastly, an extensive test campaign using both nitrogen and water will be executed to determine the VLM's performance (chapter 7 and 8). This campaign will give more insight in the thruster's functioning after the changes made to it and the test set-up. The insights gained from the tests are analysed and compared to the analytical model's output and previous works (chapter 9). This makes it possible to evaluate the achieved results of this work, draw meaningful conclusions on the research objective, and provide recommendations for future work (chapter 10 and 11).

3

Design Modifications

This chapter will discuss the adaptations envisioned to improve the current thruster and experimental set-up. These changes are meant to address the problems described in the previous chapter. The chapter is divided in improvements made to the VLM itself ([section 3.1](#)) and improvements made to the test set-up ([section 3.2](#)). These are further split in subsections dealing with disassembly and assembly of the VLM, for example. Of the test set-up improvements, the new water feed system is the most important ([subsection 3.2.2](#)). An overview of the expenses made during this thesis, is provided at the end of this chapter ([section 3.3](#)).

3.1. VLM Improvements

As introduced in the previous chapter, earlier works have highlighted some flaws in the VLM design that have only grown over the years. Leaks have steadily increased since the first assembly of the thruster, while the nozzle geometry has deviated further from the original design. The goal of this section is to identify possible solutions to address these flaws and select the optimal one for this work ([subsection 3.1.2](#)). Moreover, subsections are dedicated to the disassembly and assembly of the thruster ([subsection 3.1.1](#) and [3.1.3](#)).

3.1.1. VLM Disassembly

In order to implement changes to Cramer's VLM (VLM-LC), it needs to be disassembled. However, before this was done, some preliminary tests were executed. These preliminary tests consist of an optical characterisation, leak testing, and nitrogen tests. As described in [chapter 1](#), the nitrogen tests' goal is to gain experience in conducting and analysing tests, which will aid the later test campaigns. The optical characterisation and leak tests will be described later in [chapter 6](#) and have a more quantifiable goal. By performing these tests prior to the design modifications, the effect of them can be charted more easily. The modifications should result in an improved nozzle geometry and leak rate. The disassembly itself is not a complicated affair. However, it should be done with care. To help future iterations, a disassembly procedure is established, which can be found in [section D.1](#). The same appendix ([D](#)) also shows other procedures relevant to this work.

3.1.2. Thruster body improvements

As described by both Hutten [[28](#)] and Cramer [[15](#)], the sealing capacity of the copper blocks is not perfect. The seal is formed by mechanically clamping the copper blocks to the stainless steel. Since the copper (Cu-ETP) has a higher ductility [[11](#)], it will deform sooner and fill the gaps between the metals, creating a seal. Six bolts are used to distribute the clamping force evenly over the thruster body. However, as noted by Cramer, the sealing surface has degraded over time. This became apparent from the poor results of the polishing effort (see chapter 4 of her work). [Figure 3.1](#) shows the top and bottom blocks after polishing. The fact that only parts of the sealing surface are polished (visible as a more reflective surface), indicates that the seal has lost some of its integrity. Because of this, the leakage rate has increased over time.

(a) Top block after polishing with 6 μm .(b) Bottom block after polishing with 6 μm .**Figure 3.1:** Thruster body after polishing of the sealing surface [15].

Two options to minimise the leaks were identified by Cramer [15]; remake the sealing surface or increase the clamping force of the bolts. The first option requires a computer numerical control (CNC) machine to remove the current (damaged) sealing surface. Since the sealing surface is raised with 250 μm in comparison to the other surface, only this amount needs to be removed from the raised surface. After this, the machine can manufacture a new, functional sealing surface. This option has the added benefit that small improvements in the design of the sealing surface could be implemented. For example, chamfered (45°) edges, instead of straight ones can be used for the sealing surface. This idea of Versteeg [81] should result in a better metal-metal seal. The major drawbacks of this option are that using the CNC machine is costly and time-consuming. Cramer [15] thus opted for the alternative solution.

The second option Cramer identified was to increase the torque on the bolts in order to clamp the blocks more tightly on the nozzle profile. Originally, a torque of 1.4 Nm was sufficient for an adequate seal. Hutten [28] increased this to 1.6 Nm in his work. Eventually, Cramer tightened the bolts to a torque of 3.0 Nm, which resulted in a leakage rate of approximately 1.27%. This was deemed acceptable since the uncertainty of the used thrust and mass flow sensors has a similar order of magnitude. Cramer noticed that tightening the bolts this severely resulted in plastic deformation of the copper. Consequently, the seal will lose its integrity when the force on it is removed. Moreover, the excessive force on the copper blocks has resulted in a deformation of the nozzle exit (see Figure 3.2). The exit is no longer rectangular, but now features irregular, curved edges, making it difficult to quantify and model it.

Although tightening the bolts more presented a simple, cost-efficient solution to obtain a sufficient seal, it came with clear drawbacks. Plastic deformation of the copper and partial obstruction of the nozzle exit introduced new issues and uncertainties. Since this might be one of the reasons for the decreased thruster performance encountered by Cramer [15], it is decided to attempt to improve the situation. The goal is two-fold; achieve a sufficiently low (preferably around 1%, but 5% at most) leakage rate, and restore the original, rectangular nozzle exit. The exit should have dimensions of approximately $1078 \pm 8 \mu m$ in width and $538 \pm 8 \mu m$ in height. These were the dimensions as measured by Hutten [28], who used the same nozzle profile as this work. The nozzle characterisation is performed in chapter 6.

Multiple options to achieve the mentioned goals were identified, which are described in the next couple of subsections. The first option has been recommended by Cramer [15]; resurfacing the copper blocks. The other options take inspiration of previous works and vary in complexity. Each option will be described briefly, after which a trade-off analysis will be conducted in Figure 3.1.2. This section concludes with the execution of the selected option and discusses its results (Table 3.1.2).

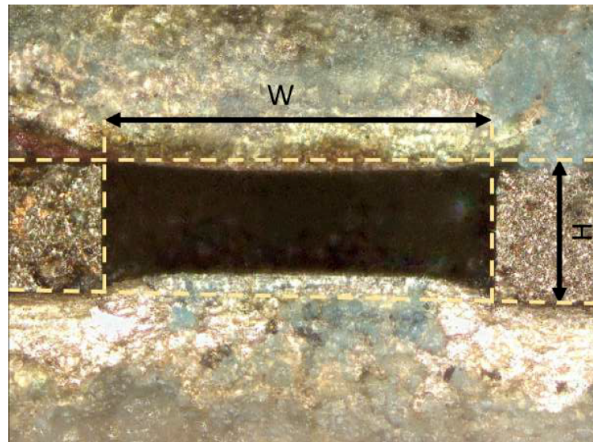


Figure 3.2: Nozzle exit after assembly and tightening by Cramer [15]. The deformation of the once-rectangular nozzle exit is clearly visible.

Resurfacing the current thruster

As mentioned before, the resurfacing will (partially) be performed by a CNC machine. The current (degraded) sealing edges might also be removed beforehand via sanding. Although this is a more inaccurate method, it can be done by hand, thus saving costs. On the other hand, the removal of the thin edges with the CNC machine will probably not require much additional time (and thus costs), so the benefits of sanding by hand might be marginal. To prevent possible mistakes by manually adapting the thruster, the idea of sanding by hand is dropped.

As mentioned above, Versteeg [81] proposed to add a 45° chamfer to the sealing edges. This will help reduce stress concentrations in the material aside from the sealing surface itself. Instead of the original straight edges, these chamfered edges could be implemented, if the thruster is resurfaced and it fits within the time- and budget constraints.

A CNC machine is available at Dienst Elektronische en Mechanische Ontwikkeling¹ (DEMO), a facility of the TU Delft that specialises in the design and development of experimental setups and prototypes. This machine will be chosen to perform the necessary operations. Versteeg [81] originally produced the thruster using the CNC mill in the TU Delft Dream Hall since he had friends there who were willing to manufacture it free of charge. Unfortunately, this is not an option for the current author, so the CNC mill of DEMO must be chosen. Based on the quotation of Versteeg, the total milling costs were estimated around €800. This included the machining of the thruster body, as well as two aluminium pieces of the top interface. All in all, the total time to manufacture the components was roughly 8 hours [81]. Since resurfacing the copper will likely require less time, the costs will be significantly less as well. After discussing the necessary operations with the DEMO team, it is estimated that resurfacing should take approximately 3 hours, which leads to a cost estimate of roughly €120 (hourly rate of €40).

The estimation above is based on purely replicating the design of Versteeg. While restoring the original sealing method should result in an adequate seal initially, it is again expected to degrade after several uses. This serves as an incentive to search for possible improvements. Several options have been identified, which will be elaborated on below. Some options maintain Versteeg's design, while others alter the design slightly.

Implementing a gasket

The most straightforward option to reduce leaking, is to implement a gasket. This is also commonly used in vacuum technologies ([32], [54]). A gasket is a softer material that is squeezed between two

¹The website of DEMO: <https://www.tudelft.nl/demo>

harder materials and fills the macro and micro gaps in the components. In this way it prevents gases and fluids from escaping between the connected components. Gaskets were also considered by Versteeg, resulting in the use of the copper thruster blocks as gaskets. This has proven to not be without drawbacks. Only polymer gaskets were mentioned as alternatives, but these were quickly disregarded due to their inability to withstand high temperatures ($>325\text{ }^{\circ}\text{C}$, [32]). Versteeg thus decided on the use of copper as gaskets. This decision was supported by the fact that this metal has a high thermal conductivity and could thus also function as a proper heat conductor. Moreover, it is easy to manufacture and assemble by hand, Versteeg argued. The sealing method worked initially. Unfortunately, as noted by others, the seal has degraded over time due to plastic deformation.

Fortunately, the challenges provided by this project are not entirely unique. The combination of high temperatures and vacuum environments is also encountered in the industrial applications [44]. Consequently, several gasket options exist to use in these situations. A wide variety of materials are available, each with their own advantages and disadvantages. After a brief background study and consulting an expert of *Wagner Gaskets & Seals*², graphite gaskets were decided to be most suitable for usage in the thruster. They combine resistance to high temperatures ($> 450\text{ }^{\circ}\text{C}$), impermeability to gases and liquids, and the possibility to produce it in irregular (non-circular) shapes [60]. After communicating the thruster's requirements, the experts at *Wagner Gaskets & Seals* recommended their Sigraflex® APX pure graphite foil with a thickness of 0.50 mm (see subsection C.1.1 for the material's datasheet). This foil is relatively safe and easy to work with and can be produced in the right shape.

The desired shape will be cut out of the foil using a laser. To simplify this operation and have some extra strength (more material) in the gasket, it was decided to replicate the shape of the thruster blocks, without the raised sealing surface. This is illustrated in Figure 3.3. It is reasoned that including the sealing surface in the design would increase the fragility of the gasket significantly. This would be especially true at the nozzle area as it would split the gasket in half. In theory, the use of the graphite gasket should eliminate the reason for the sealing surface to be there in the first place. As an additional benefit, introducing the gasket means that no new sealing surface is needed, which means that the CNC machine is not required and thus saves costs. On the other hand, the gasket can also be combined with a new sealing surface, resulting in an extra leak prevention method. The gasket's shape can be manually edited a little bit after its production to make it easier to integrate. Unfortunately, the addition of this option might lead to a different nozzle height. The severity of this effect has to be determined empirically. The argumentation above is all under the assumption that the gasket can be manufactured cheaply, which is not the case. Fortunately, Cor Wagner of *Wagner Gaskets & Seals*, was incredibly kind and willing to sponsor the production of 10 gaskets, making this option a real possibility.

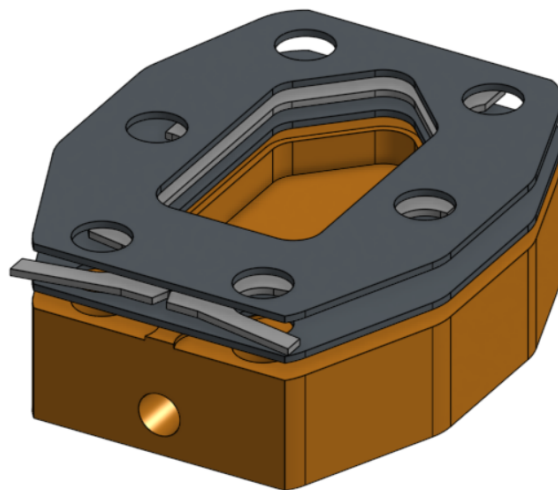
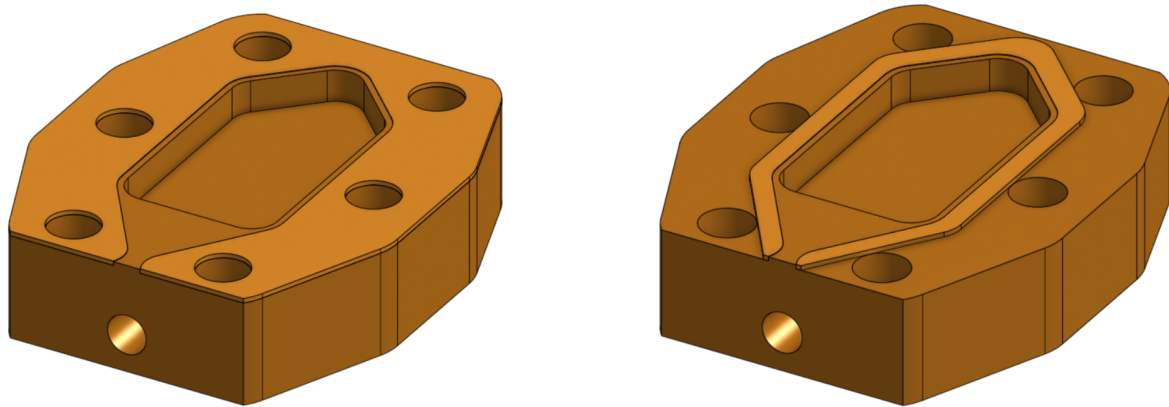


Figure 3.3: Design of a graphite sealing gasket.

²The website of *Wagner Gaskets & Seals*: <https://www.wagnergaskets.nl/>

Instead of a graphite gasket, ductile metals also offer a possibility. Like in the original design, a relatively soft metal such as copper can be used. Contrary to Versteeg's design, this metal piece will not be part of the thruster body, but will be a separate part. The goal should be that only this piece will deform (plastically). Because it is separate, it can be easily manufactured and replaced. One possibility is the addition of a copper ring around the sealing edges. This ring thus acts as a gasket. Copper is an ideal candidate as it combines high thermal conductivity with good malleability [32]. Applying this solution the VLM thruster results in an open ring that follows the current sealing edge. The ring will be slightly thicker than the current height of the seal (0.25 mm), which causes the ring to be squeezed and thus creating the seal, instead of the sealing edge of the thruster blocks. After a while, the ring will have plastically deformed too much and needs replacing. Copper sealing rings are readily available and cheap; however, they do not have the required (complex) shape. This is the major drawback of the solution; creating the right shape cannot be done by hand because of the small and precise dimensions. It requires a computer-guided machine, such as a laser cutter or wire-EDM machine. Figure 3.4 shows two designs of the envisioned copper sealing ring, one that covers the entire copper block, and one that is much slimmer. The material costs for this solution are expected to be reasonably low (\sim €20). The machining costs, however, will be more expensive. Based on an estimate obtained by Versteeg for using the wire-EDM machine of DEMO, machining the seal is estimated at around €100. Communicating the exact design with the DEMO technicians will result in a more accurate estimation.



(a) Copper sealing ring covering the entire thruster block surface.

(b) Thin copper sealing ring.

Figure 3.4: Two designs for the copper sealing ring.

Closing the nozzle profile

Gaskets are not the only possibility to reduce leaking. The leaks are thought to originate from the fact that the nozzle profile is open on two sides, which adds a lot of possible leakage locations. Closing off these sides will thus reduce the leakage issues. This can be done in several ways. For example, thin covers can be attached to the nozzle profile, or the profile can be permanently bonded to the copper blocks. An added benefit of this solution is that it fixes the nozzle profile in place, thus preventing it from deforming as much. Consequently, the uncertainties in the nozzle dimensions will be reduced as well. MEMS-based thrusters employ a similar tactic [48]. Because of their fabrication method, at least one side (the bottom) is fixed to the rest of the thruster. The other side (the top) can be fixed by anodically bonding a sheet of borosilicate glass on top or by fusion bonding it to another silicon wafer [81]. Unfortunately, due to the usage of different materials and limited (TU Delft) resources, this is not an option for the steel nozzle profile. Instead, several other options have been identified. Versteeg already considered these options in his work and established the following list:

- Glue
- Brazing
- Beam or arc welding
- Mechanical welding

Glues have been used in the past to reduce leaks [36], but often limit the maximum operating tem-

perature (300 °C). Moreover, all four bonding options will likely interfere in some way with the nozzle geometry, which should be avoided. Another drawback of closing the nozzle profile is that it is a permanent option. So, the thruster cannot be disassembled without breaking the bond. The costs and time necessary to implement one of these options varies significantly. Glueing can be done cheaply and fast; while brazing and welding requires more time and resources.

As introduced earlier, an alternative option to close the nozzle profile is to add a thin sheet (cover) of a conductive material (copper or steel) to the top and bottom of the nozzle profile, effectively closing of the open sides (Figure 3.5 illustrates this concept). These thin sheets can be made using the same machinery as the existing profile (wire-EDM) but alternative techniques, such as water jet cutting, can also be employed. The covers need to be bonded to the nozzle profile in some way, which can be done using the techniques mentioned above. The effectiveness of this option needs to be delved into more, as it introduces some new challenges. For example, this solution will result in a decreased chamber volume since it will be partially blocked by the thin sheet. Thus, it necessitates a new heat exchanger. Furthermore, the thermal conduction properties are severely altered because of the addition of extra material.

The options discussed in this section show some promise, but they also introduce a lot of new challenges. These should first be addressed, before attempting to implement one of the discussed solutions. So, more research is required to properly evaluate the effectiveness of closing the nozzle profile. However, this falls outside of the scope of this work.

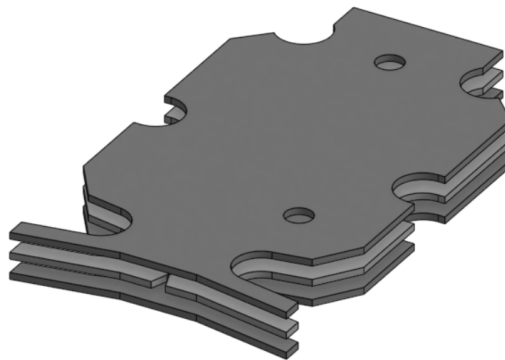


Figure 3.5: Design of a nozzle cover.

Remaking the thruster body

The final option that is considered here to improve the thruster is a completely new iteration of the current VLM design. It involves replacing a significant number of components because the materials of the thruster body and nozzle profile will be 'swapped'. The thruster body, which currently consists of copper, will be machined out of a stainless steel block using a CNC machine. The nozzle profile will be made out of a copper plate using wire-EDM. The thruster body's design will remain largely the same, but some improvements can be implemented. These improvements have already been suggested by Versteeg (see chapter 5 of his work) and include chamfering the sealing and heating chamber edges. This should result in some stress reduction in the material as well as an improved sealing surface. The nozzle profile might change slightly in design to make it easier to control the throat width. This can for example be done using guiding pins through the profile. These pins prevent the width from increasing.

The benefit of fabricating the thruster body out of a harder material (such as steel) and the nozzle profile out of a softer, more ductile material (such as copper) is that only the nozzle profile will deform. The nozzle profile itself will thus function as a sealing gasket. After a while, the created sealing surface will lose its integrity and needs replacing. However, this is much easier to realise than replacing the thruster blocks. The blocks have a lot of connections to sensors, feed lines, and structural components, while the profile has none of this. So, it is much easier to replace. Like done by Versteeg, multiple profiles

can be manufactured at once. Consequently, when the leak rate has increased to an unacceptable level (>5%), a profile can easily be exchanged for a new one.

A possible drawback of this new VLM design might be the consequences it has on the thruster's thermal characteristics. Copper is a better thermal conductor than stainless steel [11]. Unfortunately, this design change means that the heat must be transported mostly through the steel. The heat conduction will thus be less effective. As a result, the heaters have to deliver more heat (power) to the system. Whether this power increase is too severe for the current heaters, has to be investigated further. This analysis is out of the scope of this work.

Another drawback results from the use of the nozzle profile as the sealing gasket. It is meant to deform and create a tight seal. However, this might also introduce deformations and uncertainties in the nozzle's dimensions. The nozzle's width could be fixed with guiding pins, as mentioned before. The height might be more difficult to control. The severity of the deformations is hard to predict, thus this option has an increased risk compared to others.

A rough cost estimation for this new VLM design can be made, based on Versteeg's experiences. Machining the thruster blocks roughly takes 6 hours. At an hourly rate of €40, this adds up to €240. Moreover, manufacturing the new nozzle profile, will roughly cost €160, based on Versteeg's estimate. Additionally, the aluminium interface and steel tubes need to be removed from the old thruster and brazed or welded to the new thruster. Assuming the prices have not significantly changed in 4 years, brazing the steel tubes to the new thruster will cost roughly €40. In total, the discussion above result in an estimate of €440. This estimate assumes that a lot of material can be reused and does not have to be bought again.

Trade-off analysis

To determine which thruster body improvement option provides the optimal solution for this thesis, a short trade-off analysis is conducted. To keep the scope of this analysis somewhat manageable, a simple trade-off summary table is established [22]. The concepts will be judged based on several criteria, each with the same weight factor. The following criteria are established: cost, time to fabricate, time to acquire, complexity, and chance of failure/risk. The trade-off is shown in Table 3.1. This table also includes rows detailing the necessary materials and machinery involved in the concepts. Most criteria are quite straightforward and are based on preliminary estimates. For example, the expected costs, time to fabricate, and time to acquire should be kept to a minimum. Time to acquire includes the estimated shipping time. Complexity and chance of failure/risk are judged on the brief studies performed in the preceding subsections and on the author's best estimates. The trade-off graphically shows how well a concept meets a certain criterion by the use of colours (green, red, orange) and indicators (+, -, /).

Concept	Resurfacing	Graphite gasket	Copper gasket	Closing nozzle profile	Remaking thruster
Cost	€120 (/)	€0 (+)	€120 (/)	€120 (/)	€440 (-)
Time to fabricate	3 hours (+)	N.A.	3 hours (+)	3 hours (+)	9 hours (-)
Time to acquire	3 days (+)	1 week (/)	1 week (/)	1 week (/)	2 weeks (-)
Complexity	Low (+)	Low (+)	Low (+)	High (-)	High (-)
Chance of failure/ Risk	Low. Good initially, but degradation over time. (+)	Medium. Added inaccuracy in nozzle throat. (/)	Medium. Degradation over time. (/)	High. Permanent bonding, Added inaccuracy in nozzle throat (-)	High. Lots of variables and challenges.(-)
Materials	Copper thruster blocks	Graphite foil	Copper sheet	Thin steel/ Copper sheet	Steel thruster blocks Copper nozzle profile
Required machinery	CNC machine	N.A.	Wire EDM/ Water jet cutting	Wire EDM/ Water jet cutting	CNC machine Wire EDM/ Water jet cutting Welding

Table 3.1: Overview and trade-off of the different concepts for decreasing the leakage rate. Green (+) means it is the best option, while red (-) means it is the worst option of that row. Orange (/) is in between.

From the compact trade-off analysis, it can be concluded that the resurfacing option is most favourable.

It scores best overall (most plusses), while still having reasonably low costs. This outcome aligns well within the limited scope of this thesis and should be easy to execute. Resurfacing had already been suggested by previous authors, so the option is also a bit safer compared to the more innovative alternatives. DEMO will thus be contacted to perform the resurfacing operation.

As an additional measure, the graphite gasket solution will also be attempted. Since this solution could be acquired free of charge, it was deemed to be worthwhile to implement it as well. [Table 3.1](#) proves that the graphite gasket scores reasonably well in the trade-off analysis, so it is sensible to attempt integrating it. However, this solution is seen as an extra way to reduce and prevent leaks and is thus not an essential part of the realised improvements.

The other three concepts are disregarded and not further elaborated upon. They might also offer interesting solutions to the problems mentioned in this chapter, but they require more research before they can be implemented. Especially the last two concepts (closing the nozzle profile and remaking the thruster body) introduce new challenges which need to be properly addressed first. Unfortunately, this thesis's scope has its limit. Therefore, it is left for future research to properly investigate and elaborate these concepts.

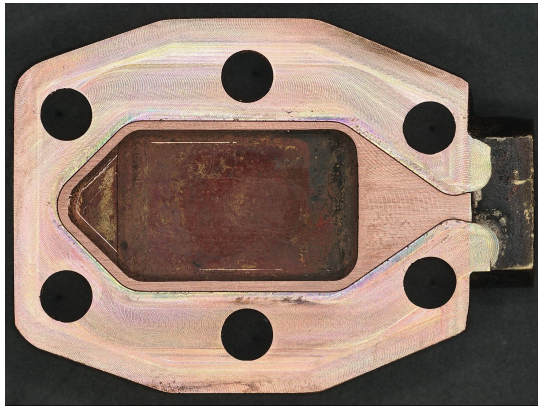
Resurface results

As described in [Figure 3.1.2](#), the copper blocks have been sent to DEMO for resurfacing using their CNC machine. It was decided to use the same design made by Versteeg, without alterations. This was done to save time and because they were not seen as essential improvements. A layer of 0.3 mm was removed to acquire a clean and new surface, after which the new sealing edge was milled. As DEMO had other assignments with more priority and no urgency was expressed, the operation took roughly one-and-a-half weeks. This was unfortunate, but this waiting period allowed for other work to be done, such as report writing. DEMO was contacted afterwards to inquire about the final costs of the resurfacing operation. Sadly, these were significantly higher than expected. The final costs for resurfacing were €642.59. Seen that the initial estimate was €120, this is an increase of over 500%. DEMO stated that their initial estimate did not include every necessary operation (e.g., programming, and milling hours). So, the total time for the resurfacing operation is approximately 16 hours, based on an hourly rate of €40. When cooperating with DEMO (or other parties), it is thus important to clearly communicate about the total time and costs beforehand to avoid unexpectedly high costs. All expenses made throughout the thesis are summarised in [Table 3.2](#) at the end of this chapter.

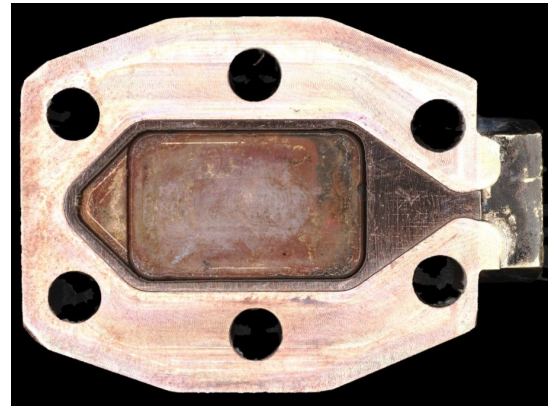
After machining, the blocks were polished using the DAP-7 polishing machine, which can be booked via Lab Servant, after following a short training³. The procedure as laid out by Versteeg and Cramer was followed for polishing. In short, diamond polish is used in consecutive steps whilst reducing grain size from 6 to 1 μm . However, seen that the passes of the CNC machine are quite rough, sandpaper with 2000 and 4000 grit was first used to get rid of the worst scratches. [Figure 3.6](#) visually shows the result of the polishing procedure on the bottom copper block. The end result is a mirror-like surface with only minor scratches visible when viewed under a certain angle. Although a few scratches remain, the surface is judged to be sufficiently flat and smooth.

To quantify the smoothness, or surface roughness, the bottom block is placed under both the Keyence VR-5000 and Keyence VK-X1000. The latter is used for measuring the surface roughness, as this was advised by technical staff due to its higher optical qualities. Using the ELWD 20X WD11 objective, the surface has been mapped and a line surface analysis was performed. This is a build-in function of the microscope software and very intuitive to use. The analysis indicated a final surface roughness of $R_a = 1.095 \mu\text{m}$. A surface roughness value around 1 μm ($\sim 1\%$ of the throat width) is deemed acceptable to prevent negative effects on the nozzle performance [39]. The found roughness value is thus accepted and with the completion of this step, the improved VLM can be assembled again.

³Contact person: P.G.Marchese@tudelft.nl



(a) Bottom copper block before polishing.



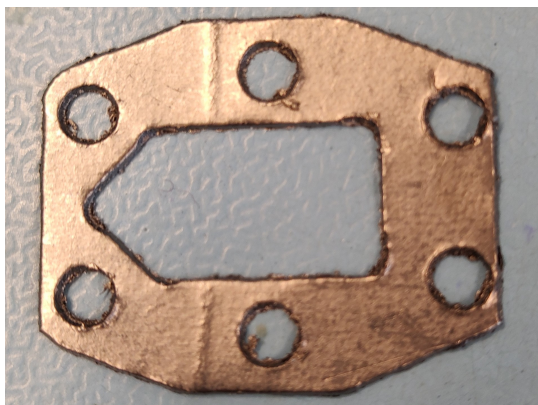
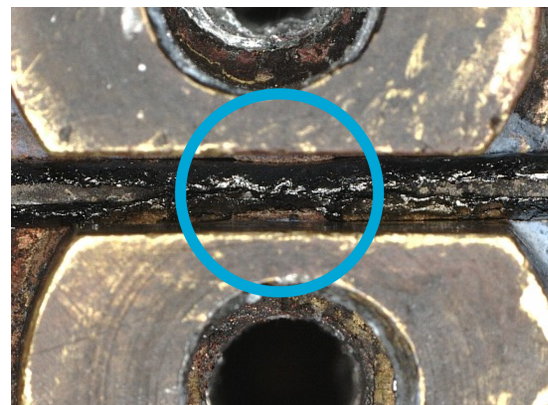
(b) Bottom copper block after polishing.

Figure 3.6: Bottom copper block before (left) and after (right) polishing.

3.1.3. VLM Assembly

Once the improvements and the polishing are finished, the VLM can be put together again. To distinguish this version from previous ones, it is given the name VLM-JV. In general, the same assembly procedure as laid out by Cramer was followed to maintain consistency. This assembly procedure, including some minor alterations can be found in [Appendix D](#). The main addition to the procedure is the implementation of the sealing gaskets on both sides of the nozzle profile. Using the cleanroom's torque wrench (FACOM A.402 0.5-2.5 Nm), the bolts are initially tightened to 0.5 Nm. This is lower than what was done previously and will likely be not enough for an acceptable leakage rate. However, with the addition of the sealing gasket, the torque required for a leak-tight seal should be lower. Therefore, a trial-and-error approach will be implemented to determine at which bolt torque the leakage rate is acceptably low. The torque will be increased gradually with steps of 0.2 Nm, until the acceptance criterion is met (leak rate below 5%, see [chapter 6](#)).

During the process of gradually increasing the torque, the nozzle area was inspected using the microscopes. It quickly became clear that the addition of the sealing gaskets resulted in several new challenges. Initially, the nozzle was completely obstructed by the gaskets ([Figure 3.7](#)), which was fixed by creating a small slit around the throat area, as shown in [Figure 3.8](#). The throat was now clearly visible, but the microscope showed that the extra layers resulted in an increased throat and exit height. This is undesirable, as it likely has a significant effect on the VLM's leak rate and performance and thus further deviates the current VLM from those used in previous theses, complicating the eventual comparison.

(a) The graphite gasket manufactured by *Wagner Gaskets & Seals*.

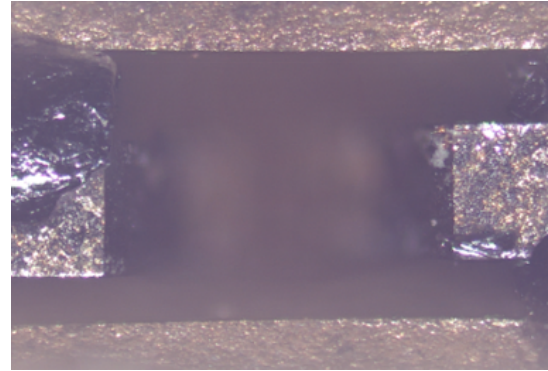
(b) View of the obstructed nozzle after implementation of the graphite gaskets.

Figure 3.7: The realised graphite gasket (left) and its effect on the nozzle area (right).

Moreover, the nozzle profile and copper blocks are not in contact with each other, leading to a highly irregular and unpredictable throat area. To solve this, more gasket material around the nozzle throat was removed in combination with an increased torque. After several attempts, the desired nozzle area where the copper and steel touch, could not be produced with the sealing gasket in place. As this was deemed more severe than the possibility of a reduced leakage rate, the sealing gasket was left out of the thruster. The resurfacing effort has hopefully resulted in an improved leak tightness and should be enough to satisfy the relevant acceptance criteria. This will be investigated later in [chapter 6](#). The eventual nozzle height was found to be equal to $471.9 \pm 11.7 \mu\text{m}$. The exact nozzle dimensions after assembly are laid out in the same chapter.



(a) The modified graphite gasket with a slit removed.



(b) View of the unobstructed nozzle after implementation of the modified graphite gaskets.

Figure 3.8: The modified graphite gasket (left) and its effect on the nozzle area (right).

VLM troubleshooting

Whilst the thruster was being adapted and assessed, some problems arose. These problems and the way in which they were dealt with, will be discussed in this subsection. Although these issues arose at different points throughout the thesis, they are all collected and discussed here for simplicity. Moreover, they were all encountered before the final tests were conducted ([chapter 7](#) and [8](#)), so they are relevant for the eventual test results.

During the assembly process, two connections of the interface came loose. The electrical wires leading to the P - T sensor were disconnected, as well as the MINSTAC tubing leading into the propellant tube. The first issue was harder to fix than initially expected. The wires were soldered to four contact pads on the sensor but three of them lost contact. Unfortunately, the contact pads could not be soldered again [71]. A new P - T sensor was thus required. To prevent mistakes due to the author's limited soldering experience, the cleanroom manager, Şevket Uludağ⁴, was asked to solder a new sensor. He did the same for Versteeg in the past, so he had already experience soldering this particular sensor. The new P - T sensor was successfully implemented.

Sadly, after a while this sensor started giving erroneous readings. During testing it was noticed that the readings from the sensor were illogical, since it reported a negative pressure when operating in a vacuum. Seen that it is an absolute pressure sensor, a negative pressure should be impossible. Thus, the sensor required replacing once again. Fortunately, a similar sensor could be acquired from the workshop. This time it was soldered by the author and implemented without further issues. Given the fact that these sensors fail relatively often in the author's experience, not much more were left in the workshop, and the relatively low cost per sensor, five new ones were bought to prevent future shortages ([Table 3.2](#)).

The MINSTAC tubing had been glued to the aluminium interface by Cramer [15]. This glued connection broke during assembly and thus required replacing. As this connection plays an important role in the

⁴M.S.Uludag@tudelft.nl

leaks encountered during leak testing, it will be discussed in depth in that chapter (see [chapter 6](#)).

Some other test equipment also needed troubleshooting before tests could be conducted. Most importantly, both cartridge heaters broke during earlier tests due to changed power supply settings. The power supplies used for controlling the heaters (Delta Elektronika ES-030-10 and SM-7020) can be set to either voltage control or current control. For this work, the heaters are controlled using the voltage control option. However, another student required the alternative option for their own experiments and changed the settings accordingly. Unfortunately, the settings were not restored afterwards, and the author did not check this before using the power supplies. As a result, both heaters received a current of 20 amperes, instead of the intended 20 volts. Since they are only designed for a maximum amperage of 3.1 amperes [82], they failed. For a brief period, the cartridges generated a lot of heat, before failing at a high temperature. Some soot build-up could be detected around the heaters. The effect this mistake may have had on the VLM's leak rate will be discussed later in [chapter 6](#). To prevent mistakes like this from happening again, the testing procedures are updated slightly (see [Appendix D](#)) and now include verifying that the power supplies are set to voltage control.

An inquiry for heater replacements was done at [Kurval BV](#), the Dutch distributor of the specific heaters used for the resistojet. Sadly, the desired heaters with the correct outer diameter ($1/8$ -Inch) had an unusual high lead time and could not be delivered before 2025, which was not an option for this work. Fortunately, two other heaters were available in the project's box, so these were implemented instead. One of these was identical to the ones used before, but the other was of longer design and contained an internal K-type thermocouple (Wattlow 24V C1J-9769 30W). Both were evaluated before implementing them and confirmed to serve up to the desired temperature range. The threaded sleeves made by Cramer [15] could be salvaged from the broken heaters and attached to the new heaters using the same high temperature sealant (*Zwaluw Fire Sealant 1200°C*, [8]). The replacement heaters served their purpose throughout both the nitrogen and water test campaigns. However, during disassembly, one of them broke again. Seen that only one functioning heater remains, it is recommended to order replacements if new tests are to be executed.

3.2. Test set-up Improvements

Besides the VLM improvements, the test set-up will also be improved. Some minor improvements to the test bench will be introduced which are described ([subsection 3.2.1](#)). More importantly, the newly developed water feed system is explained in detail, as well as some checks to evaluate its compliance with the existing test set-up ([subsection 3.2.2](#)).

3.2.1. Test bench improvements

Cramer [15] suggested to ensure that the torsional beam is level. If this is not the case, it might influence the thruster's performance, which should be avoided. Previously, a simple linear spirit level was used to inspect the levelness of the thrust bench and horizontal beam. To simplify and improve this process, a bull's eye level is purchased and attached to the beam (see [Figure 3.9](#)). This circular spirit level helps with determining whether the beam is level. To make it easier to level the beam, four bolts are added to the test bench. These levelling bolts are screwed into the four corners of the test bench and protrude from its underside. By adjusting the length with which the bolts protrude, the test bench's orientation can be fine-tuned. In this way, it is easy to ensure the bench is level. As an added benefit, the test bench's wobbling behaviour, which was noticed by Cramer, is eliminated.

The other improvement made to the test bench arises from the use of the Futek LSB200 load cell. [chapter 5](#) will further detail this load cell. For now, it is important to know that this load cell has a higher capacity (100 g) than the one used by Cramer (10 g). Since the expected thruster loads are in the range of 10 mN, the sensor will only operate in its lower measurement range. As the sensor is presumably less accurate in this range, it is beneficial to increase the loads experienced by it. Thanks to the TB-50m's design, this can be achieved quite easily. The load cell is placed closer to the point of rotation at a distance of only 25 mm. Given the fact that the original distance as used by Cramer was 175 mm, this implicates that the load exerted on the sensor is increased with a factor 7. Moreover, both

the calibration coil and VLM will be placed further from the beam's center at a distance of 145 mm and 187.5 mm, respectively. This also enhances the loads acting on the load cell.

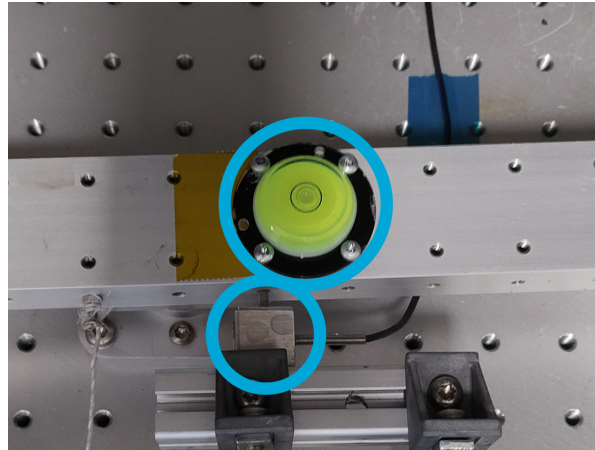


Figure 3.9: The improved test bench showing the added bull's eye level and the new load cell location closer to the rotation point.

3.2.2. Water feed system

Since this work aims to perform accurate and repeatable experiments using liquid water, a suiting feed system is required. Hutten [28] developed a feed system in which the water supply is controlled by a syringe pump (NE-1000X). By changing the settings of this pump, the volumetric flow can be set. After performing a simple calibration of the syringe pump, Hutten was able to establish a relationship to convert the volumetric flow to a mass flow (see chapter 4 of his work). He estimated a 3σ confidence interval of 0.45%. However, his test results indicated a more severe deviation of 5% to 15% from the actual mass flow rate. Hutten theorised that his conversion overestimates the actual mass flow and thus recommended to use liquid mass flow meter. This is one of the main driving factors behind the need for a new feed system. The other reason being the prevention of bubble formation inside the feed lines.

In Hutten's water feed system, flexible tubing leads from the syringe pump to the vacuum chamber. Inside, tubing leads to a MINSTAC VHS type solenoid [75], which in turn is connected to a short tube that leads to the thruster. The feed system used by Hutten is displayed in Figure 3.10. A significant issue encountered by Hutten [28], is the formation of air bubbles inside the propellant lines. These originate from two separate processes, the first of which being the filling process. In this process some air is able to slip in between the distinct filling steps. The second bubble-forming process is the degassing of the water during tests. When the valve opens, the water is suddenly exposed to vacuum environments. Consequently, the dissolved gases contained within (e.g. N_2 , O_2 , CO_2 , etc) separate and form bubbles within the tubes [84]. These air bubbles result in an irregular propellant flow, which lead to an irregular thrust production. Since a steady and predictable thrust production is desired, this situation should be avoided. So, an improved water feed system should address the problem of bubble formation and indirect mass flow measurements.

The water feed system developed in this work utilises a different working principle than the one described above (see Figure 3.12 for the new water feed system). Based on recommendations of Cramer [15], a tank-based concept was chosen instead of the syringe-based concept used by Hutten [28]. The idea is to fill a small tank with water and place it directly inside the vacuum chamber. In this way, the filling step is avoided, preventing the formation of bubbles. Fortunately, such a tank was already present inside the cleanroom. This particular tank, a Swagelok 304L HDF4 150 [67], had already been used in the past by Krusharev [36] and [64], albeit in a slightly different configuration. The cylindrical tank is made of stainless steel and has an internal volume of 150 cm³. A quick sizing estimation is performed in Figure 3.2.2 and shows that this volume is sufficient for the planned tests. The tank can withstand pressures up to 124 bar, much more than necessary for its use in this work. After filling, the tank (11)

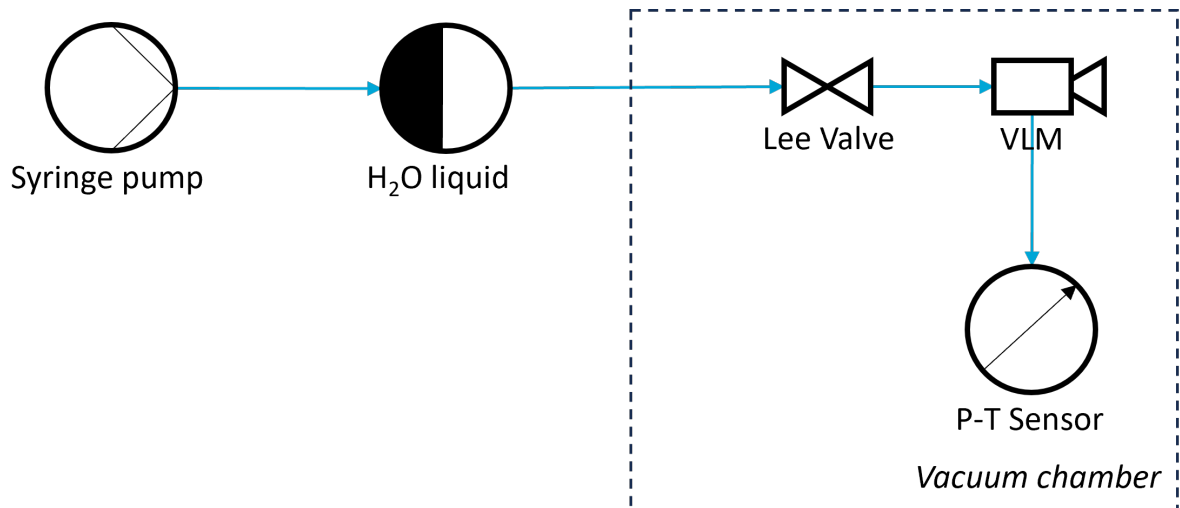


Figure 3.10: Schematic overview of the water feed system used by Hutten.

is placed vertically inside the vacuum chamber to ensure the liquid water is located near the bottom. The tank's bottom is connected to tubing leading to the mass flow meter and eventually the VLM itself.

The feed system in front of the water tank underwent several iterations before a final design was found. Initially, the tank's top was directly connected to the Swagelok Quick Connect [66] on the inside of the vacuum chamber. This enabled the pressurisation of the tank with the nitrogen feed system. However, this design also meant that air and dissolved gases are trapped inside the system and cannot be vented. Some preliminary experimentation revealed that this led to unpredictable flows and bubble formation. In order to solve this problem, the trapped air and gases should be removed before starting a test. This is achieved by implementing an additional 'venting' valve just before the Swagelok tank (12). A T-junction allows for connecting both the valve and the nitrogen feed system. The valve is also a Lee company solenoid valve, equal to the one used for the controlling the propellant flow to the VLM (8, see chapter 5). One challenge encountered in the implementation of the valve, is that the current cleanroom set-up only contains one valve control circuit. To save time and costs, it was not attempted to expand this circuit to allow for the control of both valves. Instead, two connections on the outside of the vacuum chamber can be switched manually to control one of the valves. Consequently, only one valve can be controlled at a time. Fortunately, this is not a problem for this work as the valves operate at different times. The venting valve is opened while a vacuum is being created inside the chamber. This allows for the venting of the air and dissolved gases from the feed lines and water tank. Once a sufficient vacuum is established, the venting valve is closed, and the propellant valve is connected to enable propellant flow. At this point, the tank can also be pressurised using nitrogen. These procedures are also described in Appendix D. Preliminary testing revealed that without this pressurant, no water flow would occur. Likely because of the water's surface tension and lack of pressure acting on it. This set-up gave satisfactory results as no bubble formation could be detected. Unfortunately, the realised mass flow rate still contained some problems, which will be discussed with the water tests (chapter 8). A picture showing the Swagelok tank and venting valve is included below (Figure 3.11).

The other point of improvement, the implementation of a liquid mass flow meter, could be addressed relatively easily. Two different Sensirion flow meters were available via the Space department⁵, one Sensirion SLI-0430 and one Sensirion SLI-1000. These sensors share similar characteristics, but their major point of distinction is the maximal measurable flow rate. The former one (SLI-0430) has a capacity of 80 $\mu\text{L}/\text{min}$, while the latter one (SLI-1000) has capacity of 1000 $\mu\text{L}/\text{min}$ [59]. Using a water density of 0.997 $\text{mg}/\mu\text{L}$ ⁶, this can be converted to a mass flow of 1.3 mg/s and 16.6 mg/s , respectively. Based on Hutten's work, the mass flow is expected to be around 9 mg/s . Although the liquid mass

⁵Contact person: B.T.C.Zandbergen@tudelft.nl

⁶Density of water at 25 °C and 1 atmosphere [41].

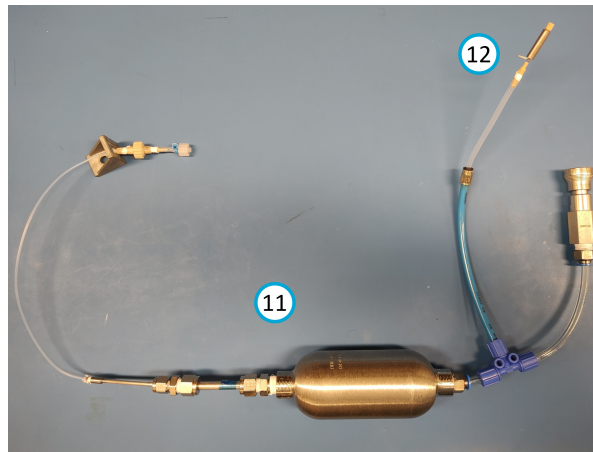


Figure 3.11: Overview of the new water feed system (excluding the mass flow meter).

flow is still subject to change, the SLI-1000 is chosen to be able to accommodate higher mass flows. This comes at the cost of a slightly reduced sensor accuracy and repeatability, but this tiny difference is deemed negligible. Sensirion's flow meter is placed directly after the water tank (7). To verify if the chosen sensor is working correctly, a simple calibration experiment was devised and executed. This calibration is described together with the other calibrations in [chapter 5](#).

[Figure 3.12](#) shows the complete schematic overview of the new water feed system. The numbers in the figure correspond to specific components used in the system, which are explained throughout the text. Since this feed system shares many similarities with the nitrogen feed system, most numbers are explained in that section (see [subsection 5.1.2](#)). All connections are made leak tight using PTFE tape that is available inside the cleanroom [24].

The system described above works by using a pressurant gas (nitrogen) to force the liquid (water) through the feed lines. As an added benefit, the gas can remove the remaining liquid droplets when the propellant tank is empty. This system has one important drawback, however. The mass flow rate is only controlled indirectly by adjusting the pressurant gas's pressure. A simple model can be developed to predict the flow leaving the tank, given the other parameters (pressure, volume, etc.). This gives more insight in the current feed system. Because of time-constraints, this is left for future work.

Several attempts were made to control the water flow more directly. The first of which is based on the use of a flow control valve [46]. Unfortunately, the valves present in the workshop (Swagelok and Legris) only work for higher flow rates and not enough time was left to search for alternatives. If a flow control valve can be found that is functional at the flow rates encountered in this work, it may be interesting to integrate it in the feed system. Another way to control the mass flow more precisely is to use the NE-1000x Syringe Pump as done by Hutten [28]. For this to work without the problems he encountered, the pump must be placed inside the vacuum chamber. Before doing this, it is essential to determine whether the pump is able to operate inside a vacuum. Moreover, the pump must be controllable from outside the vacuum chamber using the cleanroom PC. As this requires some time and effort, it is left as a suggestion for future work. The last attempt of the mass flow control was semi-successful. This concept is based on the use of Pulse Width Modulation (PWM) to restrict the flow of propellant through the solenoid valve by rapidly opening and closing it. This technique has been used before by [61], for example. Fortunately, the LabVIEW code responsible for the PWM was still present on the cleanroom PC and could easily be used again. The technique worked in regulating the water flow. However, it also introduced a lot of noise on the measured flow rate. This can be explained by the fact that the valve is rapidly changing states, which results in a choppy water flow. It is thus an inherent consequence of using PWM. Although this noisy flow data can be filtered later, it was decided to not use PWM for propellant flow control. Experiments showed that it was not necessary to achieve a somewhat stable

flow rate, so it was left out to limit the measurement noise.

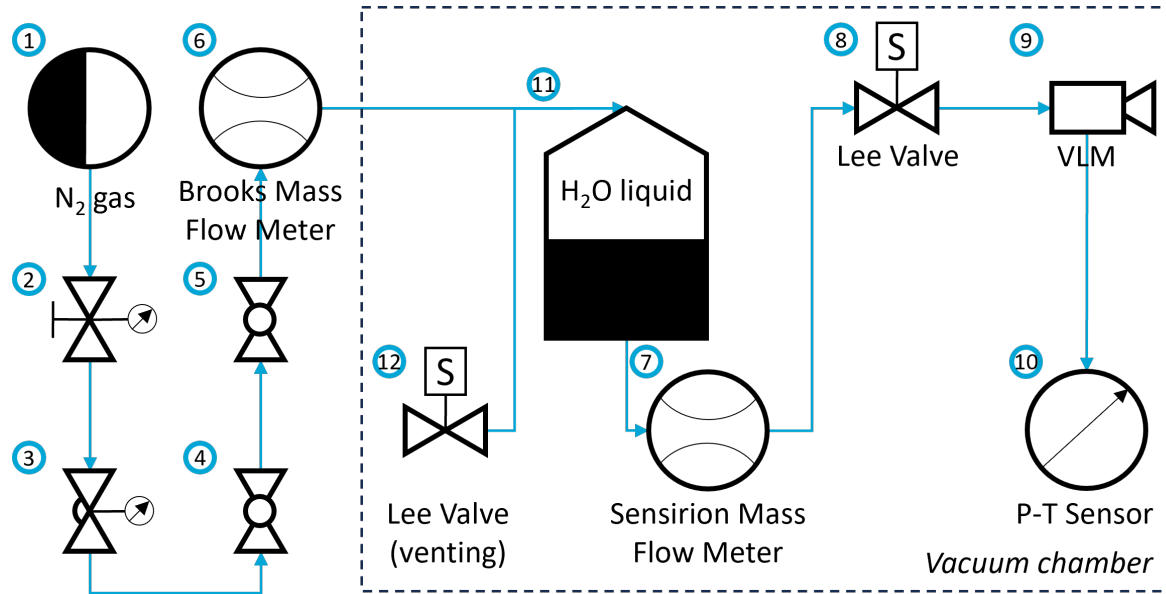


Figure 3.12: Schematic overview of the new water feed system.

Water tank sizing

A simple sizing estimation is performed to determine whether the water tank has enough capacity for the water tests. The used Sensirion mass flow meter is able to measure flow rates up to 1000 $\mu\text{L}/\text{min}$ or 16.6 mg/s. The water mass flow rate must thus be below this limit. As mentioned above, the Swagelok tank can hold up to 150 cm³ or 150 mL of water. If the maximal measurable flow rate is targeted, the maximum amount of water can be calculated easily. If the same thrust periods are targeted as for the nitrogen tests (see chapter 7), with four thrust periods of 5 minutes, the total thrust time is 20 minutes. So, the required water quantity is: $16.6 \text{ mg/s} \cdot 60 \cdot 20 \cdot 1/1000 \approx 20 \text{ g}$ or 20 mL. Even at this high flow rate, the used tank has plenty of capacity, so it is perfect for these tests.

Water vapour tolerance

Another concern for the water tests is the effect of the water vapour on some test equipment. Especially the vacuum pump (RZ 6, [80]) and vacuum chamber pressure sensor (VSP 3000, [79]) are of concern here. Two simple checks are performed to determine if the equipment can be used during the water tests.

The vacuum pump's instruction manual states that the pump has a water vapour tolerance (p_W) of 40 mbar [80]. The equation given by Pfeiffer Vacuum [51] can be used to find the water vapour capacity (Equation 3.1). This is the "maximum volume of water that a vacuum pump can continuously intake and displace in the form of water vapour under the ambient conditions of 20 °C and 1013 hPa" [51]. If the water vapour flow emitted by the VLM is lower than the pump's water vapour capacity, it can be used without issues during tests. The equation is as follows:

$$q_{m,water} = \frac{p_W \cdot S \cdot M}{R_A \cdot T} \quad (3.1)$$

In this equation, $q_{m,water}$ is the water vapour capacity, p_W is the water vapour tolerance and S is the pumping speed. The other three variables are: M , the molar mass of water (18.02 g/mol), R_A , the universal gas constant ($R_A = 8.314 \text{ J/K} \cdot \text{mol}$), and T , the absolute temperature of the water. The maximum expected temperature is taken (673.15 K), as this results in the worst-case scenario for the water vapour capacity. Furthermore, the pump has a minimum pumping speed of 5.7 m³/h. Substituting these variables in the equation, results in a water vapour capacity of 73.4 g/h. Given the fact that the

maximum desired mass flow of the water is roughly equal to 60 g/h (16.6 mg/s), the calculated vapour capacity is sufficient. In other words, the pump's limit is not reached, and it is thus safe to operate the pump during the water tests.

The used vacuum chamber pressure, the VSP 3000, has a permitted relative atmospheric moisture between 30% and 85% [79]. This means that, at a temperature of 24 °C, the saturation vapour pressure is 29.6 mbar [73]. Thus, the maximal water vapour partial pressure is 25.2 mbar. The ideal gas law can be used to quickly estimate the maximal water vapour pressure after a 20-minute thrust test (without an active vacuum pump):

$$\frac{\frac{m_{H_2O}}{M_{H_2O}} \cdot R_A \cdot T_a}{V} = \frac{\frac{20}{18.01528} \cdot 8.314 \cdot 673.14}{0.128} \cdot 0.01 = 486 \text{ mbar} \quad (3.2)$$

The volume of the vacuum chamber (V) is 128 L [27]. To find the water vapour emitted per minute the total vapour pressure (486 mbar) is divided by the total thrust time. This gives a rate of 24 mbar/min. So, after a little more than a minute, the maximum allowable relative humidity would already be reached. This may be problematic but, fortunately, an easy solution exists. As done by other works, the vacuum pump can be kept active throughout the entire test duration. This pump is able to remove 95 L/min, which is plenty for keeping the humidity within the allowable bounds. The vacuum pump should thus be turned on during the tests to keep the water vapour below the specified limit.

3.3. Expenditures

As described in this chapter, several components were ordered for this thesis. Naturally, the goal is to minimise the costs and stay within the allotted budget (€750). Unfortunately, this goal is not achieved, as the expenses total to €761.13. Thus, the budget has been exceeded with 1.5%. Fortunately, this is not a major issue but exceeding the budget should be avoided as much as possible. The budget overrun can be attributed to the unexpectedly high CNC machining costs. More direct communication with the manufacturer should prevent these mistakes from happening again. The table below (Table 3.2) shows the complete overview of the costs made during the thesis.

Component	Quantity	Expenses [€]
DEMO CNC machine	16 hours	642.59
Industrielijm XXL 10 gram	1	12.95
Industrielijm dun 28 gram & 10 mL PE/PP Primer	1	30.45
ProPlus Waterpas Rond	1	6.08
TE Connectivity MS583730BA01-50	5	69.06
Total		761.13

Table 3.2: Overview of the expenditures of this work, including VAT and shipping costs.

4

Analytical Model

This chapter will detail the development of an analytical model capable of predicting the EDM-based VLM's performance. The model developed here is based on previous efforts. It is built from the ground up in MATLAB in an effort to validate an earlier model ([Resistojet Performance Tool](#)) made by Hutten [28]. The model developed in this work is simpler and easier in use and thus better suited for providing a quick insight in the expected thruster performance. The MATLAB model is named the MATLAB Resistojet Performance Tool (M-RPT) and is included in the appendix ([Appendix E](#)). Firstly, [section 4.1](#) briefly introduces the Ideal Rocket Theory (IRT), the fundamental theory and associated equations regarding the functioning of a rocket engine. Then, [section 4.2](#) expands upon the IRT by implementing various corrections and losses. Afterwards, the results of this Modified Rocket Theory (MRT) are validated against the results acquired with Hutten's model ([section 4.3](#)). Once the models are validated, they can be used to predict the VLM performance for the planned tests ([section 4.4](#)). These predictions aid the development of the experimental set-up in the next chapter, as it determines the measurement range and sensitivity required of the test equipment.

4.1. Ideal Rocket Theory

The Ideal Rocket Theory (IRT) is an elegant and powerful theory describing a rocket engine's performance. It is relatively simple but still reasonably accurate for rough estimations. Some simplifying assumptions are made, which include [85]:

- The exhaust gases are homogeneous and have a constant composition.
- The gas (mixture) can be described with the ideal gas law, which describes the state of an ideal gas¹.
- The heat capacity of the gas (mixture) is constant.
- The flow through the nozzle is one-dimensional, steady, and isentropic.

These assumptions simplify the equations that will be introduced shortly. The equations depend on the specific medium investigated (C_p , C_v , M), nozzle dimensions (A_t , A_e), and heating chamber conditions (P_c , T_c). Moreover, two constants are important in these calculations: the gravitational constant ($g_0 = 9.806 \text{ m/s}^2$) and the universal gas constant ($R_A = 8.314 \text{ J/K}\cdot\text{mol}$). The specific gas constant (R), the ratio of specific heats (γ), as well the Vandekerckhove function (Γ), are also commonly used constants. Their definition can be found in the work of Zandbergen [85], for example. Values that depend on specific conditions (e.g. chamber temperature and pressure), such as the specific heat or viscosity, are acquired from the CoolProp database [4]. With these definitions, equations for the ideal rocket performance can be defined (subscript: $_{ideal}$). These include the mass flow through the nozzle (\dot{m}_{ideal}), the exhaust flow velocity (U_e), and the ideal produced thrust (F_{ideal}). These can be written as follows:

¹The ideal gas law: $P \cdot V = n \cdot R_A \cdot T$

$$\dot{m}_{ideal} = \frac{\Gamma \cdot P_c \cdot A_t}{\sqrt{R \cdot T_c}} \quad (4.1) \quad U_e = \sqrt{\frac{2\gamma}{\gamma-1} \cdot R \cdot T_c \cdot \left(1 - \left(\frac{P_e}{P_c}\right)^{\frac{\gamma-1}{\gamma}}\right)} \quad (4.2)$$

$$F_{ideal} = \dot{m}_{ideal} \cdot U_e + (P_e - P_a) \cdot A_e \quad (4.3)$$

$$F_{ideal} = \Gamma \cdot P_c \cdot A_t \sqrt{\frac{2\gamma}{\gamma-1} \cdot \left(1 - \left(\frac{P_e}{P_c}\right)^{\frac{\gamma-1}{\gamma}}\right)} + (P_e - P_a) \cdot A_e \quad (4.4)$$

$$\frac{A_e}{A_t} = \frac{\Gamma}{\sqrt{\frac{2\gamma}{\gamma-1} \left(\frac{P_e}{P_c}\right)^{\frac{2}{\gamma}} \left[1 - \left(\frac{P_e}{P_c}\right)^{\frac{\gamma-1}{\gamma}}\right]}} \quad (4.5)$$

Substituting Equation 4.1 and Equation 4.2 into Equation 4.3, results in the expression for the ideal thrust shown above (Equation 4.4). The ideal thrust is thus a function of a variety of factors, such as the chamber, exhaust, and ambient pressure, as well as the specific heat ratio and the nozzle throat and exit area. The pressure at the nozzle exit can be computed numerically using the formula for area ratio (Equation 4.5). Since the area ratio can be measured and is thus known, the pressure ratio (P_e/P_c) can be found using an iterative solving technique. The found pressure ratio is then substituted in Equation 4.4 to determine the ideal thrust. Note that these expressions only hold if critical conditions prevail and thus the flow in the throat is sonic (exhaust flow is supersonic). Whether this is the case, can be easily checked with Equation 4.6 [65]. As long as the pressure ratio is greater than the critical ratio, the nozzle flow is supersonic.

$$\frac{P_c}{P_e} > \frac{\gamma+1}{2}^{\frac{\gamma}{\gamma-1}} \quad (4.6)$$

Another key engine performance indicator is the specific impulse of the engine (I_{sp}). It is a measure of how efficient the engine can convert the propellant into thrust and is defined as the thrust divided by the product of the mass flow and gravitational acceleration:

$$I_{sp,ideal} = \frac{F_{ideal}}{\dot{m}_{ideal} \cdot g_0} \quad (4.7)$$

4.1.1. Characteristic Parameters and Quality Factors

The specific impulse and thrust defined in the previous section, can also be defined in an alternative manner; using the so-called characteristic parameters, which is shown below (Equation 4.8 and 4.9). These alternative definitions are useful when dealing with the quality factors that will be introduced shortly.

$$I_{sp} = \frac{C_F \cdot c^*}{g_0} \quad (4.8) \quad F = \dot{m} \cdot C_F \cdot c^* \quad (4.9)$$

These definitions introduce two new parameters, the thrust coefficient (C_F) and the characteristic velocity (c^*). The thrust coefficient indicates the amplification of the thrust due to the expansion of the gas in the rocket nozzle, while the characteristic velocity is indicative of the energy stored in the propellants that is used for propulsion [85]. In other words, the thrust coefficient is an indication of the nozzle performance, while the characteristic velocity is indicative of the propellant performance. The definitions of these parameters can be found below. The subscript $_{exp}$ is a shorthand notation for experimental, indicating the use of experimentally found values. By comparing these to their ideal counterparts, the rocket motor's performance can be easily determined. Equations 4.10 and 4.11 illustrate this well. The ideal (theoretical) characteristic velocity (c^*_{ideal}) can easily be calculated with Equation 4.10, as it depends solely on the propellant properties (Γ and R) and the chamber temperature (T_c). The experimental characteristic velocity (c^*_{exp}) is found by substituting the ideal definition into Equation 4.1,

resulting in Equation 4.11. The remaining three variables are easily measurable during tests, so they can be used to find the experimental c_{exp}^* . The theoretical thrust coefficient is also defined below in Equation 4.12.

$$c_{ideal}^* = \frac{\sqrt{R \cdot T_c}}{\Gamma} \quad (4.10)$$

$$c_{exp}^* = \frac{P_c \cdot A_t}{\dot{m}_{exp}} \quad (4.11)$$

$$C_{F,ideal} = \frac{F_{ideal}}{P_c \cdot A_t} \quad (4.12)$$

For the upcoming analysis, it is essential to clearly distinguish between the ideal performance, as predicted by the Ideal Rocket Theory, and the real, experimental performance. Due to the simplifying assumptions listed earlier, these do not overlap. To quantify this difference between the ideal and real rocket performance, a couple of quality factors are introduced. These are defined as the ratio between the experimental and ideal values. The quality factor of the thrust coefficient is also known as the nozzle quality (ξ_n), while the characteristic velocity equivalent is called the heating or combustion quality (ξ_c). For a resistojet, the combustion quality is assumed to be equal to 1 as no combustion takes place. Furthermore, thrust (ξ_F) and specific impulse (ξ_{Isp}) also have their own associated quality factors. These four quality factors are defined below (Equation 4.13 to 4.16). Especially the ξ_{Isp} is of interest in this work, as it is a good performance indicator. Previously found values range from 0.44 to 0.88 [15, 81].

$$\xi_n = \frac{C_{F,exp}}{C_{F,ideal}} \quad (4.13)$$

$$\xi_c = \frac{c_{exp}^*}{c_{ideal}^*} \quad (4.14)$$

$$\xi_F = \frac{F_{exp}}{F_{ideal}} = C_d \cdot \xi_n \cdot \xi_c \quad (4.15)$$

$$\xi_{Isp} = \frac{I_{sp,exp}}{I_{sp,ideal}} = \xi_n \cdot \xi_c \quad (4.16)$$

Another important quality factor is the discharge factor (C_d), which is the ratio of experimental to ideal mass flow rate (Equation 4.17). It is an indication of the amount of flow blockage due to friction effects in the throat area. For rocket motors with a high Reynolds number (higher than 100,000), this discharge factor is less important, as the real mass flow rate nears the ideal mass flow rate in this case. Therefore, the discharge factor is close to unity (or at least 0.98, [85]). However, for engines with a low Reynolds number (lower than 22,000), which applies to the VLM under investigation (see chapter 2), this is not the case, and the mass flow rates can differ significantly from each other [25, 31]. This can also be seen from previous VLM experiments where discharge coefficients ranging from 0.68 to 0.88 were found.

Lastly, seen that the heating quality does not provide sufficient insight in the heating performance of the motor, another quality factor has been used by Hutten [28]. This heating efficiency (η_{heat}) is defined in Equation 4.18. It is an indication of the efficiency with which the heaters transfer heat to the propellant. The power of the heater is represented by P_{heat} , while h_c represents the specific enthalpy of the hot propellant in the heating chamber. h_0 is the specific enthalpy of the stored (unheated) propellant. A significant amount of heat will not be absorbed by the passing propellant and will be lost due to conduction to other parts (to the tubes and interface, for example) and radiation to the environment. The results of previous tests indicate a heating efficiency between 19% and 36% [15, 28].

$$C_d = \frac{\dot{m}_{exp}}{\dot{m}_{ideal}} \quad (4.17)$$

$$\eta_{heat} = \frac{\dot{m}_{exp} \cdot (h_c - h_0)}{P_{heat}} \quad (4.18)$$

4.2. Modified Rocket Theory

The quality factors and their values introduced above indicate that the thruster does not behave like an ideal rocket motor. Some significant differences are found between the ideal and real performance. This discrepancy arises from a multitude of different factors, such as the presence of a boundary layer

in the flow and losses due to flow divergence. As these factors have a noticeable effect on the VLM performance, it is insightful to incorporate them in a model. This brings the model closer to reality and thus helps in improving the model's predictions. The model developed in this section is called the Modified Rocket Theory (MRT). Previous efforts have focused especially on boundary layer formation and its effect on the propellant flow and thus the discharge coefficient (C_d). For a detailed discussion on the modelling of this and other factors, please refer to the discussions of Versteeg [81] (chapter 4) and Hutten [28] (chapter 2), which in turn are based on earlier works of Jansen [29] and [42]. Here, only the most important findings are discussed briefly.

4.2.1. Modified Discharge Coefficient

An important parameter to judge a flow is the Reynolds number (Re). It relates the inertial and viscous forces present in a fluid flow. For low Reynolds numbers, a significant boundary layer will form in which viscous forces are dominant. This is a layer of fluid close to a surface where the fluid's velocity approaches zero. The presence of this boundary layer reduces the flow's momentum and effective throat area, which in turn reduces the thruster's output. To characterise this effect, the throat Reynolds number is useful (Re_t). It can be defined in multiple ways but the ones that will be used in this work are the ones shown in Equation 4.19 and 4.21. These Reynolds numbers are constructed by the ideal mass flow (\dot{m}_{ideal}), the geometrical or effective throat hydraulic diameter ($D_{ht,geo}$ or $D_{ht,eff}$), the fluid's dynamic viscosity in the chamber (μ_c), and the throat area (A_t). Especially the second parameter ($D_{ht,geo}$ or $D_{ht,eff}$), the characteristic length, is contested and varies for different works. Since the nozzle is rectangular, the ideal definition is chosen as shown in Equation 4.20. The geometrical throat hydraulic diameter consists of the throat area and the throat width (W_t) and height (H_t). The subscript geo is added to emphasize that geometrical (ideal) dimensions are used, instead of reduced dimensions due to the boundary layer (see subsection 4.2.2). This is captured by the real throat Reynolds number ($Re_{t,real}$) of Equation 4.21. It uses the effective throat hydraulic diameter to simulate viscous losses [28]. This definition of the Reynolds number will later be used in the analysis of the thrust tests (chapter 7 and 8).

$$Re_{t,ideal} = \frac{\dot{m}_{ideal} \cdot D_{ht,geo}}{\mu_c \cdot A_t} \quad (4.19)$$

$$D_{ht,geo} = 2 \cdot r_t = \frac{2 \cdot A_t}{W_t + H_t} \quad (4.20)$$

$$Re_{t,real} = \frac{\dot{m}_{ideal} \cdot D_{ht,eff}}{\mu_c \cdot A_t} \quad (4.21)$$

$$D_{ht,eff} = \frac{2 \cdot A_t \cdot C_{d,KH}}{\sqrt{4 \cdot A_t \cdot C_{d,KH} + (W_t - H_t)^2}} \quad (4.22)$$

The discharge coefficient itself can be modelled in numerous ways, some based on analytical relations [70], while others are based on semi-empirical relations [38, 31]. The relation developed by Kuluva and Hosack [38] will be used here, because it is easier in use and to maintain consistency with previous works. It is shown in Equation 4.23 and introduces some new parameters. The r_c represents the radius of curvature at the nozzle throat (260 μm), while r_t represents the nozzle throat radius, which is found by halving the throat hydraulic diameter (Equation 4.20). It is important to point out that the authors intended the use of the equation for supersonic nozzles where $0 \leq r_c/r_t \leq 20$ and $50 \leq Re_{t,ideal} \leq 10^5$. Based on the nozzle throat radii and Reynolds numbers found by previous works, both conditions are satisfied. The outcome of the modelled discharge coefficient will be shown at the model verification section (4.3.)

$$C_{d,KH} = \left(\frac{r_c + 0.05 \cdot r_t}{r_c + 0.75 \cdot r_t} \right)^{0.019} \cdot \left(1 - \left(\frac{r_c + 0.1 \cdot r_t}{r_t} \right)^{0.21} \right) \cdot \left(\frac{1}{\sqrt{Re_{t,ideal}}} \right) \cdot (0.97 + 0.86 \cdot \gamma) \quad (4.23)$$

4.2.2. Modified Thrust Coefficient

The discharge coefficient is not the only parameter that is affected by the presence of the boundary layer. This layer of slow-moving fluid also extends into the diverging part of the nozzle, which effectively reduces the momentum of the exhaust gases. Moreover, heat is lost to the walls of the nozzle. Consequently, the produced thrust is also negatively affected. Spisz, Brinich, and Jack [63] characterised

these losses experimentally using hydrogen for conical nozzles with $500 \leq Re_t \leq 18,000$ and $25 \leq A_e/A_t \leq 150$. While the nozzle expansion area ratio, ϵ or A_e/A_t , for the EDM-based VLM is smaller, it is still deemed to be reasonable to use Spisz's relation for this work. This relation and the associated definition of $Re_{t,wall}$ can be found below (Equation 4.24 and 4.25). The adapted wall Reynolds number ($Re_{t,wall}$) shown here is a result of a conversion of Spisz's Reynolds number to the one used for this work (see chapter 2 of Hutten [28] for a more detailed explanation).

$$C_{F,loss} = \frac{17.6 \cdot \exp(0.0032 \cdot \frac{A_e}{A_t})}{\sqrt{Re_{t,wall}}} \quad (4.24) \quad Re_{t,wall} = C_{d,KH} \cdot \frac{\mu_c}{\mu_t} \cdot Re_{t,ideal} \cdot \left(\frac{T_t}{T_{t,wall}} \right)^{5/3} \quad (4.25)$$

The propellant temperature at the throat is represented by T_t and the temperature of the throat wall by $T_{t,wall}$. Spisz uses two different temperature ratios ($T_t/T_{t,wall}$) for his cold tests (21 °C) and hot tests ($\sim 1,950$ °C); 0.857 and 1.388, respectively. To represent the VLM's design better and simplify the equations somewhat, an important assumption is made here. The wall temperature at the throat is assumed to be equal to the chamber temperature (T_c). This is done because the entire thruster is heated and has approximately the same temperature. With this assumption and the use of the Ideal Rocket Theory, the temperature ratio can be approximated with Equation 4.26. Combining this result with Equation 4.24 and 4.25, results in the final thrust coefficient loss factor shown in Equation 4.27.

$$\frac{T_t}{T_{t,wall}} \approx \frac{T_t}{T_c} = \frac{2}{\gamma + 1} \quad (4.26) \quad C_{F,loss} = \frac{17.6 \cdot \exp(0.0032 \cdot \frac{A_e}{A_t})}{\sqrt{\left(C_{d,KH} \cdot \frac{\mu_c}{\mu_t} \cdot Re_{t,ideal} \cdot \left(\frac{2}{\gamma+1} \right)^{5/3} \right)}} \quad (4.27)$$

The validity of this assumption should be investigated further, however. Because of the colder propellant flowing past the throat's wall, it is likely to have a lower temperature as the heating chamber. The temperature ratio will therefore possibly be greater, leading to a slight overestimation of the thrust coefficient loss. A quick sensitivity analysis is conducted to determine the effect of this assumption. It leads to a difference in thrust coefficient loss between 1.4% (cold tests) and 34.0% (hot tests) with regards to the values found by Spisz's formula. The assumption thus has a noticeable effect on the modelled thrust. To determine the validity of this assumption, further research is required, which will be left for future work.

Besides the boundary layer, another effect also reduces the produced thrust. This effect arises from the fact that the exhaust gases diverge radially when exiting the nozzle throat. The Ideal Rocket Theory assumes that the propellants only exit the nozzle in the axial direction, which is not true in reality. Due to this effect, some thrust is lost. Berton [5] established analytical derivations that depend on the nozzle design to estimate these flow divergence losses. Berton derived the equation shown below (Equation 4.28) for the divergence loss ($C_{\theta,div}$) of a two-dimensional nozzle. The only parameter required for this correction factor is the nozzle exit plane divergence half angle (in radians), θ_{div} . The divergence loss is multiplied with the ideal thrust coefficient of Equation 4.12, while the thrust coefficient loss is subtracted from it. The final modelled thrust coefficient is thus defined as shown in Equation 4.29. Seen that the EDM-based VLM has a divergence half angle of 20°, the divergence loss reduced the thrust coefficient with roughly 2%.

$$C_{\theta,div} = \frac{\sin(\theta_{div})}{\theta_{div}} \quad (4.28) \quad C_{F,model} = C_{\theta,div} \cdot C_{F,ideal} - C_{F,loss} \quad (4.29)$$

4.2.3. Modified Rocket Theory

The previous two subsections introduced modifications to the IRT, resulting in the [MRT](#). These modifications lead to a better approximation of the real VLM performance. The final modified formulas used to calculate the thruster's behaviour are shown below ([Equation 4.30 to 4.33](#)). The subscript *model* indicates that this is the value resulting from the Modified Rocket Theory. The next section will compare the model's output with that of Hutten to verify their outputs are similar.

$$\xi_{n,model} = \frac{C_{F,model}}{C_{F,ideal}} \quad (4.30) \quad I_{sp,model} = \xi_{n,model} \cdot I_{sp,ideal} \quad (4.31)$$

$$F_{model} = C_{d,KH} \cdot \xi_{n,model} \cdot F_{ideal} \quad (4.32) \quad \dot{m}_{model} = C_{d,KH} \cdot \dot{m}_{ideal} \quad (4.33)$$

4.3. Model validation

As mentioned before, the model described in the previous section has been developed in MATLAB. It is included in full in [Appendix E](#). To distinguish it from Hutten's [RPT](#) made in Python, this model is called the MATLAB Resistojet Performance Tool (M-RPT). Since it is based on the same equations as Hutten [\[28\]](#), it should result in a similar output, given equal inputs. The MATLAB model can thus be used to validate Hutten's model, which in turn also validates this model. To do this, the models are given equal inputs, based on tests done by Versteeg [\[81\]](#). If the outputs of both models are within 1% of each other, the models are regarded to be validated. Since the equations should be the same for both, the output should also be the same, hence the small acceptance margin. The validation is shown in [Table 4.1](#). Since the MATLAB model does not have an integrated error propagation function, no errors are included for the M-RPT output.

The models show excellent overlap (< 1%), so the MATLAB model (M-RPT) and Python model ([RPT](#)) are in agreement. Both models can thus be used henceforth to estimate the VLM's performance. The models have their unique advantages and disadvantages. So, selecting a model depends on the specific use case. The MATLAB model is easier and faster to use and thus convenient to quickly get an estimate. However, MATLAB is an expensive software and thus not widely available. Python on the other hand, is free to use and thus accessible for almost any user. Moreover, this model ([RPT](#)) is more comprehensive as it also integrates an error propagation method [\[28\]](#). Another benefit of this model is that it is also capable of analysing the test data. It can load the raw test data (TDMS file produced by LabVIEW) directly and analyse them to calculate the VLM's performance parameters. Because of these properties, Hutten's Resistojet Performance Tool will be used from this point forward. In hindsight, the development of the M-RPT was not as essential as initially thought. Some time and effort have been lost on its development as the model will not be used further. Fortunately, it was still useful in validating the [RPT](#) and it will hopefully prove to be valuable to other works.

Input				
Parameter	Nitrogen		Nitrogen	
T_c [K]	305.5 ± 5.8		670.7 ± 5.8	
P_c [mbar]	1356 ± 50		1660 ± 100	
P_a [mbar]	1.84 ± 0.29		2.09 ± 0.32	
A_t [10 ³ μm ²]	70.6 ± 4.8		70.6 ± 4.8	
A_e [10 ³ μm ²]	531.7 ± 5.1		531.7 ± 5.1	
H_t [μm]	496 ± 4		496 ± 4	
θ [°]	20 ± 0		20 ± 0	
Output				
	RPT	M-RPT	RPT	M-RPT
IRT				
F [mN]	15.45 ± 1.16	15.45	19.02 ± 1.69	19.02
\dot{m} [mg/s]	21.78 ± 1.69	21.78	17.87 ± 1.63	17.87
I_{sp} [s]	72.34 ± 0.73	72.34	108.6 ± 0.62	108.6
MRT				
F [mN]	11.44 ± 0.97	11.44	12.10 ± 1.32	12.10
ξ_F [-]	0.74 ± 0.01	0.74	0.64 ± 0.01	0.64
\dot{m} [mg/s]	20.74 ± 1.65	20.75	16.68 ± 1.57	16.68
$Re_{t,ideal}$ [-]	3759 ± 257	3759	1755 ± 140	1755
I_{sp} [s]	56.25 ± 0.51	56.25	73.98 ± 1.22	73.98
$\xi_{I_{sp}}$ [-]	0.78 ± 0.01	0.78	0.68 ± 0.01	0.68
C_d [-]	0.95 ± 0.00	0.95	0.93 ± 0.00	0.93

Table 4.1: Validation of the Resistojet Performance Tool (RPT) developed by Hutten [28] and the M-RPT developed in this work. The errors are absolute values.

4.4. Test predictions

With the analytical model established, some predictions can be made regarding the tests planned for this thesis. Both nitrogen tests and water tests will be conducted and will be treated in their respective subsections (subsection 4.4.1 and 4.4.2). The test plans will be treated briefly to determine the inputs that should be given to the RPT (chamber pressure and temperature). The other required inputs involve the nozzle geometry, which has not been characterised yet. The optical characterisation, which leads to the nozzle's dimensions, is discussed in detail in chapter 6 and will not be repeated here. Only the results of this chapter are used here. The predictions made in this section help manage expectations for the actual tests. As discussed in other works and chapter 2 of this work, the model has a limited applicability to the experimental results. Especially the predicted discharge coefficient and specific impulse efficiency differed significantly from the measured values. Despite this, the model's predictions are still useful in establishing the expected order of magnitude of the parameters, which helps inform the design of the experimental set-up in the next chapter (5). The final chapter, chapter 9, will compare the model's output with the test results in an attempt to validate it.

4.4.1. Nitrogen tests

The nitrogen test campaign has been structured similarly to the tests conducted by Cramer [15] to enhance comparability. Five different tests will be conducted, each at either a different chamber temperature (T_c) or a different chamber pressure (P_c). Table 4.2 summarises this test campaign. These are designed to evaluate the thruster's behaviour at different pressure and temperature levels and to verify if these results are in accordance with the established theory. Moreover, this test campaign has also been used by Hutten [28] and Cramer [15], so it also serves as a verification or comparison for those results.

Test ID	P_c [bar]	T_c [°C]
N2-10-020	1.0	20 ²
N2-10-200	1.0	200
N2-15-200	1.5	200
N2-10-300	1.0	300
N2-10-400	1.0	400

Table 4.2: Overview of the nitrogen test campaign.

Before conducting the experiments, it is insightful to have an idea of what can be expected from them. The first indication can be inferred from the theoretical model established in this chapter. The test campaign involves varying the temperature and pressure inside the heating chamber. Equation 4.4 indicates that altering the chamber temperature will have no effect on the (ideal) thrust (F_{ideal}). Instead, the mass flow (\dot{m}_{ideal}) will reduce for an increase in temperature (Equation 4.1). This effect is cancelled out by an equal increase in the exhaust velocity (U_e , Equation 4.2). Since the thrust remains constant and the mass flow decreases, Equation 4.7 shows that the specific impulse ($I_{sp,ideal}$) will increase. Increasing the chamber pressure, on the other hand, will have a different effect on these parameters. According to the same formulas, the mass flow will increase, while the exhaust velocity will not change noticeably. Consequently, the thrust will increase. Given that both the thrust and mass flow increase with the same rate, their effects cancel each other out for the specific impulse (Equation 4.7). The $I_{sp,ideal}$ should thus remain constant. The output of the MRT is shown in Table 4.3. As expected, the mass flow decreases when the chamber temperature is raised from 20 °C to 400 °C, while it increases for a higher chamber pressure. The specific impulse also shows the expected behaviour. A decreasing trend can be observed in the modelled thrust, which can be attributed to the decreasing throat Reynolds number.

	N2-10-020		N2-10-200		N2-15-200		N2-10-300		N2-10-400	
	Value	± [%]	Value	± [%]	Value	± [%]	Value	± [%]	Value	± [%]
Input										
T_c [K]	293	2.4	473	1.5	473	1.5	573	1.2	673	1.0
P_c [mbar]	1000	5.0	1000	5.0	1500	3.3	1000	5.0	1000	5.0
P_a [mbar]	5.00	15.0	5.00	15.0	5.00	15.0	5.00	15.0	5.00	15.0
A_t [$10^3 \mu\text{m}^2$]	122.6	7.1	122.6	7.1	122.6	7.1	122.6	7.1	122.6	7.1
A_e [$10^3 \mu\text{m}^2$]	487.8	3.1	487.8	3.1	487.8	3.1	487.8	3.1	487.8	3.1
H_t [μm]	499.1	2.3	499.1	2.3	499.1	2.3	499.1	2.3	499.1	2.3
Output (MRT)										
F [mN]	14.19	9.5	12.77	10.3	20.78	8.6	12.11	10.3	11.52	10.6
ξ_F [-]	0.75	1.3	0.68	2.0	0.73	1.3	0.64	2.2	0.61	2.5
\dot{m} [mg/s]	27.24	8.9	21.12	9.1	31.99	8.0	19.03	8.8	17.41	8.8
$Re_{t,ideal}$ [-]	4354	9.4	2397	9.3	3596	8.5	1900	9.1	1567	8.8
I_{sp} [s]	53.13	1.2	61.63	1.5	66.26	0.9	64.90	1.7	67.48	2.0
ξ_{Isp} [-]	0.79	1.1	0.72	1.7	0.77	1.1	0.68	1.9	0.65	2.2
C_d [-]	0.96	0.2	0.94	0.3	0.95	0.2	0.94	0.3	0.93	0.3

Table 4.3: Input and output of the Resistojet Performance Tool (RPT) showing the predicted parameters of the planned nitrogen test campaign.

4.4.2. Water tests

The tests using water as propellant will be rather different compared to those performed with nitrogen, both from an operational perspective as well as a modelling perspective. The efforts described in this

²This test is conducted at ambient, or room temperature, which in practise will be around 20 °C, but it can vary slightly.

work have only once before been attempted by Hutten [28], although with notable differences. The most important change made with respect to Hutten's work is the feed system. Instead of a syringe-based feed system, this feed system is tank-based, as described in detail in [chapter 3](#). The chamber pressure is harder to control compared to the nitrogen tests as the water enters the chamber as a (partial) liquid. To simplify the modelling, it is assumed that the chamber pressure will be 1.0 bar. Whether this assumption holds true, should be checked later. The temperature is varied from 200 to 400 °C. This test plan is summarised in [Table 4.4](#).

Test ID	P_c [bar]	T_c [°C]
H2O-10-200	1.0	200
H2O-15-300	1.0	300
H2O-15-400	1.0	400

Table 4.4: Overview of the water test campaign.

In terms of test predictions, the process is rather similar compared to the previous subsection. The analytical model can be consulted for an initial indication of the expected performance. In theory, there is not a significant difference between gaseous nitrogen and gaseous water as propellants. Some parameters are different, such as the specific gas constant (R), which is greater for water, and the specific heat ratio (γ) and viscosity (μ_c), which are smaller for water. Naturally, the equations remain the same. Moreover, most (geometrical) input parameters remain unchanged as well. Because of these effects, the water mass flow is expected to be smaller, while the thrust stays roughly constant compared to a similar nitrogen test (same T_c). The specific impulse is therefore expected to increase.

In principle, raising the chamber temperature should have a similar effect on the thrust, mass flow, and specific impulse as described in [subsection 4.4.1](#). However, the chamber pressure is not a directly controllable variable during the actual tests. Consequently, it is likely to vary from test to test. This means that the mass flow and thus also the F and I_{sp} are harder to predict. Stating predictions for the current experimental set-up is thus difficult but it will improve with subsequent iterations. More tests will lead to more data on the thruster behaviour, and this will improve the predictions that can be made beforehand. The output of the MRT is shown in [Table 4.5](#). These results also align with the expectations discussed in this section. Whether the predictions shown in [Table 4.3](#) and [4.5](#) are comparable to the measurements, will be discussed in [chapter 9](#).

	H2O-10-200		H2O-15-300		H2O-15-400	
	Value	± [%]	Value	± [%]	Value	± [%]
Input						
T_c [K]	473	1.5	573	1.2	673	1.0
P_c [mbar]	1000	3.3	1000	5.0	1000	5.0
P_a [mbar]	5.00	50.0	5.00	50.0	5.00	50.0
A_t [$10^3 \mu\text{m}^2$]	122.6	7.1	122.6	7.1	122.6	7.1
A_e [$10^3 \mu\text{m}^2$]	487.8	3.1	487.8	3.1	487.8	3.1
H_t [μm]	499.1	2.3	499.1	2.3	499.1	2.3
Output (MRT)						
F [mN]	13.68	9.6	12.88	10.2	12.12	10.5
ξ_F [-]	0.72	1.6	0.67	1.9	0.63	2.3
\dot{m} [mg/s]	16.72	8.8	15.01	9.0	13.70	9.0
$Re_{t,ideal}$ [-]	2917	9.3	2106	9.1	1608	9.2
I_{sp} [s]	83.45	1.3	87.52	1.6	90.19	1.9
$\xi_{I_{sp}}$ [-]	0.75	1.3	0.71	1.7	0.68	2.0
C_d [-]	0.95	0.2	0.94	0.3	0.94	0.3

Table 4.5: Input and output of the Resistojet Performance Tool (RPT) showing the predicted parameters of the planned water test campaign.

5

Experimental Set-up

This fifth chapter will detail the set-up that has been used to perform the various experiments described in this work. All experiments have been conducted in the cleanroom of the Aerospace Faculty. The distinct elements that make up the complete set-up are described in the first part of this chapter ([section 5.1](#)). The second part deals with the calibration of some of this test equipment ([section 5.2](#)), while the last section of the chapter ([5.3](#)) describes the error propagation. The majority of the test equipment is equal to that used by Cramer [15], which aids the reproducibility of her work. Notable exceptions, such as the changed load cell, will be discussed in more detail. The parts that remain the same will only be described briefly, as they have already been discussed extensively in other works [15]. The new water feed system has already been discussed in [chapter 3](#).

5.1. Test equipment

The test equipment used for the experiments has been collected and iterated upon by previous students. Some other equipment was already available in the TU Delft cleanroom. Most importantly, the Heraeus vacuum chamber [27] and connected Vacuubrand vacuum pump [80] enable the tests to be conducted in a vacuum. During the experimental phase of this thesis, this vacuum pump needed to be serviced by the author, before it could be used again. The cleanroom manager provided the necessary manuals to execute this servicing operation [80, 78]. The pump contains an oil lubrication system and an oil mist filter to ensure smooth and safe operation. The pump's oil reservoir was nearly empty and required filling, while the filter reservoir was full and required emptying. New pump oil was obtained via Johan Boender¹ of the Aircraft Hall, who also discarded the dirty oil from the filter in a yellow container in the hall. After completion of these tasks, the pump could be used safely again without further maintenance.

The whole test set-up is placed inside the vacuum chamber. Several vacuum pas-throughs make it possible to connect the various sensors, actuators, and DAQs with the outside environment. Only some components will be described in detail, based on relevance to this work. This includes the thrust bench (TB0-50m), the feed system, and some sensors.

5.1.1. Thrust bench

The test bench used for this thesis is the same one used by Cramer [15], namely the TB-50m (see [Figure 2.4b](#)). It is a torsional test bench, which was developed by Janssens [30] and calibrated again by Takken [69]. The thrust bench consists of a horizontal beam, suspended on a low friction bearing. The thruster is placed on one end of the beam, while the load cell is placed on the opposite side. When the VLM produces thrust, it causes a rotation, which is distributed through the beam to the load cell. The sensor subsequently registers this rotation with a change in voltage. More on the workings of this sensor is described in [subsection 5.1.3](#).

¹J.C.A.Boender@tudelft.nl

The thrust bench has a calibrated range from 0 - 12.3 mN with an uncertainty of $\pm 1.43\%$ [69]. This upper limit was due to overheating of the calibration coil. According to [chapter 4](#), the expected produced thrust is between 11.5 and 20.8 mN. While this is higher than the range Takken calibrated it for, it should still be sufficient for the tests. Originally, Janssens designed the test bench to work with loads up to 50 mN, so the expected loads fall within this limit. Moreover, by adjusting the moment arms of the loads, the forces can be manipulated to meet the calibration range. Previously, Versteeg [81] and Hutten [28] used the TB-5m test bench, which uses a pendulum structure and a low-friction pivot to measure the thrust [6]. Cramer opted for the torsional bench instead, since it does not depend on the centre of gravity, contrary to the TB-5m. This dependency on the centre of gravity has been identified to cause issues during testing [28]. Hutten hypothesised that this dependency was responsible for irregularities in the thrust data, which made it harder to analyse. This effect was especially noticeable in the water test data, as (liquid) water has a significantly higher density than (gaseous) nitrogen. Therefore, it has a significantly more pronounced impact on the centre of gravity.

Besides being independent on the centre of gravity, the TB-50m has another advantage over the TB-5m. Since the horizontal beam has a lot of threaded M3 holes, it is relatively simple to alter the position of components. In this way, it is easy to adjust the moment arm acting on the load cell. This has already been described in [chapter 3](#) and it will be elaborated upon later in this chapter ([section 5.2](#)).

5.1.2. Feed system

The (nitrogen) feed system is identical to the one used by Versteeg [81]. It is schematically represented in [Figure 5.1](#). A high pressure (max. 200 bar) nitrogen gas cylinder (1) provides the propellant for the experiments². Before reaching the VLM, the propellant first passes a series of valves, gauges, and regulators. The gas first encounters a high pressure shut-off valve (2), after which a pressure regulator valve (3) reduces the high pressure to a low pressure. By turning this valve a certain distance, the downstream pressure can be set between 0 and 16 bar. A low pressure shut-off valve (4) with a distinct red handle is placed directly after the regulator. After the shut-off valve, the tubing splits into three separate directions, enabling a nitrogen supply for three distinct experiments. These experiments use the rightmost path, which can be selected with the yellow selection valve (5). The Brooks 5850S mass flow meter (6) is connected to the right path and can both measure and control the N_2 mass flow. In this work, only the measuring feature has been used. The meter can measure volumetric flows between 0 and 2 L_n/min . The subscript n indicates that this holds for 'normal' conditions, meaning for a temperature of 0 °C (273.15 K) and a pressure of 1.013 bar (1 atmosphere). Given these conditions, an adapted version of the ideal gas law can be used to convert this volumetric flow rate to a mass flow rate, which is more useful in the context of this work. The following equation is used:

$$\dot{m} = \frac{M \cdot P \cdot \dot{V}}{R_A \cdot T} \quad (5.1)$$

The equation above gives a nitrogen mass flow range between 0 and 41.7 mg/s. The following values were used to come to this range: $M_{N_2} = 28.014 \text{ g/mol}$ and $\dot{V} = 2/60 L_n/s$. The 'normal' values for the temperature and pressure were used. This mass flow range is sufficient for the expected mass flow, as the expected flow will be lower than the upper limit, based on the results of previous theses and the predictions of the MRT ([chapter 4](#)). After passing through the meter, the nitrogen enters a flexible plastic tube which can be connected to the vacuum pass-through. This connection is established using a Swagelok Quick Connect [66]. Inside the vacuum chamber, the flow first encounters a solenoid valve from The Lee Company (7) and finally enters the VLM (8) where a small P - T sensor measures the chamber pressure (9).

²Contact Gassenteam Logistiek en Milieu (email: gasteam@tudelft.nl) to replace an empty N_2 gas cylinder with a new one.

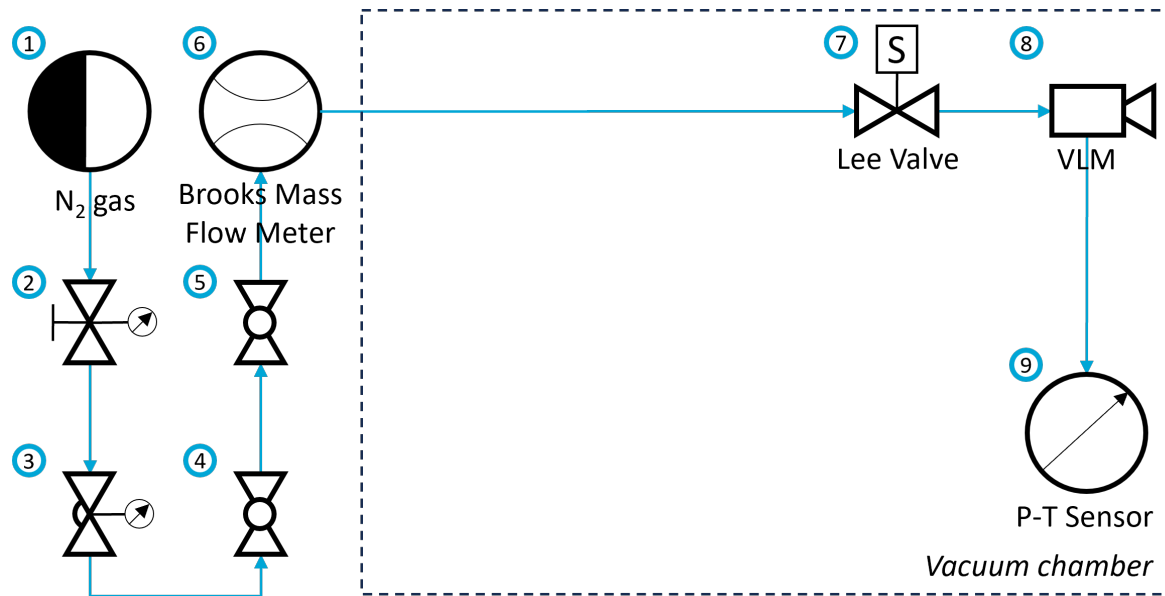


Figure 5.1: The nitrogen feed system.

5.1.3. Sensors

Several sensors record the physical parameters that are of interest for this work. Together, they measure the mass flow, the thrust, and the temperature and pressure at multiple locations (thrust chamber and vacuum chamber, for example). A nearly complete overview of the used equipment can be found in [Appendix A](#). The sensor errors will be discussed at the end of this chapter ([section 5.3](#)).

Brooks 5850S Mass Flow Controller

The Brooks 5850S Mass Flow Controller [9] can both measure and control the (N_2) mass flow. However, it will only be used to measure the mass flow in this work. As explained in [subsection 5.1.2](#), it can measure flows between 0 and 41.65 mg/s. The 5850S cannot measure liquid mass flows, necessitating the implementation of a different meter for liquid flows. More on this can be found in [subsection 3.2.2](#).

Sensirion SLI-1000

The newly introduced Sensirion SLI-1000 [59] measures the liquid (water) mass flow. It uses the thermal properties of the water to determine the rate of the flow. Thanks to the provided SCC1-USB cable and Sensirion's Sensor Viewer software, the mass flow can be easily measured without further work. The sensor is discussed in more detail in [subsection 3.2.2](#) and calibrated later in this chapter ([section 5.2](#)).

Futek LSB200

The Futek LSB200 [19] is a miniature load cell with a capacity of 100 g, meaning it is capable of measuring loads up to approximately 1000 mN (1 N). It has a rated output (RO) of 1.0893 mV/V and is excited with 5 V. Thus, when fully loaded (100 g), the load cell will output 5.4465 mV. Seen that this voltage change is quite subtle, an amplifier is used to make the signal easier to analyse (see [subsection 5.1.5](#)). More information on this process can be found in the next section ([5.2](#)). The sensor's datasheet can be found in [Appendix C](#). The load cell used previously (Futek LRF400, [15]) would be better suited for this work. This sensor is designed to measure smaller loads (capacity of 10 g), which is better fitting for the expected loads. However, the LRF400 broke during another thesis and was replaced with the LSB200.

Vacuubrand VSP 3000 pressure sensor

The Vacuubrand VSP 3000 pressure sensor [79] is located inside the vacuum chamber. The sensor is of the Pirani-type which measures the vacuum pressure based on the thermal conductivity of the surrounding gas. It is used to measure the ambient pressure inside vacuum chamber. The VSP 3000 is limited to a maximum pressure of 1000 mbar, so it cannot measure pressures higher than this, which

is usually the case with atmospheric pressure. The lower limit of the sensor is $1 \cdot 10^{-3}$ mbar or 0.1 Pa, which is far below the desired vacuum pressure. As mentioned by Hutten [28], the VSP 3000 may be less accurate when operated during the water tests. He suggested an alternative, the VSK 3000, which will perform better with water vapour. Unfortunately, this sensor is quite expensive. Moreover, the accuracy of the ambient pressure's readings is not essential to the VLM performance. Therefore, the VSP 3000 is kept but with an increased uncertainty of $\pm 50\%$ for the water experiments.

TE Connectivity MS5837-30BA

The TE Connectivity MS5837-30BA [71] is a P - T sensor, meaning it is able to measure both the pressure and temperature at its interface. It is located at the aluminium interface where it measures the chamber pressure and the interface temperature. A separate thermocouple is placed near the chamber to measure its temperature. The MS5837-30BA is an absolute sealed gauge pressure sensor with a maximum temperature rating of 85 °C. Care must be taken that this limit is not reached to ensure a proper functioning sensor. The P - T sensor is connected via the NI USB-8451 and USB-6008 to the cleanroom PC. As mentioned in chapter 3, the sensor is quite fragile and required replacing on multiple occasions.

Thermocouples

Several K-type thermocouples are used throughout the experiments (TME KA02). These sensors are composed of two different metals [76], which produce a voltage difference when heated. The most essential thermocouple is situated between the copper block and nut to measure the chamber temperature. It was previously placed between the nozzle profile and copper blocks and thus closer to the actual chamber. However, this could reduce the VLM's leak tightness. Moreover, since the entire thruster is heated by the cartridge heaters, the temperature will be approximately the same for both locations. Both measurement locations are thus expected to be valid. Another thermocouple is attached to the pressure sensing tube to monitor its temperature. The thermocouples are connected to the PC via the NI USB-9162.

5.1.4. Actuators

Only four actuators are used in the experimental set-up. A Lee company VHS® Series 2-Way Dispense Solenoid Valve is used to control the propellant supply. It is normally closed but opens by means of a spike and hold circuit. Using Pulse-width modulation, the valve can also be partially opened to control the flow rate. This technique is not used for the nitrogen tests, but might be of interest for the water tests. More on this is discussed in chapter 3. The Vacuubrand RZ 6 is a pump that creates a (near) vacuum inside the vacuum chamber [80]. The VTDC is used for calibration, while the Watlow 1/8-Inch FIREROD® Cartridge Heaters increase the temperature of the VLM [82]. To prevent them from overheating, they are immersed in a thermal paste consisting of a gallium-indium-tin alloy [15]. The Varying Turn-Density Coil (VTDC) consists of a permanent magnet, suspended inside a coil with a varying turn-density. By changing the current through this coil, the position of the magnet can be controlled. This actuator has been designed by Bijster [6], and subsequently calibrated by Takken [69] and Teixeira [72]. It has been used previously for calibrating the test bench and this will be its purpose here as well. This calibration process and the following outcomes will be discussed in detail in subsection 5.2.2.

5.1.5. Data Acquisition Devices

Multiple National Instruments (NI) data acquisition (DAQ) devices are used throughout the set-up. Some are situated inside the vacuum chamber to read sensor data, such as the NI USB-8451 and NI-9211 that read the P - T sensor and thermocouple data, respectively. The DAQ devices are connected to the cleanroom PC. The Scaime CPJ is an amplifier that amplifies the load cell signal [57]. It features both an adjustable span (0.15 - 12 mV/V) and zero point. More information on how the amplifier is used can be found in subsection 5.2.1. Its datasheet is included in Appendix C. The Scaime CPJ is used along with the DAQ 6008 to convert the analogue signal to a digital signal. An internal low-pass filter of 10 Hz is used to block high-frequencies (e.g. noise). The load cell data is sampled at 30 Hz to avoid the Nyquist frequency. Both the amplifier and DAQ were borrowed from the Meetshop³, a facility provided by the faculty of Mechanical Engineering.

³Contact person: J.A.Brenkman@tudelft.nl

5.1.6. Power supplies

Five distinct Delta Elektronika power supplies are used to power the individual components of the test set-up. Two of these are used to power the solenoid valve via a spike and hold circuit. E-030-10 provides an initial spike (24V) to activate the valve, after which D-030-10 takes over with a lower voltage (3.2V) to keep the valve opened. Two other power supplies provide the necessary wattage for the two cartridge heaters. The last power supply supplies an adjustable current to the VTDC, thereby controlling the permanent magnet's position and thus the force acting on the thrust bench. Other components are either powered via their own power cords, or via the cleanroom PC (see [section A.4](#)).

5.1.7. Software

The software used during this work predominantly uses LabVIEW 2019 and had already been developed iteratively by previous students. Fortunately, this VLM DAQ software did not require significant changes. Only minor changes were made to accommodate personal preferences, but these do not warrant an extensive discussion. The software can be found on the cleanroom PC in the author's folder. The files necessary for executing tests are mentioned in the procedures ([Appendix D](#)). The most notable improvement to the LabVIEW software is the automation of the thrust tests. Previously, the Lee valve had to be opened and closed manually with the click of a button. With the new version, the intervals can be inserted before the tests after which the software ensures the valve switches states at the correct time (every 5 minutes). The automation of this process enables the test conductor to focus on more important aspects of a test.

Another notable change to the software is the addition of the Sensirion Sensor Viewer software [58]. It was installed on the cleanroom PC via an USB and can be found on the PC's Desktop. The sensor viewer software is specifically made to read the SLI-1000's output and requires no further processing. [Figure 5.2](#) shows what this software looks like. It uses a sampling frequency of approximately 14 Hz and saves the data in a CSV file, which can be easily opened and read by the RPT made by Hutten [28]. The time and flow rate values are extracted, and the flow rate is converted to mg/s instead of the saved $\mu\text{L}/\text{min}$ (see [subsection 3.2.2](#)). To further streamline the measurement process, the liquid flow measurement process can be integrated in the already existing VLM DAQ software. This is left for future work, however.

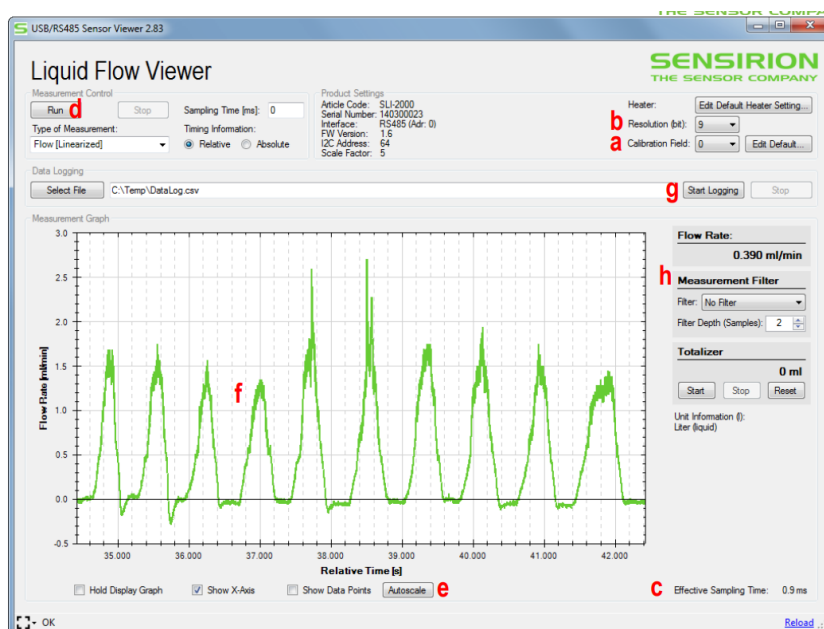


Figure 5.2: The Sensirion Sensor Viewer used to measure the liquid mass flow [58].

5.2. Calibrations

Before testing can commence, it is important to calibrate the test equipment. This calibration should verify that the measured values are within the expected bounds and showcase consistency. Over time, a sensor's output may display drift, which does not necessarily pose a problem if handled well. By calibrating the sensors beforehand, this undesired behaviour can be mapped and compensated for. It should also help to detect a faulty sensor, which can subsequently be replaced. The most important calibrations, that of the load cell, the Varying Turn-Density Coil, and the liquid mass flow meter will be treated in their respective subsections ([subsection 5.2.1](#), [5.2.2](#), and [5.2.3](#)).

A lot of equipment used during testing either directly or indirectly, is not calibrated in this thesis. Instead, the functioning of this equipment underwent a 'sanity check'. For example, the $P-T$ sensor's output has been read out via LabVIEW and showed an expected output (room temperature and a pressure around 1 atmosphere⁴). The same principle was employed to determine the functionality of other sensors and equipment, such as the thermocouples, the power supplies, and the mass flow controller. This last sensor is hard to directly perform a sanity check on, as it is not feasible to estimate a mass flow rate of a transparent gas by eye. However, it is simple to check whether the mass flow rate is comparable to those measured in previous work. The easiest test to quickly simulate is the cold flow test, as only a vacuum is required. This check resulted in a measured N_2 flow rate of approximately 16.9 mg/s, which is comparable to both Cramer's and Versteeg's results [81, 15]. Especially when accounting for the increased throat area, which increases the flow rate. Lastly, the vacuum chamber features an integrated pressure sensor, the Vacuubrand VSP 3000 [79]. It is not calibrated independently. However, its output can be compared to the $P-T$ sensor's output. Regarding the fact that the Vacuubrand sensor maxes out at 1 bar, it is only usable at levels lower than atmospheric pressure. Both sensors show a similar output in vacuum conditions, although a varying difference is present. This can likely be attributed to a combination of both sensor's measurement uncertainty and will not be investigated further (see [section 5.3](#) for more information). The $P-T$ sensor's data is solely used for the chamber pressure (P_c), while the Vacuubrand's data is only used for the ambient pressure data (P_a).

5.2.1. Load cell calibration

The load cell used in this work (Futek LSB200, [19]) is different to the one used in the previous work (Futek LRF400, [18]), as described in [subsection 5.1.3](#). It was recently calibrated and used by Gomes [23] but, as will be explained shortly, the used settings are different and thus those results cannot be used for this work. The load cell is connected to the cleanroom PC via the Scaime CPJ amplifier and NI USB-6008 DAQ to read out its data via LabVIEW. The amplifier is required to boost the signal, which is in the millivolt range, to an easier to distinguish volts range. Before usage, the correct sensor sensitivity must be selected. The Scaime CPJ datasheet (see [section C.3](#)) explains this procedure. The Futek LSB200 is powered with 5V, has a capacity of $100\text{ g} \pm 0.155\text{ g}$ (1.52 mN ⁵), and a sensitivity of 1.0893 mV/V. The way in which this error is calculated will be explained in [section 5.3](#). The analytical model showed that the maximum load to be measured is approximately 20 mN, but to have some leeway, 50 mN (or 5 g) is chosen. According to the datasheet, the required sensor sensitivity can now be determined as follows:

$$\text{Sensitivity} = \frac{5\text{ g}}{100\text{ g}} \cdot 1.0893\text{ mV/V} = 0.054\text{ mV/V} \quad (5.2)$$

Unfortunately, this sensitivity falls below the selection range. The smallest option (position X) is therefore chosen. Besides the sensitivity, the amplifier also features three potentiometers (P1, P2, and P3) that are used to fine-tune the zero level (P2 and P3) and the gain (P1). In theory, the gain should be set in such a way that the maximum voltage (10V) is measured at the maximum load (50 mN), so that the full range of the amplifier is used. In practise, however, this maximum load is still significantly smaller than the gain can amplify. Therefore, the gain is set to the maximum to still reach the highest obtainable resolution.

⁴1 atmosphere is defined as being equal to 101,325 Pa.

⁵A gravitational constant of 9.80665 m/s^2 is used to convert masses to weights.

The sensor capacity mentioned earlier means that the sensor can measure loads up to 100 g, which is far greater than the expected loads produced by the VLM. An important note is that the sensor is likely less accurate in its lower measurement range [15]. Fortunately, by carefully choosing the placement of the cell on the test bench, this can be partially compensated for. A load cell designed for smaller loads, like the LRF400, would be better, but the Futek LSB200 is currently the only load cell available in the cleanroom.

After preparing the amplifier, the behaviour of the load cell can be characterised. This is done by employing the same method as described by many others (Takken [69], Cramer [15], Gomes [23], etc.); placing known weights on the sensor and recording the voltage output. For this calibration, the load cell is placed vertically on an even surface. To chart what voltage is being output for a certain applied load, weights are placed on the load cell one at a time. These weights have known masses, which are verified using the cleanroom's scale, the Mettler Toledo AG245 (accuracy of 0.1 mg, [77]). This process should result in a linear relationship between the applied load and the measured voltage. The table and corresponding figure below (Table 5.1 and Table 5.2) summarise this calibration. From the data, the following linear relation (rounded to three decimals) can be derived:

$$V_{LSB200} = 0.026 \cdot F_{LSB200} + V_{intercept} \quad (5.3)$$

$V_{intercept}$ is the intercept value shown in the figure (0.016). It will not be used further, since the zero-level is highly variable and it can be easily accounted for by using the difference between the applied load and the zero-level (ΔF_{LSB200} or ΔV_{LSB200}), instead of the absolute value (F_{LSB200}). The linear fit has an R^2 value of 1.000, proving the load cell's behaviour is highly linear and the established function fits exceptionally well [83]. For the experiments, the found relationship will be used in the opposite way as it will be used to convert the measured voltage to the exerted load. Thus, the relationship that will be used henceforth is as follows:

$$F_{LSB200} = 38.52 \cdot \Delta V_{LSB200} \pm 1.52 \text{ mN} \quad (5.4)$$

Mass [g]	Weight [mN]	Voltage [V]
20.00	196.17	5.11
10.00	98.08	2.56
5.00	49.05	1.30
4.00	39.22	1.04
3.00	29.42	0.78
2.00	19.62	0.52
1.00	9.85	0.27
0.63	6.17	0.18
0.39	3.80	0.12
0.29	2.82	0.10
0.22	2.12	0.07
0.50	4.91	0.14
0.20	1.96	0.07
0.10	0.98	0.05

Table 5.1: Measured mass, weight, and voltage for the load cell calibration.

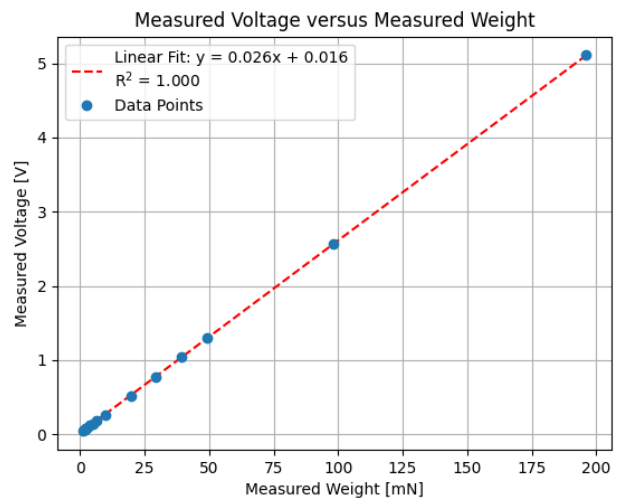


Table 5.2: Measured weight and voltage including the determined linear relationship.

5.2.2. Thrust bench calibration

Apart from the load cell calibration, another important component of the test set-up is the Varying Turn-Density Coil (VTDC). It has been extensively used in the past and is essential in the calibration process. By controlling the current through it, a known force is generated. The higher the current, the higher the force. This relation can then be used to calibrate the TB-50m thrust bench and determine how the force measured by the load cell corresponds to the force generated by the VTDC. To characterise this generated force, the thrust bench is calibrated extensively. The calibration campaign is shaped after the campaign performed by Cramer [15], who found unexpected results (see chapter 6 of her work). In an effort to find the root of this unexpected behaviour and produce an explanation and solution, this calibration campaign is more comprehensive. Three factors will be altered over the course of the campaign: the vacuum state (yes or no), the test bench state (empty or full), and the heaters' state (on or off). The vacuum reached during testing was always below 15 mbar, while the heaters were set to ensure a chamber temperature (T_c) of either 200°C or 300°C. The empty test bench includes only the essential components for the tests (VTDC and load cell), while the full test bench includes all components listed in the previous section (see also Appendix A). Figure 5.3 shows the two test bench states. The different factors are varied in such a manner to locate the cause of the unexpected TB-50m characteristics. LabVIEW is used to raise the current through the coil in a step-wise fashion, which should result in a similar increase in the exerted load. The current is increased with 0.5 A every 30 seconds. After 16.5 minutes (16.5 A), the current is removed, and the measured load should return to the zero-level. Every calibration test is repeated three times, resulting in three datasets for every test. Table 5.3 summarises the calibration campaign and names the separate tests.

Test ID	Vacuum State	Test Bench State	Heaters State
CAL-000	No	Empty	Off
CAL-100	Yes	Empty	Off
CAL-010	No	Full	Off
CAL-110	Yes	Full	Off
CAL-111a	Yes	Full	On (200°C)
CAL-111b	Yes	Full	On (300°C)

Table 5.3: Overview of the TB-50m thrust bench calibration campaign.

Several of Cramer's recommendations were implemented to improve the results of the calibration process. Firstly, the test bench was levelled before the campaign. This process had been simplified by the improvements described in chapter 3. An uneven test bench influences the results as an additional vertical component is added to the force, instead of a purely horizontal component. Secondly, the calibrations were done in quick succession in two days, to limit the effect of varying external factors, such as temperature and humidity. Thirdly, all wires coming from the VLM were routed through the test bench's rotation point to restrict their influence on the readings. The wires can add a resistive force to the rotational movement, which leads to an added uncertainty to the measured load [52]. Lastly, Krusharev [36] reported that the maximum mass the TB-50m supports is 360 g. So, it must be checked whether the total mass on the test bench is lower than this maximum. Due to an oversight, this has not been done in this work and is thus left as a recommendation for improvement for follow-up research.

The Varying Turn-Density Coil used in the experimental set-up was first developed by Bijster [6], a previous master student who also developed the TB-5m as part of the master thesis. Bijster developed a calibration method for the coil that involves the Mettler Toledo AG245 scale and a power supply unit. The load read-out of the scale is directly proportional to the current through the coil. By following Bijster's procedure, a coil sensitivity of 833 $\mu\text{N/A}$ with a standard error of estimation of 6.19 μN was found. For the used magnet, Bijster predicted a sensitivity of $912 \pm 67.2 \mu\text{N/A}$. So, the found value falls outside of the predicted range. According to Bijster, this discrepancy is explained by a smaller gradient of the magnetic field, which in turn is explained by geometrical differences between the model and the actual coil. This proves that the VTDC's performance is highly dependent on its physical state.

The coil has been calibrated multiple times after Bijster. In 2020, Versteeg [81] found a coil sensitivity of $826 \pm 6 \mu\text{N/A}$, which closely agreed with an earlier calibration of Jansen [29] in 2016. The most recent calibration was performed in 2024 by Teixeira [72], who found an even lower sensitivity of $813 \pm 0.6 \mu\text{N/A}$. Over the years, there seems to be a decreasing trend in the coil's sensitivity. This trend is seemingly inconsistent as the sensitivity barely dropped between 2016 and 2020, while it reduced significantly between 2020 and 2024. Following Bijster's reasoning, the shift can (partially) be attributed to geometrical differences with the original coil. Small deviations in the coil's placement may accumulate to a reduced magnetic field gradient. Another contributing factor may be the gradual loss of the permanent magnet's magnetic moment. This can occur naturally and can be amplified by certain external influences, such as exposure to heat or electromagnetic fields [12]. A thorough investigation involving a magnetometer could shed more light on the reasons behind this negative coil sensitivity slope. However, this is left for future work. The sensitivity found by Teixeira [72], $813 \pm 0.6 \mu\text{N/A}$, will be used from now on, as it is the most recently found value.

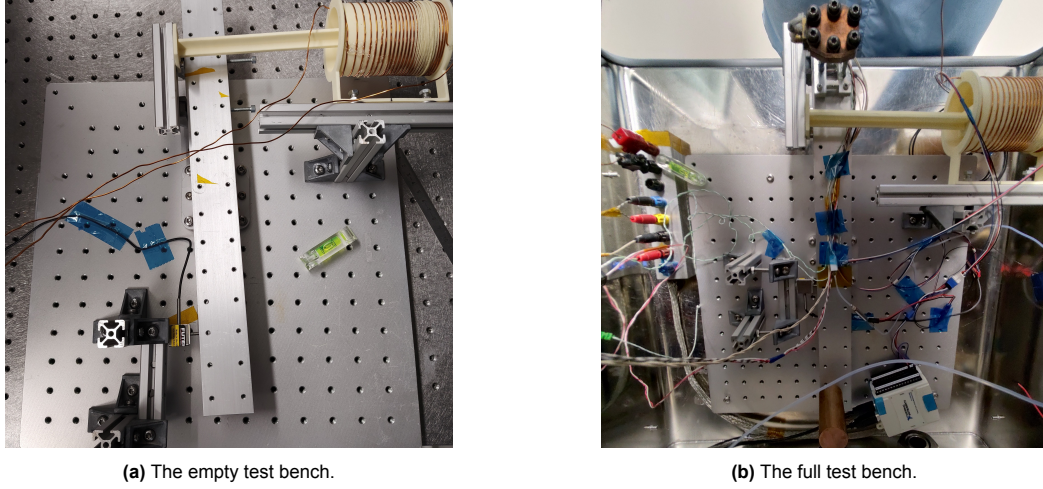


Figure 5.3: The two TB-50m test bench states used for the calibration campaign.

One last important factor to consider in converting the force exerted by the VTDC to the force measured by the load cell, is the moment arm of both points. An advantage the TB-50m has, is that by changing the distance of the coil or load cell to the rotation point, the load can be easily amplified or diminished. The used load cell has a capacity of approximately 1000 mN, while the maximum expected load of the VLM is roughly 20 mN. The VTDC can produce 0.813 mN per ampere. Takken [69] recommended to not use currents above 16 A to avoid overheating of the coil. Thus, the total load that can be produced is in the lower range of the load cell's capacity ($\sim 1\%$), which leads to less accurate readings, as the standard deviations will play a bigger role in this range [19]. Acquiring a load cell with a smaller capacity is therefore recommended for subsequent VLM experimentation. Since this was not possible for this work, an alternative method was employed to amplify the measured load.

By modifying the distances to the center of the thrust bench, the ratio with which the loads are affected can be altered. By placing the load cell closest to the rotation point (d_{LSB200}), at a distance of 25 mm, and the VTDC furthest from it ($d_{VTDC} = 145 \text{ mm}$), this ratio is maximised. In other words, the force produced by the coil and measured by the load cell, is multiplied by 5.8. The measured distances have a different associated uncertainty, due to the way the components are attached to the TB-50m. The load cell is directly connected to the test bench using an M3 bolt. The horizontal beam is a rectangular profile with threaded holes at every 25 mm. No specific information was found on the uncertainty associated with the hole locations. It is thus assumed to be negligible. The distance to the VTDC on the other hand, is determined with a ruler and its uncertainty is estimated at 3 mm. To find the combined uncertainty, a simple relation is used that will be used further in this work. The same method was also employed by both Versteeg and Cramer, thus easing comparisons. The errors are considered to be

simple average errors [40] and are combined as shown below (Equation 5.5). Consequently, the ratio uncertainty is 0.12. Equation 5.6 summarises this discussion and this result will be used henceforth to convert the produced load to the measured load for the thrust bench calibration.

$$\Delta z = \left(\frac{\Delta x}{x} + \frac{\Delta y}{y} \right) \cdot z = \left(\frac{0}{25 \text{ mm}} + \frac{3 \text{ mm}}{145 \text{ mm}} \right) \cdot 5.8 = \pm 0.12 [-] \quad (5.5)$$

$$F_{LSB200} = \frac{d_{VTDC}}{d_{LSB200}} \cdot F_{VTDC} = (5.8 \pm 0.12) \cdot F_{VTDC} \quad (5.6)$$

As mentioned at the beginning of the section, the current through the coil is increased with steps of 0.5 A every 30 seconds. When the current reaches 16.5 A, it is removed and the force acting on the thrust bench stops. Figure 5.4 and 5.5 shows the results of the CAL-111a calibration test (vacuum, full test bench at 200 °C). This calibration will be analysed in detail here, but the analysis is applicable to all six calibration tests. Graphs of all tests are included in the appendix (see section B.1). The first graph (top) of Figure 5.4 shows an essential issue that was also encountered by Cramer; load signal drift. The first 30 seconds of data show a load of approximately 0.5 mN, while the final 30 seconds show 0 mN. Both the start and end periods should show a similar load, which is not the case unfortunately. Note that these loads do not have to be 0 mN necessarily (due to zero-point shift), as long as they show an equal value. While the drift for CAL-111a is fairly small (0.5 mN), it was found to be notably bigger for others (2.5 mN, CAL-000). Unfortunately, the magnitude and direction of the drift (decreasing or increasing) is seemingly random and requires an even more elaborate calibration campaign to fully comprehend. For now, the drift will be compensated for to allow for a better comparison between the three iterations that are done for each calibration test. This drift compensation is done by fitting a linear function through the first and last 20 seconds of the calibration. This can be seen in the top graph of Figure 5.4, where the dotted red line shows the fitted linear function. This is then subtracted from the original load (solid blue line) to arrive at the corrected load (solid green line in bottom graph). This compensation process is done for all calibration tests.

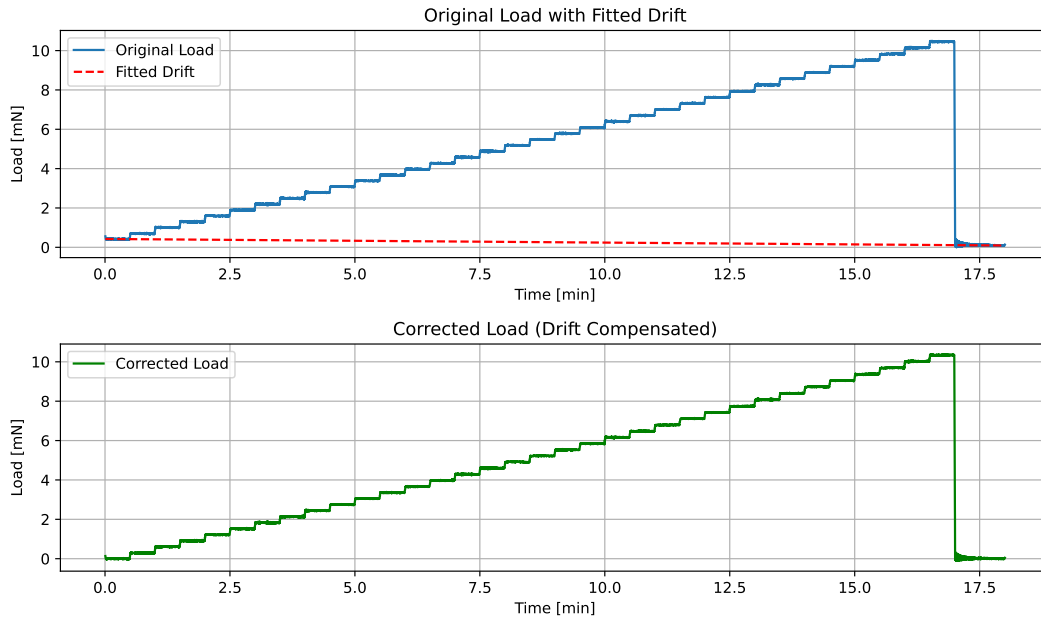


Figure 5.4: Drift compensation process for the TB-50m thrust bench calibrations in vacuum and with a full test bench at 200 °C (CAL-111a). Top shows the original load and fitted linear function. Bottom shows the corrected load.

After compensating for the drift, the mean load value at each current step is calculated. However, the loads measured from 8.5 amps onwards are disregarded. This has also been done by Cramer, as the

signal seems to drift more for higher currents. The top left graph of Figure 5.5 clearly illustrate this as well. This effect can likely be attributed to overheating of the coil, which leads to irregular behaviour of the VTDC. A straight line is fitted through the mean load values of all three datasets. The left graphs of 5.5 show the original (uncompensated drift) loads, while the right graphs are produced with drift compensation. The differences between the three datasets are clearly reduced when compensating for the drift. Because of this improvement, the drift compensated data (right graphs) are used in the further analysis.

The fitted lines are all highly linear ($R^2 = 1.000$), even for the uncompensated data. This is a clear improvement with regards to the results found by Cramer. So, the improvements mentioned in this section have resulted in a more linear test bench behaviour. Moreover, the fitted slopes (a [mN/A]) exhibit a reduced deviation, resulting in a smaller error. Lastly, the measured forces are normalised for a current level of 8 ampere ($F_{VTDC,8A}$ [mN]). The standard deviations are calculated for the normalised forces and measured slopes. The results of the TB-50m thrust bench calibration campaign are summarised in Table 5.4.

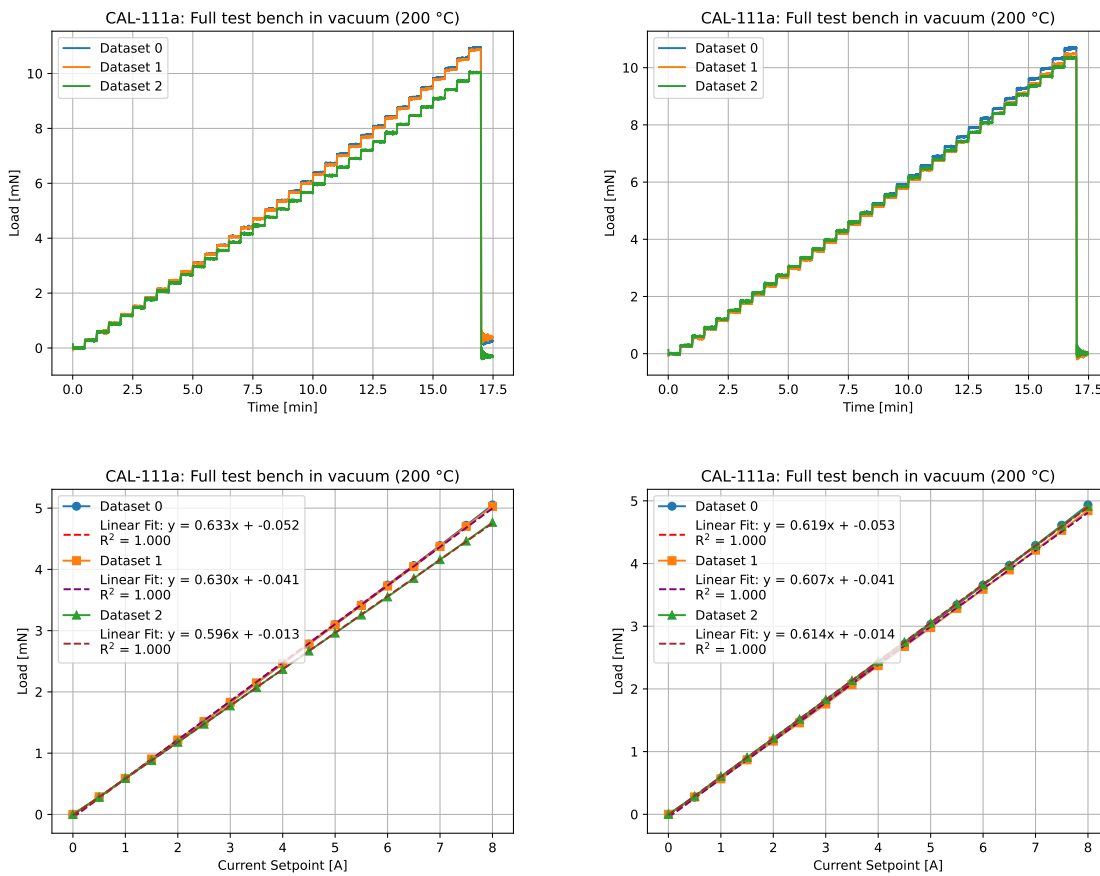


Figure 5.5: Results of the TB-50m thrust bench calibrations in vacuum and with a full test bench at 200 °C (CAL-111a). The left graphs show the original loads, while the right graphs show the loads with drift compensation.

The table below (Table 5.4) shows a much improved result of the thrust bench calibration campaign, compared to the results found by Cramer [15]. The normalised forces and slopes found for each calibration test are quite comparable and vary little. The average normalised force is 4.658 mN with a standard variation (3σ) of ± 0.35 (7.5%). The average slope is 0.602 mN/A with a standard variation of ± 0.04 (7.0%). A notable outlier in this analysis is CAL-000 (and CAL-111b to a lesser extent). This test shows a significantly higher error compared to the others, which can clearly be seen in its graphs (see section B.1). The first of the three calibration datasets shows a severely different behaviour than

the other two. The exact cause of this behaviour is unknown and requires more research. A possible reason for this deviating performance may be due to friction in the thrust bench's bearing or a different coil behaviour due to a changing temperature. Since this extreme deviation was not noticed on other occasions, it is left for future work to find the exact cause of it.

Interestingly, the average slope found in this section (0.602 mN/A) is lower than the VTDC sensitivity reported earlier (0.813 mN/A). In theory, these values should overlap since the coil is not altered. Instead, the slope found during the calibration campaign is 25% lower. This can likely be attributed to the addition of the TB-50m thrust bench to the system. The force generated by the VTDC is not directly measured by a scale but is indirectly measured by a load cell via the thrust bench. As discussed earlier, this bench possibly adds some friction to the system, which results in a reduced sensitivity. It is important to keep this conclusion in mind for the thrust analysis performed in [chapter 7](#) and [8](#) as it might influence those results as well. It is also advised to investigate the TB-50m's characteristics further in a subsequent work. The exact reasons behind the drift behaviour are still not fully known. Moreover, the deviating behaviour of some tests are not completely understood. To improve the reliability of the results found using the TB-50m, more research is advised.

Test ID	$F_{VTDC,8A}$ [mN]	a [mN/A]
CAL-000	4.679 ± 1.646 (35.2%)	0.601 ± 0.069 (11.5%)
CAL-100	4.428 ± 0.457 (10.3%)	0.573 ± 0.011 (1.9%)
CAL-010	4.627 ± 0.532 (11.5%)	0.605 ± 0.012 (1.9%)
CAL-110	4.661 ± 0.556 (11.9%)	0.606 ± 0.018 (2.9%)
CAL-111a	4.784 ± 0.382 (7.9%)	0.613 ± 0.006 (1.0%)
CAL-111b	4.766 ± 0.810 (17.0%)	0.616 ± 0.019 (3.1%)
Average	4.658 ± 0.350 (7.5%)	0.602 ± 0.042 (7.0%)

Table 5.4: Overview of the TB-50m thrust bench calibration results.

5.2.3. SLI-1000 calibration

Contrary to all other equipment described in this chapter, the Sensirion SLI-1000 has not been used before. It was acquired in an unopened, bright green box via Barry Zandbergen and can now be found in a cupboard at the far end of the cleanroom. Although the sensor is brand new, it is still important to calibrate it. This calibration should verify that it is functioning correctly. This calibration has been executed in collaboration with Pârvulescu [50], who extensively describes the process in his work (chapter 6).

For the calibration of the SLI-1000, inspiration was taken from Hutten [28], who performed a similar calibration for the syringe pump (see chapter 4 of his work). The same syringe pump (ProSense NE-1000X2) is used to pump a constant volumetric flow rate via the flow meter into a beaker. This beaker is placed on the Mettler Toledo AG245 scale to determine its mass. The system is connected using MINSTAC 062 tubing. [Table 5.6](#) shows the calibration set-up. The scale and beaker are shown on the left of the picture, the SLI-1000 in the middle, and the pump and syringe on the right. The beaker is partially filled with water and the end of the tubing is submerged in this water. This is done to eliminate the effects of surface tension on the measurements. Moreover, it is ensured that the tubing does not touch the beaker to avoid unwanted noise from this interaction. By measuring the start and end mass of the beaker after a certain time period, the mass flow rate can be easily measured. The times are recorded using a stopwatch. The mass flow rate can then be converted to a volumetric flow rate (\dot{V}_{AG245}) using the density of water (0.997 mg/ μ L). Sensirion's sensor directly measures the volumetric flow rate ($\dot{V}_{SLI-1000}$). Six different tests were conducted at slightly different pump settings, resulting in the table below ([Table 5.5](#)).

This table shows that there is a difference between the volumetric flow rate measured using the AG245 scale and the liquid mass flow meter. However, this difference is fairly small ($\sim 1\%$) and is greatest

(4.5%) for a low flow rate. The discrepancy is even smaller when taking evaporation of the water into account. As this was not done consistently for all six tests, this effect is ignored. The results shown in Table 5.5 indicate that the Sensirion SLI-1000 measurements closely align with those done with the scale. This confirms that the sensor is functioning correctly and can thus safely be used for the water tests. The sensor's error is treated in the next section (5.3). Due to the rough nature of the calibration performed here, no sensor accuracy is reported here. These results are used solely to verify the sensor functioning. Instead, the outcome of the error analysis of section 5.3 will be used further ($\pm 5.03\%$).

Test ID	\dot{V}_{AG245} [$\mu\text{L}/\text{min}$]	$\dot{V}_{SLI-1000}$ [$\mu\text{L}/\text{min}$]
1	706	717
2	709	713
3	544	547
4	546	547
5	545	547
6	61	64

Table 5.5: Measured volumetric flow rates for the SLI-1000 calibration.

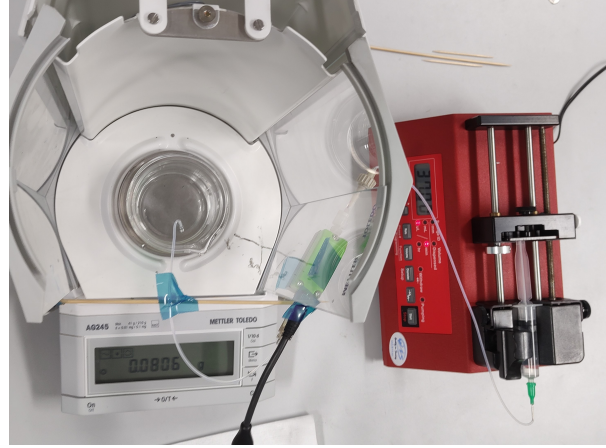


Table 5.6: Top view of the SLI-1000 calibration set-up.

5.3. Error Propagation

All sensors mentioned in the preceding sections contain errors. These are usually provided by the manufacturers as confidence bounds and give insight in the accuracy and reliability of a sensor. Previous works have characterised already most of the equipment used in the experimental set-up, with a few exceptions; a different load cell (LSB200, [19]) is used and a liquid mass flow meter (SLI-1000, [59]) is added. The errors of these sensors will be treated a bit more in-depth, while the others are taken from the work of Cramer [15]. An important note here is that it is assumed that the sensor errors are systematic and random in nature and can thus not be eliminated by taking multiple measurements [35]. The errors that will be presented throughout this thesis are usually in the form of three times the standard deviation (3σ), which is computed using the formula shown below (Equation 5.7). In short, it captures the amount of variation of a parameter around a mean value. By taking the triple of the standard deviation, 99.7% of all values should be captured, if the data is normally distributed [35]. Equation 5.8 shows how the root mean square (RMS) value is calculated, which will be used to calculate the test averages in chapter 7 and 8. In these formulae, N represents the total number of elements in the dataset, x_i the value of the i -th element, and \bar{x} the mean of the elements.

$$3\sigma = 3 \cdot \sqrt{\frac{1}{N} \sum_{i=1}^N (x_i - \bar{x})^2} \quad (5.7)$$

$$\text{RMS} = \sqrt{\frac{1}{N} \sum_{i=1}^N x_i^2} \quad (5.8)$$

Since most of the test equipment was directly adopted from Cramer, the confidence bounds for the same sensors are considered unchanged. These have all been summarised in Table 5.7. One important point to consider is the fact that the Brooks 5850S Mass Flow Controller was likely last calibrated by Ganani [20], more than 5 years ago. Ganani found a significant disparity between the sensor's output pre- and post-calibration. Before he sent the sensor for calibration, 10 years passed since the last calibration. It is thus reasonable to assume that the mass flow meter's output found in this (and possibly previous) work is different to the actual flow rate. However, as data on this possible discrepancy is not available, the error as reported in Brooks Instrument [9] will be used and is reported in the table below.

It will be left for future research to calibrate the meter once again.

The replacement of the Futek LRF400 with the LSB200 means the uncertainty associated with the new sensor needs to be calculated. According to Futek [19], a couple of factors influence the sensor's error: nonlinearity, hysteresis, and non-repeatability. These have values of $\pm 0.1\%$, $\pm 0.1\%$, $\pm 0.05\%$ of the LSB200's rated output (RO), respectively. Additionally, two errors are temperature related; the temperature shift zero, and temperature shift span. These add an additional error of $\pm 0.018\%$ of RO/ $^{\circ}\text{C}$, and $\pm 0.036\%$ of load/ $^{\circ}\text{C}$. The temperature is assumed to be quite stable, so the temperature related errors will stay constant throughout the experiments. Adding the squares roots of these errors results in the following total sensor error:

$$3\sigma = \sqrt{0.1^2 + 0.1^2 + 0.05^2 + 0.018^2 + 0.036^2} = 0.155\% \text{ of RO} \quad (5.9)$$

The reported rated output of the Futek LSB200 is 1.0893 mV/V. So, for a full load (100 g) and an excitation voltage of 5 V, the sensor should output 5.44 mV. Implementing the error of Equation 5.9, results in a deviation of only 8.4 μV . However, like the signal itself, the error will also be amplified by the Scaime CPJ amplifier. It is thus best to continue using the error in percentages and add this to the final measured thrust. Moreover, the amplifier itself also introduces some uncertainty to the thrust signal. Scaime [57] lists an accuracy of 0.05% and a maximum temperature span drift of 0.02%/ $^{\circ}\text{C}$. One last error that is easy to overlook is the error associated with the VLM placement. The thruster is placed at a certain distance from the test bench's rotation point (d_{VLM}). This distance measurement is not exact and done by eye, which introduces yet another uncertainty. For the final tests, the VLM was placed at a distance of 187.5 mm, but this value is estimated to vary with ± 2 mm. This results in an additional distance uncertainty of $\pm 1\%$. The amplifier and distance deviations should all be combined with the deviation computed in the equation above (Equation 5.9). The result is the total standard deviation of the load cell, amplifier, and distance, which is found to be approximately 1.08%. This value is reported in Table 5.7. The distance uncertainty contributes significantly to the standard deviation. Improving this measurement thus directly leads to less error in the thrust measurement.

Lastly, the liquid mass flow meter's uncertainty needs to be addressed. The sensor's performance is neatly detailed by Sensirion AG [59]. Three parameters are applicable to this work: the accuracy (5% of measured value), repeatability (0.5% of measured value), and temperature coefficient (0.1% of measured value/ $^{\circ}\text{C}$). A mounting orientation sensitivity (1% of full scale) is also listed but it is disregarded as the sensor is mounted horizontally on the test bench. Once again it is assumed that the temperature does not vary significantly. Combining these errors as done in Equation 5.9, results in a total deviation of 5.03%. This error will be used further for the SLI-1000. The standard deviations reported below will be implemented in the test results of later chapters.

Sensor	Parameter	Standard deviation (3σ)
Futek LSB200 & Scaime CPJ	F_T	$\pm 1.08\%$
Sensirion SLI-1000	\dot{m}_{H_2O}	$\pm 5.03\%$
Brooks 5850S	\dot{m}_{N_2}	$\pm 0.7\%$ (max)
Vacuubrand VSP 3000	P_a	$\pm 15\%$ (N_2) $\pm 50\%$ (H_2O)
TE Connectivity MS5837-30BA	P_c	± 50 mbar (0 - 45 $^{\circ}\text{C}$) ± 100 mbar (-20 - 85 $^{\circ}\text{C}$)
ES 030-10 & SM-7020	P_{heat}	$\pm 0.2\%$
K-type thermocouple	T_c	± 7.5 $^{\circ}\text{C}$ (max)

Table 5.7: The confidence bounds of the test equipment [15].

6

Preliminary Tests

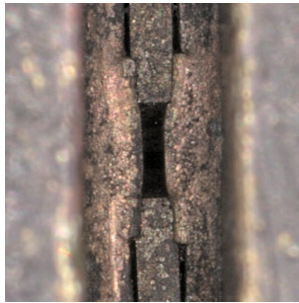
In this chapter, two important preliminary tests will be detailed that are essential before commencing the nitrogen and water tests. The preliminary tests conducted here contain the optical characterisations (section 6.1) and leak tests (section 6.2), which aim to capture the nozzle geometry and VLM leak rate, respectively. Both tests are essential for the final tests. They are conducted at three different moments throughout the thesis period. To easily distinguish these moments, they are named as done in chapter 2. VLM-LC2 refers to the thruster that is inspected before implementing the changes of chapter 3. This is done to observe the impact of these changes. VLM-LC2 is essentially the same thruster as used by Cramer [15] but it may have degraded more over time, so it is given a unique name. VLM-JV1 is the thruster that was obtained after the improvements of the third chapter and before tests had been executed. VLM-JV2, on the other hand, is the thruster after concluding the test campaign.

By conducting the preliminary tests at different times, the changing state of the thruster can be charted. This gives more insight in the degradation of the thruster because of the tests. The information acquired from these tests can then be used to improve the VLM's design and test results. The final nozzle geometry and leak rate found in this chapter (VLM-JV2) will be used in the upcoming chapters (chapter 7 and 8). The chapter ends with important conclusions and recommendations based on the results achieved here (section 6.3).

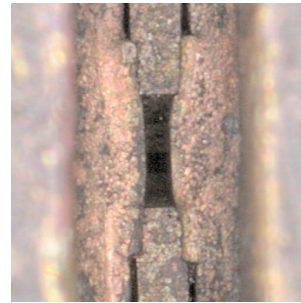
6.1. Optical Characterisations

The optical characterisations that will be described in this section are meant to characterise the VLM's nozzle geometry. The desired outcome of these preliminary tests is a list of the essential nozzle dimensions. This list includes the throat width and height (W_t and H_t), the exit width and height (W_e and H_e), and both areas (A_t and A_e). Ideally, these dimensions should be as close as possible to the original design values [81] and the measured values found by Hutten [28] (VLM-RH). These do not overlap due to manufacturing errors and other external influences. Since this work uses the same nozzle profile as Hutten, it is desirable to match the dimensions found by this author as closely as possible. To quantify if the nozzle dimensions are somewhat comparable to Hutten's values, a maximum deviation of 10% is established. This 10% is based on the inherent uncertainties found in the optical characterisation process (more on this later) and the accuracy of the analytical model. If the measured parameters of this work exceed this margin, they cannot be compared fairly to Hutten's results. As mentioned in the introduction to this chapter, several separate optical characterisations have been performed for this thesis. In total, the nozzle has been inspected three times; one time before implementing improvements (VLM-LC2) on 06-05, one time directly after making improvements (VLM-JV1) on 05-08, and a final time after concluding all thrust tests (VLM-JV2) on 30-09. These optical characterisations are described in their respective subsections (subsection 6.1.1, 6.1.2, and 6.1.3). The results of the final optical characterisation (VLM-JV2) will be used for the next chapters and has already been used for the predictions of chapter 4.

Previous works have already visually inspected the resistojet before. However, the nozzle throat itself remained invisible in these inspections [81]. A combination of microscopic dimensions (throat width of only $130\text{ }\mu\text{m}$) and difficult lighting conditions make it nearly impossible to measure the throat region directly. Moreover, the addition of the threaded blocks by Cramer [15], make this even more difficult as even less light enters the nozzle area. One of the goals of the optical characterisations of this work is to make the throat area visible so it can be measured directly. To achieve this, the Vaporising Liquid Micro-resistojet has been inspected using a combination of the Keyence VR-5000 digital microscope and the Keyence VK-X1000 confocal scanning microscope. Both are available in the physics laboratory of the Aerospace Faculty and can be booked via [Lab Servant](#) after following a short instruction¹. The VR-5000 uses digital lenses and triangulation to obtain a 3D image, while the VK-X1000 combines laser and optical techniques to obtain high resolution pictures [33, 34]. As mentioned before, the nozzle throat remains difficult to image, as the microscope lights cannot penetrate that deeply inside the thruster. However, by increasing the brightness of the pictures, the nozzle can be made visible. This is displayed in [Figure 6.1](#). The throat width can now directly be determined using a combination of the microscope's proprietary software and Inkscape, a free open-source vector graphics editor. Both allow for drawing precise lines on a picture. Since the pictures made using the microscopes contain a scale for reference, the pixel size can be easily correlated with the actual size. The microscope software does this automatically, making it easy to work with.



(a) The nozzle throat without increased brightness.



(b) The nozzle throat with increased brightness.

Figure 6.1: The nozzle throat can be made visible by increasing the picture's brightness (VLM-LC2).

6.1.1. VLM-LC2

Before disassembly of the VLM (VLM-LC2), a visual inspection was conducted to learn more on its physical state. The focus of this inspection was on the nozzle area, as significant deformations had already been noted around this area [15]. By increasing the pictures' brightness, the throat width (W_t) can be measured directly and was found to be approximately $213.9 \pm 11.7\text{ }\mu\text{m}$ (see [Table 6.1](#) for all results). This deviation is based on an uncertainty of 2 pixels, where a single pixel is equal to a distance of $5.85\text{ }\mu\text{m}$. Although Cramer used an indirect extrapolation method to find the throat width, it is relatively close to the measured value with a discrepancy of only $13.8\text{ }\mu\text{m}$. This value falls within the confidence bounds established by that work. The result achieved here thus lend credibility to the extrapolation method of determining the throat width. Based on this information, both methods seem equally valid in measuring the throat area. Seen that the differences are negligible, this work will employ the technique described earlier as it is free of assumptions.

Given the fact that the copper deformation partially obscures the nozzle throat (see [Figure 6.1](#)), it is impossible to measure the throat height directly. This value is thus found by assuming that the throat height (H_t) is equal to the unconstrained exit height (H_e), which is found by measuring the thickness of the nozzle profile. Note that it is assumed here that the nozzle profile's thickness does not change whether it is constrained or not. This assumption is based on the calculation performed by Cramer, who found that the nozzle profile's stainless steel will hardly deform under the applied compressive force [15]. The thickness measurement showed a thickness between 490.1 and $508.0\text{ }\mu\text{m}$. As this quite a wide range, the average between these extremes is taken with the uncertainty value defined earlier. Consequently, a value of $499.1 \pm 11.7\text{ }\mu\text{m}$ is found for the throat height. As stated earlier,

¹Contact person: P.G.Marchese@tudelft.nl

the nozzle profile's thickness is assumed to stay constant, meaning it can be measured in an unconstrained (uncompressed) state. Under this assumption, the measured thickness is also applicable for the constrained (compressed) state. It is therefore recommended to measure the nozzle profile again after a subsequent VLM disassembly. A micrometer, as used by Versteeg [81], should suffice for this purpose. Unfortunately, this was an oversight in this work, hence the necessity of the assumption made above. To prevent this oversight for future iterations, it is recommended to measure the nozzle profile's thickness shortly before assembly. This recommendation is also integrated in the assembly and disassembly procedures that can be found in [Appendix D](#).

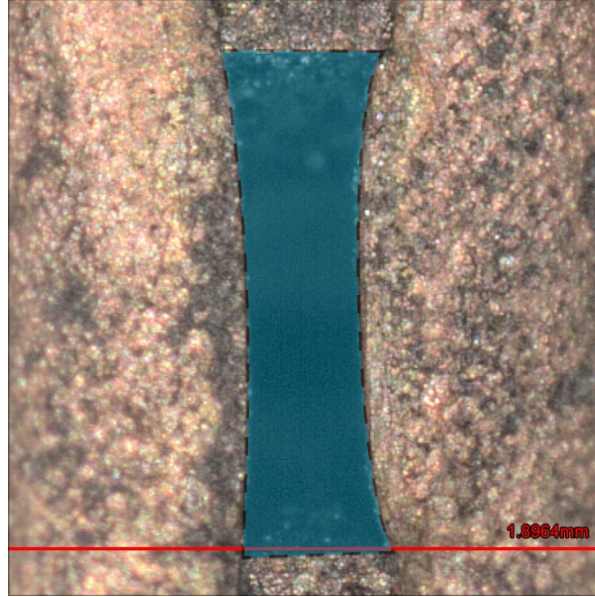


Figure 6.2: Illustration of the nozzle exit area (A_e) measurement process (VLM-LC2).

The picture shown in [Figure 6.2](#), is used to determine the exit width (W_e) and height (H_e). Unfortunately, due to extreme deformations, the exit height is quite irregular and decreases as it moves away from the profile's edges. The minimal exit height is thus found directly in front of the nozzle throat and is equal to $256.2 \pm 11.7 \mu m$, which is nearly half the design value. The exit width is more straightforward to determine and is found to be equal to $1145.5 \pm 11.7 \mu m$. Because of the deformations, the exit area (A_e) is determined by tracing the edges of the copper blocks and nozzle profile as illustrated in the relevant figure ([6.2](#)). The Inkscape software is able to calculate the area, based on the drawn shape. Due to this alternative method, the uncertainty associated with the exit area is determined differently. It is based on several independent attempts of tracing the nozzle exit area. Each resulted in a slightly different shape, which has a noticeable effect on the measured area. To capture this effect, the uncertainty is estimated to be $\pm 15.0 \cdot 10^3 \mu m^2$.

Contrary to the exit, the nozzle throat is still believed to be rectangular, allowing for a simple calculation of its area. Moreover, the related uncertainty is based on the uncertainties of the throat width and height (both $\pm 11.7 \mu m$) and calculated using the same method as described in the previous chapter ([5](#)). All relevant nozzle parameters and uncertainties have been summarised in [Table 6.1](#). The values found by both Hutten (VLM-RH) and Cramer (VLM-LC) have been included as well to highlight the changes over the years. A complete overview of the throat parameters, including Versteeg's measurements, is provided in [Table B.1](#) of [Appendix B](#).

As explained above, the throat height was based on an averaged measurement of the nozzle profile thickness. Cramer [15] roughly employed the same method but found a height of almost $23 \mu m$ more. While this could still fall within the uncertainty bounds indicated by that work, it is still a noteworthy

difference. Measuring the (unconstrained) nozzle profile with a micrometer is thus advisable and will lead to more consistent results. Table 6.1 also reveals two other peculiar effects; the throat and exit width has increased, while the exit height has decreased. These trends will also return in the next subsections. The widening of the nozzle might be attributed to creep of the stainless steel and will be discussed more extensively in subsection 6.1.2. The height decrease on the other hand, has also been described by Cramer and is a result of copper deformation due to an excessive clamping force. The combination of these effects lead to a significantly enlarged throat area and a reduced exit area, leading to a much smaller area ratio compared to the design value ($-62.4\% \pm 4.6\%$).

Parameter	Design	VLM-RH		VLM-LC		VLM-LC2	
$H_t [\mu m]$	500	538	± 8	522	± 34.3	499.1	± 11.7
$W_t [\mu m]$	130	140	± 11	200.1	± 16.2	213.9	± 11.7
$A_t [10^3 \mu m^2]$	65	75.3	± 7.0	104.5	± 15.3	106.8	± 8.3
$H_e [\mu m]$	500	538	± 8	315.6	± 10.8	256.2	± 11.7
$W_e [\mu m]$	1072.5	1078	± 8	1138.1	± 5.4	1145.5	± 11.7
$A_e [10^3 \mu m^2]$	536	580.0	± 12.9	359	± 14.0	331.1	± 15.0
$A_e/A_t (\epsilon) [-]$	8.25	7.70	± 0.89	3.44	± 0.64	3.10	± 0.38

Table 6.1: Measured nozzle parameters of the Vaporising Liquid Micro-resistojet, before improvements (VLM-LC2).

6.1.2. VLM-JV1

The optical characterisation process performed prior to the nitrogen and water tests is very similar to the one performed in subsection 6.1.1. The VLM is placed under both the Keyence VR-5000 and VK-X1000 to capture the nozzle region. Tweaking the microscope's settings allows for a somewhat clear image of this area of interest. Thanks to the changes made in chapter 3, the captured images show a much more rectangular nozzle region, compared to the images made before the resurfacing. Figure 6.3 shows both the nozzle exit and throat area, which can both be visualised by fine-tuning the lighting settings and the microscope's focus. The results discussed below are summarised in Table 6.2.

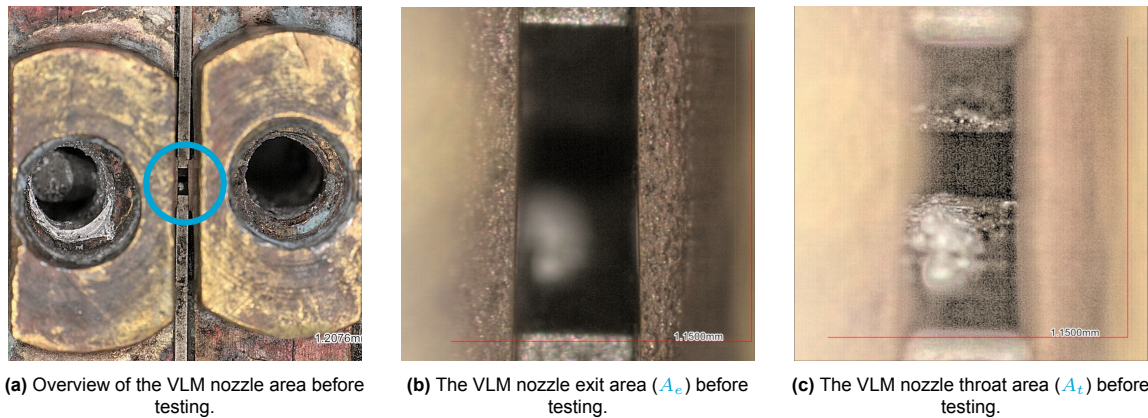


Figure 6.3: The Vaporising Liquid Micro-resistojet nozzle, after improvements (VLM-JV1).

These pictures show that the throat and exit widths have increased again, compared to previous measurements. They are determined to be $232.8 \pm 11.7 \mu m$ and $1179.1 \pm 11.7 \mu m$, respectively. Since the exit area's sides are not quite parallel, the width is slightly larger when measured on the left side of the picture compared to the right side ($\pm 6.8 \mu m$). To incorporate this variation, the average value is taken of both extremes. This misalignment between the exit sides can be explained when zooming out, as shown in Figure 6.3a. The nozzle profile is squeezed in between the copper but its sides are not squeezed evenly. The upper part of the profile touches the bottom copper block (right in the picture), whereas the lower part almost touches the top block (left in the picture). This can be explained by the

fact that the outer parts of the nozzle profile are not supported by the sealing edge like the inner parts. Because of this design, the nozzle profile still has a little wiggle room left, which leads to this situation. This effect is much smaller at the nozzle throat, as it is more supported there and thus has less room to move. Consequently, the sides at the throat are nearly parallel and thus the throat width is a consistent measurement (Figure 6.3c). The misalignment at the exit is not considered to be an issue as its effect is negligibly small and only results in a 0.2%.

Unlike the throat height, which is assumed to remain constant ($499.1 \mu\text{m}$), the exit height found in Table 6.2, is worth discussing in depth. Like the exit width, it is an averaged number taken from two extremes (457.9 and $486.0 \mu\text{m}$). The height measured at the bottom of Figure 6.3b is larger than the one measured at the top of the picture. This difference is larger than the variation in widths (6%) and also seemingly originates from a different source. Once again, zooming out reveals the cause of this discrepancy (see Figure 6.3a). This picture shows that the nozzle profile edge is not flush with the copper sealing edge. Instead, the copper protrudes slightly and moves in front of the profile. This effect is more noticeable on the top right of the picture, as there more of the nozzle profile is hidden behind the copper ridge. The bottom right corner also shows this, but to a lesser extent. This variation likely comes from a difference in contact surface area. Due to a small misalignment of the two blocks, the copper in the upper right corner interfaces with less steel, which increases the local pressure. Consequently, the copper deforms more in this area than in the lower right corner where the area is greater and thus the pressure is lower. This effect is much less pronounced on the left side of the picture, as the interface areas are much more equal. The misalignment stems from the way the blocks are connected. Small manufacturing errors described in previous works, allow for a bit of play in the bolt holes. These are used for connecting and aligning the blocks. So, this play likely caused the skewed edges of the nozzle exit. This result is a strong argument for ensuring proper alignment of the blocks and nozzle profile. This is also emphasised in the relevant procedure (section D.2).

As described extensively above, the nozzle's exit is not a perfect rectangle but contains some skewed edges. Although the exit area's shape is much improved compared to the one before machining, it is still not perfect. Therefore, it is decided to determine the exit area with the same method as done in subsection 6.1.1, namely by tracing its edges and calculate it using Inkscape. This is seen as a more accurate method than simply multiplying the height and width. Employing this method results in an area of $555.2 \pm 10.0 \cdot 10^3 \mu\text{m}^2$. Note that the uncertainty is less than in the previous subsection, as it is an easier shape to trace and thus less prone to errors. To quantify the discrepancy between the tracing method and the alternative, the area has also been calculated based on the average width and height, resulting in an area of $556.5 \pm 19.3 \cdot 10^3 \mu\text{m}^2$. These areas are remarkably close to one another ($\sim 0.2\%$), lending credibility to the method of averaging the dimensions. Still, the tracing method result is shown in Table 6.2 to maintain consistency with subsection 6.2.2 and because the error is smaller. The throat area is determined by simple multiplications, following the same logic.

Parameter	Design	VLM-RH		VLM-LC2		VLM-JV1	
$H_t [\mu\text{m}]$	500	538	± 8	499.1	± 11.7	499.1	± 11.7
$W_t [\mu\text{m}]$	130	140	± 11	213.9	± 11.7	232.8	± 11.7
$A_t [10^3 \mu\text{m}^2]$	65	75.3	± 7.0	106.8	± 8.3	116.2	± 8.6
$H_e [\mu\text{m}]$	500	538	± 8	256.2	± 11.7	471.9	± 11.7
$W_e [\mu\text{m}]$	1072.5	1078	± 8	1145.5	± 11.7	1179.1	± 11.7
$A_e [10^3 \mu\text{m}^2]$	536	580.0	± 12.9	331.1	± 15.0	555.2	± 10.0
$A_e/A_t (\epsilon) [-]$	8.25	7.70	± 0.89	3.10	± 0.38	4.78	± 0.44

Table 6.2: Measured nozzle parameters of the Vaporising Liquid Micro-resistojet, after improvements (VLM-JV1).

Figure 6.3 proves that the nozzle region is much more rectangular and has less deformations thanks to the resurfacing effort. This helps in characterising the important parameters, as they adhere more to the original design. Interestingly, these parameters show that the width increased again. This seems to be a consistent trend over the years and becomes evidently clear when inspecting the complete

overview in [Appendix B](#). It is not entirely clear what causes this widening, but it is likely not because of wear of the nozzle profile. The temperatures reached inside the VLM are 400 °C at most, which is far below the melting range of the stainless steel (~ 1400 °C, [11]). Also, the propellants used do not interact with the material and contain no abrasive particles. Some abrasive material may come from the small filter placed in front of the nozzle by Cramer [15], but no signs of wear were seen when inspecting this component. Lastly, and most importantly, the thruster has not been used in between the optical characterisation efforts of [subsection 6.1.1](#) and this subsection. The first optical characterisation was performed before the modifications of [chapter 3](#), while the second optical characterisation took place before the nitrogen tests. Therefore, no additional wear could affect the nozzle profile. Despite this, the width has still increased noticeably. Thus, wear cannot be the dominating factor behind this. Creep of the stainless steel might explain the width increase. This phenomenon causes materials to slowly deform under stress, even when this stress is below the yield strength of the material [11]. The nozzle profile is under constant stress in the assembled state. Moreover, the copper may enhance this deformation by moving inside the nozzle area. A clear example of this can be found when looking at Cramer's optical characterisation and the characterisation done in the previous subsection ([Figure 6.1](#)). In those pictures, the copper has clearly flowed in between the nozzle exit and might also push it further apart. This effect, in combination with creep already affecting the nozzle dimensions, might explain the reason behind the widening. This theory might be interesting to investigate further, but that is outside the scope of this work. By constraining the nozzle profile's width in some manner (using guiding pins through the profile, for example), the widening could be prevented. Consequently, the nozzle's dimensions change less and stay closer to the design values, which aids the reproducibility of future tests. This and other improvements will be discussed in more detail in [chapter 11](#).

Despite the issues mentioned above, the modifications described in [chapter 3](#) did result in a significant improvement of the exit height as proven by [Table 6.2](#). Although the measured height is still a bit under Hutten's value of 538 μm (difference of -12.3%), it is far closer than the value found for VLM-LC2 (difference of roughly -50%). This can also clearly be seen in the new exit area, which is currently only -4.3% off from VLM-RH, whereas it was -42.9% off before. Consequently, the area ratio is improved compared to the situation before the improvements (-60%). However, with a difference of -37.9%, it is still a far cry from Hutten's area ratio of 7.70. This results can be mainly attributed to the widening situation discussed above as it has a severe effect on the throat width especially. [Table 6.3](#) summarises these results and provides a comparison of the current throat parameters with the values found by Hutten [28].

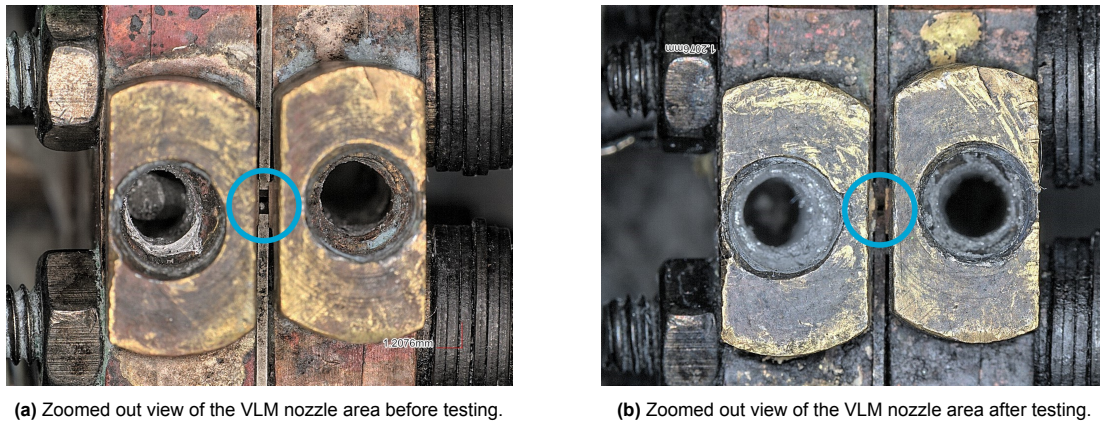
Parameter	VLM-RH		VLM-JV1		Difference
H_t [μm]	538	± 8	499.1	± 11.7	-7.2%
W_t [μm]	140	± 11	232.8	± 11.7	+66.3%
A_t [$10^3 \mu\text{m}^2$]	75.3	± 7.0	116.2	± 8.6	+54.3%
H_e [μm]	538	± 8	471.9	± 11.7	-12.3%
W_e [μm]	1078	± 8	1179.1	± 11.7	+9.4%
A_e [$10^3 \mu\text{m}^2$]	580.0	± 12.9	555.2	± 10.0	-4.3%
A_e/A_t (ϵ) [-]	7.70	± 0.89	4.78	± 0.44	-37.9%

Table 6.3: Comparison of the measured nozzle parameters of VLM-RH and VLM-JV1.

6.1.3. VLM-JV2

To capture the effect of the nitrogen and water tests on the VLM's state, a final optical characterisation is performed in this subsection. The goal of this is twofold; to qualitatively characterise the nozzle's physical state after testing and to quantify the nozzle parameters again. This optical characterisation is performed shortly after concluding the tests (within 10 days). Its outcome is thus seen as indicative of the nozzle dimensions during the tests.

When inspecting the VLM under the microscopes, some subtle changes can be noted compared to the



(a) Zoomed out view of the VLM nozzle area before testing.

(b) Zoomed out view of the VLM nozzle area after testing.

Figure 6.4: Zoomed out views of the VLM nozzle areas before (VLM-JV1, left) and after (VLM-JV2, right) testing.

VLM's state before the tests. Figure 6.4 shows a side-by-side comparison of the VLM before and after testing. Seen that the lighting conditions in these pictures are not the same, it is hard to compare them fairly. In general, one thing can be observed from these zoomed out pictures. Some dark-coloured debris build-up on the thruster's surface can be distinguished. This accumulation of debris was also present after previous tests and is thus not uprising. It is a result of operating the engine and will not be analysed further. Other than that, the thruster looks quite unchanged, based on these pictures.

Zoomed in pictures of the nozzle throat area are shown in Figure 6.5. Due to the presence of debris around the nozzle, it was challenging to focus the microscope. Despite this, some subtle changes can be distinguished. The copper deformation that was noticed in the previous subsection has continued, which can be seen by the slight bulging of the copper sides. Because of this, the exit height has decreased again, despite the efforts described in chapter 3. This copper deformation may have also contributed to an increased throat and exit width. Because of some minor variations in the measured exit height and width, an averaged value is taken for both. The exit area is once again determined by tracing the image. Because the acquired images are harder to analyse, an increased uncertainty of $\pm 15.0 \cdot 10^3 \mu m^2$ is adopted. The results of this final optical characterisation are shown in Table 6.4. This table summarises all three optical characterisations performed in this work.

Parameter	Design	VLM-RH		VLM-LC2		VLM-JV1		VLM-JV2	
$H_t [\mu m]$	500	538	± 8	499.1	± 11.7	499.1	± 11.7	499.1	± 11.7
$W_t [\mu m]$	130	140	± 11	213.9	± 11.7	232.8	± 11.7	245.6	± 11.7
$A_t [10^3 \mu m^2]$	65	75.3	± 7.0	106.8	± 8.3	116.2	± 8.6	122.6	± 8.7
$H_e [\mu m]$	500	538	± 8	256.2	± 11.7	471.9	± 11.7	408.7	± 11.7
$W_e [\mu m]$	1072.5	1078	± 8	1145.5	± 11.7	1179.1	± 11.7	1189.8	± 11.7
$A_e [10^3 \mu m^2]$	536	580.0	± 12.9	331.1	± 15.0	555.2	± 10.0	487.8	± 15.0
$A_e/A_t (\epsilon) [-]$	8.25	7.70	± 0.89	3.10	± 0.38	4.78	± 0.44	3.98	± 0.40

Table 6.4: Measured nozzle parameters of the Vaporising Liquid Micro-resistojet, after testing (VLM-JV2).

Table 6.5 summarises the deviation of the nozzle compared to Hutten's values. While the changes of chapter 3 initially reduced these deviations, they are shown to slowly increase again. The width shows a consistent increase, while the exit height decreases over time. These effects have a major impact on the nozzle geometry and thus also on the thruster performance. The nozzle parameters found in this subsection will be used in the analysis of the nitrogen and water test results. This is done as the tests were executed mid-September, which is closer to this optical characterisation (30-09) than the previous one (05-08). It is thus believed that these measured parameters are closer to those during the actual testing.

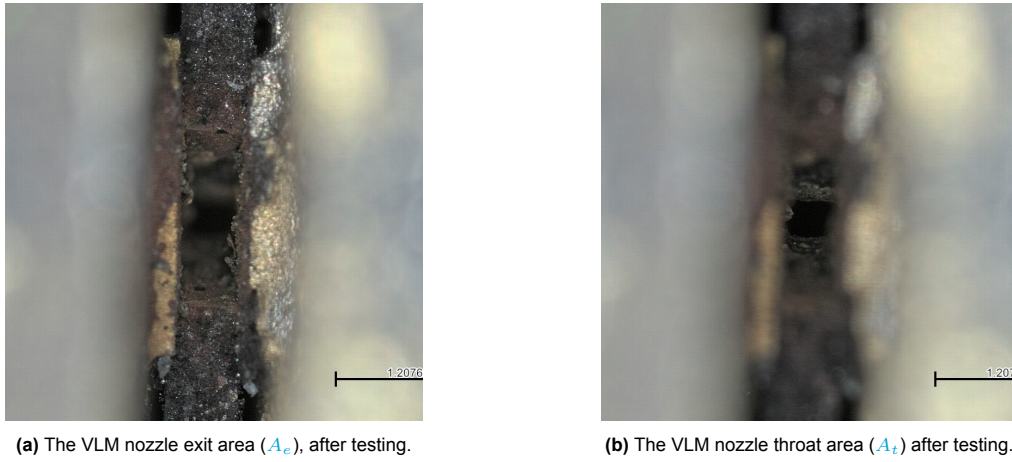


Figure 6.5: The Vaporising Liquid Micro-resistojet nozzle after testing (VLM-JV2).

Unfortunately, some of the important parameters (A_t and A_e/A_t) deviate more than 10% from Hutten's values. This is more than the maximum allowable deviation established at the beginning of the section. Since these differences result in a different thruster behaviour, the outcome of the later tests cannot be compared directly to Hutten's results. For example, the increased throat area will result in a greater predicted mass flow rate and thrust. Note that this does not mean that the planned tests cannot continue. However, it means that the test results obtained here will differ from other works. The verification that will be done in [chapter 9](#) will take this into account.

Parameter	VLM-RH		VLM-JV2		Difference [%]
H_t [μm]	538	± 8	499.1	± 11.7	-7.2
W_t [μm]	140	± 11	245.6	± 11.7	+75.4
A_t [$10^3 \mu m^2$]	75.3	± 7.0	122.6	± 8.7	+62.8
H_e [μm]	538	± 8	408.7	± 11.7	-24.0
W_e [μm]	1078	± 8	1189.8	± 11.7	+10.4
A_e [$10^3 \mu m^2$]	580.0	± 12.9	487.8	± 15.0	-15.9
A_e/A_t (ϵ) [-]	7.70	± 0.89	3.98	± 0.40	-48.3

Table 6.5: Comparison of the measured nozzle parameters of VLM-RH and VLM-JV2.

After inspecting the nozzle throat three times at different periods, it is clear that it exhibits noticeable changes. Over a time period of only 2 months, the nozzle may show deformations of over 10%. From these results, it can be concluded that it is essential to perform optical characterisations shortly before and after testing. This information then aids in determining the nozzle performance more accurately. To emphasise this conclusion, it is integrated in the procedures of [Appendix D](#). It may be so that the rapid nozzle changes are unique to this work and did not occur in previous works. Those results may thus still be insightful. Small misalignment errors may be the cause behind the quick geometry changes discovered in this thesis. As described earlier in this chapter, the nozzle profile and thruster blocks are not properly aligned. The current thruster design and the used bolts make it difficult to ensure proper alignment [15]. These small misalignments may result in an uneven stress distribution in the copper blocks. The copper therefore deforms locally and moves into the nozzle exit area. The nozzle profile is then pushed apart as a result of this copper deformation. This phenomenon might explain the relatively quick decrease of the exit height and increase of the throat and exit widths (both increase with $\sim 10 \mu m$). Ensuring proper alignment of essential VLM parts may thus help prevent nozzle deformations. Further research is advised to thoroughly investigate this phenomenon. Another solution may also be

to implement more structural design changes, such as adding guiding pins for the nozzle profile or fabricating the thruster body out of a less ductile material. These recommendations will be treated in [chapter 11](#).

6.2. Leak tests

Similar to the optical characterisations described above, three separate leak tests have been performed for this thesis (before and after the modifications and once after concluding the tests). They are also given the same names as [section 6.1](#) and will be discussed in their own subsections ([subsection 6.2.2](#), [6.2.3](#), and [6.2.4](#)). Moreover, [subsection 6.2.3](#) also introduces an additional, preliminary leak test, called VLM-JV0. This is done to distinguish it from the final results achieved in that subsection, which use the customary name (VLM-JV1). Besides these subsections, this section also has subsections dedicated to the general leak test plan ([subsection 6.2.1](#)) and the effects of leaks on test results ([subsection 6.2.5](#)).

6.2.1. Leak test plan

Propellant leaks have a negative effect on the effective mass flow leaving the thruster through the nozzle. Since the mass flow is measured in the feed system, before entering the vacuum chamber (see [Figure A.1](#)), it does not measure the effective mass flow. The leak tests thus indirectly give a clearer insight in the true mass flow. To judge the impact of the leaks and determine what an acceptable leak rate is, the analytical model's predictions are important. As shown in [Table 4.3](#), the uncertainty of the predicted mass flow is roughly 9%, which is comparable to that found by Hutten [28]. That work allowed a maximum leakage rate of 5% for a full flow rate of 17.5 mg/s at a pressure delta of 1 bar, as this is still below the predicted uncertainty. As discussed in the previous section, More severe leaks will have a noticeable effect on the performance parameters and need to be accounted for. It is therefore recommended to avoid leaks greater than 5% and address them before continuing with testing (see [section D.3](#)). Based on this, the acceptance criteria are established as shown in [Table 6.6](#). Most importantly, the fourth criterion (AC-LK-4) will determine whether the leaks should be addressed or can safely be disregarded. When the leaks exceed 5% of the expected full flow rate (0.875 mg/s) at 1 bar, they should ideally be sealed. If this is not feasible, the leak rate must be deducted from the measured flow rate to obtain a more accurate estimate of the true flow rate. [subsection 6.2.5](#) will discuss this in more depth, as well as the impact of leaks on the VLM's performance.

Acceptance criterion	Description
AC-LK-1	The chamber pressure (P_c) is measured over time through the P - T sensor.
AC-LK-2	The nitrogen's temperature (T_{N_2}) is measured over time through the P - T sensor.
AC-LK-3	The nitrogen's temperature (T_{N_2}) stays within 1 °C.
AC-LK-4	The maximum leak rate (\dot{m}_L) is 5% of the full flow rate (17.5 mg/s).

Table 6.6: Acceptance criteria for the leak tests.

The leak tests are conducted similarly to those described in earlier works (e.g. [81], [28], etc.). All tests are conducted under ambient pressures and temperatures. The leak rate is determined by measuring the chamber pressure drop (\dot{P}_c) over time using the P - T sensor. The slope of the P_c is extracted, which can be used to calculate the leak rate (\dot{m}_L) in mg/s at a certain pressure difference using the same formula as Hutten [28]:

$$\dot{m}_L = \frac{\dot{P}_c \cdot V \cdot M}{R_A \cdot T_{N_2}} \quad (6.1)$$

In this equation, V is the internal volume of VLM, which will change slightly due to the modifications of [chapter 3](#). M is the molar mass of nitrogen (28.014 g/mol), while R_A is the universal gas constant that is defined earlier in this work ([chapter 4](#)). The temperature is recorded by the same sensor as the chamber pressure. It has been verified that the temperature remained fairly constant for all conducted leak tests ($\Delta T_{N_2} < 1$ °C). AC-LK-3 is thus accepted for all tests presented in this section. Furthermore, AC-LK-1 and AC-LK-2 are also accepted and will not be discussed further.

As stated earlier, the leak tests are all executed under ambient conditions (no vacuum and no heating), which differs from the final experiments. These will all be executed in a vacuum and most will also be done at elevated temperatures. More importantly, some experiments will involve water as propellant. To acquire some insight in the effect of varying these parameters, a simple conversion is established, based on Hutten's work. The outcome of this conversion will show that switching from nitrogen to water and raising the temperature will result in a lower leak rate. Consequently, when the leak rates found for nitrogen at ambient conditions are acceptable ($\dot{m}_L < 5\%$), they are also acceptable for different conditions. In order to find an applicable relation, it is important to determine whether the flow rate can be considered viscous or molecular. Amesz [2] and Rottländer, Umrath, and Voss [55] provide the following guideline; leak rates (q_L) greater than 10^{-4} mbar·L/s are considered laminar viscous flows, while leak rates smaller than 10^{-6} mbar·L/s are molecular flows. In short, laminar viscous flows occur at relatively high pressures and are driven by viscosity, while molecular flows occur in vacuum environments and are driven by collisions with the walls. The leaks dealt with in this, and previous works can easily be calculated as follows:

$$q_L = \dot{P} \cdot V = 11.8 \text{ mbar/s} \cdot \frac{2,430 \text{ mm}^3}{10^6} = 2.86 \cdot 10^{-2} \text{ mbar} \cdot \text{L/s} \quad (6.2)$$

Note that the values used here are taken from subsection 6.2.3. The order of magnitude of the leaks is thus 10^{-2} , which can safely be considered to be a laminar viscous flow. For this condition, the formula below (Equation 6.3) can be used to convert the leak rate to different gas types (gas A and B , [55]).

$$q_{L,A} \cdot \mu_A = q_{L,B} \cdot \mu_B \quad (6.3) \quad \dot{m}_{L,B} = \frac{q_{L,A} \cdot \mu_A \cdot M_B}{\mu_B \cdot R_A \cdot T_B} \quad (6.4)$$

The leak rate can be calculated from the leak test and the viscosities (μ) at certain conditions can be acquired using the CoolProp library [4]. The leak rate (in mg/s) for different gases can thus easily be determined by rewriting Equation 6.3 and combining it with Equation 6.1, which results in Equation 6.4. The parameters denoted with A are taken from the (N_2) leak tests performed in this chapter and form the baseline for the conversion. By substituting the parameters donated with B for the desired values (H_2O), the mass flow rate for different conditions can be determined. For example, the leak rate of water vapour at 300 °C (573.15 K) and a pressure difference of 1 bar would result in a leak rate of 0.009 mg/s (see Equation 6.5), while it would be 0.010 mg/s for nitrogen. That is a reduction of 71.1% (water) and 68.1% (nitrogen) compared to the (unheated) leak rate of nitrogen (0.032 mg/s) at the same pressure difference. Out of the equations presented here follows that the leak rate will decrease for both elevated temperatures and the use of water as propellant. Consequently, if the measured leak rate is acceptable, it will also be acceptable for the water experiments.

$$\dot{m}_{L,H_2O} = \frac{2.86 \cdot 10^{-2} \cdot 1.76 \cdot 10^{-5} \cdot 18.02 \cdot 10^{-3}}{2.03 \cdot 10^{-5} \cdot 8.314 \cdot 573.15} \cdot 10^5 = 0.009 \text{ mg/s} \quad (6.5)$$

6.2.2. VLM-LC2

Before disassembly of the VLM (VLM-LC2), a leak test was conducted to learn more on its physical state and to see whether the leaks have increased after Cramer's tests. Since the thruster has not been modified yet, the internal VLM remains unchanged ($V = 2,422 \text{ mm}^3$, [15]). The average temperature value (T_N) found during these tests was roughly 24 °C. The results from these tests have been summarised in Table 6.7 and can be seen in Figure 6.6.

Parameter	VLM-HV2	VLM-RH	VLM-LC	VLM-LC2
\dot{m}_L [mg/s]	0.122	0.240	0.223	0.681
\dot{m}_L/\dot{m}_{tot} [%]	0.70	1.37	1.27	3.89

Table 6.7: Measured leak rate of the Vaporising Liquid Micro-resistojet, before improvements (VLM-LC2).

The measured leak rate found at a pressure delta of 1 bar (VLM-LC2) is equal to 0.681 mg/s (3.89% of full mass flow). It is still below the maximal allowable rate of 5%, thus satisfying the most important acceptance criterion (AC-LK-4). The other three criteria are also accepted. As shown in the table above (6.7), the leak rate found by Hutten (VLM-RH) was 0.240 mg/s (1.37%), while that found by Cramer (VLM-LC) was 0.223 mg/s (1.27%). So, the leak rate found by this work has tripled with regards to Cramer's result. Those leak tests were conducted before her test campaign, while these results have been obtained after her test campaign. This significant increase of the leak rate may thus be attributed (partially) to the test campaign. It is an indication that the nitrogen tests may have a detrimental effect on the thruster's state. This degradation thus provides a strong argument for conducting leak tests directly before and after testing, as written in the procedures (Appendix D). On the other hand, some time has passed between Cramer's tests and these leak tests (~ 4 months). As shown in the previous section, the VLM's nozzle changes quite significantly over time. These changes may not apply exclusively to the nozzle region and may also be present in other parts of the thruster. The achieved seal may thus degrade over time, which might also explain the increased leak rate. At this point in time, it is impossible to determine which effect causes the higher leak rate. Performing leak tests close to the thrust tests, may give more insight into the exact causes. Nevertheless, the tripling of the leaks is worrisome, and provides a solid argument for addressing the issue, which has been done in chapter 3.

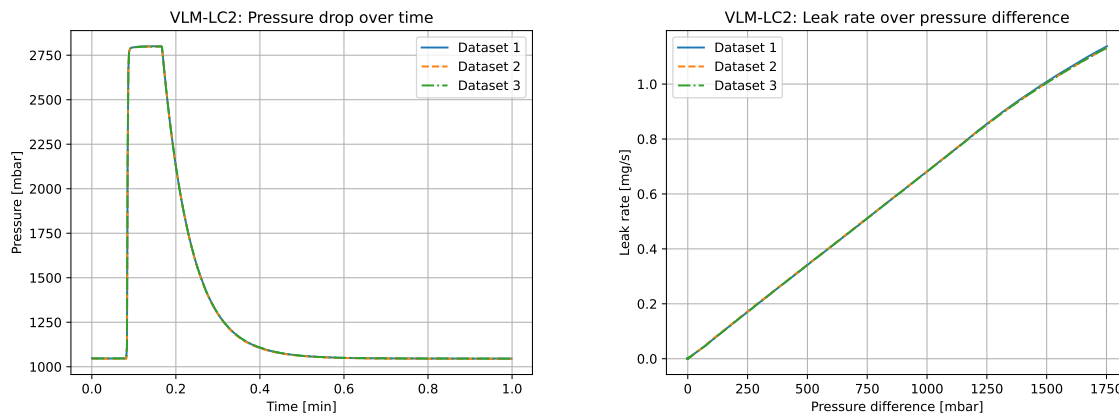


Figure 6.6: Measured leak rate of the Vaporising Liquid Micro-resistojet, before improvements (VLM-LC2).

6.2.3. VLM-JV1

In chapter 3 modifications to the thruster and its connections were introduced. Part of these modifications' aim is to reduce the leaks measured in the previous subsection. To discover the effectiveness of the improvements, a new leak test campaign is performed. The results of these tests give insight in the severity of the leaks ($< 5\%$) and determine whether they should be taken into account in the data processing for the thrust tests later. In this subsection, two different leak tests will be covered. One was executed directly after the improvements of the third chapter and is named VLM-JV0 to distinguish it from the later leak tests (VLM-JV1). The tests with VLM-JV0 showed that there were some leaks present at several locations. As will be described in this subsection, these leaks were stopped successfully, after which new leak tests were conducted. These later leak tests are thus named VLM-JV1.

The process of measuring the pressure drop and converting it to a leak rate using Equation 6.1, has already been described in subsection 6.2.1. The same parameters are used in this test campaign (same M and constant T_{N_2}), except for the internal volume (V). A longer propellant tube (~ 262 mm) with an unchanged internal diameter of 1.016 mm [75] has been used, which leads to an internal volume of 212.4 mm³. Moreover, the N₂ inlet tube was also filled by 95% porous foam by Cramer. This leads to an equal internal volume for this part as for the pressure sensor tube (518 mm³). The last change is the volume of the copper blocks. The CNC machine removed 0.3 mm of the material to make a new sealing edge (see section 3.1). Therefore, the volume of the blocks is slightly reduced. The volume decrease

is estimated from the nozzle profile layer, as it follows the same perimeter as the sealing edge. The area of the circumference is found by dividing the nozzle profile's volume (140 mm^3) by its thickness (0.5 mm) and multiplying it with the removed thickness (0.3 mm). This leads to a removed volume of two times 84 mm^3 (168 mm^3), which is taken into account in the table below (Table 6.8). The eventual total internal volume of VLM-JV is close to the original volume as estimated by Versteeg: $2,430 \text{ mm}^3$. This volume thus applies for all upcoming leak tests.

Parameter		VLM-HV2	VLM-JV1
Bottom copper block	$[\text{mm}^3]$	596	512
Nozzle profile layer	$[\text{mm}^3]$	140	140
Top copper block	$[\text{mm}^3]$	614	530
N ₂ inlet tube	$[\text{mm}^3]$	545	518
Pressure sensor tube	$[\text{mm}^3]$	518	518
Tube to solenoid valve	$[\text{mm}^3]$	48	212
Total (V)	$[\text{mm}^3]$	2,461	2,430

Table 6.8: Internal volume of Vaporising Liquid Micro-resistojet.

Much effort was put into reducing the leaks as much as possible for this thesis. As described in chapter 3, the sealing gasket has been left out as it interfered with the nozzle's shape. Without it, the expected rectangular nozzle shape was obtained, which has been characterised in the previous section (subsection 6.1.2). The bolts were tightened to a torque of 1.6 Nm . As this was found to satisfy acceptance criterion AC-LK-4. However, before this could be achieved, some more improvements were required. During the initial leak testing process (VLM-JV0), more leaks were discovered that had not been noted before. All leak locations could be pinned to the interface areas of two components (e.g. between the propellant tube and the aluminium interface or between the propellant tube and the copper block). Figure 6.7 indicates these leakage locations. Whether these were present before or have originated during the (dis)assembly phase, is unknown. Since they resulted in substantial leaks, some time was taken to stop them. Fortunately, this was eventually achieved quite well as will be described below. The results of the leak tests with VLM-JV0 will only be shown briefly (Table 6.9 and Figure 6.9) and will not be treated in depth, as it is only of interest to illustrate the impact the upcoming improvements.

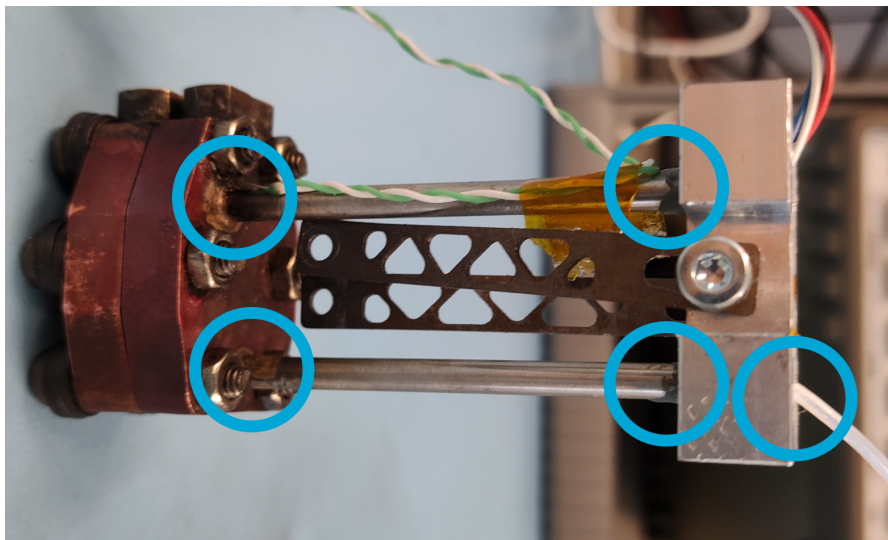
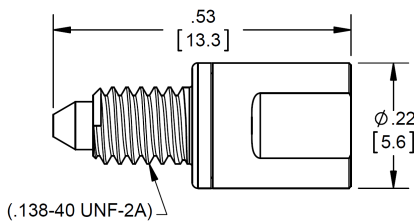


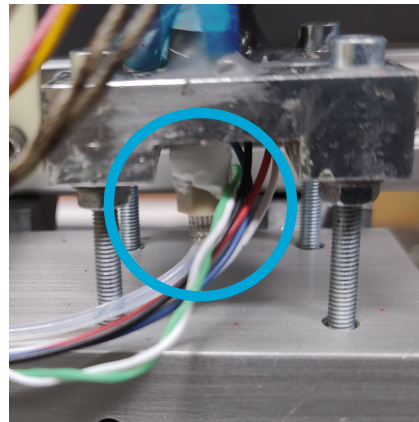
Figure 6.7: The leakage locations identified on VLM-JV0. The leaks occur at the interfaces between two component.

The leaks between the steel tubes and the aluminium interface could be eliminated by applying additional metal glue to the problematic surfaces. This is the same glue that is used to keep the tubes themselves in place (Bison Kombi Metaal, [7]). The leaks on the other side of the steel tubes are a bit more complicated to address. These tubes are connected to the copper blocks via a brazed connection [15]. The complicating factor is the temperatures reached in this area, which is equal to the chamber temperature (T_c) and will thus reach a maximum value of 400 °C. The metal glue cannot withstand such high temperatures, which is why it was opted to use Zwaluw Fire Sealant 1200 °C [8]. This is the same sealant used by Cramer to attach the threaded sleeves to the cartridge heaters. Sadly, the used fire sealant was already opened for quite a while, which has probably led to some degradation of the material. At the moment of implementation, this has been overlooked however.

The last leak location is the connection between the PTFE propellant tube and the aluminium interface. In the past, this tube had been glued to the aluminium interface using a combination of a specific glue (Industrielijm) and a primer (see Table 3.2). The same process was followed for this work but, after three attempts, leaks could still be detected at this interface. To combat this, as well as provide an easier connection for future use, a MINSTAC safety screen (062 MINSTAC Safety Screen, [75]) has been implemented. This component forms the connection between a MINSTAC tube and another non-proprietary part and can be seen in Figure 6.8a. To accommodate the safety screen, the interface has been adapted slightly. This is done by enlarging the existing hole of the aluminium interface and adding a specific thread (.138-40 UNF-2A) to it. The safety screen can now easily be (un)screwed into the interface, allowing for a simple and reusable connection. Additionally, some Teflon tape is wrapped around the safety screen's thread to further eliminate leakages. The mentioned changes resulted in a leak tight solution in this area. One drawback of the MINSTAC solution is the fact that it takes up more physical space. Consequently, it necessitates additional space between the interface and the test bench, when the VLM is attached to it (see Figure 6.8b). This could easily be achieved by adding some self-locking nuts to the assembly.



(a) The 062 MINSTAC Safety Screen used to eliminate leakage [75].



(b) The safety screen implemented in the raised interface.

Figure 6.8: The implementation of the 062 MINSTAC Safety Screen in the aluminium interface (VLM-JV1).

Once the leaks were dealt with, the new leak tests could commence (VLM-JV1). The same procedure as laid out by Cramer was used (see Appendix C of her work). The addition of the threaded blocks (cartridge holders) by Cramer, as well as the cartridge heaters themselves, make it difficult to properly block the nozzle exit using a rubber piece. It is therefore advised to execute the leak tests without the heaters. Some trial-and-error is required to properly clamp a rubber piece to the VLM. The quality of the blockage can be judged by the sound of escaping gas. The lack of an audible gas flow probably indicates a sufficiently blocked nozzle. For these leak tests, the chamber pressure (P_c) was set to roughly 2.4 bar, which allows for a proper conversion of the leak rate (see subsection 6.2.1). Since these tests take place under ambient conditions, the pressure differential is roughly 1.4 bar. In other words, it is close to the maximum planned chamber pressure of 1.5 bar. An average N_2 temperature of 21.5 °C was found for all three tests. This value is used to convert the leak rate from mbar/s to mg/s.

Fortunately, after a lot of effort, the leak rate finally is sufficiently low ($\dot{m}_{L,VLM-JV1} = 0.032$ mg/s, 0.18%). Table 6.9 displays the achieved leak rate compared to those found previously, while Figure 6.9 graphically shows the difference between VLM-JV0 and VLM-JV1. As mentioned earlier, the full mass flow rate used to calculate the percentages in the table is equal to 17.5 mg/s. However, section 6.1 already discussed that the mass flows of this work will likely be higher due to the changed nozzle dimensions. Despite this, the rate of 17.5 mg/s is still used to ease the comparison with previous works.

Parameter	VLM-HV2	VLM-RH	VLM-LC	VLM-LC2	VLM-JV0	VLM-JV1
\dot{m}_L [mg/s]	0.122	0.240	0.223	0.681	0.345	0.032
\dot{m}_L/\dot{m}_{tot} [%]	0.70	1.37	1.27	3.89	1.97	0.18

Table 6.9: Measured leak rate of the Vaporising Liquid Micro-resistojet, after improvements (VLM-JV1).

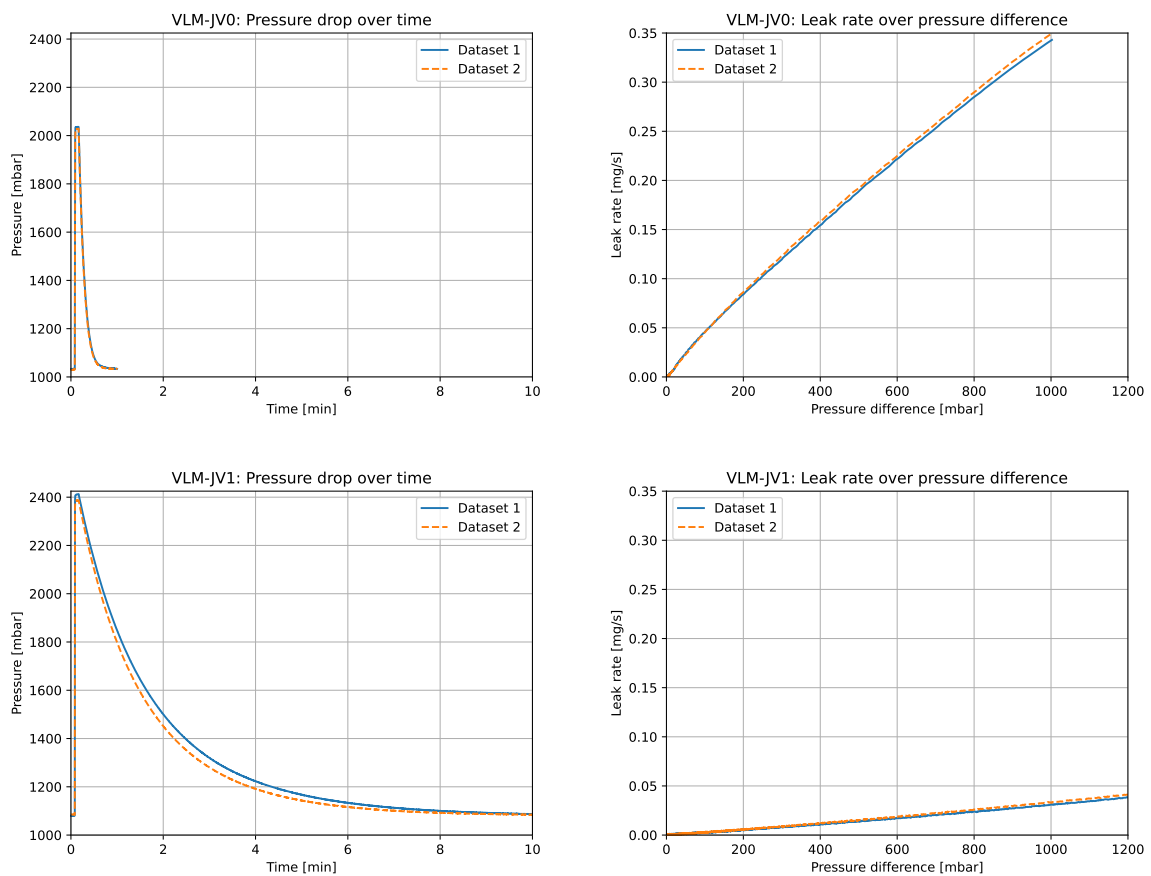


Figure 6.9: Measured leak rate of the Vaporising Liquid Micro-resistojet, after improvements (VLM-JV1).

As apparent from both the table (6.9) and the figure (6.9), the leaks are reduced significantly and only account for 0.18% of the full mass flow. The most important acceptance criterion is thus satisfied (AC-LK-4). The first two (AC-LK-1 and AC-LK-2) are thus also indirectly satisfied. AC-LK-3 has also been checked and confirmed for this test (see subsection 6.2.1). The temperature was found to vary with only ~ 0.3 °C, thus proving that the constant temperature assumption is valid. Seen that the leak rate is minimal, it can, in theory, safely be neglected for the upcoming thrust tests. However, the last leak tests (subsection 6.2.4) will prove that this is not the case.

The established leak rate of 0.032 mg/s is the lowest value since Versteeg's first tests, proving that the changes made were effective. This positive result can be attributed to the resurfacing effort, as well as the various other improvements mentioned in this subsection. Next iterations are thus recommended to implement (some of) these steps if the leak rate is found to have increased again. While the resurfacing turned out to be more expensive than expected, a simple and free polishing procedure might already lead to improved leak-tightness. Furthermore, the application of metal glue and sealant is also not a time-consuming or costly operation and greatly recommended when leaks arise at these locations again.

6.2.4. VLM-JV2

To investigate if the nitrogen and water tests have a significant effect on the leak rate, a new leak test campaign was executed after the thrust test. This campaign is identical to those performed earlier and are labelled as VLM-JV2. The acceptance criteria (see Table 6.6) and the internal volume ($V = 2,430 \text{ mm}^3$) remain unchanged. Just like before, the leak tests are conducted under ambient conditions using nitrogen gas. However, the leak rate will be different for the water vapour, as shown in subsection 6.2.1.

Unfortunately, it quickly became apparent that a major leak has arisen since the last leak tests. Using a soapy liquid (Electrolube DDF), this leak could be easily located at the interface between the pressure sensing tube and the copper block (see Figure 6.10a). Furthermore, some rough, light-coloured material could be observed around this area. This material was not present in such a shape before. Moreover, black soot surrounded this area and covered part of the aluminium casing (see Figure 6.10b and 6.10c). This might come from the brazing material used to connect the steel tube to the copper block. A malfunctioning heater is likely the reason behind the new leak. As described in chapter 3, the heater received too much current, causing it to fail. For a brief moment, the heater became too hot, raising the temperature of the copper brazing material above its limit ($\sim 700 \text{ }^\circ\text{C}$, [47]), causing it to break down. Unfortunately, the impact of this was only noticed after the test campaign. If it were noticed earlier, an attempt could be made to reduce the leaks by applying high temperature sealant or redoing the brazed connections. Like Krusharev [36], high temperature silicone could also be used but this limits the T_c to $300 \text{ }^\circ\text{C}$. Due to time constraints, this will be left for future work. To prevent similar problems in the future, care should thus be taken to check the heaters before use and disregarding malfunctioning ones. According to Oerlikon Metco [47], copper brazing material is rated for $370 \text{ }^\circ\text{C}$. So, temperatures close to this limit should ideally be avoided or a different brazing material should be used. An improved VLM design could eliminate the brazing material altogether by connecting the steel tubes in another manner. A threaded connection combined with high temperature sealant might work as well, for example.

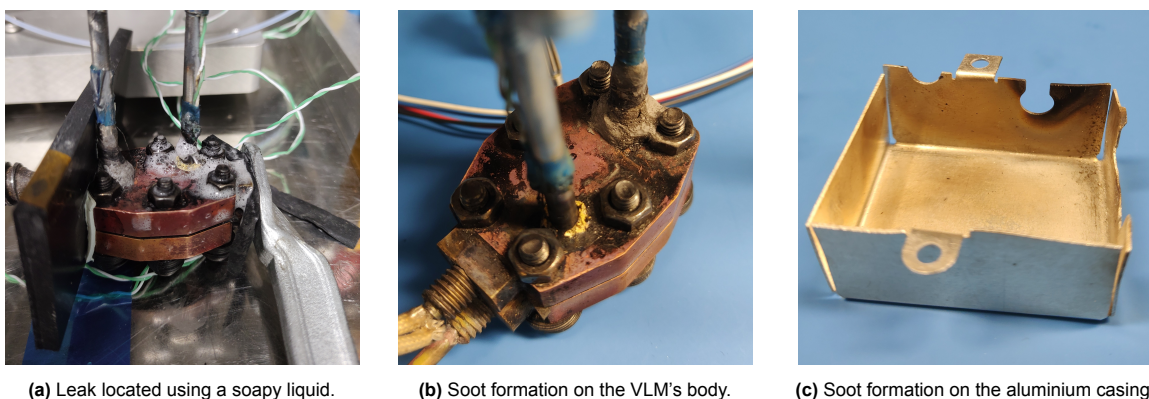


Figure 6.10: Observation of a major leak and soot formation on the Vaporising Liquid Micro-resistojet, after testing (VLM-JV2).

Sadly, the discovered leak is substantial, which was confirmed by the leak tests themselves. Nearly a third of the nitrogen flow (28%) escapes via the new leak. The outcome is shown in Table 6.10 and Figure 6.11. An estimated leak rate of 4.93 mg/s is found at 1 bar. This clearly is a massive degradation of the thruster's leak-tightness and AC-LK-4 cannot be accepted. The leak rate is significantly higher

than the maximum of 5% and should thus be addressed. Sadly, this was only noticed after finishing the test campaign, so nothing could be attempted to improve the situation. This leak was likely also present during both the nitrogen and water experiments. As stated in the introduction of this section, such a significant leak will certainly have an effect on the thruster's performance and must thus be considered. Therefore, the next subsection will briefly treat the leak's impact on the VLM's behaviour.

Parameter	VLM-HV2	VLM-RH	VLM-LC	VLM-LC2	VLM-JV1	VLM-JV2
\dot{m}_L [mg/s]	0.122	0.240	0.223	0.681	0.032	4.93
\dot{m}_L/\dot{m}_{tot} [%]	0.70	1.37	1.27	3.89	0.18	28.16

Table 6.10: Measured leak rate of the Vaporising Liquid Micro-resistojet, after testing (VLM-JV2).

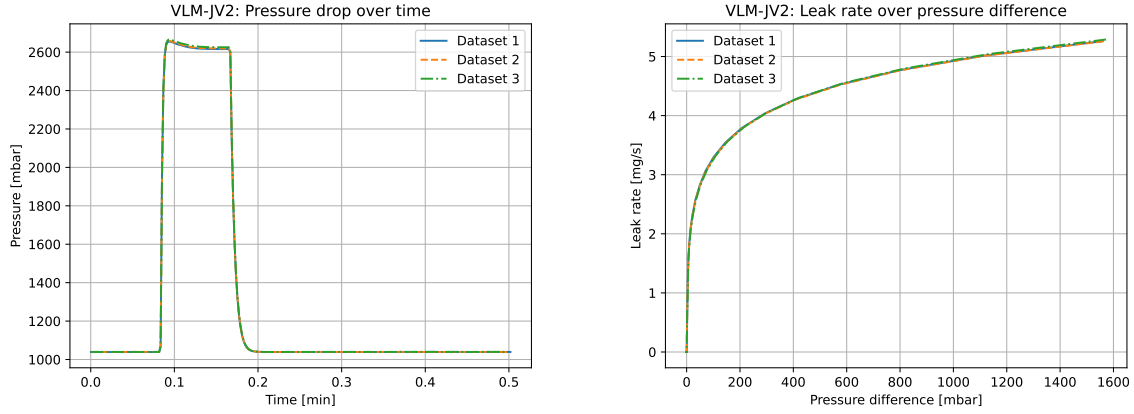


Figure 6.11: Measured leak rate of the Vaporising Liquid Micro-resistojet, after testing (VLM-JV2).

6.2.5. Effects of leaks on the results

As described in the previous subsection, a substantial leak has been discovered after conducting the experiments. This leak is thought to already be present during the tests, so it needs to be accounted for. This subsection will discuss the effect this leak has on the actual mass flow. At first glance, the measured (N_2) mass flow seems unaffected because it is measured before entering the vacuum chamber (see Figure A.1). In reality, a significant portion of the propellant is lost due to the leak and will not be converted into useful energy. The produced thrust will therefore be lower.

As subsection 6.2.4 showed, the leaks amount to nearly a third of the total mass flow (4.93 mg/s or 28%). These tests were conducted under ambient temperature and pressure conditions (no vacuum). This differs from the conditions to which the VLM is exposed to during testing (vacuum, high temperatures, and different propellants). The actual leak rate will therefore vary from test to test. subsection 6.2.1 already discussed this variation with temperature and propellant, which is summarised in Equation 6.4. The presence of a vacuum will have a different effect on the mass flow rate, depending on whether or not the flow is choked (critical conditions prevail, see chapter 4). Properly determining this is challenging, as the exact parameters are unknown. To simplify the process, it is assumed that choked conditions prevail in the leak flow. This is based on the fact that the chamber pressure (P_c) is significantly higher (over 2.5 times) than the ambient pressure (P_a) for both vacuum and non-vacuum conditions. The chamber pressure for the leak tests (no vacuum) is higher (2.6 bar) than those used during the experiments. So, this assumption holds for both situations. A more thorough analysis is required to determine the validity of this assumption, but this is left for other works.

Equation 6.4 can be used to gain insight in the leak rates during the actual experiments. The parameters of the two test campaigns (Table 4.2 and 4.4) can be used in this equation to find the adjusted leak rates. In short, the chamber pressure (P_c) and temperature (T_c) will vary between 1.0 and 1.5 bar

and 20 and 400 °C, respectively. Equation 6.5 has already illustrated this process. The leak tests with VLM-JV2 have all been conducted under ambient conditions. Since the pressure drop is measured over time, the leak rates at different pressure differences can be read from Figure 6.11. Only the leak rates at a ΔP of 1.0 and 1.5 bar are of interest here. These were found to be 4.93 mg/s and 5.23 mg/s, respectively. The correct parameters can then be used to convert the N_2 leak rates at room temperature to nitrogen or water leak rates at varying temperatures. These estimated leak rates (\dot{m}_L) are then subtracted from the predicted mass flows of Table 4.3 and 4.5 (\dot{m}_{MRT}) to acquire a corrected mass flow rate (\dot{m}_{corr}). Table 6.11 summarises the outcome of this process. The confidence bounds of the predicted mass flows are kept to simplify the process. These calculated leak rates will also be subtracted from the actual measured mass flows of the upcoming tests. This will hopefully result in a more accurate outcome of the test campaign. chapter 9 will discuss this in more depth.

Note that the analysis above also assumes that the leak's size remains constant, even for changing temperatures. A quick estimation using copper's temperature expansion coefficient ($16 \cdot 10^{-6}$ m/m°C) proves this assumption is valid for the applicable temperature range [74]. Even a temperature increase of 400 °C only results in a hole expansion of less than 1% [11]. It would be interesting to further analyse the leaks described in this and previous works. For example, the leak size and location could be of interest in the further analysis of the VLM. However, this is left as a suggestion for future efforts.

Test ID	Estimated leak rate \dot{m}_L [mg/s]	Predicted mass flow \dot{m}_{MRT} [mg/s]	Corrected mass flow \dot{m}_{corr} [mg/s]
N2-10-020	4.93 (18.1%)	27.24 ± 8.9%	22.31 ± 8.9%
N2-10-200	2.21 (10.4%)	21.12 ± 9.1%	18.91 ± 9.1%
N2-15-200	2.34 (7.3%)	31.99 ± 8.0%	29.65 ± 8.0%
N2-10-300	1.59 (8.4%)	19.03 ± 8.8%	17.44 ± 8.8%
N2-10-400	1.22 (7.0%)	17.41 ± 8.8%	16.19 ± 8.8%
H2O-10-200	2.20 (13.1%)	16.72 ± 8.8%	14.52 ± 8.8%
H2O-15-300	1.45 (9.6%)	15.01 ± 9.0%	13.56 ± 9.0%
H2O-15-400	1.02 (7.5%)	13.70 ± 9.0%	12.68 ± 9.0%

Table 6.11: Estimated leak rates (and % of predicted flows) for the different test conditions and resulting corrected mass flow rates.

6.3. Discussion

This chapter described the two preliminary tests executed in this thesis. Although the tests themselves are not unique to this work, their outcomes are. section 6.1 has shown that the nozzle geometry changes quite significantly over time. Moreover, the nozzle's dimensions of VLM-JV1 and VLM-JV2 differ significantly from those of Hutten [28]. Since the differences are greater than 10%, the thrust test results of chapter 7 and 8 cannot be compared fairly to Hutten's results. While they are still insightful, they will likely show a noticeable deviation. Added to this, is the presence of a major leak near the pressure sensing tube. section 6.2 has shown that the leak is substantial (> 5%) and needs to be taken into account while examining the thrust test results. Since quite some assumptions are made regarding this leak, the validity of the thrust test results is questionable. Unfortunately, this leak was only discovered after conducting the experiments. In hindsight, the thrust tests should not have been conducted before stopping the leak. Since the situation was discovered too late, this was not possible for this work. Next iterations are advised to address major leaks like this, before continuing with testing.

Although the outcomes of this chapter are worrisome, they provide a strong argument for conducting more preliminary tests. As discussed before, optical characterisations and leak tests should be conducted prior to thrust tests, as well as post thrust tests. This has also been integrated in the new procedures (see Appendix D).

7

Nitrogen Tests

This chapter will describe the nitrogen test campaign. The nitrogen tests have been executed in parallel to the water tests, so there is some overlap between both campaigns. The focus of this chapter is solely on the planned nitrogen tests (Table 7.1) and their results (section 7.2 and 7.3) chapter 9 will compare the nitrogen and water test results, as well as the results of other works. As discussed extensively in the previous chapter (6), optical characterisations and leak tests are conducted before (VLM-JV1) and after the experiments (VLM-JV2). These have shown that the VLM contains a substantial leak, which will likely have an impact on its behaviour. This will also be addressed in section 7.3 at the end of the chapter.

chapter 4 already introduced the test campaign, which is structured similarly to Cramer's [15]. To summarise, five different tests were conducted at different chamber temperatures (T_c) and pressures (P_c , see Table 7.1). The campaign is constructed in such a way to determine if the VLM's behaviour is in accordance with the established theory. The next section (7.1) will describe the test plan in more detail.

Test ID	P_c [bar]	T_c [°C]
N2-10-020	1.0	20
N2-10-200	1.0	200
N2-15-200	1.5	200
N2-10-300	1.0	300
N2-10-400	1.0	400

Table 7.1: Overview of the nitrogen test campaign.

7.1. Test plan

During the tests, several parameters will be recorded directly. These have been listed in Table 7.2 and are identical to those of Cramer since no significant changes were made to the set-up's sensors. The feed system is nearly identical to the one used for the water tests (please refer to subsection 3.2.2), except for the water tank and the solenoid valve, which have been removed. This version of the feed system is included in section A.3. The sensors used for capturing the parameters have been described in chapter 5 and remain largely the same, except for the changes described in chapter 3.

Parameter	Description	Measurement location
F	Thrust force	Load cell near the torsion beam's centre.
\dot{m}_{N_2}	Nitrogen Mass Flow	Before entering the vacuum chamber ¹ .
P_a	Ambient Pressure	Inside the vacuum chamber.
P_c	Chamber Pressure	End of the pressure sensing tube.
T_c	Chamber Temperature	Clamped between nut and copper block.
T_{tube}	Propellant tube temperature	Top of the pressure sensing tube (outside).
I_{heat}	Heater Current	Internally measured by the power supply.
V_{heat}	Heater Voltage	Internally measured by the power supply.

Table 7.2: Overview of the measurement parameters for the nitrogen tests.

The tests will follow the same procedures as those laid out by Cramer [15]. For one test, four thrust periods will be created by opening the propellant valve at intervals of 5 minutes². This should allow sufficient time for the VLM to reach steady state conditions. The transient behaviour will be mostly disregarded in the upcoming data analysis. Prior to testing, all test hardware will be turned on and given enough time to heat up, as advised by Versteeg [81]. A vacuum will be created of at least 15 mbar to replicate the vacuum conditions of earlier test campaigns. The thruster will be heated up to the desired temperature and allowed to settle before commencing a test. The propellant tube temperature (T_{tube}) is only measured to check that the maximum operating temperature of the P - T sensor (85 °C) is not reached. Once all equipment is ready for testing, a calibration using the VTDC is done. The calibration will also be performed directly after the thrust test. This is done to obtain some insight in the zero point drift measured by the load cell, and it will help in correcting for drift during the data analysis. The heater power (P_{heat}) can easily be computed by multiplying the heater current and voltage. It can then be used to compute the heating efficiency (η_{heat}). The other relevant performance parameters ($Re_{t,real}$, I_{sp} , ξ_{Isp} , and C_d) will also be computed from the measurement parameters as described in chapter 4.

Acceptance criterion	Description
AC-N2-1	All parameters from Table 7.2 are measured over time through the correct sensors.
AC-N2-2	The exhaust is supersonic.
AC-N2-3	The performance parameters ($Re_{t,real}$, I_{sp} , ξ_{Isp} , C_d , and η_{heat}), can be determined with an accuracy of 15% or smaller.
AC-N2-4	The measured thrust (F) remains constant during operation.
AC-N2-5	The measured mass flow (\dot{m}_{N_2}) remains constant during operation.
AC-N2-6	The measured ambient pressure (P_a) reaches 15 mbar at most.
AC-N2-7a	The measured chamber pressure (P_c) remains constant during operation.
AC-N2-7b	The average chamber pressure (P_c) is within 5% of the target.
AC-N2-8a	The measured chamber temperature (T_c) remains constant during operation.
AC-N2-8b	The average chamber temperature (T_c) is within 5% of the target.

Table 7.3: Acceptance criteria for the nitrogen tests.

To judge whether a test is successful and can be accepted, several acceptance criteria will be established. These are meant to ensure all necessary parameters are measured and their values are somewhat to be expected. Since the experiments share close similarity to previous works, the acceptance criteria presented in Table 7.3 are also alike. Constant during operation is defined as having a maximum deviation of $\pm 1\%$ from the average value (excluding sensor noise). The addition of AC-N2-6 makes sure the tests take place in a similar vacuum compared to earlier works.

¹ See Figure A.1

² Note that the valves to the N_2 propellant tank will stay opened throughout the tests. This ensures a steady mass flow.

7.2. Test results

This section will describe the test results of [N2-10-300](#). However, this discussion is applicable for all five tests. Moreover, the water test results that will be discussed in [section 8.2](#), were also obtained at a chamber temperature of 300 °C. The raw data collected by the VLM DAQ software is saved in a TDMS file format. This file is subsequently read by a Python script and used for the data analysis. Thankfully, most scripts were already constructed by others [15], so the author could easily pick-up from there. Changes were made where necessary and will be detailed below. To aid possible successors to this work, the essential scripts used for this thesis are added to the [GitHub repository](#) made by Hutten [28].

Most data can be interpreted and plotted directly. However, some data requires further processing before it can be analysed. For example, the mass flow data is measured in standard cubic centimetre per minute (SCCM) which must first be converted to the more usable mg/s. This can simply be done by multiplying the mass flow data in SCCM with the density of nitrogen (1.1648 mg/cm^3)³ and dividing it by 60 to find the mass flow in milligram per second. The power is directly calculated and saved by the LabVIEW program and thus requires no further treatment. The Python script uses the valve data, which switches between 0 (fully closed) and 255 (fully opened), to find the four thrust periods. The data is then cut so only these periods are used in the further data analysis. Furthermore, the first 20 and last 3 seconds of the intervals are removed to eliminate the transient behaviour. However, the thrust data is treated differently, due to a different transient behaviour as will be treated in depth later. Only the latter half of the load data is used (147 seconds in total). From the cut data, important information such as the averages and standard deviations (σ) are calculated. These averages are then combined by computing the root mean square (RMS) and 3σ values, which have been defined in an earlier chapter ([section 5.3](#)). The values presented in [Table 7.4](#) are determined using the methods described there. The most insightful data is plotted in [Figure 7.3](#). The other tests can be found in [section B.4](#). However, before discussing these results and determining whether the acceptance criteria are satisfied, the load data requires some more elaboration.

Test ID	T_c [°C]	P_c [mbar]	\dot{m}_{N_2} [mg/s]	P_a [mbar]	F [mN]	P_{heat} [W]
N2-10-020	36.97 ± 15.73	1013.26 ± 28.16	19.25 ± 0.04	9.17 ± 0.10	6.77 ± 0.11	-
N2-10-200	199.59 ± 0.34	1001.16 ± 1.06	15.38 ± 0.01	7.28 ± 0.61	5.29 ± 0.08	10.41 ± 0.15
N2-10-300	299.32 ± 0.19	997.99 ± 2.29	13.36 ± 0.00	6.37 ± 0.39	4.79 ± 0.06	17.77 ± 0.50
N2-10-400	399.14 ± 0.08	997.15 ± 6.51	12.43 ± 0.10	5.66 ± 0.48	4.12 ± 0.10	27.98 ± 0.69
N2-10-200	199.59 ± 0.34	1001.16 ± 1.06	15.38 ± 0.01	7.28 ± 0.61	5.29 ± 0.08	10.41 ± 0.15
N2-15-200	199.29 ± 0.10	1492.36 ± 1.22	23.93 ± 0.12	10.45 ± 0.11	8.59 ± 0.13	13.16 ± 0.15

Table 7.4: Averaged results and measurement errors of the nitrogen tests.

7.2.1. Drift correction

As treated in detail by Cramer [15], the load cell signal shows a noticeable drift. This drift has also been observed during this work and was already compensated for during the thrust bench calibration of [chapter 5](#). The direction and magnitude of the drift varies from test to test. It seems to be at least partially temperature related as the drift's size increases for an increasing chamber temperature. More research is required to fully characterise this behaviour though. The drift likely originates from a combination of the VLM, load cell, amplifier, and test bench. Of these, the test bench is suspected to have the most significant influence as already noted in the fifth chapter. This suspicion arises from the author's experience during the test campaign during which it was observed that a tiny disturbance could have a major impact on the measured load. A small force applied to the test bench could result in a changed equilibrium point and thus a different zero point. Friction in the test bench's bearing may explain this behaviour. One argument to support this suspicion is the suspected observation of 'sticky friction'. During a test run a sudden, unexpected jump in measured load of 0.5 mN could be observed. This can clearly be seen in the third thrust period of [Figure 7.1](#). A repeat test was conducted to see if

³Density of nitrogen at 20 °C and 1 atmosphere [41].

this behaviour persisted, but this was not the case. Seen that no other parameter showcased abnormal behaviour that might lead to this effect, it is thought to originate from friction in the test bench [52]. As already mentioned in [section 5.2](#), a more thorough calibration and test campaign is required to fully understand this behaviour.

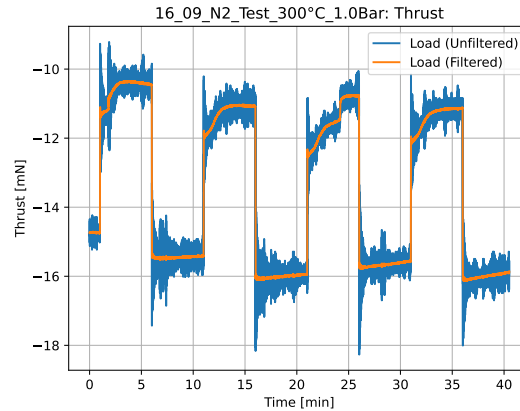


Figure 7.1: Observation of 'sticky friction' in the measured load (nitrogen test at 300 °C and 1.0 bar).

For now, the same drift-correction method as Cramer [15] is used. [Figure 7.2](#) visually demonstrates this process. A quadratic curve is fitted through the off periods and subsequently subtracted from the load data. In the example shown in the figure ([7.2](#)), this correction shifts the thrust upwards and aligns the off periods with the x-axis. The result shows a nicely aligned and seemingly consistent thrust behaviour. A consequence of this procedure is that the thrust signal is tilted slightly, which can clearly be seen when comparing the off periods before and after the drift correction. Another drift-correction technique, tailor made for every single off period, might be better to prevent this tilt in the data. Since this tilt effect is minimal, it is left as a recommendation for future improvements.

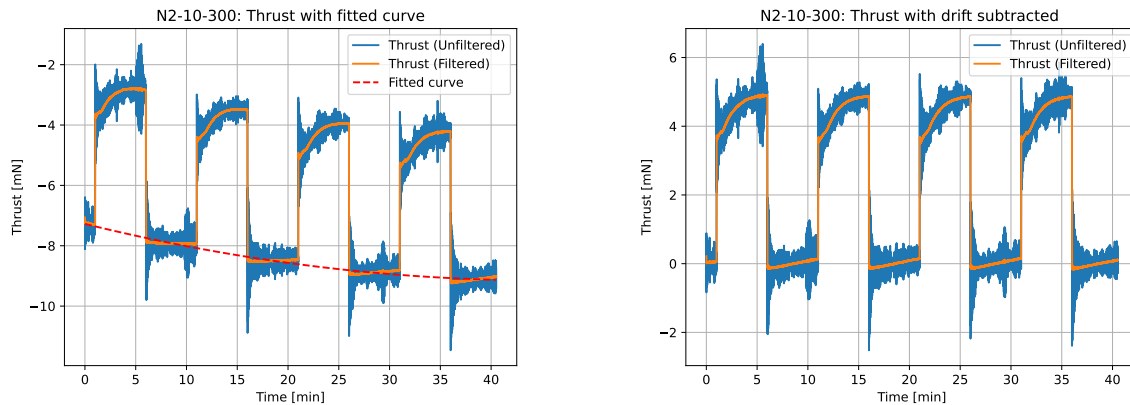


Figure 7.2: Drift compensation process for the nitrogen test at 300 °C and 1.0 bar (N2-10-300).

7.2.2. Results processing

As shown in the legends of several figures, some shown data is filtered. A Savitzky-Golay filter is used for this purpose, which fits polynomials of degree 1 (linear) to a 1-second window [56]. This is especially effective in the smoothing of the noisy load data. As reported in multiple other works (Gomes [23] and Takken [69], for example), this noise can be attributed to external influences, such as footsteps in the hallway and even the movement of the [AE](#) building due to wind. Other parameters (mass flow, heater

power, and chamber pressure) are also filtered using the Savitzky-Golay filter to improve clarity.

As described before, the values and uncertainties reported in Table 7.4 originate from the root mean square and standard deviation values found during the tests. Although these values show little deviation (6% at most), it is not the complete picture. Unfortunately, these deviations do not include the sensor uncertainties established earlier in section 5.3. These will have to be added to the measurement error as illustrated in that same section. The values with the final errors are shown in Table 7.5 and Table B.3 (includes relative errors). These will be used for the calculations of the performance parameters.

The errors of the chamber pressure and temperature found for the cold flow test (N2-10-020) are treated differently. Comparing these errors to those of other tests, it is clear that they are significantly higher than the rest. The cause of this can be seen when investigating the chamber temperature (see Figure B.10), which steadily declines from 47 °C to below 30 °C. It is likely that the thruster was not given enough time to cool down from a previous test, before starting this test. This downwards slope can also be seen in the measured chamber pressure, albeit to a lesser extent. Consequently, the calculated averages and standard deviations are off from the nominal values. As this can be explained by an operational error and not by inexplicable VLM behaviour, the corresponding acceptance criteria (AC-N2-7a, AC-N2-7b, AC-N2-8a, and AC-N2-8b) are still considered to be satisfied for this test (N2-10-020). With these total errors and averaged results (Table 7.5), the quality factors ($Re_{t,real}$, I_{sp} , $\xi_{I_{sp}}$, η_{heat} , and C_d) can finally be determined. This is done using the equations defined in chapter 4. As explained in the fourth chapter of this work, the uncertainty propagation is taken from the RPT of Hutten [28], because this was used by the previous two works and thus aids in maintaining consistency. The resulting performance parameters are shown in the table below (7.6).

Test ID	T_c [°C]	P_c [mbar]	\dot{m}_{N_2} [mg/s]	P_a [mbar]	F [mN]	P_{heat} [W]
N2-10-020	36.97 ± 17.4	1013.26 ± 57.4	19.25 ± 0.14	9.17 ± 1.38	6.77 ± 0.13	-
N2-10-200	199.59 ± 7.51	1001.16 ± 50.0	15.38 ± 0.11	7.28 ± 1.25	5.29 ± 0.10	10.41 ± 0.15
N2-10-300	299.32 ± 7.50	997.99 ± 50.1	13.36 ± 0.09	6.37 ± 1.03	4.79 ± 0.08	17.77 ± 0.50
N2-10-400	399.14 ± 7.50	997.15 ± 50.4	12.43 ± 0.13	5.66 ± 0.98	4.12 ± 0.11	27.98 ± 0.69
N2-10-200	199.59 ± 7.51	1001.16 ± 50.0	15.38 ± 0.11	7.28 ± 1.25	5.29 ± 0.10	10.41 ± 0.15
N2-15-200	199.29 ± 7.50	1492.36 ± 50.0	23.93 ± 0.21	10.45 ± 1.57	8.59 ± 0.16	13.16 ± 0.15

Table 7.5: Averaged results and total errors of the nitrogen tests.

Test ID	$Re_{t,real}$ [-]	I_{sp} [s]	$\xi_{I_{sp}}$ [-]	η_{heat} [-]	C_d [-]
N2-10-020	3313 ± 482 (14.5%)	35.86 ± 0.74 (2.1%)	0.52 ± 0.02 (3.6%)	-	0.69 ± 0.06 (9.3%)
N2-10-200	1939 ± 271 (14.0%)	35.07 ± 0.71 (2.0%)	0.41 ± 0.01 (2.2%)	0.27 ± 0.03 (12.5%)	0.69 ± 0.06 (8.5%)
N2-10-300	1498 ± 212 (14.2%)	36.56 ± 0.66 (1.8%)	0.39 ± 0.01 (2.0%)	0.22 ± 0.03 (12.8%)	0.66 ± 0.06 (8.8%)
N2-10-400	1243 ± 178 (14.3%)	33.80 ± 0.97 (2.9%)	0.33 ± 0.01 (3.0%)	0.18 ± 0.02 (13.0%)	0.67 ± 0.06 (9.0%)
N2-10-200	1939 ± 271 (14.0%)	35.07 ± 0.71 (2.0%)	0.41 ± 0.01 (2.2%)	0.27 ± 0.03 (12.5%)	0.69 ± 0.06 (8.5%)
N2-15-200	2965 ± 393 (13.3%)	36.60 ± 0.75 (2.1%)	0.43 ± 0.01 (2.3%)	0.34 ± 0.04 (10.9%)	0.72 ± 0.05 (7.4%)

Table 7.6: Quality factors of the nitrogen tests.

7.2.3. Acceptance criteria

Now all the required results are in place, the acceptance criteria of Table 7.3 can be checked. As becomes clear from the discussion above, all parameters were measured successfully, satisfying AC-N2-1. Moreover, Table 7.6 proves that all performance parameters could be determined with a maximum uncertainty of 14.9%. So, AC-N2-3 can also be checked off. Most acceptance criteria involving constant operation (AC-N2-5, AC-N2-7a, and AC-N2-8a) are also satisfied. Moreover, the chamber temperature and pressure both are within 5% of their target, fulfilling AC-N2-7b and AC-N2-8b. The ambient pressure reached 10.45 mbar at most, so AC-N2-6 is also satisfied. The remaining two ac-

ceptance criteria, [AC-N2-2](#) (supersonic exhaust) and [AC-N2-4](#) (constant thrust), require some more elaboration.

Whether supersonic conditions prevail in the nozzle exit can be determined with [Equation 4.6](#). This was checked for every test and found to be true for each one. [AC-N2-2](#) is thus also accepted. Lastly, the average thrust variation had to fall within $\pm 1\%$. The summarised results show that this is not the case for a single test. The deviation varies from 1.3% ([N2-10-300](#)) to a maximum of 2.4% ([N2-10-400](#)). Based on this, [AC-N2-4](#) cannot be accepted. This was also the case for Cramer's tests, who had even higher deviations (6.3% at most). Although the thruster behaviour will be treated more in detail in the next section ([7.3](#)), this acceptance criterion might require some changing. It is probably a little bit too strict and could be relaxed to an allowable deviation of 2.5%. Hutten [\[28\]](#) did not include a separate criterion for the thrust, as it cannot be controlled directly, so that is also an option. For now, the [AC-N2-4](#) will be relaxed to allow for a maximum deviation of 2.5%. With this alteration, this criterion can also be accepted and thus the tests can be considered a success.

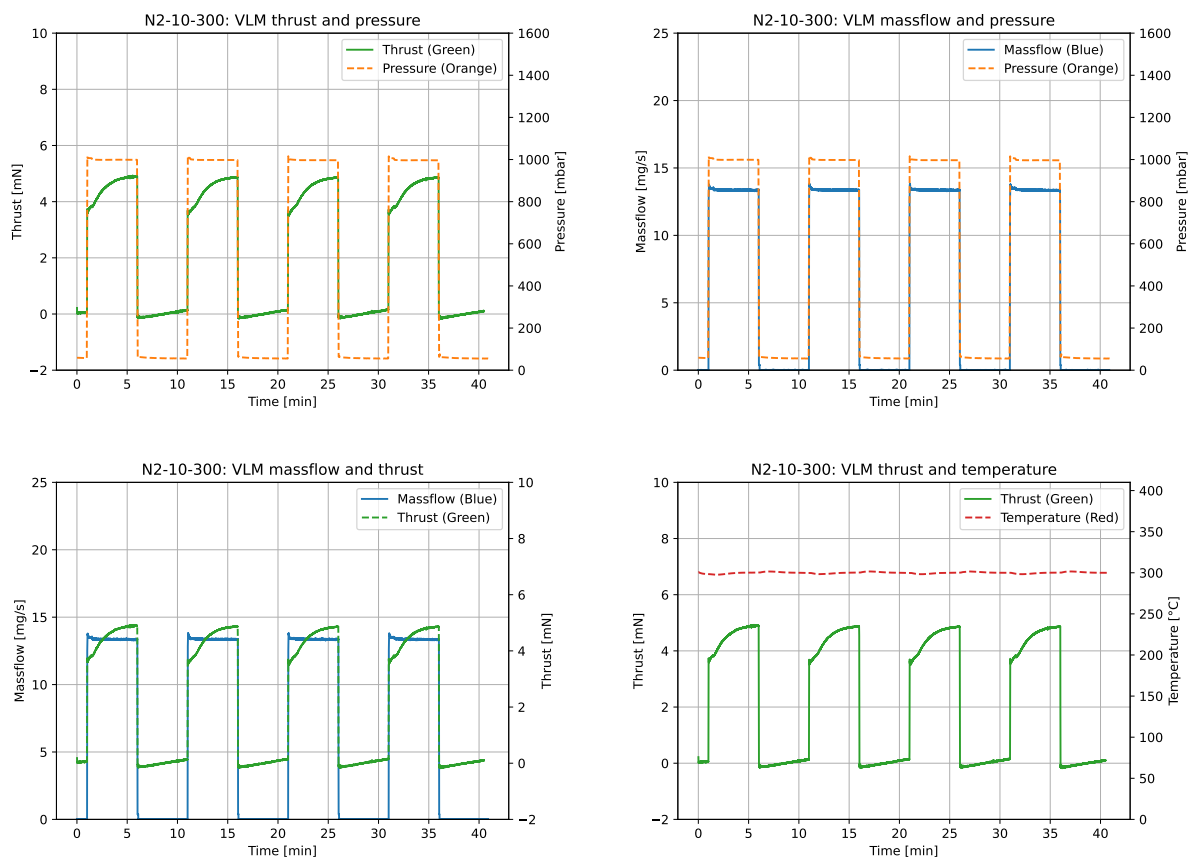


Figure 7.3: Measured parameters of the nitrogen test at 300 °C and 1.0 bar ([N2-10-300](#)).

7.3. Test discussion

Now that the test results are processed and the acceptance criteria are checked, the data itself can be analysed a bit more. This section will not yet compare the results of this work to those of predecessors. That will be reserved for [chapter 9](#). Instead, the data will be judged based on the expected behaviour described in [subsection 4.4.1](#). In short, an increase in chamber temperature should lead to a decrease in mass flow and an increase in specific impulse. Furthermore, the thrust should stay constant. An increase in chamber pressure should lead to a higher thrust and mass flow and an unchanged specific impulse. [Table 7.5](#) and [Table 7.6](#) are consulted to see if this behaviour is indeed observable.

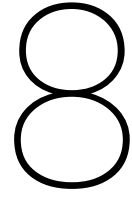
Unfortunately, the VLM's performance is not in accordance with the expected behaviour. Instead of a constant thrust, a clear negative trend can be observed. Moreover, the specific impulse decreases as well, except for the one of [N2-10-300](#). The measured mass flow, on the other hand, seems to exhibit the expected decrease. Increasing the chamber pressure results in an increased thrust and mass flow, as expected. However, the specific impulse also increases with 4% with respect to the test done at the same temperature (200 °C), while it should stay roughly constant. In short, the test results do not agree well with the expected behaviour.

No obvious reasons for this unexpected behaviour can be found within the measurement data. To find the root of this problem, the results must be inspected a little bit deeper. It is suspected that problems might (partially) be attributed to the leaks that have arisen during the test campaign (see [chapter 6](#)). As described in the previous chapter, the actual mass flow is likely smaller than the measured value. [Table 6.11](#) displays the estimated leak rates for the different tests. Unfortunately, this leak correction process cannot explain the negative I_{sp} trend. Even when applying this process to the measured mass flow rates, the trend persists. This is illustrated in [Table 7.7](#).

The declining thrust is also part of the reason behind the unexpected VLM behaviour. It should remain constant for a higher T_c . Since this is not the case, the specific impulse declines, which also results in a problematic specific impulse efficiency. The low thrust production likely originates from two separate causes; the previously mentioned leaks, and the TB-50m thrust bench. [Equation 4.3](#) shows that the thrust output is directly correlated to the mass flow output. Consequently, when this mass flow is lower than expected, it directly results in a lower thrust. The exact mass flow rate is not known and can only be estimated. It is therefore possible that the leak rate estimation is not true to reality and that the leak rates increase for higher temperatures. This could then explain the declining thrust output. Furthermore, as described extensively in [chapter 5](#), the used torsional test bench is found to reduce the VTDC's sensitivity with $\sim 25\%$. Although this effect needs to be researched more, it is possible that the TB-50m adds friction to the system. This friction might also affect the measured thrust as the load cell measures a 25% lower thrust production. The actual produced thrust may thus be 1.25 greater than the ones shown in [Table 7.5](#). Although this can be compensated for by multiplying the measured thrust with a correction factor of 1.25, it does not halt the negative thrust trend. Unfortunately, not enough information is available at this point in time to determine the exact cause of the results obtained in this chapter. The high leak rate seems the most likely reason, but more research is required to fully understand the problematic thruster performance. In [chapter 9](#), this performance is compared to those found by other works, which may shed more light on the problem.

Test ID	Estimated leak rate \dot{m}_L [mg/s]	Measured mass flow \dot{m}_{meas} [mg/s]	Corrected mass flow \dot{m}_{corr} [mg/s]
N2-10-020	4.93 (25.6%)	19.25 \pm 0.14	14.32 \pm 0.14
N2-10-200	2.21 (14.3%)	15.58 \pm 0.11	13.17 \pm 0.11
N2-15-200	2.34 (9.8%)	23.93 \pm 0.21	21.59 \pm 0.21
N2-10-300	1.59 (11.9%)	13.36 \pm 0.09	11.77 \pm 0.09
N2-10-400	1.22 (9.8%)	12.43 \pm 0.13	11.21 \pm 0.13

Table 7.7: Estimated leak rates (and % of measured flows) and resulting corrected mass flow rates for the different tests.



Water Tests

This chapter will describe the water test campaign, as well as its results. As mentioned in the preceding chapter, the nitrogen and water tests were executed in parallel, so they are believed to share some important characteristics, such as the leak rate and nozzle geometry. These have been described in [chapter 6](#). Moreover, the unexpected VLM behaviour discussed in [section 7.3](#), will likely also persist in these tests. The water test results will be compared those of Hutten [28] in [chapter 9](#).

The water tests will be a bit different compared to those performed with nitrogen. Moreover, they are different to those done by Hutten. The main difference is the used feed system and its effect on the test procedures. This will be described in the first section of this chapter ([section 8.1](#)). In this feed system, which has been detailed in [chapter 3](#), the mass flow cannot be controlled directly. The purpose of the redeveloped feed system is that it should eliminate some of the problems experienced by the previous attempt, such as the formation of bubbles inside the propellant lines and the initial propellant rush. The addition of a liquid mass flow meter (Sensirion SLI-1000, see [chapter 5](#)) should also result in more accurate mass flow data. Whether the new feed system's purpose is achieved, will become clear from the results and discussion of this chapter ([section 8.2](#) and [8.3](#)).

8.1. Test plan

The tests campaign presented here is a bit more extensive compared to Hutten's campaign (see [Table 8.1](#)). Two more chamber temperature (T_c) variations are added to capture more of the thruster's behaviour under different circumstances. Note that the chamber pressure (P_c) parameter is replaced with a pressurant pressure (P_p). Due to the nature of these tests and the fact that the water is only vaporised inside the thrust chamber, it is difficult to control the chamber pressure. This is in contrast to the nitrogen tests where the N_2 pressure could easily be controlled by adjusting the pressure regulator valve. The N_2 serves as a pressurant to the water inside the tank. The gas has a dual purpose; it forces the water through the propellant lines and inside the thruster and, at the end of the test, it removes the remaining water from the feed lines so that little to no water is left in them. This helps in preventing the leftover water from influencing subsequent tests. Note that pressurant pressure is different for the test conducted at 200 °C (1.0 bar instead of 1.5 bar). This was an operational oversight, but it seemed to have little influence on the mass flow. These pressures were found using a trial-and-error method.

Test ID	P_p [bar]	T_c [°C]
H2O-10-200	1.0	200
H2O-15-300	1.5	300
H2O-15-400	1.5	400

Table 8.1: Overview of the water test campaign.

Similar to the nitrogen test campaign of [chapter 7](#), several parameters will be recorded here as well. These remain largely unchanged, except for the replacement of the nitrogen mass flow (\dot{m}_{N_2}) recording with the water mass flow (\dot{m}_{H_2O}) recording. The overview of the measurement parameters is shown in [Table 8.2](#). The structure of these tests also remains quite comparable to the previous tests' structure. However, instead of four thrust periods of each 5 minutes long, these tests feature extended thrust periods. The thrust periods are 10 minutes long, followed by an equally long off period. This gives the VLM more time to reach steady state conditions and more time to reach the desired temperature after propellant shut-off. One water test will feature only two thrust periods. This adapted procedure is also described in [subsection 8.1.1](#). Originally, the nitrogen test structure was maintained (periods of 5 minutes) but extensive initial testing showed this was insufficient time for the thruster to reach a somewhat steady state. Hence the adapted procedures. Other actions, such as the pre-heating of the thruster and the establishing of a sufficient vacuum, described in the original procedures remain the same.

Parameter	Description	Measurement location
F	Thrust force	Load cell near the torsion beam's centre
\dot{m}_{H_2O}	Water Mass Flow	Between the water tank and solenoid valve ¹
P_a	Ambient Pressure	Inside the vacuum chamber
P_c	Chamber Pressure	End of the pressure sensing tube
T_c	Chamber Temperature	Clamped between nut and copper block
T_{tube}	Propellant tube temperature	Top of the pressure sensing tube (outside)
I_{heat}	Heater Current	Internally measured by the power supply
V_{heat}	Heater Voltage	Internally measured by the power supply

Table 8.2: Overview of the measurement parameters for the water tests.

The water tests will also be judged against certain acceptance criteria. These are based on the same as those of the nitrogen test campaign, with a few exceptions. The criteria involving the chamber pressure have been removed for the same reason the chamber pressure was removed as part of the test plan. Besides, the parameters that should remain constant during operation (F , \dot{m}_{H_2O} , and T_c), are allowed to have a maximum deviation of $\pm 5\%$ (excluding sensor noise). This is done to allow for a bit more flexibility since this is the first time water tests are conducted in this manner. Subsequent iterations can focus on reducing these deviations. This water campaign is mainly concerned with improving on the operational aspect of the experiments and characterising the VLM's behaviour with water, rather than achieving low uncertainties. This is also the reason for the increased confidence bounds of [AC-H2O-3](#). The acceptance criteria are listed in [Table 8.3](#).

Acceptance criterion	Description
AC-H2O-1	All parameters from Table 8.2 are measured over time through the correct sensors
AC-H2O-2	The exhaust is supersonic
AC-H2O-3	The performance parameters ($Re_{t,real}$, I_{sp} , ξ_{Isp} , C_d , and η_{heat}), can be determined with an accuracy of 30% or smaller
AC-H2O-4	The measured thrust (F) remains constant during operation
AC-H2O-5	The measured mass flow (\dot{m}_{H_2O}) remains constant during operation
AC-H2O-6	The measured ambient pressure (P_a) reaches 15 mbar at most
AC-H2O-7a	The measured chamber temperature (T_c) remains constant during operation
AC-H2O-7b	The average chamber temperature (T_c) is within 5% of the target

Table 8.3: Acceptance criteria for the water tests.

¹See [Figure A.2](#)

8.1.1. Test procedures

As alluded to before, the water test procedures are quite similar to the nitrogen test procedures, aside from a few key differences. These originate from the usage of a different propellant feed system. The adapted procedures are included in the appendix for future reference (see [section D.3](#)).

The main differences involve the filling of the water tank, before connecting it to the rest of the feed system. The water used throughout these tests is demineralised water, which is available in a large container inside the cleanroom. A syringe is used to fill the propellant tank. Furthermore, an additional (venting) valve is added to the system in front of the water tank. As described in [chapter 3](#), this venting valve can be opened to expose the water to the vacuum inside the vacuum chamber. This allows the trapped air and gases inside the system to escape and prevents bubble formation. As there is only one connection for both the venting and propellant valves, their connection needs to be switched manually at the back of the vacuum chamber. The venting valve is opened throughout the environmental set-up of the tests (evacuation of the chamber). After this, the electrical connections are switched, and the propellant valve can be controlled. The first valve thus stays closed throughout the rest of the thrust tests. The liquid mass flow is measured using Sensirion's proprietary software and combined later with the rest of the data. This is done in Python and this script is added to the earlier mentioned [GitHub repository](#).

8.2. Test results

The water tests were conducted with varying success. It proved hard to achieve a somewhat consistent behaviour. The mass flow was found to be difficult to control, which would translate to an irregular thrust and chamber pressure. After a lot of trial-and-error tests, some reasonable results were achieved. The best three will be presented in this report. The most interesting results of [H2O-15-300](#) are showcased in [Figure 8.1](#). All relevant figures of the water experiments can be found in [section B.5](#).

The same data processing techniques are adopted as used in [chapter 7](#). As described in [subsection 5.1.7](#), the liquid mass flow is measured and stored separately from the other parameters. This data is added to the other data in Python, after which it can be processed. Since the Sensirion software stores the mass flow in $\mu\text{L}/\text{min}$, it is first converted to mg/s . The water mass flow signal exhibits quite some noise, so it is filtered using the Savitzky-Golay filter [56]. The first 90 and the last 3 seconds of the data is removed to isolate the steady-state behaviour, while only the latter half of the thrust period is used for extracting the thrust performance. This increased buffer is done as it became apparent from the experiments that the VLM requires more time to reach steady conditions. The averages and standard deviations are acquired in the same manner as detailed earlier in this work. The sensor error once again will be added on top of the measurement error. Finally, the averaged results with the total errors are displayed in [Table 8.4](#). The first experiment ([H2O-15-200](#)) consists of only a single thrust period because of an oversight. Consequently, the standard deviations of this test are generally higher as they are not averaged over two periods. A results table that includes the confidence bounds in percentages can be found in [section B.5](#). The same section also shows the graphs of the [H2O-15-200](#) and [H2O-15-400](#) tests. Note that the final test (with a target temperature of $400\text{ }^{\circ}\text{C}$) is split in two parts (a and b). This has no particular reasons but is the result of a slight operational mistake in which the data was recorded separately. Using the results of [Table 8.4](#), the quality factors can be computed. The method of the previous chapter is adopted for this end. These factors and their uncertainties are shown in [Table 8.5](#).

Test ID	$T_c\text{ [}^{\circ}\text{C]}$	$P_c\text{ [mbar]}$	$\dot{m}_{\text{H}_2\text{O}}\text{ [mg/s]}$	$P_a\text{ [mbar]}$	$F\text{ [mN]}$	$P_{\text{heat}}\text{ [W]}$
H2O-10-200	174.49 \pm 27.3	851.83 \pm 133	5.99 \pm 1.50	8.26 \pm 5.76	5.94 \pm 0.73	40.02 \pm 2.30
H2O-15-300	279.25 \pm 8.44	743.95 \pm 81.1	6.30 \pm 0.72	6.49 \pm 3.42	4.15 \pm 0.21	40.02 \pm 0.08
H2O-15-400	337.07 \pm 20.3	899.74 \pm 95.2	5.87 \pm 1.04	7.52 \pm 4.05	5.25 \pm 1.25	40.00 \pm 0.08

Table 8.4: Averaged results and total errors of the water tests.

Test ID	$Re_{t,real} [-]$	$I_{sp} [s]$	$\xi_{I_{sp}} [-]$	$\eta_{heat} [-]$	$C_d [-]$
H2O-10-200	1564 ± 530 (33.9%)	101.1 ± 28.2 (27.9%)	0.95 ± 0.27 (28.2%)	0.41 ± 0.14 (34.9%)	0.39 ± 0.12 (30.2%)
H2O-15-300	1144 ± 245 (21.4%)	67.17 ± 8.40 (12.5%)	0.56 ± 0.07 (12.6%)	0.46 ± 0.10 (21.7%)	0.52 ± 0.09 (17.3%)
H2O-15-400	1030 ± 266 (25.8%)	91.20 ± 27.07 (29.7%)	0.73 ± 0.22 (29.8%)	0.45 ± 0.11 (25.5%)	0.42 ± 0.09 (22.0%)

Table 8.5: Quality factors of the water tests.

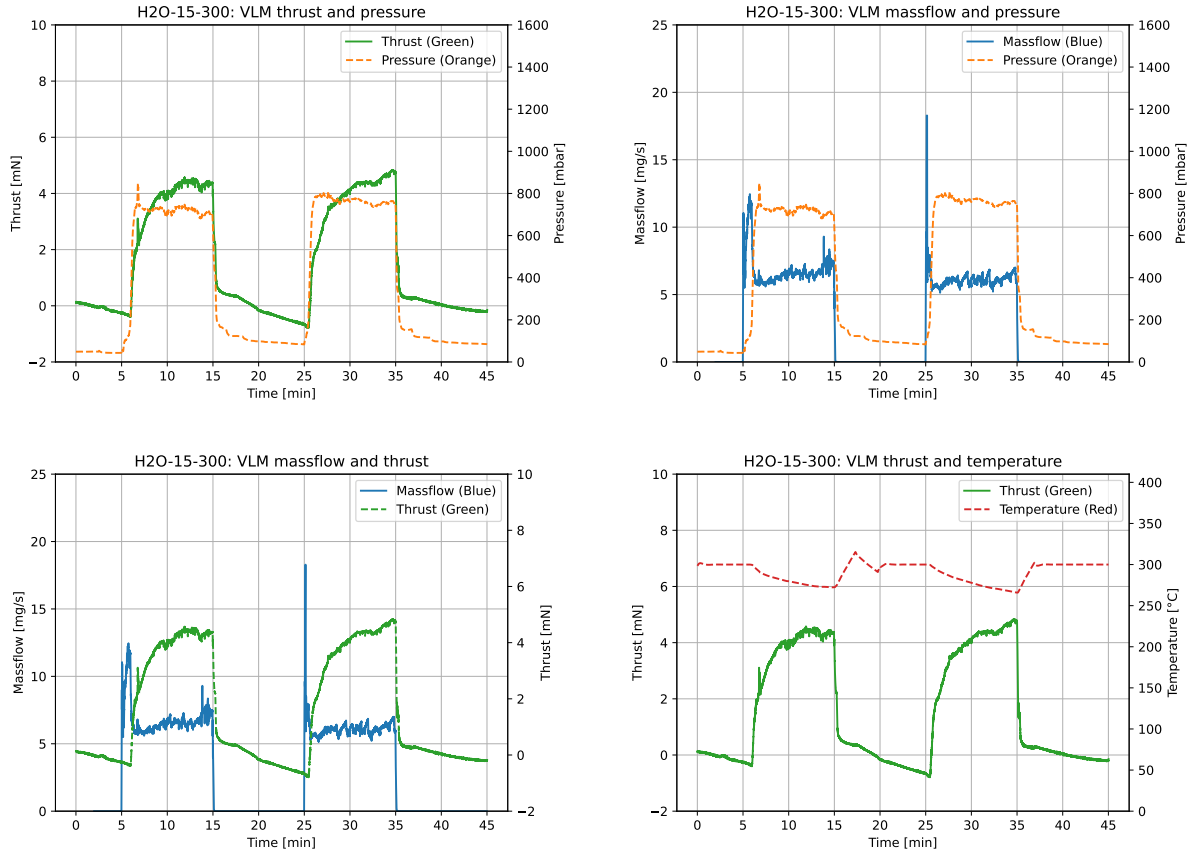


Figure 8.1: Measured parameters of the water test at 300 °C and 1.5 bar (H2O-15-300).

8.2.1. Acceptance criteria

Before discussing the measured results, the acceptance criteria of Table 8.3 need to be reviewed. All desired parameters were measured over time through the necessary sensors, thus satisfying AC-H2O-1. Supersonic conditions are once again checked via Equation 4.6 and were present for all three tests. AC-H2O-2 is thus also accepted. Unfortunately, the remaining acceptance criteria cannot be accepted. As becomes clear from Table 8.5, the quality factors contain a significant uncertainty. The lowest deviation is 12.5%, while the highest is 34.9%. Even with the increased confidence bounds (30%), the acceptance criterion is not met. However, when disregarding the test at 200 °C or by increasing the confidence bounds to 35%, AC-H2O-3 can still be met. This shows that having only a single thrust period leads to a significant uncertainty, which negatively impacts the rest of the parameters. That does not mean that the other two tests perform better. These also fail to meet the majority of the criteria. All criteria involving constant operation (F , \dot{m}_{H_2O} , and T_c) state that the parameter's uncertainties should fall within $\pm 5\%$. Sadly, these are not met for a single test. Thus, AC-H2O-4, AC-H2O-5, AC-H2O-7a, and AC-H2O-7b are all failed. The ambient pressure criterion (AC-H2O-6) is met for all tests. To summarise, only three of the eight acceptance criteria are satisfied. This clearly indicates that the tests, as they have been described in this chapter, must be considered unsuccessful. The next section will describe the observed performance in more detail and tries to provide more insight into the test results.

8.3. Test discussion

As mentioned in the test predictions section (4.4.2), the thruster's performance is hard to predict beforehand. The test set-up makes it so that the chamber pressure is not a controllable variable anymore, leading to more uncertainty in the performance. This can be clearly seen when raising the chamber temperature, for example. During the nitrogen tests of the previous chapter, this would result in a decreased mass flow. This relation does not hold true for the water tests. On the contrary, the mass flow seems to behave rather chaotically. It rises for a chamber temperature of 279.25 °C, but falls again for a higher chamber temperature 337.07 °C. In an attempt to find the reasons behind the measured results, the data will be analysed a bit more extensively in this section. Comparison to the MRT's output and Hutten's results is reserved for the next chapter 9.

The plots of Figure 8.1 and those in the appendix (section B.5) show what is happening during the tests. The ambient pressure graph will not be discussed as it does not show an interesting or unique curve. Starting with the mass flow (\dot{m}_{H_2O}), it immediately becomes clear that it is rather erratic. This aligns with the author's experiences in trying to achieve a constant flow. Despite a lot of trial-and-error, the mass flow continues to be difficult to control. It is unsure where this erratic signal originates from. No bubbles were detected during the experiment, which would otherwise help explain sudden mass flow changes. The starting flow shows a significant peak before settling to a somewhat consistent flow. The flow is not completely constant however, since it slightly increases towards the end of the thrust period with roughly 1 mg/s. This could be due to the decrease in chamber temperature over time. Table 8.6 once again shows the estimated leak rate and the corrected mass flow as a result of the correction process. Whether this correction has any merit, will be determined in chapter 9.

Test ID	Estimated leak rate \dot{m}_L [mg/s]	Measured mass flow \dot{m}_{meas} [mg/s]	Corrected mass flow \dot{m}_{corr} [mg/s]
H2O-10-200	2.20 (36.7%)	5.99 ± 1.50	3.79 ± 1.50
H2O-15-300	1.45 (23.0%)	6.30 ± 0.72	4.85 ± 0.72
H2O-15-400	1.02 (17.4%)	5.87 ± 1.04	4.85 ± 1.04

Table 8.6: Calculated leak rates (and % of measured flows) and resulting corrected mass flow rates for the different tests.

The chamber pressure (P_c) also exhibits interesting behaviour. The second period's pressure is clearly higher than the first with approximately 50 mbar. This increase might be explained by some leftover water in the thruster. In between both thrust periods and after the last period, the chamber pressure does not reach the same lower limit as before the propellant flow. This might indicate that some propellant is left inside the thruster which could condense and accumulate in the propellant and pressure sensing tubes. These tubes have a lower temperature than the chamber and are located underneath it, so some liquid water may flow into these tubes. This could influence the P - T sensor, explaining the rise in pressure. Apart from that, the pressure is relatively stable, although a minor decrease of 30 mbar can be distinguished during a single thrust period. This can likely be attributed to the chamber temperature decrease.

The chamber temperature (T_c) plot clearly shows some major temperature variations. Once the propellant starts flowing, the temperature drops rapidly (more than 25 °C and even more than 100 °C for H2O-15-400). In response, the heaters are turned on to their maximum (~40 W). Despite this, the heaters are not able to stop the temperature from decreasing substantially. This decline seems to reduce a little bit over time but does not seem to reach an equilibrium soon. Hutten [28] did not encounter this problem and was able to maintain a fairly consistent chamber temperature at even higher mass flows. It is believed that this might be explained by the fact that one of heaters used in this work is longer and does not penetrate fully into the thruster (see chapter 3). It thus loses more heat to the environment and is less efficient. Moreover, Hutten used a different conducting material between the heater and the copper blocks, namely copper grease. This work uses a gallium-indium-tin alloy for this purpose [15]. This alloy has a notably lower thermal conductivity value than copper (16.5 versus 388

W/m-K, [21, 11]). So, this may also help explain why it is more difficult to maintain the chamber temperature. During minute 15 to minute 25 the chamber reaches the desired temperature again. However, a temperature spike ($\sim 312^\circ\text{C}$) is clearly distinguishable around minute 17. This can directly be attributed to the PID-controller used for controlling the heaters. For unknown reasons, this PID-controller did not perform well during the water campaign and had to be reset during test runs. If the author did not intervene, the heaters would be running on full power for longer, raising the temperature even more. This intervention can clearly be seen in the power plot by the sudden drop to 0 W around minute 17 and 37. For future water tests, the PID-controller should be improved to eliminate this unwanted behaviour. The temperature drops even lower during the second thrust period, which can probably be attributed partially to the sensor uncertainty, since it does not seem to originate from other parameters.

Lastly, the thrust itself (F) must be analysed. Like the nitrogen tests, it takes some time to build up the thrust. This build-up takes longer for these experiments. After 5 minutes, the thrust increase seems to slow down and move towards a steady-state of approximately 4.2 mN. The second thrust period is a little bit higher, which is probably caused by the higher chamber pressure. Noteworthy is the fact that the thrust does not build up immediately; it takes 30 to 60 seconds after opening the propellant valve before a change can be noticed. In fact, this can be seen in nearly all plots, except for the mass flow one. This is easily explained by the fact that it takes some time for the liquid water to travel from the valve to the thruster. This time is less for the second thrust period, as still some water is left in the tubing. This leftover water probably slowly evaporates out of the thruster which might explain the non-zero measured thrust and its steady negative slope during the down period. This could also help explain the higher (compared to its level prior to thrusting) chamber pressure during this period. When the propellant valve is closed (minute 15 and 35), the parameters drop much more quickly. That is because the propellant that is left is not pushed towards the thruster any more, almost instantly stopping the propellant supply. By moving the valve closer to the thruster, this delayed VLM response can be reduced.

The tests described in this section have resulted in some interesting thruster behaviour. For example, the ξ_{Isp} of H2O-10-200 seems really high. This is not realistic and can be explained by the low measured flow rate. Based on the acceptance criteria, the tests are not accepted, and new attempts should be made to acquire more reliable results. The measured parameters show a high variation which leads to uncertain results. This variation can be attributed to an erratic mass flow and an un-maintainable thruster temperature. These issues should be addressed, before attempting to replicate the water tests. If the chamber temperature and mass flow can be controlled more precisely and with less chaotic jumps, the other parameters will likely also show an improvement. A reduction in the mass flow rate may also help to relieve the heaters. A lower flow implicates less heat is lost to the water and the thruster cools down less quickly. This should prevent the chamber temperature from varying as much.

A final note is that the errors of these results could be reduced significantly by inspecting a smaller timeframe. Like Hutten, only the last minute could be extracted to calculate the averages and standard deviations. This results in smaller confidence bounds and thus helps in meeting the acceptance criteria more easily. This is not done here to maintain consistency with the previous chapter. It is left thus left as an idea for next iterations.

Validation & Verification

In this chapter the most important results found throughout the different chapters will be reviewed. First, they will be compared to the analytical model developed in [chapter 4](#) in an attempt to validate the [MRT](#). This is described in [section 9.1](#). The second section will compare the tests results of this work to those of previous works ([section 9.2](#)). This is done to try to verify the results and characterise the changing Vaporising Liquid Micro-resistojet behaviour.

9.1. Validation of the Analytical Model

Like the previous works, the eventual purpose of conducting the experiments is to attempt to validate the analytical model. This can be done if the measured and predicted parameters are in close agreement with each other. A difference of 10% is deemed an acceptable limit for the moment as this was also used in previous works. Simplifying assumptions made in the model and inherent uncertainties in the measured parameters, limit the accuracy with which predictions can be made. Previous works have shown that there is a significant disparity between the measured (experimental) and predicted (analytical) performance. On the one hand, the modelled thrust, mass flow, and specific impulse could be predicted quite precisely as shown by Versteeg [81] and Hutten [28] (see [chapter 2](#)). On the other hand, the modelled discharge coefficient and specific impulse quality could not be validated. The differences between the analytical and experimental results have only worsened over time as proven by Cramer [15]. For example, the measured F and I_{sp} are significantly off from the predicted values (differences of -50% and -25%). The other performance parameters follow a similar trend. Unfortunately, these disparities were found to be too substantial to validate the model. As shown in previous chapters ([chapter 7](#) and [chapter 8](#)), the performance decrease has continued, resulting in even worse results. It is thus unlikely that the model can be validated with these results. Nevertheless, the output of the Modified Rocket Theory will be compared to the test results to quantify the performance decrease.

Like previous chapters, this section will only discuss a specific test in detail. To maintain consistency, the nitrogen and water tests at 300 °C are chosen for this. However, the discussion is applicable to the other tests as well. Their results are included in [section B.6](#). First, the nitrogen tests are discussed. [Table 9.1](#) shows the disparity between the analytical model and the test results for the nitrogen test conducted at 300 °C and 1.0 bar ([N2-10-300](#)). The differences shown in the table are substantial. The maximum difference is almost 60%, while the minimum is 21%. Not a single parameter has a deviation close to or less than 10%, not even for the other four tests. It thus quickly becomes clear that the actual VLM performance has moved even further from the predicted performance. This can also clearly be seen in [Figure 9.1](#). This figure visualises the major discrepancies between the modelled and measured performance of the nitrogen tests. The specific impulse quality ($\xi_{I_{sp}}$) and discharge coefficients (C_d) are shown (including errors), since they nicely illustrate the thruster's performance. Graphs for the water tests are not included for conciseness, but these graphs would show even worse results.

Parameter	Model (MRT)	Test	Difference [%]
\dot{m} [mg/s]	19.03 ± 8.8%	13.36 ± 0.7%	-29.8
F [mN]	12.11 ± 10.3%	4.79 ± 1.7%	-60.4
ξ_F [-]	0.64 ± 2.2%	0.25 ± 2.8%	-60.4
Re_t [-]	1900 ± 9.1%	1498 ± 14.2%	-21.2
I_{sp} [s]	64.9 ± 1.7%	36.56 ± 1.8%	-43.7
$\xi_{I_{sp}}$ [-]	0.68 ± 1.9%	0.39 ± 2.0%	-42.6
C_d [-]	0.94 ± 0.3%	0.66 ± 8.8%	-29.8

Table 9.1: Comparison of the modelled and measured parameters for the nitrogen test at 300 °C and 1.0 bar (N2-10-300).

Parameter	Model (MRT)	Test	Difference [%]
\dot{m} [mg/s]	15.01 ± 9.0%	6.30 ± 10.3%	-58.0
F [mN]	12.88 ± 10.2%	4.15 ± 4.8%	-67.8
ξ_F [-]	0.67 ± 1.9%	0.22 ± 5.2%	-67.8
Re_t [-]	2106 ± 9.1%	1144 ± 21.4%	-45.7
I_{sp} [s]	87.52 ± 1.6%	67.17 ± 12.5%	-23.2
$\xi_{I_{sp}}$ [-]	0.71 ± 1.7%	0.56 ± 12.6%	-21.1
C_d [-]	0.94 ± 0.3%	0.52 ± 17.3%	-44.7

Table 9.2: Comparison of the modelled and measured parameters for the water test at 300 °C and 1.5 bar (H2O-15-300).

The differences are even worse for the water tests, as shown in Table 9.2. For these tests, the maximum deviation has grown to 68%, while the minimum deviation remains 21%. As explained in chapter 8, the water tests were not accepted. Those results deviated too much from the desired values, so it is logical that the outcome of this comparison is even worse than the nitrogen one. Although the input parameters (T_c and P_c) can be adapted to align more closely with the actual values during testing, it will not result in a major improvement. This also holds for the leak correction process described earlier. The corrected mass flow rates of Table 6.11 ($\dot{m}_{MRT,corr}$), 7.7, and 8.6 ($\dot{m}_{meas,corr}$) can be compared to each other to see if this correction brings the mass flows closer together. This is done in Table 9.3. As can be seen from the third column of this table (Difference [%]), it does not reduce the mass flow discrepancy in a significant way. The mass flow correction procedure is thus sadly not effective in closing the gap between the measured and predicted performance. Since it is a quite simplistic correction, this is not surprising.

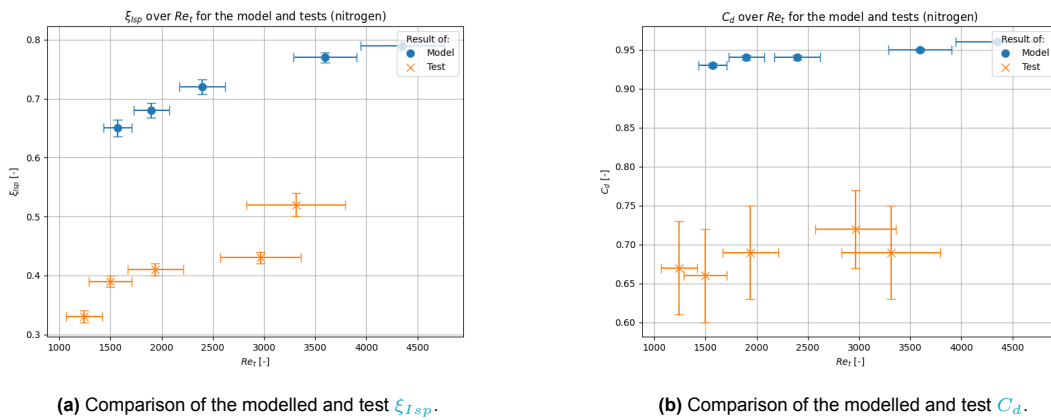


Figure 9.1: Comparison of the modelled and test performance for the different nitrogen tests.

However, the leaks described in [chapter 6](#) still have a major impact on the measured VLM performance. Their impact has already been discussed in a previous chapter ([7](#)). A leak directly affects the mass flow rate and produced thrust, and thus also impacts all quality factors. Moreover, the changing nozzle dimensions ([chapter 6](#)) and the thrust bench ([chapter 5](#)) also affect the VLM performance. The impact of these factors is not fully understood and difficult to model and is thus not incorporated in the [MRT](#). These factors widen the gap between the modelled and measured parameters. To increase the accuracy of the model's predictions, it is best to first address the problems mentioned throughout this thesis. It is difficult to pinpoint the exact cause of the degraded performance and likely originates from multiple sources. Tackling the issues of VLM-JV2 (leaks and changing nozzle shape) and performing a more extensive thrust bench calibration, are good starting points. After these issues are addressed, an attempt can be made to validate the model again. Unfortunately, the model cannot be validated in this work.

Test ID	Predicted mass flow $\dot{m}_{MRT,corr}$ [mg/s]	Measured mass flow $\dot{m}_{meas,corr}$ [mg/s]	Difference [%]
N2-10-020	22.31 ± 8.9%	14.32 ± 1.0%	-35.8 ± 9.0%
N2-10-200	18.91 ± 9.1%	13.17 ± 0.8%	-30.3 ± 9.1%
N2-15-200	29.65 ± 8.0%	21.59 ± 1.0%	-27.2 ± 8.1%
N2-10-300	17.44 ± 8.8%	11.77 ± 0.8%	-32.5 ± 8.8%
N2-10-400	16.19 ± 8.8%	11.21 ± 1.2%	-30.8 ± 8.9%
H2O-10-200	14.52 ± 8.8%	3.79 ± 39.5%	-73.9 ± 40.5%
H2O-15-300	13.56 ± 9.0%	4.85 ± 14.8%	-64.2 ± 17.4%
H2O-15-400	12.68 ± 9.0%	4.85 ± 21.5%	-61.8 ± 23.3%

Table 9.3: Comparison of the corrected mass flow rates of the model ($\dot{m}_{MRT,corr}$) and measurements ($\dot{m}_{meas,corr}$).

9.2. Verification of the test results

This section will compare the results of this work with those of others. This is done to try to verify the thrust test results of [chapter 7](#) and [8](#). A maximal difference of 15% is deemed an acceptable limit for this verification since this was also the required accuracy of the performance parameters ([AC-N2-3](#)). As discussed before, the VLM's state used for testing differed quite significantly from previous states. For example, the nozzle geometry differs substantially from the one measured by Hutten [[28](#)] (ϵ is almost 50% smaller). Moreover, the leaks discovered during preliminary testing ([chapter 6](#)) will also have a major impact on the test results. Therefore, the results obtained during this thesis will vary significantly from other works. To quantify this, the nitrogen tests will be compared to those of Versteeg [[81](#)], Hutten [[28](#)], and Cramer [[15](#)]. Only two nitrogen tests can be compared as different authors conducted different tests. Therefore, the nitrogen test at 200 ° and 1.5 bar ([N2-15-200](#)) are compared in the upcoming subsection ([subsection 9.2.1](#)). A comparison of the nitrogen tests at ambient temperature and 1.0 bar can be found in the appendix ([section B.6](#)). As only Hutten conducted tests with water, these are the only results that can be used for the verification. Therefore, the water tests at 300 °C are analysed in [subsection 9.2.2](#).

9.2.1. Nitrogen tests

Before analysing the test results, it is important to note that some of the values presented are calculated slightly differently by different works. For example, to find the N_2 mass flow in mg/s, it must first be converted using the nitrogen density. It was found that a different value has been used for this by Hutten compared to this and Cramer's work. This work uses the nitrogen density at ambient temperature (20 °C), which is found to be 1.1648 kg/m³ [[4](#)]. Hutten on the other hand uses the nitrogen density at 0 °C (1.2503 kg/m³). Seen that the temperature of the nitrogen stored in the tank is probably closer to 20 °C, Hutten's mass flow is likely an overestimation of nearly 7%. Although this will not be taken into account in the verification, it is important to be aware that assumptions like these can influence the results as well.

Table 9.4 shows the test results obtained by four different authors. Moreover, Figure 9.2 visualises the thruster behaviour by plotting the $\xi_{I_{sp}}$ and C_d . Each author used the same EDM-based VLM, although its state changes quite significantly, which can be seen by the changing nozzle dimensions. Leaks are unfortunately more difficult to identify from this table, but were known to have a significant affect on the results of this work. The operating parameters are roughly the same; T_c of approximately 200 °C and P_c of roughly 1.5 bar. By analysing the table and figures, it quickly becomes apparent that the results obtained with the VLM-JV2 are quite different to the other results. However, the results of Cramer seem to align more closely with these results. Two groups can be distinguished; Versteeg and Hutten on the one hand and Cramer and Vaes on the other hand.

Input						
Parameter	Versteeg		Hutten		Cramer	
T_c [K]	482.0	± 5.8	473.2	± 1.5	472.8	± 6.6
P_c [mbar]	1510	± 10	1498	± 50	1516	± 50
P_a [mbar]	2.16	± 0.33	8.1	± 1.60	27.12	± 4.07
A_t [$10^3 \mu m^2$]	70.6	± 4.8	75.3	± 7.0	104.4	± 15.3
A_e [$10^3 \mu m^2$]	532	± 5.1	580	± 12.9	359	± 14.0
H_t [μm]	496	± 4	538	± 8	522	± 34.3
W_t [μm]	142.3	± 9.6	140	± 11	200.1	± 16.2
ϵ [-]	7.53	± 0.49	7.70	± 0.89	3.44	± 0.64
Output						
F [mN]	12.78	± 0.08	13.73	± 0.37	8.75	± 0.17
\dot{m}_{N_2} [mg/s]	16.76	± 0.12	17.7	± 0.8	20.21	± 0.08
P_{heat} [W]	-	-	8.96	± 0.19	11.09	± 0.03
$Re_{t,real}$ [-]	2412	± 48	2183	± 367	2566	± 264
I_{sp} [s]	77.75	± 0.75	79.3	± 2.14	44.14	± 0.92
$\xi_{I_{sp}}$ [-]	0.84	± 0.01	0.86	± 0.07	0.53	± 0.03
C_d [-]	0.87	± 0.08	0.86	± 0.07	0.70	± 0.04
η_{heat} [-]	0.43	-	0.37	-	0.34	± 0.03

Table 9.4: Comparison of the results for N2-15-200 with different authors.

It was already known that the results of the first two authors closely aligned with each other, which can also clearly be seen in the figures (9.2). The improvements made in this thesis should have returned the VLM to its original state and thus bring it closer to that performance. Unfortunately, this has not been successful. Instead, the thruster's behaviour is closer to the one measured by Cramer, albeit a little bit worse. Important parameters, such as the thrust, mass flow, and discharge coefficient are quite similar. Although they do not perfectly align, as illustrated by the decreased specific impulse quality, they prove that these thrusters are comparable. For example, the measured mass flow rate is higher in this work, which can likely be attributed to the greater nozzle throat area. This also explains the higher throat Reynolds number and lower specific impulse and specific impulse quality. However, when accounting for the leaks as shown in Table 9.3, the mass flow is reduced, and the quality factors move closer towards each other. The I_{sp} increases from 36.6 s to 40.3 s, for instance. Moreover, the $\xi_{I_{sp}}$ becomes 0.47, instead of 0.43. This proves that the output of VLM-LC and VLM-JV2 is comparable. Despite this positive result, the leak correction process is not adopted for the verification, as it is deemed too speculative and cannot be verified.

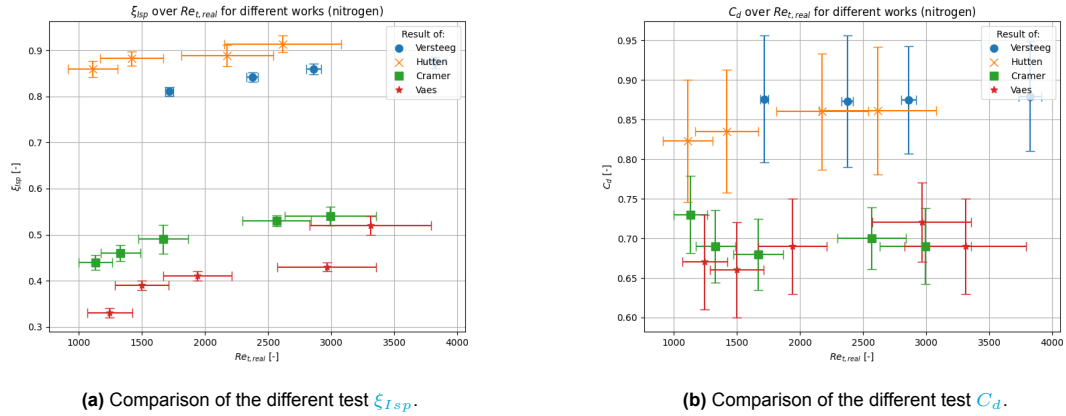


Figure 9.2: Comparison of the test performance for the nitrogen tests with different authors.

It has already been mentioned before that the problems surrounding the VLM make it hard to determine the exact cause behind the measured results. At least, these results show that performance is still quite comparable to Cramer's, despite the significant leak of VLM-JV2. This author worked with the same thrust bench (TB-50m) and also had difficulties with the nozzle geometry. Based on this verification, it seems likely that the changing of the test bench and nozzle dimensions results in a significantly different VLM performance. Because those are the main differences between the first and last two works. Although Cramer's results and the results of this work follow a similar trend, they are too far apart for verification ($> 15\%$). The conclusion to this subsection is thus similar to the conclusion of [section 9.1](#); the test results cannot be verified in this work. Based on this conclusion, it is recommended to conduct nitrogen tests using both the TB-50m and the TB-5m (pendulum test bench) that is used by Versteeg and Hutten. By constructing the tests in such a way as to keep all other factors constant, the test bench's influence on the VLM performance can be isolated. In this way, it can be determined if the test bench is responsible for the decreased performance measured by Cramer and this work. Otherwise, the different nozzle geometry of these works seems a likely origin of the lower quality factors.

9.2.2. Water tests

[Table 9.5](#) and [Figure 9.3](#) show the water test results obtained by this work and Hutten. As stated in [chapter 8](#), the tests performed in this work were not accepted. This was decided based on the established acceptance criteria ([Table 8.3](#)). The test results differed too much from the desired performance as no stable thruster operation could be achieved. As a result, the water test results can also not be verified here. Nevertheless, it is still insightful to briefly analyse and compare these results with those of Hutten.

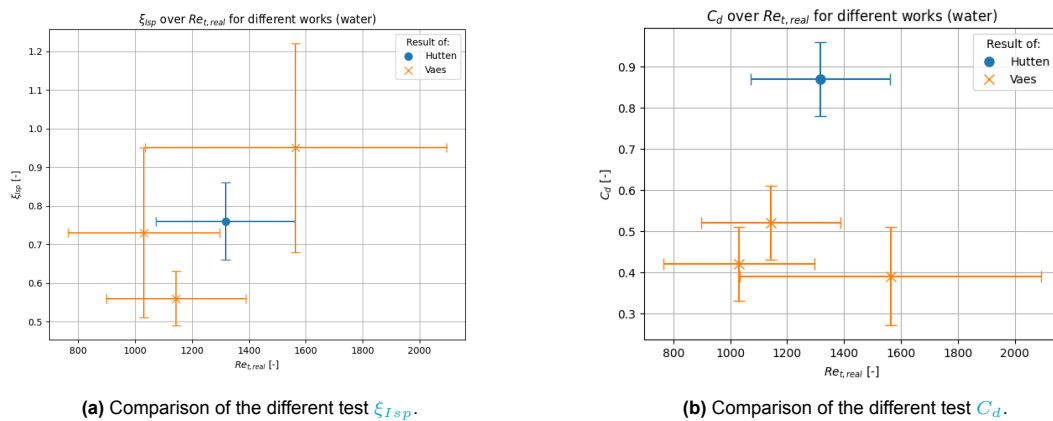


Figure 9.3: Comparison of the test performance for the water tests with different authors.

Input				
Parameter	Hutten		Vaes	
T_c [K]	573	± 3.6	552	± 8.44
P_c [mbar]	1017	± 55	744	± 81.1
P_a [mbar]	5.5	± 2.75	6.49	± 3.42
A_t [$10^3 \mu m^2$]	75.3	± 7.0	122.6	± 8.7
A_e [$10^3 \mu m^2$]	580	± 12.9	488	± 15.0
H_t [μm]	538	± 8	499	± 11.7
W_t [μm]	140	± 11	245.6	± 11.7
ϵ [-]	7.70	± 0.89	3.98	± 0.40
Output				
F [mN]	8.18	± 1.03	4.15	± 0.21
\dot{m}_{H_2O} [mg/s]	8.7	± 0.45	6.30	± 0.72
P_{heat} [W]	36.42	± 0.03	40.02	± 0.08
$Re_{t,real}$ [-]	1317	± 244	1144	± 245
I_{sp} [s]	95.2	± 13.0	67.17	± 8.40
$\xi_{I_{sp}}$ [-]	0.76	± 0.10	0.56	± 0.07
C_d [-]	0.87	± 0.09	0.52	± 0.09
η_{heat} [-]	0.71	± 0.10	0.46	± 0.10

Table 9.5: Comparison of results for H2O-15-300.

The table shows that the input parameters are all quite far apart from each other (T_c differs with more than 25%, for example). The nozzle dimensions are also significantly different, which leads to different results, as shown in the previous subsection. It is thus not surprising that the outputs are also quite different from one another. The plots shown in Figure 9.3 capture this quite well. Hutten's measurements are significantly different from the measurements of this thesis. Moreover, the accuracy of these measurements is quite low, which makes it difficult to draw reliable conclusions. The negative trend observed in the nitrogen test data, seems to persist in this data. The VLM's performance has degraded too much in comparison to Hutten's performance. Consequently, it cannot be verified based on this data. The issues discussed earlier in this, and previous chapters need to be addressed first before the test results can be verified.

10

Conclusion

This chapter will look back on the preceding chapters and extract the most important insights gained throughout the work. This is done to determine whether the original research objective, as established in [chapter 1](#), has been achieved. The research objective states the following:

To adapt the thruster and test set-up to allow for improved results using gaseous nitrogen and liquid water as propellants and to analyse the VLM performance by comparison to previous experiments.

To determine if this objective has been achieved, the research questions found in the introduction will be answered. These questions have informed the direction of this thesis and are thus essential for this work. They will be answered one by one, based on the work presented here. The next chapter ([11](#)) summarises the most important recommendations given throughout this work.

- **RQ.1:** How can the thruster be adapted to allow for improved thrust test results?

The thruster has been adapted in [chapter 3](#). The resurfacing and subsequent polishing efforts described there have led to an improved nozzle geometry, as well as an excellent leak-tightness as seen in [chapter 6](#). These improvements help in reducing uncertainties and thus leads to more accurate thrust tests. Unfortunately, as described in the same chapters, problems have also been discovered. The nozzle's dimensions worsened over time ($> 10\%$) and a major leak has been detected ($> 5\%$). Moreover, a longer replacement heater had to be used during the thrust tests, which may have been less efficient as it could not keep the chamber temperature stable during the water tests ([chapter 8](#)). These issues could not be solved during the thesis, so the final thrust test results did not improve compared to those of Cramer ([chapter 9](#)). The changing nozzle geometry and high leak rate are likely causes for the decreased VLM performance. These problems thus need to be addressed first to allow for improved thrust test results. Following this observation, it is strongly recommended to perform preliminary tests directly before and after conducting thrust tests.

- **RQ.2:** How can the experimental set-up be adapted to allow for improved thrust test results?

Several methods have been employed throughout this work to improve the experimental set-up. Small changes were made to the existing set-up, such as adapting the moment arm of the load cell and adding a bull's eye level to the test bench. Moreover, levelling bolts are used to ensure the TB-50m is level and stable ([chapter 3](#)). Furthermore, a new water feed system has been developed in the same chapter. This feed system was successful in improving the thrust test results in two ways: it eliminated bubble formation in the lines, and it could directly measure the mass flow rate with an accuracy of 5%. This has been achieved by developing a tank-based feed system capable of venting air to the environment. Moreover, the implementation of the Sensirion SLI-1000 allowed for direct liquid mass flow rate measurements, reducing its uncertainty. Unfortunately, the achieved mass flows were not stable ($\pm 25\%$), which might be attributed to a combination of leaks and an unstable chamber temperature ([chapter 8](#)).

An extensive thrust bench calibration campaign has been executed to characterise the TB-50m's influence (chapter 5). Although this calibration yielded more consistent results compared to Cramer, it still displayed erratic behaviour. Compensating for the load signal drift improved the results, which revealed that the test bench likely adds friction to the system. This friction influences the thrust measurements, and it may reduce the measured load up to 25%. More research using both the TB-50m and TB-5m is advised to draw meaningful conclusions from these findings.

- **RQ.3:** How does the VLM performance compare to that found by Versteeg [81], Hutten [28], and Cramer [15]?
 - **RQ.3a:** What is the measurement accuracy of the test results?
 - **RQ.3b:** How do the quality factors compare to those found by the previous works?

The nitrogen tests have been measured with a similar accuracy as previous works (chapter 7). All quality factors could be measured with a maximum error of 14.5%, thus satisfying the established acceptance criteria. Unfortunately, the water tests were not as successful (chapter 8). They show confidence bounds greater than 30% and were thus not accepted. Improvements must be implemented to reduce these errors to an acceptable level (preferably 15%).

As shown in chapter 9, the VLM-JV2 performance deviates significantly from that of Versteeg and Hutten. The quality factors are reduced with roughly 50% ($\xi_{I_{sp}}$) and 20% (C_d). The produced thrust is also much smaller (> 30%). As discussed before, this may be attributed to the degraded thruster state, as well as the use of a different test bench. However, the measured performance agrees much more closely with that found by Cramer ($\Delta\xi_{I_{sp}} = 19\%$ and $\Delta C_d = 3\%$). Although there are some deviations still, these can likely be explained by the mentioned issues. Despite this, the test results differed too much (> 15%) for verification. This is also the conclusion on the validation of the analytical model (> 10%).

The water tests are compared to Hutten's tests. Unfortunately, the results of this work were not accepted due to the failing of the acceptance criteria (chapter 8). The thruster failed to operate consistently within a maximum deviation of 5%. Instead, the thrust, mass flow and chamber temperature varied between 3% and 24%. Performing a valid comparison is thus challenging. Nevertheless, the same negative trend as with the nitrogen tests could be observed. It is thus important to first address the raised problems, before conducting water tests again.

The research objective stated at the beginning of this thesis, is only partially achieved. Numerous adaptations were implemented, some more successful than others. However, more work is required to obtain improved results and bring the VLM's performance closer to the one found by Versteeg and Hutten, instead of the degraded performance measured by Cramer and this work. Issues regarding the changing nozzle geometry and leaks must be addressed to realise this. Moreover, the torsional test bench (TB-50m) must be investigated more to determine its influence on the thruster's output. These and other recommendations will be provided in the final chapter (11).

11

Recommendations

In this final chapter, the most important recommendations made throughout the thesis are summarised. These should help possible successors to this work with experimenting on the EDM-based VLM. Although the lessons learned here may also be of interest to other micropropulsion-related research. To maintain an easy overview, this chapter is split in a VLM ([section 11.1](#)) and an experimental set-up section ([section 11.2](#)).

11.1. Vaporising Liquid Micro-resistojet

The first set of recommendations involve the VLM itself. It has already seen some significant changes throughout the years and has also been adapted in this work ([chapter 3](#)). Some recommendations involve minor changes, while others are more complicated. An easy improvement is the implementation of a new Watlow heater [\[82\]](#). As mentioned in the third chapter, one of these broke and could not be replaced in time. It is recommended to replace the longer, less efficient heater with a new one. This should hopefully also help in improving the (water) thrust tests. Moreover, the way the heaters are fastened to the thruster (using external threaded blocks) might be improved. It was noted during the optical characterisations and leak tests ([chapter 6](#)) that these blocks make it more difficult to perform the preliminary tests. They make it harder to picture the nozzle exit area and also make it difficult to block the nozzle with a rubber piece. By adding an internal thread to the copper blocks themselves, these external threaded blocks can be removed, simplifying the preliminary tests. The heaters can then be screwed directly into the VLM itself. This might also improve the heating efficiency a little bit as the heaters are in more contact with the thruster. This efficiency can possibly be increased further by replacing the gallium-indium-tin thermal paste [\[21\]](#) with copper grease [\[28\]](#). It has a higher thermal conductivity and may thus be better to use.

The leak discovered during the preliminary tests also needs fixing. It is thought that this leak originates from the brazed connection between the copper blocks and pressure sensing tube. This connection can be redone using the same brazing method. This is quite costly however (\sim €120). A cheaper, temporary fix is the application of a thermal sealant to stop the leak. A new *Zwaluw Fire Sealant 1200 °C* [\[8\]](#) tube can be acquired and used for this, which is quite cheap (\sim €10). Krusharev [\[36\]](#) also mentioned the use of high temperature silicon in effectively eliminating leaks. Unfortunately, this limits the chamber temperature to a maximum of 300 °C. Another option is to redesign the brazed connection entirely. Instead of a brazed connection, a screwed connection can be implemented. After adding some thread to the steel tubes and copper blocks, they can be screwed into each other, allowing for a non-permanent connection. This also helps in making the thruster more adaptable. Thermal sealant can then be added to ensure a leak-proof connection.

The other problem discovered during the preliminary tests, deals with a changing nozzle geometry. This discovery has led to the recommendation to always perform an optical characterisation and leak

test shortly before and after conducting experiments (see [Appendix D](#)). Moreover, it is recommended to measure the nozzle profile's thickness using a micrometer, before assembly. It was found that the nozzle's width increases noticeably over time, while the nozzle's exit height decreases. These two effects require individual solutions. The widening of the nozzle profile is thought to (partially) originate from misalignments due to a subpar VLM assembly. This can be attributed to the bolts used during the assembly. They do not fit the holes perfectly, allowing for some wiggle-room in the design. Using bolts with tighter tolerances, should help in aligning the VLM components better. Moreover, the addition of alignment pillars and supports on the copper blocks may help constrain the nozzle profile and prevent it from deforming. Corresponding alignment holes in the nozzle profile have to be added for this to work. If these alignment pillars can be manufactured with a high precision, they can prevent the nozzle from widening.

The reduction in nozzle exit height can be counteracted by applying the minimum required torque for leak-tightness. This can be achieved by resurfacing the copper blocks from time to time, which is quite costly (€543). Alternatively, a quick and cheap polishing and cleaning process may also help reduce leaks. Moreover, in this thesis a graphite sealing gasket has been developed and manufactured. Unfortunately, these negatively impacted the nozzle area and were thus disregarded. However, still 8 of these gaskets are left in the project's box (see [Table A.2](#)). Renewed efforts may lead to their successful implementation in the VLM. They are designed specifically to reduce leaks.

The last recommendation involving the VLM, is to investigate a full redesign of it (see [chapter 3](#)). Some of the geometry changes can be attributed to the materials used. Copper is a ductile metal and thus prone to deformations. By making the thruster body out of a less ductile material (like stainless steel), it will deform less. The nozzle profile, on the other hand, can be made out of copper. In this design, it functions as both a nozzle and a sealing gasket. Copper sealing gaskets are widely used in vacuum technologies [32, 54], so lessons can be learned from there. A drawback is that these gaskets need replacing after use, so a few need to be manufactured to allow for multiple assembly and disassembly cycles. Another challenge is once again the ductility of the copper. This feature is advantageous for its use as a gasket, but less useful for unchanging nozzle dimensions. Moreover, stainless steel has a lower thermal conductivity than copper, so more heat is required to achieve the desired chamber temperature. More research is thus advised to solve the challenges posed by this alternative design.

11.2. Experimental set-up

The second set of recommendations involve the experimental set-up used for the thrust tests. This includes the thrust bench, sensors, test procedures, etc. As described in [chapter 2](#), the test set-up has seen some major changes throughout the various iterations. Most notably, the TB-5m has been replaced for the TB-50m to eliminate the challenges encountered of a changing centre of gravity. However, as seen in this work, the TB-50m provides its own challenges. Based on the calibration and thrust test campaigns, it is suspected that the thrust bench adds unwanted friction to the system. This might be part of the reason behind the decreased thrust production. It is thus recommended to further analyse this phenomenon. For example, thrust tests can be performed using both the TB-5m and TB-50m. Since the same thruster is used, the results should be similar. If this is not the case, the problem is likely found in one of the thrust benches.

Another improvement involves the used load cell. The Futek LSB200 has been used in this work. However, its capacity (1000 mN) is quite high for the loads produced by the VLM (~ 10 mN). It is therefore recommended to order a new load cell with a smaller capacity. Such a sensor is designed for a smaller load range and should thus be more accurate. For example, the same load cell as used by Cramer can be used again (Futek LRF400), which had a capacity of 100 mN.

Furthermore, the new water feed system can be improved as well. As described in the water test procedures ([section D.3](#)), the connections for the two valves (venting and propellant) have to be switched manually. By constructing a second solenoid valve control circuit and adapting the LabVIEW software

accordingly, this process can be eliminated. Moreover, the mass flow cannot be controlled directly with the new feed system. A way to solve this is by integrating a syringe pump inside the vacuum chamber. The same syringe pump as Hutten can be used (ProSense NE-1000X2), which can be found in the cleanroom. By combining this pump with the rest of the new feed system, the mass flow can be controlled and measured more precisely. However, for this to work, the syringe pump must function inside a vacuum environment, and it must be connected to the cleanroom PC to control it from the outside. This needs to be checked first, for this solution to work.

Another, more involved, fix for the unpredictable mass flow rate, is the idea of pre-heating the water. Since the water is only heated and vaporised inside the thrust chamber, it is hard to control the thrust parameters. If the water is already heated before entering the VLM, it may lead to more stable results. This can be achieved with the addition of an immersible heater inside the propellant tank. However, the temperature is limited to 50 °C because of the Sensirion flow meter [59]. The water can also be heated via the steel propellant tube, but this might also lead to overheating of the P - T sensor (85 °C). Thus, for this idea to work, more research is advised.

Finally, a simple improvements involves the solenoid valve that controls the propellant flow. It was noticed during the tests of [chapter 8](#) that a small, unpredictable amount of water is left between the propellant valve and thruster during the off periods. As this may influence the test results slightly, it is advised to move the valve closer to the VLM, which reduces the amount of leftover water. Moreover, these tests also revealed some issues with the used PID-controller. It did not respond well and had to be activated manually to prevent further issues. It is not known where this problems come from, as it was not an issue during the nitrogen tests. It is thus advised to trace the root of this problem, before conducting water tests again.

These recommendations hopefully aid a successor in conducting successful nitrogen and water tests.

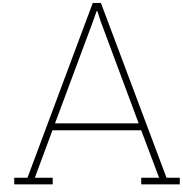
Bibliography

- [1] Alba Orbital. "The PocketQube Standard". In: *Alba Orbital, TU Delft, and Gauss Srl* (2018). Issue 1.
- [2] J. Amesz. "Conversion of Leak Flow-Rates for Various Fluids and Different Pressure Conditions". In: (1966), pp. 1–28.
- [3] R.L. Bayt. "Analysis, Fabrication and Testing of a MEMS-Based Micropropulsion System". Ph.D. Thesis. Cambridge, MA, 1999. URL: <https://dspace.mit.edu/handle/1721.1/8970>.
- [4] I.H. Bell et al. "Pure and Pseudo-pure Fluid Thermophysical Property Evaluation and the Open-Source Thermophysical Property Library CoolProp". In: *Industrial & Engineering Chemistry Research* 53.6 (2014), pp. 2498–2508. DOI: [10.1021/ie4033999](https://doi.org/10.1021/ie4033999). eprint: <http://pubs.acs.org/doi/pdf/10.1021/ie4033999>. URL: <http://pubs.acs.org/doi/abs/10.1021/ie4033999>.
- [5] J.J. Berton. "Divergence Thrust Loss Calculations for Convergent-Divergent Nozzles: Extensions to the Classical Case". In: NASA-TM-105176 (1991). URL: <https://ntrs.nasa.gov/citations/19910019867>.
- [6] R.J.F. Bijster. "Design, Verification and Validation of a Micropropulsion Trust Stand". In: *Delft University of Technology* (2014).
- [7] Bison International B.V. 6305951 - BISON KOMBI METAAL BLISTER 24 ML NL/FR. Accessed: 07-12-2024. 2024. URL: <https://www.bison.net/nl-nl/producten/bison-kombi-metaal-blister-24-ml-nlfr>.
- [8] Den Braven. *Zwaluw Fire Sealant 1200°C*. Technische Datasheet. 2024.
- [9] Brooks Instrument. *Brooks® Smart-Series Digital Mass Flow Meters and Controllers: Installation and Operation Manua*. Models 5800-S. 2008.
- [10] California Polytechnic State University. "CubeSat Design Specification, Rev 14.1". In: (2022). CP-CDS-R14.1.
- [11] W.D. Callister and D.G. Rethwisch. *Materials Science and Engineering: An Introduction*. 9th ed. Hoboken, NJ: Wiley, 2014. ISBN: 978-1-118-32457-8.
- [12] Peter Campbell. *Permanent Magnet Materials and their Application*. Cambridge University Press, 1994. ISBN: 9780511623073. DOI: <https://doi.org/10.1017/CB09780511623073>.
- [13] A. Cervone et al. "Green micro-resistojet research at Delft University of Technology: the new frontiers of Cubesat propulsion". In: *CEAS Space Journal* 9.1 (2016), pp. 111–125. DOI: [10.1007/s12567-016-0135-3](https://doi.org/10.1007/s12567-016-0135-3).
- [14] L.J.M. Cramer. "Literature Study: A study into vaporising liquid micro-resistojets". In: *Delft University of Technology* (2023).
- [15] L.J.M. Cramer. "The advancement of the Vaporising Liquid Micro-resistojet design of the TU Delft". In: *Delft University of Technology* (2024).
- [16] M. De Athayde Costa e Silva. "MEMS Micropropulsion: Design, Modeling and Control of Vaporizing Liquid Microthrusters". In: *Delft University of Technology* (2018). URL: <https://doi.org/10.4233/uuid:57f725e1-b3f3-455c-83ce-9156b2123c88>.
- [17] M. De Athayde Costa e Silva et al. "A review of MEMS micropropulsion technologies for CubeSats and PocketQubes". In: *Acta Astronautica* 143 (Feb. 2018). DOI: [10.1016/j.actaastro.2017.11.049](https://doi.org/10.1016/j.actaastro.2017.11.049).
- [18] Futek. *Model LRF400: Load Cell Tension and Compression*. Accessed: 14-05-2024. n.d. URL: <https://www.futek.com/store/load-cells/low-profile-load-cells/low-profile-LRF400>.

- [19] Futek. *Model LSB200: Low Capacity Miniature S-Beam Jr. Load Cell*. Accessed: 13-08-2024. n.d. URL: <https://www.futek.com/store/load-cells/s-beam-load-cells/miniature-s-beam-LSB200/FSH03870>.
- [20] C.S. Ganani. "Micronozzle performance: a numerical and experimental study". In: *Delft University of Technology* (2019). URL: <http://resolver.tudelft.nl/uuid:94162987-534c-4912-ac68-55b26df20585>.
- [21] Geratherm Medical AG. *Safety Data Sheet acc. to Guideline 93/112/EC*. Accessed: 22-11-2024. 2004. URL: <https://web.archive.org/web/20130923003113/http://www.rgmd.com/msds/msds.pdf>.
- [22] E.K.A. Gill. *Generating, evaluating and selecting concepts*. AE4-S12: Space Systems Engineering. 2021.
- [23] D.A.M.D. Gomes. "Development and Testing of a Thermal Propulsion Laboratory Model Development and Testing of a Thermal Propulsion". In: *Delft University of Technology* (2024).
- [24] Grifon. *PTFE-TAPE DIN-EN*. Technical Datasheet. 2024.
- [25] S.P. Grisnik, T.A. Smith, and L.E. Saltz. "Experimental Study of Low Reynolds Number Nozzles". In: AIAA-87-0992 (1987).
- [26] D.C. Guerrieri et al. "Selection and Characterization of Green Propellants for Micro-Resistojets". In: *Journal of Heat Transfer* 139.10 (May 2017), p. 102001. ISSN: 0022-1481. DOI: 10.1115/1.4036619. eprint: https://asmedigitalcollection.asme.org/heattransfer/article-pdf/139/10/102001/6216591/ht_139_10_102001.pdf. URL: <https://doi.org/10.1115/1.4036619>.
- [27] Heraeus - Thermo. *Vacuum Drying Oven: VT 6060 M / VT 6130 M*. 5003393. 2005.
- [28] R. Hutten. "Vaporizing Liquid Micro-resistojet experimentation". In: *Delft University of Technology* (2021). URL: <http://resolver.tudelft.nl/uuid:960550ce-eb34-4f3d-873a-1f2a6f4763f0>.
- [29] E.H.W. Jansen. "Improvement and validation of test stand performance for novel micropropulsion systems". In: *Delft University of Technology* (2016). URL: <http://resolver.tudelft.nl/uuid:28f0b7fa-1288-4e32-88fd-2e138745714a>.
- [30] S. Janssens. "Design of a micro propulsion test bench". In: *Delft University of Technology* (2009).
- [31] A.N. Johnson et al. "Numerical Characterization of the Discharge Coefficient in Critical Nozzles". In: *Proceedings of the 1998 NCSL Workshop & Symposium*. 1998, pp. 407–418. URL: https://tsapps.nist.gov/publication/get_pdf.cfm?pub_id=830599.
- [32] K. Jousten, ed. *Handbook of Vacuum Technology*. 2nd ed. Weinheim, Germany: Wiley-VCH, 2016. ISBN: 978-3-527-41338-6. DOI: 10.1002/9783527688265. URL: <https://onlinelibrary.wiley.com/doi/book/10.1002/9783527688265>.
- [33] Keyence. *Confocale 3D-laserscanmicroscop: VK-X-reeks*. 2018.
- [34] Keyence. *Instant 3D Profielmeter: VR-reeks*. 2018.
- [35] L. Kirkup and R. B. Frenkel. *An Introduction to Uncertainty in Measurement: Using the GUM (Guide to the Expression of Uncertainty in Measurement)*. Cambridge University Press, 2006. DOI: <https://doi.org/10.1017/CB09780511755538>.
- [36] I. Krusharev. "Micro-Thruster Development: Propulsion System for the DelFFi Mission". In: *Delft University of Technology* (2015). URL: <http://repository.tudelft.nl/>.
- [37] E. Kulu. "Nanosats Database". In: *Nanosats Database* (2024). Accessed: 29-10-2024. URL: www.nanosats.eu.
- [38] N.M. Kuluva and G.A. Hosack. "Supersonic Nozzle Discharge Coefficients at Low Reynolds Numbers". In: *AIAA Journal* 9.9 (1971), pp. 1876–1879.
- [39] F. La Torre. "Gas flow in miniaturized nozzles for micro-thrusters". PhD thesis. 2011. URL: <http://repository.tudelft.nl/record/uuid:176902dc-7234-414c-af5b-87ef11ec6dc1>.

- [40] V. Lindberg. "Uncertainties and Error Propagation: Part I of a manual on Uncertainties, Graphing, and the Vernier Caliper". In: *Louisiana State University, Department of Geology & Geophysics* (2000). URL: <https://www.geol.lsu.edu/jlorenzo/geophysics/uncertainties/Uncertaintiespart2.html>.
- [41] Linstrom, P.J. and Mallard, W.G. "NIST Chemistry WebBook, SRD 69". In: (2023). DOI: [10.18434/T4D303](https://doi.org/10.18434/T4D303). URL: <https://doi.org/10.18434/T4D303>.
- [42] R.A. Makhan. "Performance of the MEMS Vaporizing Liquid Microthruster using cold nitrogen gas as propellant An experimental study". In: (2018).
- [43] S. Miller et al. "Survey and Performance Evaluation of Small-Satellite Propulsion Technologies". In: *Journal of Spacecraft and Rockets* 58.1 (2021), pp. 222–231. DOI: [10.2514/1.A34774](https://doi.org/10.2514/1.A34774).
- [44] MKS Instruments. *CF Component: Ultra High Vacuum Fittings*. 2023. URL: <http://www.mks.com/>.
- [45] J. Mueller. "Thruster options for microspacecraft: A review and evaluation of existing hardware and emerging technologies". In: *Jet Propulsion Laboratory* (1997). DOI: [10.2514/6.1997-3058](https://doi.org/10.2514/6.1997-3058). URL: <https://arc.aiaa.org/doi/abs/10.2514/6.1997-3058>.
- [46] Parker Legris & Nycoil. *Catalog 3500LEG/NYC*. 2024.
- [47] Oerlikon Metco. *An Introduction to Brazing*. 4th ed. 2014. URL: <http://www.oerlikon.com/metco>.
- [48] A. Pappadimitriou. "Performance Evaluation of a Vaporizing Liquid Microthruster using nitrogen and water as propellants". In: *Delft University of Technology* (2021). URL: <http://repository.tudelft.nl/>.
- [49] K.I. Parker. "State-of-the-Art for Small Satellite Propulsion Systems". In: *NASA/Goddard Space Flight Center* (2016). URL: <https://ntrs.nasa.gov/citations/20160010571>.
- [50] A. Pârvulescu. "Experimental Study and Test Preparation for New Generation MEMS Vaporising Liquid Microthrusters". In: *Delft University of Technology* (2024). URL: [url%20=%20%7Bhttp://repository.tudelft.nl/%7D,](http://repository.tudelft.nl/).
- [51] Pfeiffer Vacuum. *Water vapor tolerance / water vapor capacity*. Accessed: 18-11-2024. 2024. URL: <https://know-how-book.pfeiffer-vacuum.com/en/>.
- [52] J.E. Polk et al. "Recommended Practices in Thrust Measurements". In: *IEPC-2013-440*. Washington, DC, 2013. URL: https://hpepl.ae.gatech.edu/papers/2013_IEPC_Polk.pdf.
- [53] J. Puig-Suari, C. Turner, and R.J. Twiggs. "CubeSat: The Development and Launch Support Infrastructure for Eighteen Different Satellite Customers on One Launch". In: (1999). California Polytechnic State University and Stanford University.
- [54] A. Roth. *Vacuum Sealing Techniques*. 1st ed. Pergamon Press, 1966.
- [55] H. Rottländer, W. Umraht, and G. Voss. "Fundamentals of leak detection". In: *Leybold* 199 (2016), pp. 1–9. URL: www.leybold.com.
- [56] A. Savitzky and M.J.E. Golay. "Smoothing and Differentiation of Data by Simplified Least Squares Procedures". In: *Analytical Chemistry* 36.8 (1964), pp. 1627–1639. ISSN: 15206882. DOI: [10.1021/ac60214a047](https://doi.org/10.1021/ac60214a047).
- [57] Scaime. *CPJ - CPJ2S: Notice d'utilisation*. NU-CPJ-FE-1106. n.d. URL: <https://scaime.com/product/post/cpj---cpj2s>.
- [58] Sensirion AG. *Application Note for Liquid Flow Sensors: Analog Cable Configurator*. Version 1, April 2017. 2017. URL: <https://www.sensirion.com>.
- [59] Sensirion AG. *SLI Liquid Flow Meter Series*. Version 13, January 2020. 2020. URL: <https://www.sensirion.com>.
- [60] SGL Carbon GmbH. *SIGRAFLEX®: Flexible graphite foil for industrial sealing [metric]*. 2019. URL: <https://www.sigraflex.com/downloads/>.
- [61] S. Silvestrini. "Closed-loop Thrust Magnitude Control System for Nano- and Pico-Satellite Applications". In: *Delft University of Technology* (2017). URL: <http://repository.tudelft.nl/>.

- [62] S. Singh. "Design, Fabrication and Characterization of MEMS Micro-resistojet Thrusters". In: *Delft University of Technology* (2023). URL: <http://resolver.tudelft.nl/uuid:103b1edc-c3d4-4a44-9309-f9748fe9eace>.
- [63] E.W. Spisz, P.F. Brinich, and J.R. Jack. "Thrust Coefficients of Low-Thrust Nozzles". In: NASA TN D-3056 (1965). URL: <https://ntrs.nasa.gov/api/citations/19650027295/downloads/19650027295.pdf>.
- [64] P.E.P. Stohr. "CICR: The characterization and design of a CubeSat Integrated COTS Resistojet thruster". In: *Delft University of Technology* (2016). URL: <http://repository.tudelft.nl/>.
- [65] G.P. Sutton and O. Biblarz. *Rocket Propulsion Elements*. 7th. John Wiley & Sons, 2001. ISBN: 978-81-265-2577-5.
- [66] Swagelok. *Quick-Connects: QC, QF, QM, and QTM Series*. MS-01-138. 2022.
- [67] Swagelok. *Sample Cylinders, Accessories, and Outage Tubes*. MS-01-177. 2024.
- [68] M.N. Sweeting. "Modern Small Satellites-Changing the Economics of Space". In: *Proceedings of the IEEE* 106.3 (2018), pp. 343–361. DOI: [10.1109/JPROC.2018.2806218](https://doi.org/10.1109/JPROC.2018.2806218).
- [69] A. Takken. "Development of a high temperature Solar Thermal Propulsion engine". In: *Delft University of Technology* (2021). URL: <http://repository.tudelft.nl/>.
- [70] S.P. Tang and J.B. Fenn. "Experimental Determination of the Discharge Coefficients for Critical Flow through an Axisymmetric Nozzle". In: *AIAA Journal* 16.1 (1978), pp. 41–46.
- [71] TE Connectivity. *MS5837-30BA: Ultra Small Gel Filled Pressure Sensor*. 2015. URL: <https://www.te.com/en/product-CAT-BLPS0017.html>.
- [72] G.A. Teixeira. "Performance Evaluation of a MEMS-based Low Pressure Micro-Resistojet (LPM)". In: *Delft University of Technology* (2024). URL: [url%20=%20%7Bhttp://repository.tudelft.nl/%7D,](http://repository.tudelft.nl/%7D).
- [73] The Engineering Toolbox. *Moist Air - Relative Humidity*. Accessed: 18-11-2024. 2004. URL: https://www.engineeringtoolbox.com/relative-humidity-air-d_687.html.
- [74] The Engineering Toolbox. *Thermal Expansion - Linear Expansion Coefficients*. Accessed: 27-10-2024. 2003. URL: https://www.engineeringtoolbox.com/linear-expansion-coefficients-d_95.html.
- [75] The Lee Company. "9th Edition Electro-Fluidic Systems Handbook". In: *Electro-Fluidic Systems Division* (2019). URL: <https://www.theleeco.com/insights/9th-edition-electro-fluidic-systems-handbook/>.
- [76] TME. *KA02 Fine Wire (Fibre Glass) Thermocouple Sensor Type 'K'*. Accessed: 21-11-2024. URL: <https://www.farnell.com/datasheets/1718911.pdf>.
- [77] Mettler Toledo. *Operating instructions METTLER TOLEDO AG balances*. 11780182D. 2004.
- [78] Vacuubrand. *Accessories for Rotary vane pumps: Instructions for assembly*. 20999002. 2023.
- [79] Vacuubrand. *Pressure transducer*. 20901073. 2023. URL: <https://shop.vacuubrand.com/en/vacuum-sensor-vsp-3000-20636163.html>.
- [80] Vacuubrand. *Rotary vane pumps: Instructions for use*. 20901073. 2019.
- [81] H.S.E. Versteeg. "Novel fabrication method for a hot gas supersonic micro-thruster". In: *Delft University of Technology* (2020). URL: <http://resolver.tudelft.nl/uuid:ac2482ad-0f8e-4569-8bd4-fd11bd6327bd>.
- [82] Watlow. *1/8-Inch FIREROD® Cartridge Heaters*. STL-1-8FR-1116. 2016.
- [83] S. Weisberg. *Applied Linear Regression*. 4th ed. Hoboken, NJ: John Wiley & Sons, 2014. ISBN: 978-1-118-38608-8.
- [84] A.J. Wilson. "Vacuum Degasification of Water". In: (1979).
- [85] B.T.C. Zandbergen. *Thermal Rocket Propulsion*. 2.09. 2022.



Experimental Set-up

This appendix provides an overview of the experimental set-up used in this work. It details the equipment that is used (section A.1), as well as the components left in the project's box (section A.2). These components can be used by possible successors and are found in the box marked with the author's name. This box is located in the cleanroom workshop. section A.3 shows an overview of the feed systems used for this thesis. The final section (A.4) shows the electrical diagram used for connecting the various electronics to the experimental set-up.

A.1. Equipment overview

Sensors	Function
Brooks 5850S [9]	Measures the (gaseous) mass flow. Can also be used to control the mass flow.
Futek LSB200 [19]	Measures the load applied to the sensor. Used to measure the thrust.
K-Type Thermocouple [76]	Measures the temperature at its outer end. Primarily used to measure the chamber temperature.
Mettler Toledo AG245	Scale used to verify the masses used for the load cell calibration.
Sensirion SLI-1000 [59]	Measures the liquid (water) mass flow.
TE Connectivity MS5837-30BA [71]	Measures the chamber pressure and the temperature of the interface (P - T sensor).
VACUUBRAND VSP 3000 [79]	Measures the pressure inside the vacuum chamber.
Actuators	Function
The Lee Company Solenoid Valve (The Lee Company, 2024)	Controls the supply of propellant to the heating chamber.
Vacuubrand RZ 6 [80]	Generates a vacuum in the vacuum chamber.
Varying Turn-Density Coil [6]	Generates a known force, which is used for thrust bench calibration.
Watlow $\frac{1}{8}$ -Inch FIREROD® Cartridge Heaters [82]	Generates heat to heat the thrust chamber.
Watlow 24V C1J-9769 30W [82]	Replacement heater used during later tests (3.1.3).

Data Acquisition Devices	Function
NI USB-8451	Reads the MS5837-30BA P - T sensor data.
NI USB-6008	Powers the MS5837-30BA P - T sensor (2.5V).
NI USB-6008	Reads the LSB200 data.
NI PCI-6229	Interfaces with both CB-68LP breakout boards.
NI-9211	Reads the thermocouple data.
Scaime CPJ [57]	Amplifies the LSB200 signal.
VACUUBRAND DCP 3000 [79]	Reads the VACUUBRAND VSP 3000 data.
Power supplies	Function
Delta Elektronika D-030-10	Power supply for the hold driver.
Delta Elektronika E-030-10	Power supply for the spike driver.
Delta Elektronika ES-030-10	Power supply for one of the two heating elements.
Delta Elektronika SM-7020	Power supply for one of the two heating elements.
Delta Elektronika SM-7020-D	Power supply for the VTDC.

Table A.1: Overview of the various components that contribute to the experimental set-up.

A.2. Component inventory

Sensors	Quantity	Description
Futek LSB200 [19]	1	Measures the load applied to the sensor. Used to measure the thrust.
K-Type Thermocouple [76]	1	Measures the temperature at its outer end.
K-Type Thermocouple (broken, [76])	2	Broken K-Type thermocouples.
K-Type Connector [76]	2	Connects a K-Type thermocouple to a data acquisition device.
J-Type Connector [76]	2	Connects a J-Type thermocouple to a data acquisition device.
TE Connectivity MS5837-30BA [71]	5	Measures the chamber pressure and the temperature of the interface (P - T sensor).
TE Connectivity MS5837-30BA (integrated, [71])	1	Integrated P - T sensor with MINSTAC tubing.
Actuators	Quantity	Description
Solenoid Valve (24 V) (The Lee Company, 2024)	2	Controls the supply of propellant to the heating chamber.
Watlow $\frac{1}{8}$ -inch FIREROD® Cartridge Heaters [82]	2	Generate heat to heat the thrust chamber.
Watlow $\frac{1}{8}$ -inch FIREROD® Cartridge Heaters (Broken, [82])	4	Broken heaters.
Consumables	Quantity	Description
BISON Kombi Metaal [81]	24 mL	Glue used to attach the P - T sensor to the aluminum interface.
LVM-700-30-GIS-PST Liquid Metal-Paste [21]	50g	Used as conductor between the heaters and the VLM.

Osborn unipol metal polish [81]	125 mL	Used to polish the VLM.
Miscellaneous	Quantity	Description
Rubbers	1	Used to block the nozzle during leak tests.
Syringe (10 mL, [28])	1	Used to insert water in the tank.
Aluminum interface Versteeg	1	Interface used by Versteeg and Hutten that connects the VLM to the pendulum test bench
MINSTAC components [75]	N/A	Several MINSTAC components used for the feed system.
Tube cutter [81]	1	Used to cut tubes to a certain length.
Metal foam [81]	1	Used as heat exchanger.
Wagner sealing gaskets [60]	8	Used to help reduce leaking.
Nuts & bolts	N/A	Variety of nuts and bolts used for connecting various components.
Paper basket	1	Used to contain various weights.
Low friction pulley	1	Used to translate a vertical force into a horizontal force.
LEGO construction [81]	1	Used to clamp the nozzle profile under a certain angle.
Aluminium foil [81]	1	Used as spacer by Versteeg.
Aluminium plate	1	N/A
Steel plate	1	N/A
Nozzle profile (1 mm, [81])	2	Nozzle profile not used during testing.
Nozzle profile (0.5 mm, [81])	1	Old nozzle profile used during testing by Versteeg
Tube holder [81]	1	3D printed tube holder used during assembly of the VLM.

Table A.2: Inventory of the project's designated box. This excludes the equipment used during testing. Note that this list is not complete and subject to changes. The box is marked with the author's name and situated in the cleanroom workshop.

A.3. Feed systems

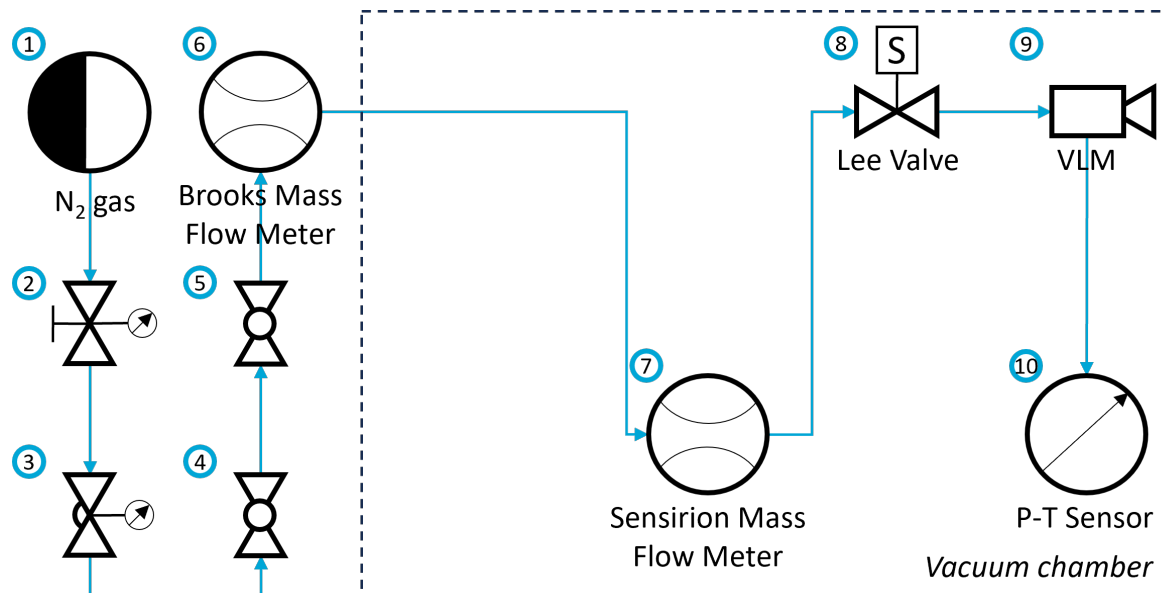


Figure A.1: The nitrogen feed system used during the final nitrogen test campaign.

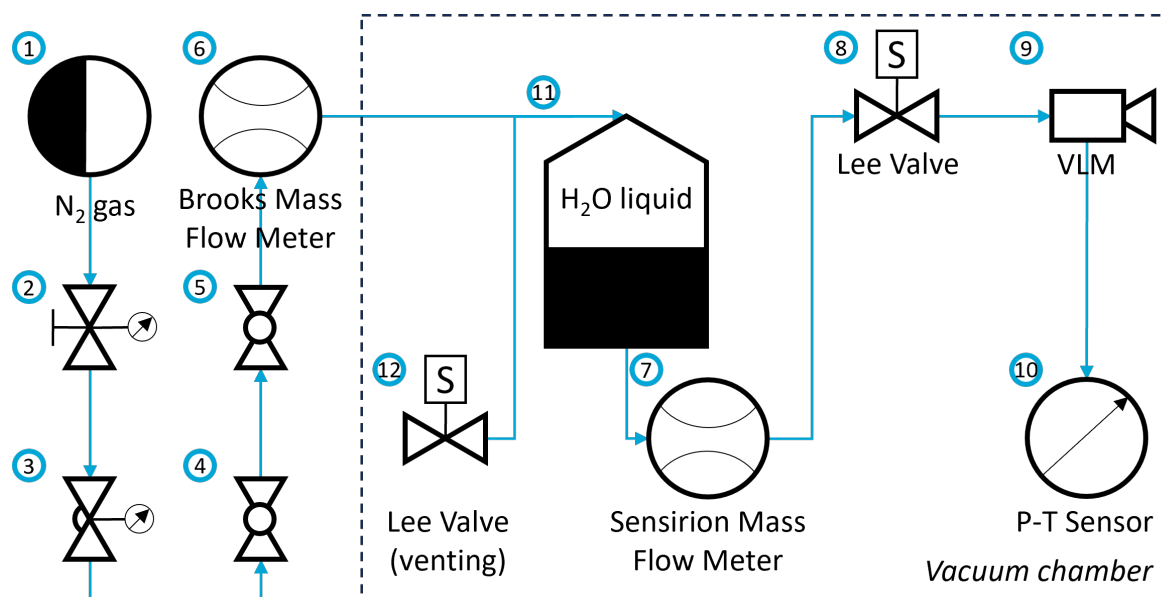
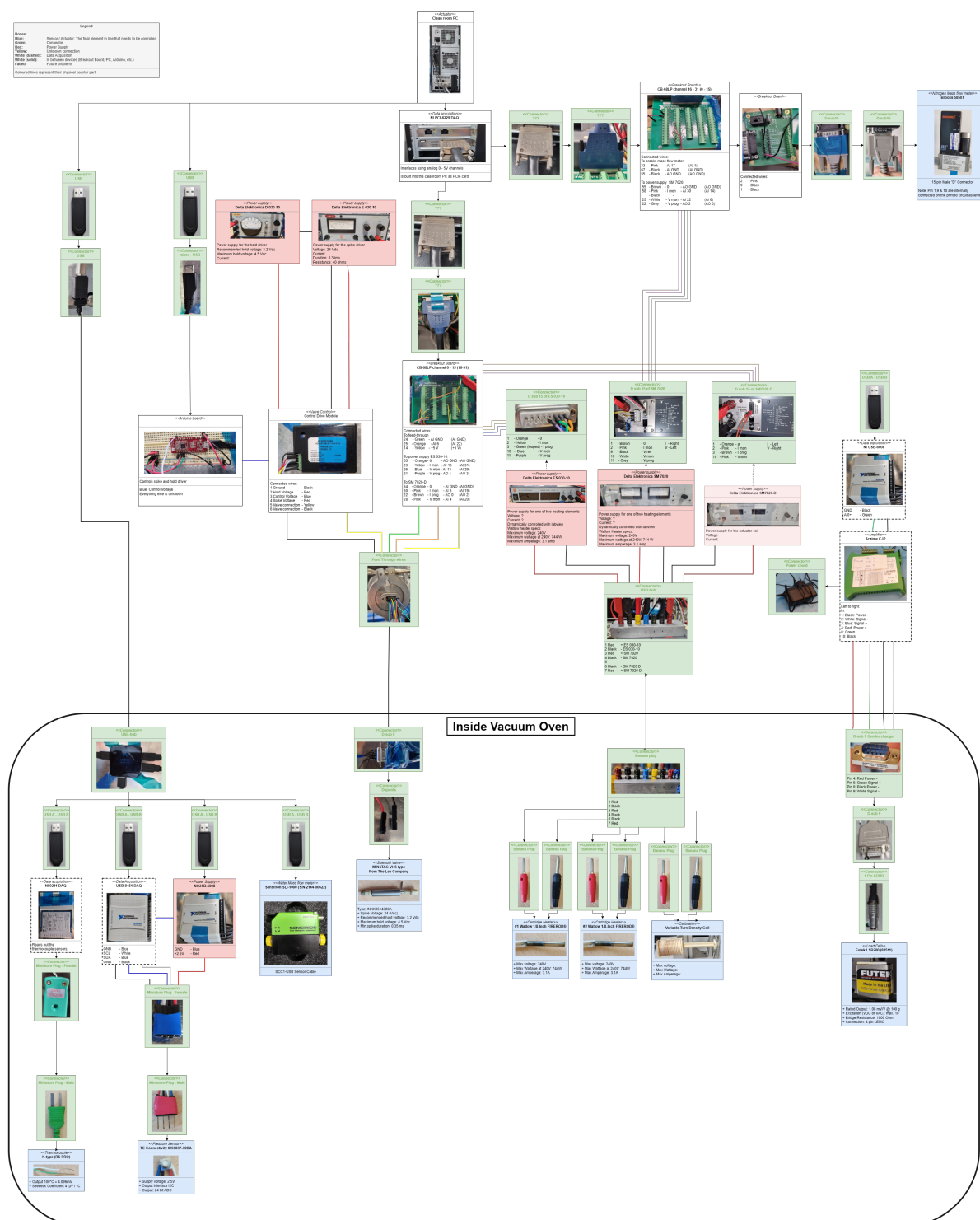


Figure A.2: The water feed system used during the final water test campaign.

A.4. Electrical Diagram

Author: L.J.M. Cramer
Modified by: J.J.A. Vaes
Version: 1.2
Date: 29-11-2024



B

Test Data

This appendix includes all data acquired throughout this work and is structured in a similar manner.

B.1. Calibrations

This section shows the results of the TB-50m thrust bench calibration campaign, which is described extensively in [chapter 5](#). Six different calibration tests were performed that are repeated three times each. The most insightful graphs of this calibration campaign are shown here.

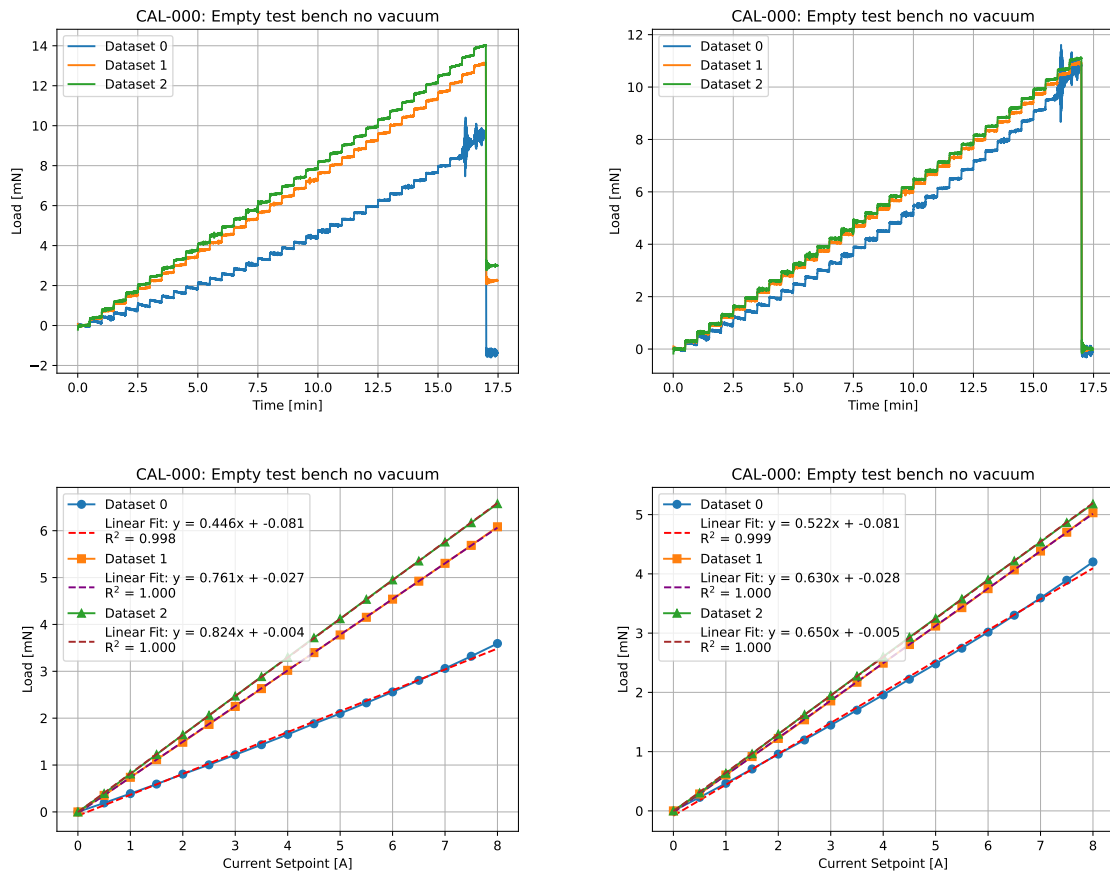


Figure B.1: Results of the TB-50m thrust bench calibrations with an empty test bench (CAL-000). The left graphs show the original loads, while the right graphs show the loads with drift compensation.

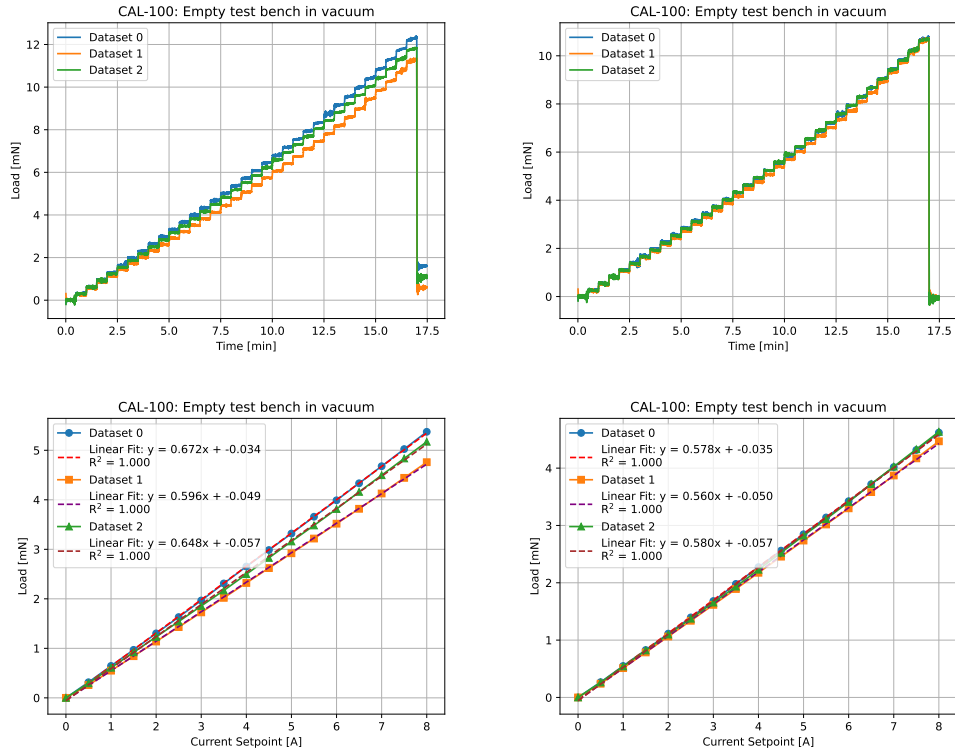


Figure B.2: Results of the TB-50m thrust bench calibrations in vacuum and with an empty test bench (CAL-100). The left graphs show the original loads, while the right graphs show the loads with drift compensation.

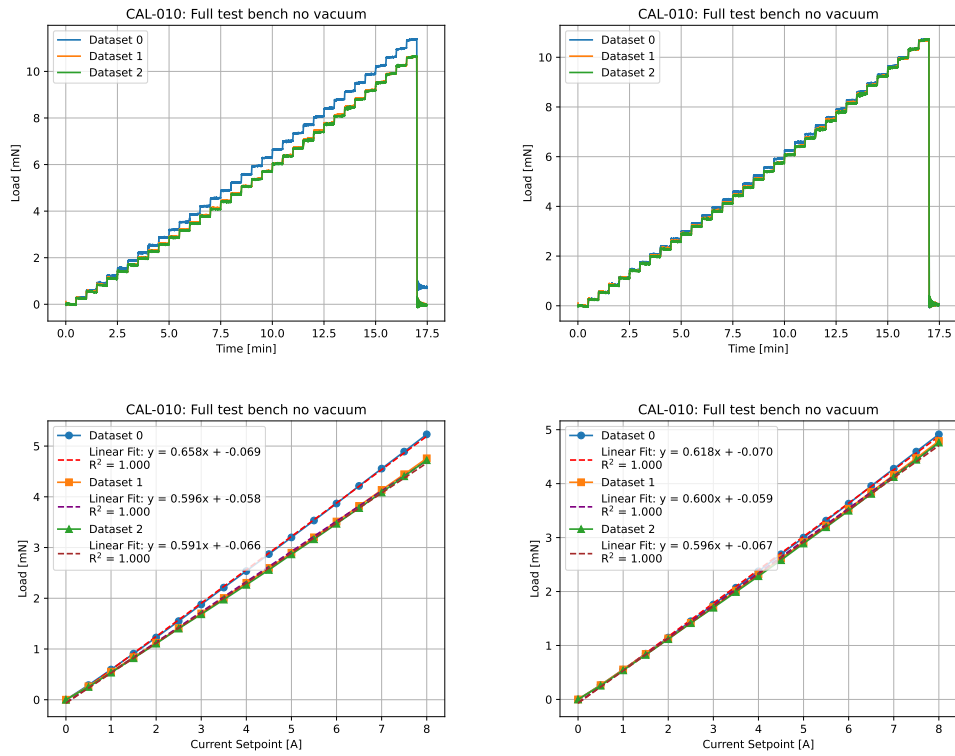


Figure B.3: Results of the TB-50m thrust bench calibrations with a full test bench (CAL-010). The left graphs show the original loads, while the right graphs show the loads with drift compensation.

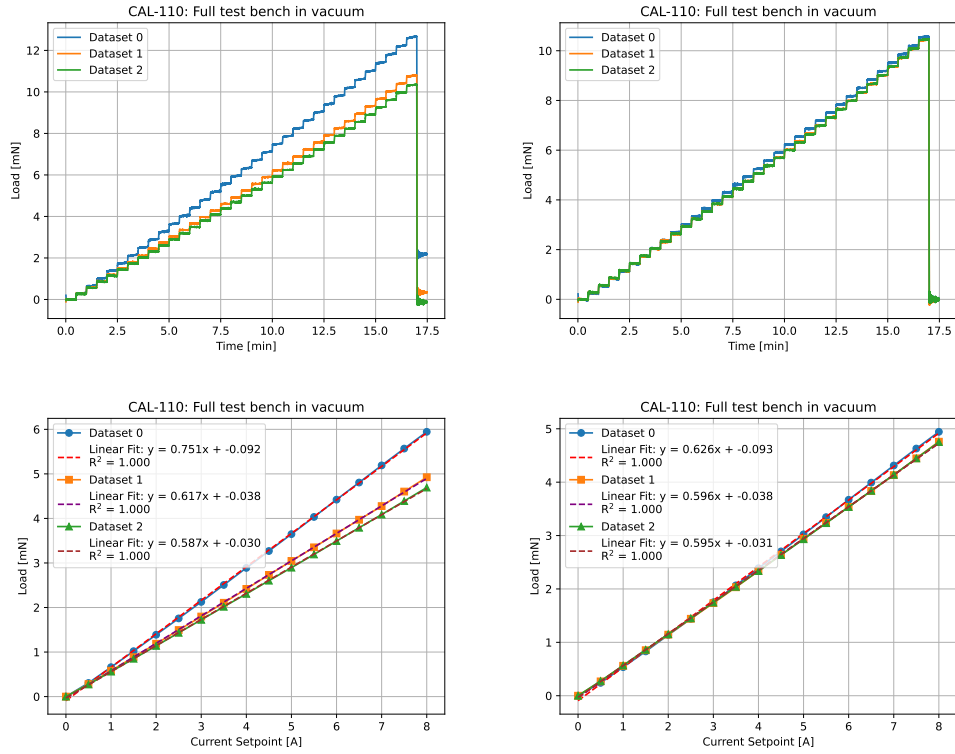


Figure B.4: Results of the TB-50m thrust bench calibrations in vacuum and with a full test bench (CAL-110). The left graphs show the original loads, while the right graphs show the loads with drift compensation.

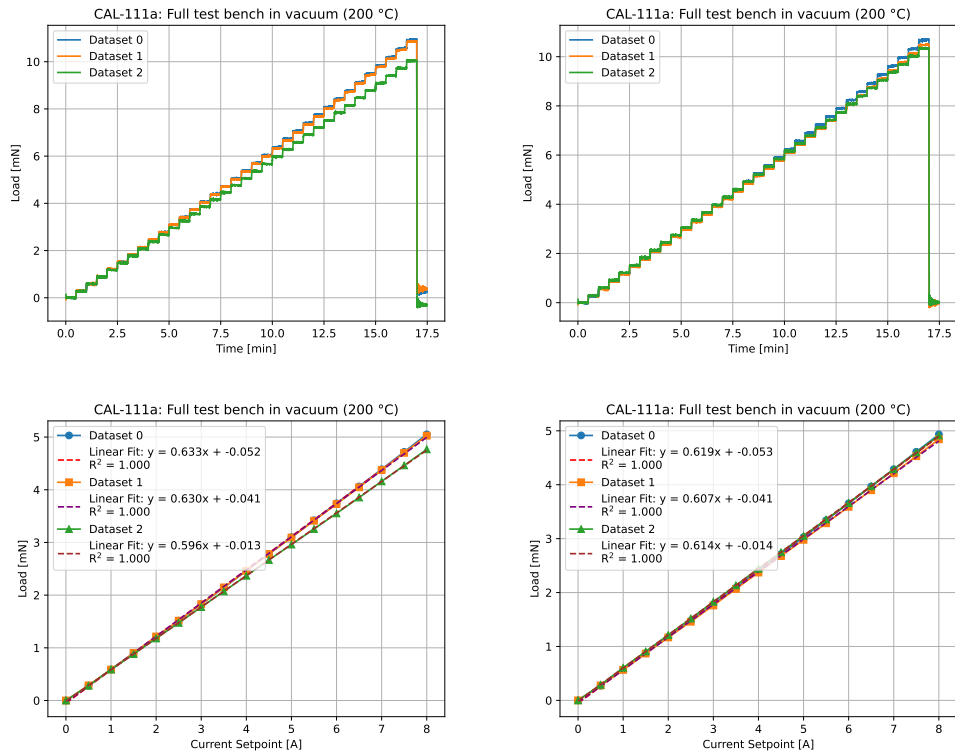


Figure B.5: Results of the TB-50m thrust bench calibrations in vacuum and with a full test bench at 200 °C (CAL-111a). The left graphs show the original loads, while the right graphs show the loads with drift compensation.

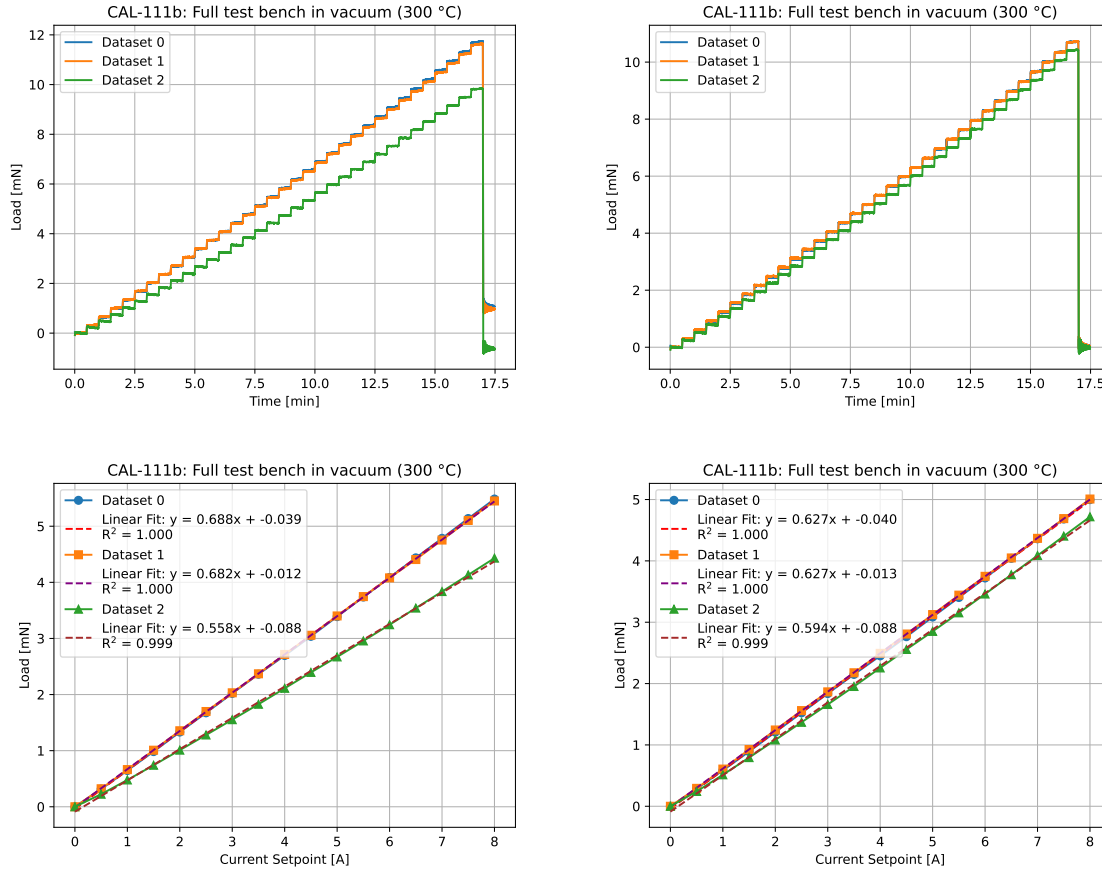


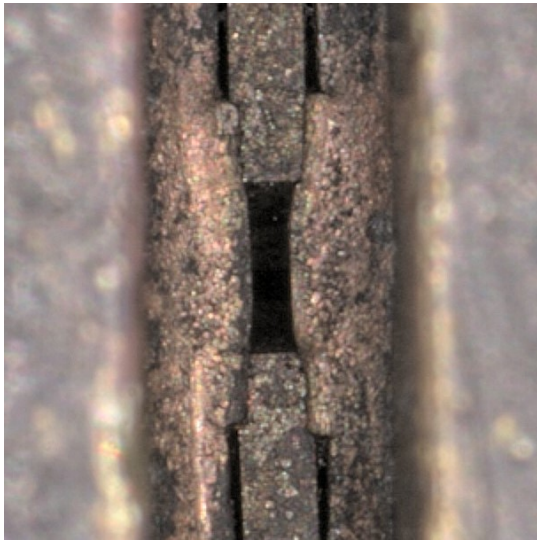
Figure B.6: Results of the TB-50m thrust bench calibrations in vacuum and with a full test bench at 300 °C (CAL-111b). The left graphs show the original loads, while the right graphs show the loads with drift compensation.

B.2. Optical Characterisation

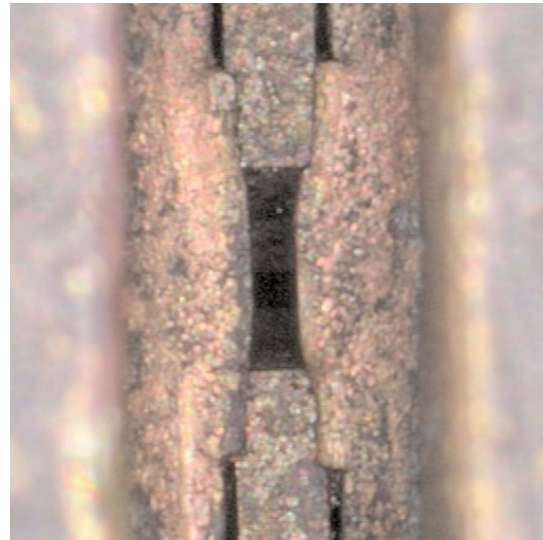
This section summarises the optical characterisations that have been performed for this and previous theses (see Table B.1 and Figure B.7). The process of measuring the nozzle parameters has been described extensively in chapter 6. A discussion of the found results is also provided in this chapter. As proven by this work, the nozzle's dimensions are subject to changes and should thus always be measured directly before and after propellant tests (see also Appendix D). As described in chapter 11 of this work, more structural changes are required to counteract these dimensions changes.

Parameter	Design	VLM-HV2	VLM-RH	VLM-LC	VLM-LC2	VLM-JV1	VLM-JV2
H_t [μm]	500	496 \pm 4	538 \pm 8	522 \pm 34.3	499.1 \pm 11.7	499.1 \pm 11.7	499.1 \pm 11.7
W_t [μm]	130	142.3 \pm 9.6	140 \pm 11	200.1 \pm 16.2	213.9 \pm 11.7	232.8 \pm 11.7	245.6 \pm 11.7
A_t [$10^3 \mu m^2$]	65	70.6 \pm 5.3	75.3 \pm 7.0	104.5 \pm 15.3	106.8 \pm 8.3	116.2 \pm 8.6	122.6 \pm 8.7
H_e [μm]	500	496 \pm 4	538 \pm 8	315.6 \pm 10.8	256.2 \pm 11.7	471.9 \pm 11.7	408.7 \pm 11.7
W_e [μm]	1072.5	1071.9 \pm 5.6	1078 \pm 8	1138.1 \pm 5.4	1145.5 \pm 11.7	1179.1 \pm 11.7	1189.8 \pm 11.7
A_e [$10^3 \mu m^2$]	536	531 \pm 7.1	580.0 \pm 12.9	359 \pm 14.0	331.1 \pm 15.0	555.2 \pm 10.0	487.8 \pm 15.0
A_e/A_t (ϵ) [-]	8.25	7.53 \pm 0.67	7.70 \pm 0.89	3.44 \pm 0.64	3.10 \pm 0.38	4.78 \pm 0.44	3.98 \pm 0.40

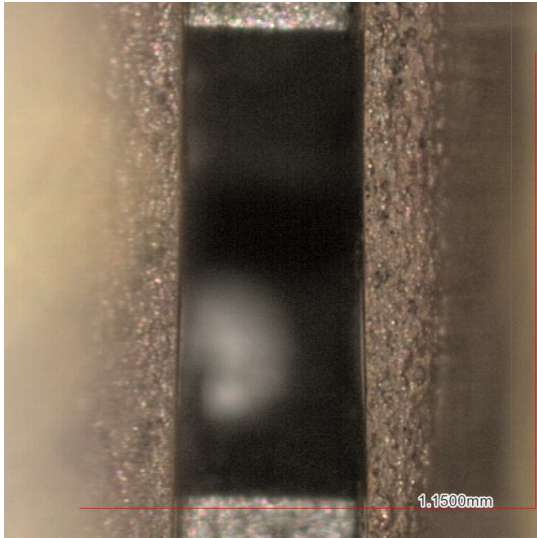
Table B.1: Total overview of the measured nozzle parameters of the Vaporising Liquid Micro-resistojet.



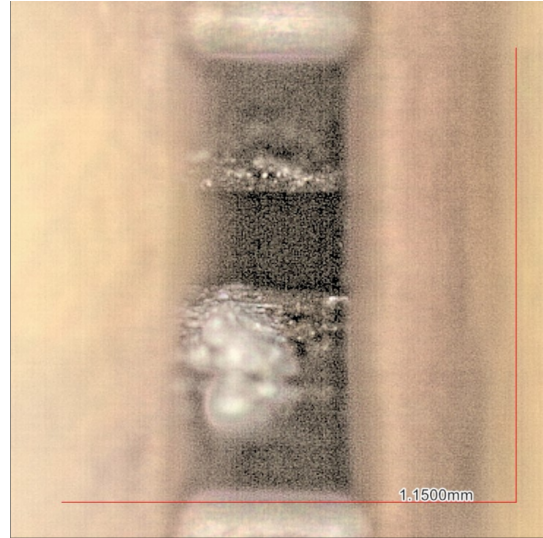
(a) The VLM nozzle exit area (A_e), before improvements (VLM-LC2).



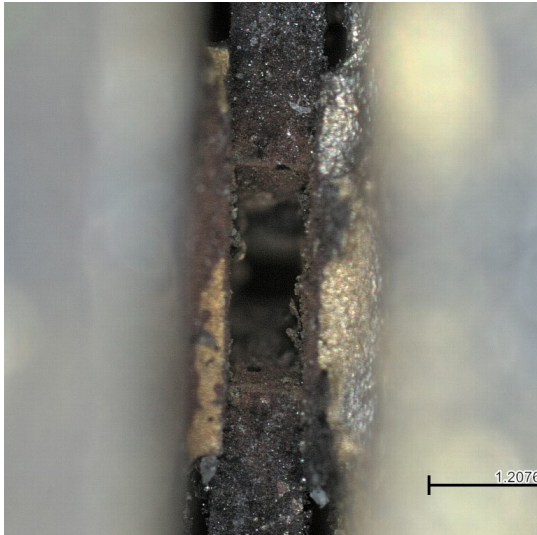
(b) The VLM nozzle exit area (A_e), before improvements (VLM-LC2).



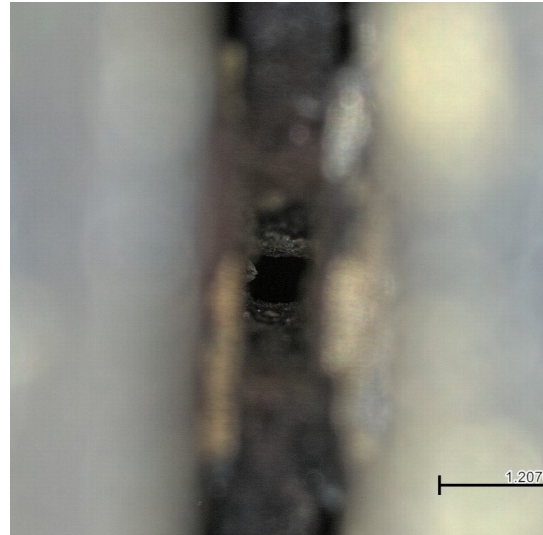
(c) The VLM nozzle exit area (A_e), after improvements (VLM-JV1).



(d) The VLM nozzle throat area (A_t), after improvements (VLM-JV1).



(e) The VLM nozzle exit area (A_e), after testing (VLM-JV2).



(f) The VLM nozzle throat area (A_t), after testing (VLM-JV2).

Figure B.7: Total overview of the measured nozzle parameters of the Vaporising Liquid Micro-resistojet.

B.3. Leak Tests

This section summarises the leak tests that have been performed for this and previous theses (see Table B.2 and Figure B.8 and B.9). The process of measuring the leak rate has been described extensively in chapter 6. A discussion of the found results is also provided in this chapter. Unfortunately, the final leak rate (VLM-JV2) exceeds the established limit of 5%, resulting in a significant performance reduction. This shows the important of measuring the leak rate directly before and after propellant tests (see also Appendix D). Major leaks like this should be addressed first, before commencing nitrogen and water tests.

Parameter	VLM-HV2	VLM-RH	VLM-LC	VLM-LC2	VLM-JV0	VLM-JV1	VLM-JV2
\dot{m}_L [mg/s]	0.122	0.240	0.223	0.681	0.345	0.032	4.93
\dot{m}_L/\dot{m}_{tot} [%]	0.70	1.37	1.27	3.89	1.97	0.18	28.16

Table B.2: Total overview of the measured leak rates of the Vaporising Liquid Micro-resistojet.

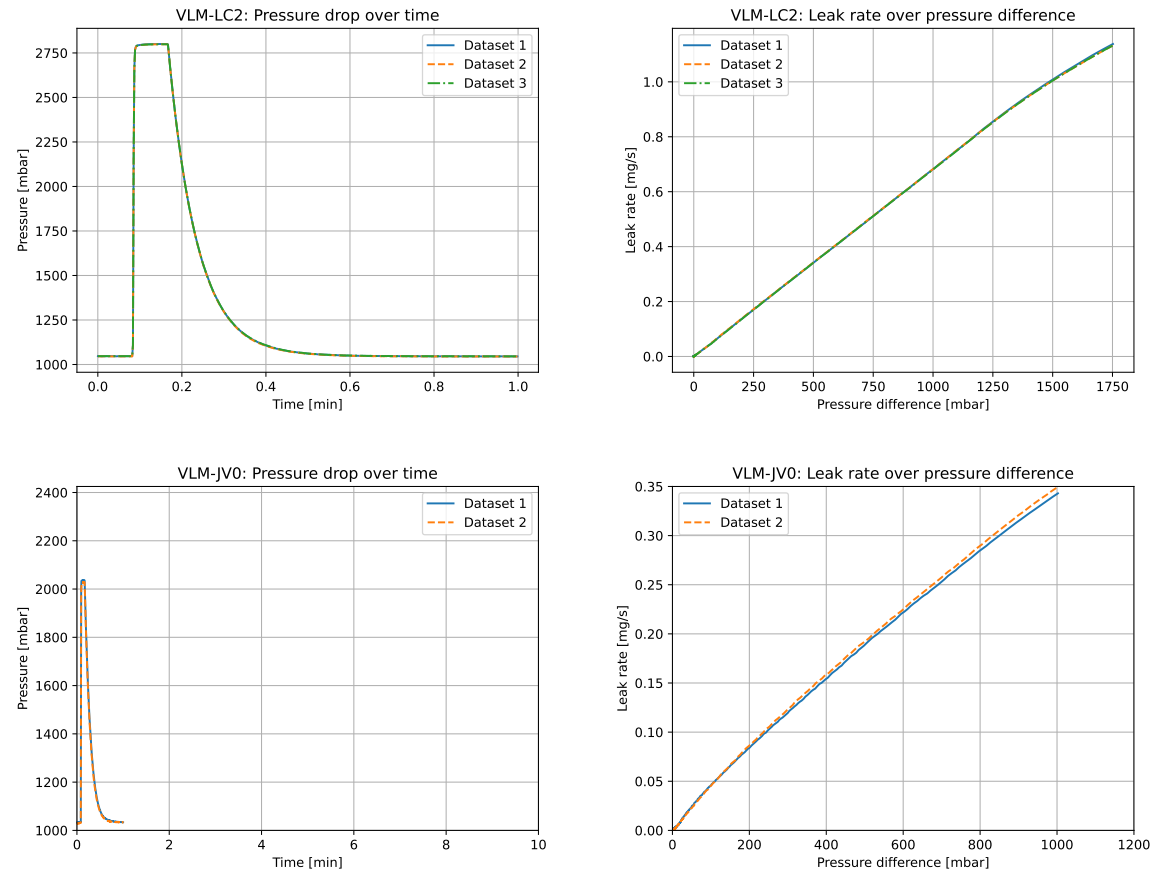


Figure B.8: Total overview of the measured leak rates of the Vaporising Liquid Micro-resistojet.

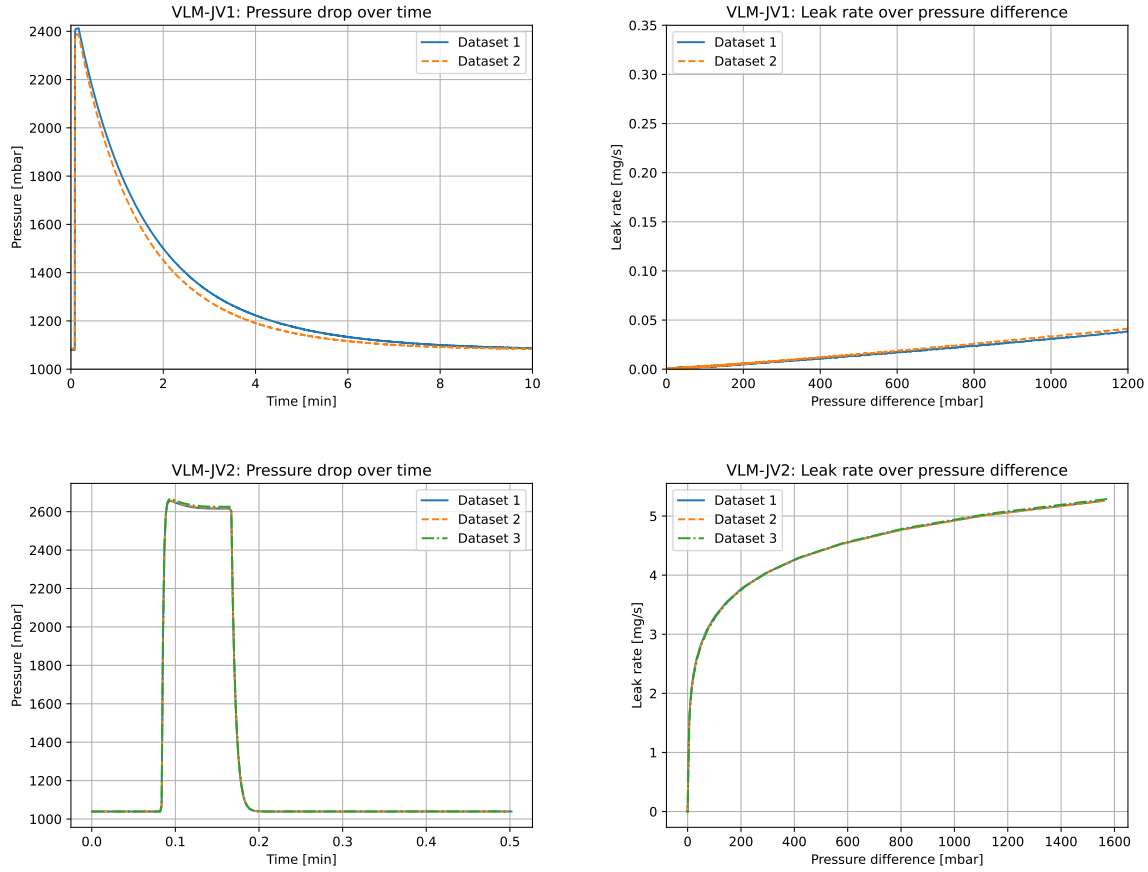


Figure B.9: Total overview of the measured leak rates of the Vaporising Liquid Micro-resistojet.

B.4. Nitrogen Tests

This section shows the most important results of the nitrogen test campaign, which is described extensively in [chapter 7](#). Five different tests have been conducted with varying parameters (T_c and P_c), summarised in [Table 7.1](#). Each tests features four thrust periods of 5 minutes each. [Table B.3](#) shows the summarised results of all tests, including the absolute and relative errors. [Table B.4](#) shows the quality factors of the nitrogen tests, including the absolute and relative errors.

Test ID	T_c [°C]	P_c [mbar]	\dot{m}_{N_2} [mg/s]	P_a [mbar]	F [mN]	P_{heat} [W]
N2-10-020	36.97 ± 17.4 (47.1%)	1013.26 ± 57.4 (5.7%)	19.25 ± 0.14 (0.7%)	9.17 ± 1.38 (15.1%)	6.77 ± 0.13 (1.9%)	-
N2-10-200	199.59 ± 7.51 (3.8%)	1001.16 ± 50.0 (5.0%)	15.38 ± 0.11 (0.7%)	7.28 ± 1.25 (17.2%)	5.29 ± 0.10 (1.9%)	10.41 ± 0.15 (1.4%)
N2-10-300	299.32 ± 7.50 (2.5%)	997.99 ± 50.1 (5.0%)	13.36 ± 0.09 (0.7%)	6.37 ± 1.03 (16.2%)	4.79 ± 0.08 (1.7%)	17.77 ± 0.50 (2.8%)
N2-10-400	399.14 ± 7.50 (1.9%)	997.15 ± 50.4 (5.1%)	12.43 ± 0.13 (1.1%)	5.66 ± 0.98 (17.3%)	4.12 ± 0.11 (2.7%)	27.98 ± 0.69 (2.5%)
N2-10-200	199.59 ± 7.51 (3.8%)	1001.16 ± 50.0 (5.0%)	15.38 ± 0.11 (0.7%)	7.28 ± 1.25 (17.2%)	5.29 ± 0.10 (1.9%)	10.41 ± 0.15 (1.4%)
N2-15-200	199.29 ± 7.50 (3.8%)	1492.36 ± 50.0 (3.4%)	23.93 ± 0.21 (0.9%)	10.45 ± 1.57 (15.0%)	8.59 ± 0.16 (1.9%)	13.16 ± 0.15 (1.1%)

Table B.3: Averaged results and absolute errors of the nitrogen tests.

Test ID	$Re_{t,real} [-]$	$I_{sp} [s]$	$\xi_{I_{sp}} [-]$	$\eta_{heat} [-]$	$C_d [-]$
N2-10-020	3313 \pm 482 (14.5%)	35.86 \pm 0.74 (2.1%)	0.52 \pm 0.02 (3.6%)	-	0.69 \pm 0.06 (9.3%)
N2-10-200	1939 \pm 271 (14.0%)	35.07 \pm 0.71 (2.0%)	0.41 \pm 0.01 (2.2%)	0.27 \pm 0.03 (12.5%)	0.69 \pm 0.06 (8.5%)
N2-10-300	1498 \pm 212 (14.2%)	36.56 \pm 0.66 (1.8%)	0.39 \pm 0.01 (2.0%)	0.22 \pm 0.03 (12.8%)	0.66 \pm 0.06 (8.8%)
N2-10-400	1243 \pm 178 (14.3%)	33.80 \pm 0.97 (2.9%)	0.33 \pm 0.01 (3.0%)	0.18 \pm 0.02 (13.0%)	0.67 \pm 0.06 (9.0%)
N2-10-200	1939 \pm 271 (14.0%)	35.07 \pm 0.71 (2.0%)	0.41 \pm 0.01 (2.2%)	0.27 \pm 0.03 (12.5%)	0.69 \pm 0.06 (8.5%)
N2-15-200	2965 \pm 393 (13.3%)	36.60 \pm 0.75 (2.1%)	0.43 \pm 0.01 (2.3%)	0.34 \pm 0.04 (10.9%)	0.72 \pm 0.05 (7.4%)

Table B.4: Quality factors of the nitrogen tests.

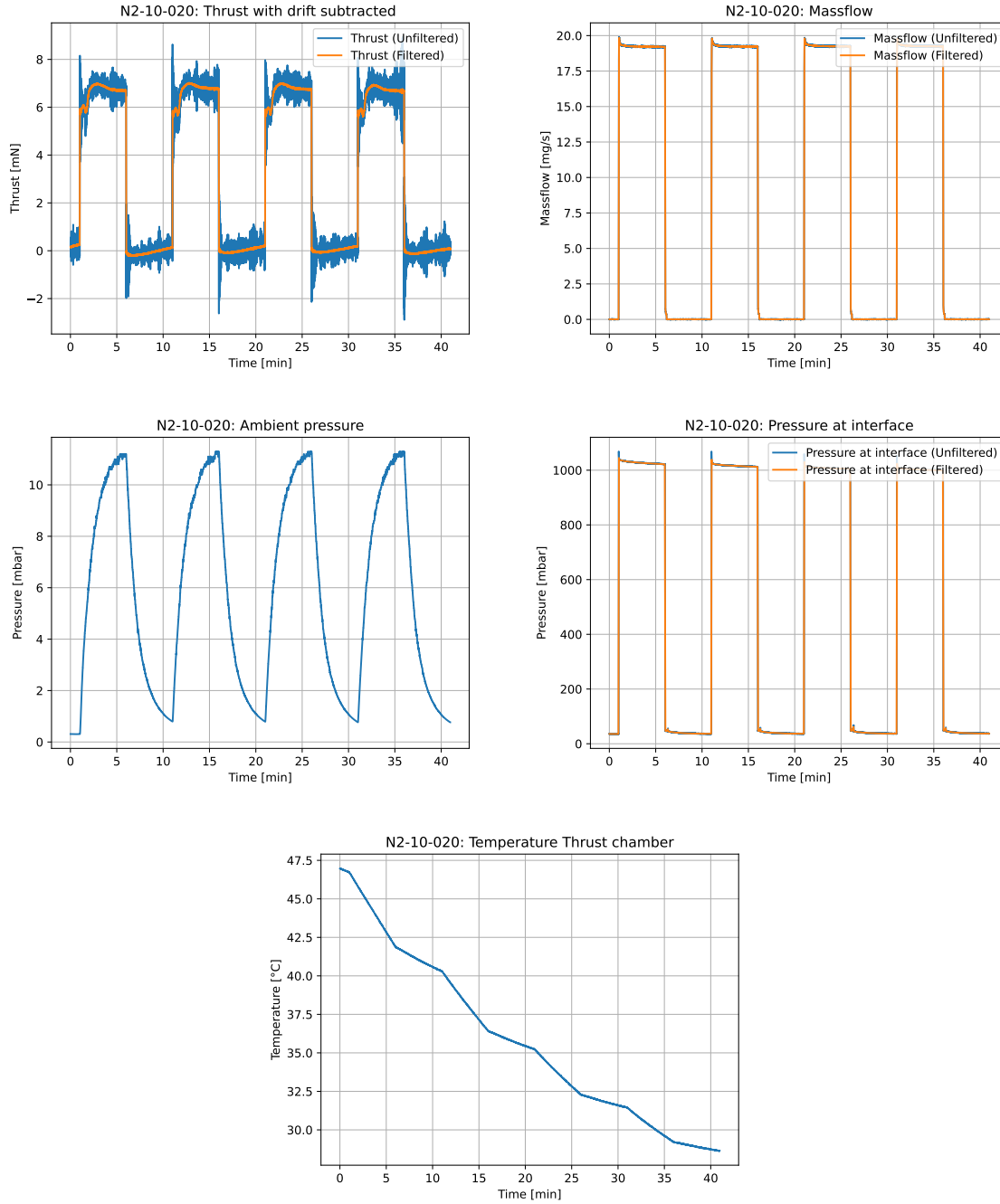


Figure B.10: Measured parameters of the nitrogen test at 20 °C and 1.0 bar (N2-10-020).

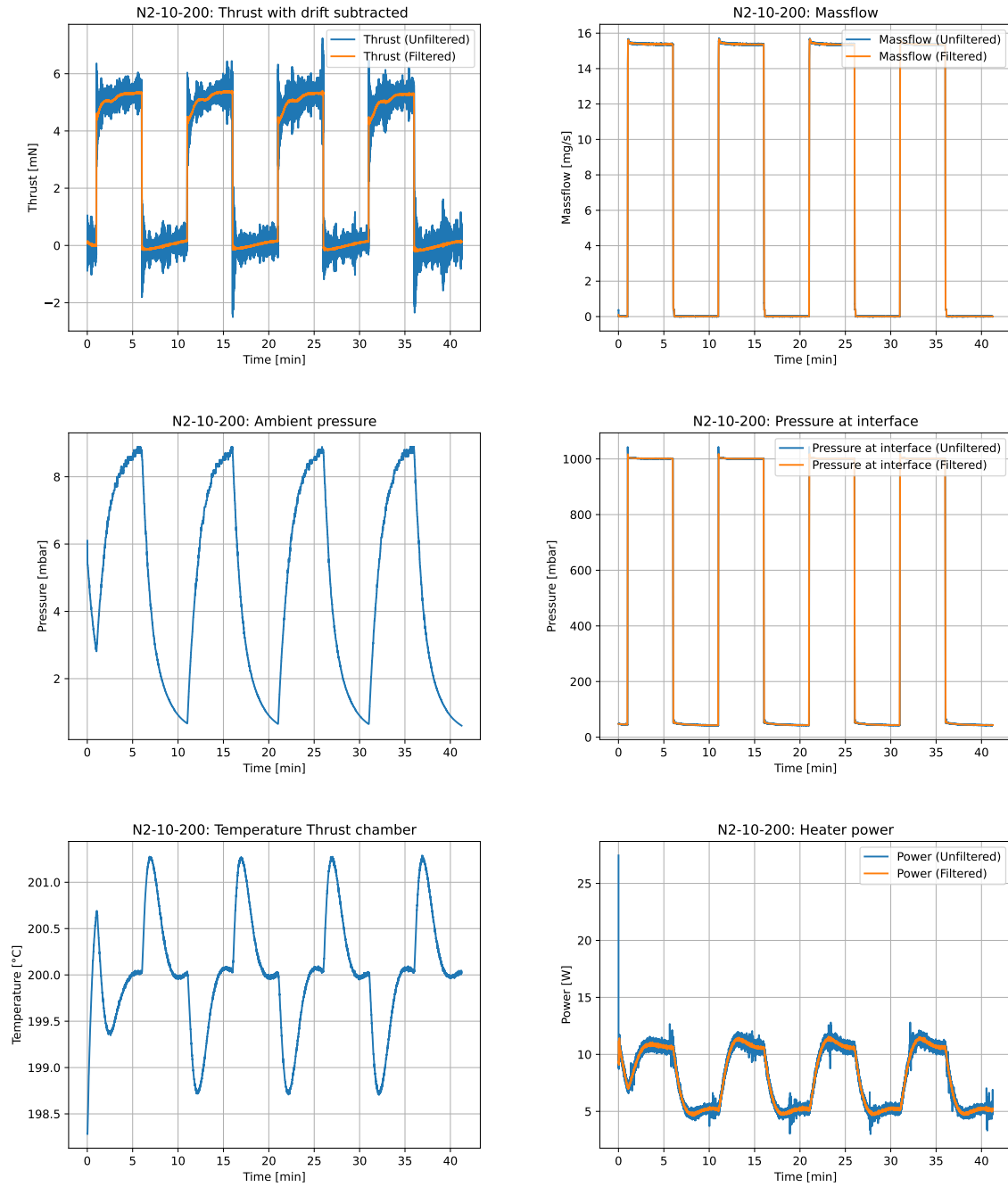


Figure B.11: Measured parameters of the nitrogen test at 200 °C and 1.0 bar (N2-10-200).

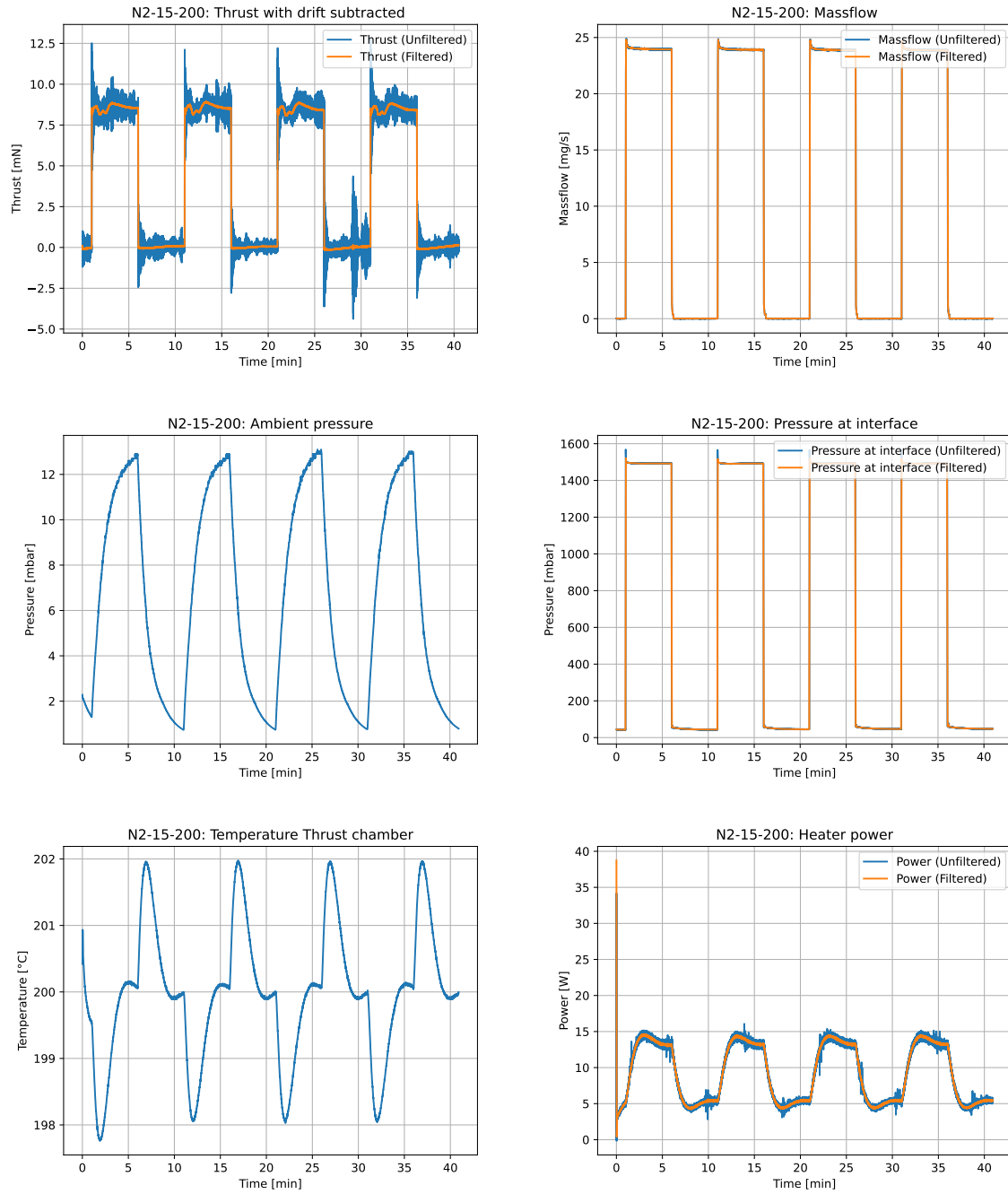


Figure B.12: Measured parameters of the nitrogen test at 200 °C and 1.5 bar (N2-15-200).

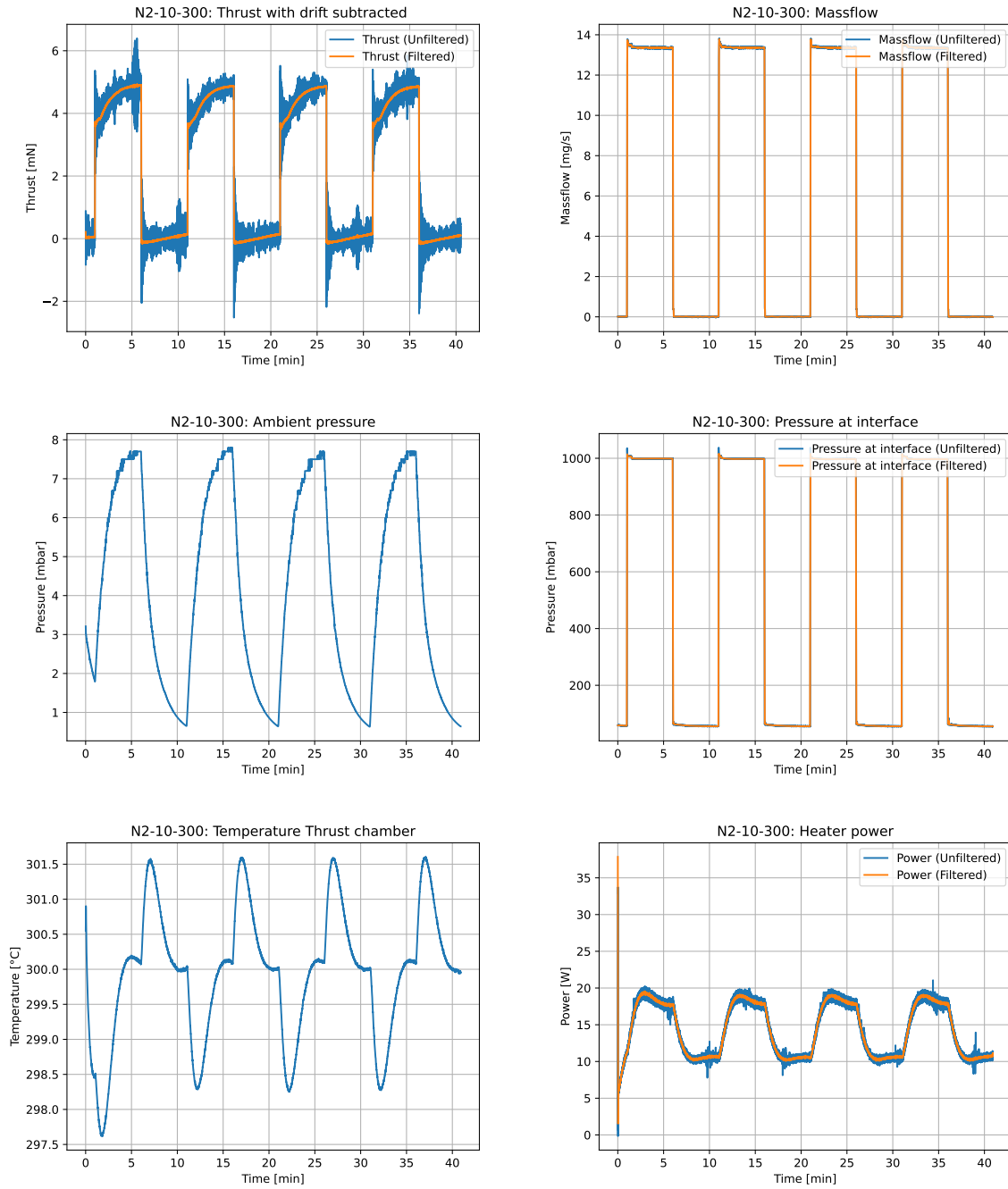


Figure B.13: Measured parameters of the nitrogen test at 300 °C and 1.0 bar (N2-10-300).

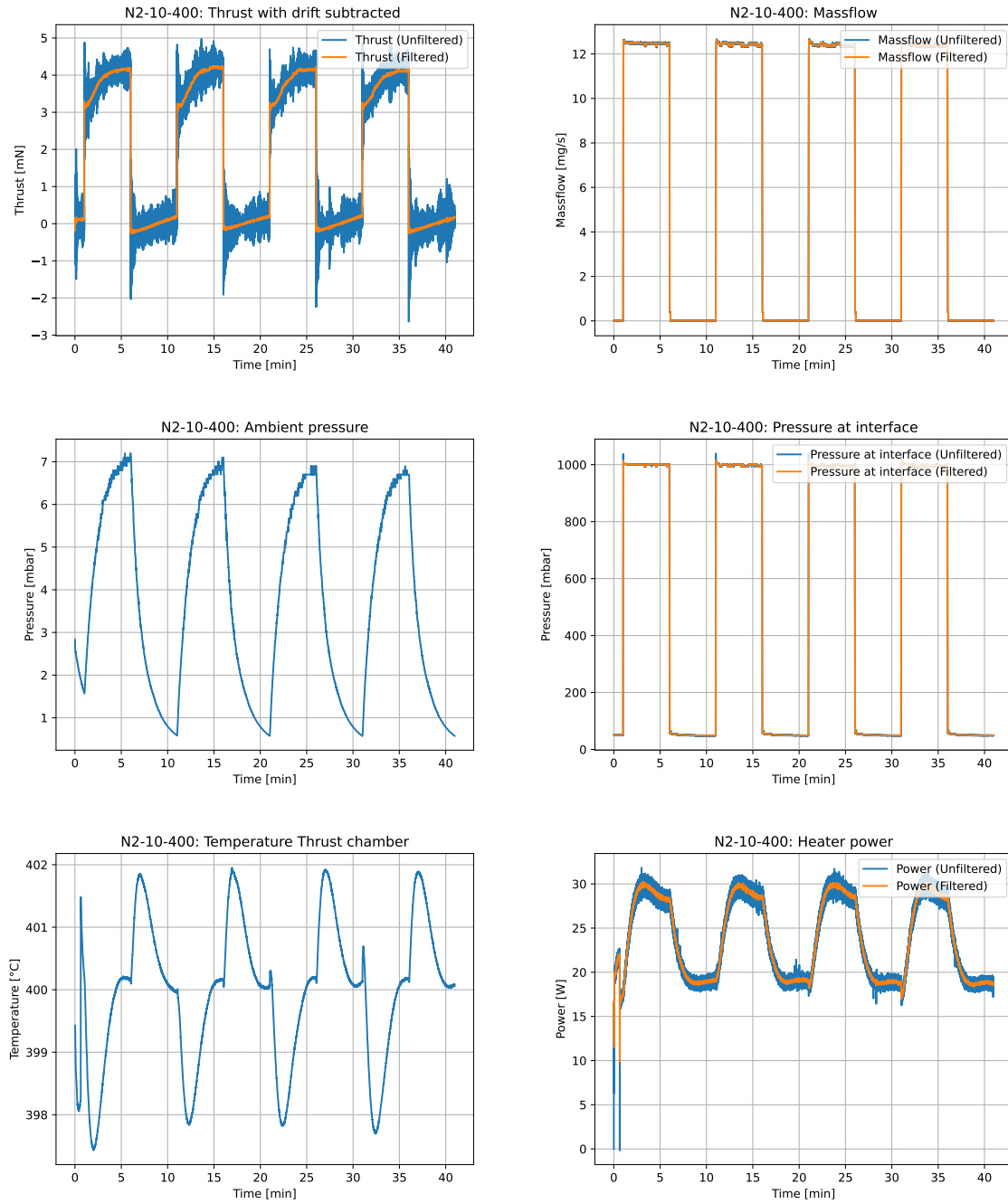


Figure B.14: Measured parameters of the nitrogen test at 400 °C and 1.0 bar (N2-10-400).

B.5. Water Tests

This section shows the most important results of the water test campaign, which is described extensively in [chapter 8](#). Three different tests have been conducted with varying chamber temperatures (T_c), summarised in [Table 8.1](#). Each tests features two thrust periods of 10 minutes each. [Table B.5](#) and [B.6](#) show the summarised results of all tests, including the measurement and total errors. [Table B.7](#) shows the quality factors of the water tests, including the absolute and relative errors.

Test ID	T_c [°C]	P_c [mbar]	\dot{m}_{H_2O} [mg/s]	P_a [mbar]	F [mN]	P_{heat} [W]
H2O-10-200	174.49 ± 26.2 (15.0%)	851.83 ± 122.7 (14.4%)	5.99 ± 1.48 (24.7%)	8.26 ± 4.01 (48.6%)	5.94 ± 0.73 (12.3%)	40.02 ± 2.30 (5.7%)
H2O-15-300	279.25 ± 3.88 (1.4%)	743.95 ± 63.79 (8.6%)	6.30 ± 0.65 (10.3%)	6.49 ± 1.09 (16.8%)	4.15 ± 0.20 (4.8%)	40.02 ± 0.01 (0.0%)
H2O-15-400	337.07 ± 18.8 (5.6%)	899.74 ± 81.06 (9.0%)	5.87 ± 1.00 (17.0%)	7.52 ± 1.50 (20.0%)	5.25 ± 1.25 (23.8%)	40.00 ± 0.00 (0.0%)

Table B.5: Averaged results and measurement errors of the water tests.

Test ID	T_c [°C]	P_c [mbar]	\dot{m}_{H_2O} [mg/s]	P_a [mbar]	F [mN]	P_{heat} [W]
H2O-10-200	174.49 ± 27.3 (15.6%)	851.83 ± 132.5 (15.6%)	5.99 ± 1.50 (25.1%)	8.26 ± 5.76 (69.7%)	5.94 ± 0.73 (12.3%)	40.02 ± 2.30 (5.8%)
H2O-15-300	279.25 ± 8.44 (3.0%)	743.95 ± 81.05 (10.9%)	6.30 ± 0.72 (11.5%)	6.49 ± 3.42 (52.8%)	4.15 ± 0.21 (4.9%)	40.02 ± 0.08 (0.2%)
H2O-15-400	337.07 ± 20.3 (6.0%)	899.74 ± 95.24 (10.6%)	5.87 ± 1.04 (17.8%)	7.52 ± 4.05 (53.8%)	5.25 ± 1.25 (23.8%)	40.00 ± 0.08 (0.2%)

Table B.6: Averaged results and total errors of the water tests.

Test ID	$Re_{t,real}$ [-]	I_{sp} [s]	$\xi_{I_{sp}}$ [-]	η_{heat} [-]	C_d [-]
H2O-10-200	1564 ± 530 (33.9%)	101.1 ± 28.2 (27.9%)	0.95 ± 0.27 (28.2%)	0.41 ± 0.14 (34.9%)	0.39 ± 0.12 (30.2%)
H2O-15-300	1144 ± 245 (21.4%)	67.17 ± 8.40 (12.5%)	0.56 ± 0.07 (12.6%)	0.46 ± 0.10 (21.7%)	0.52 ± 0.09 (17.3%)
H2O-15-400	1030 ± 266 (25.8%)	91.20 ± 27.07 (29.7%)	0.73 ± 0.22 (29.8%)	0.45 ± 0.11 (25.5%)	0.42 ± 0.09 (22.0%)

Table B.7: Quality factors of the water tests.

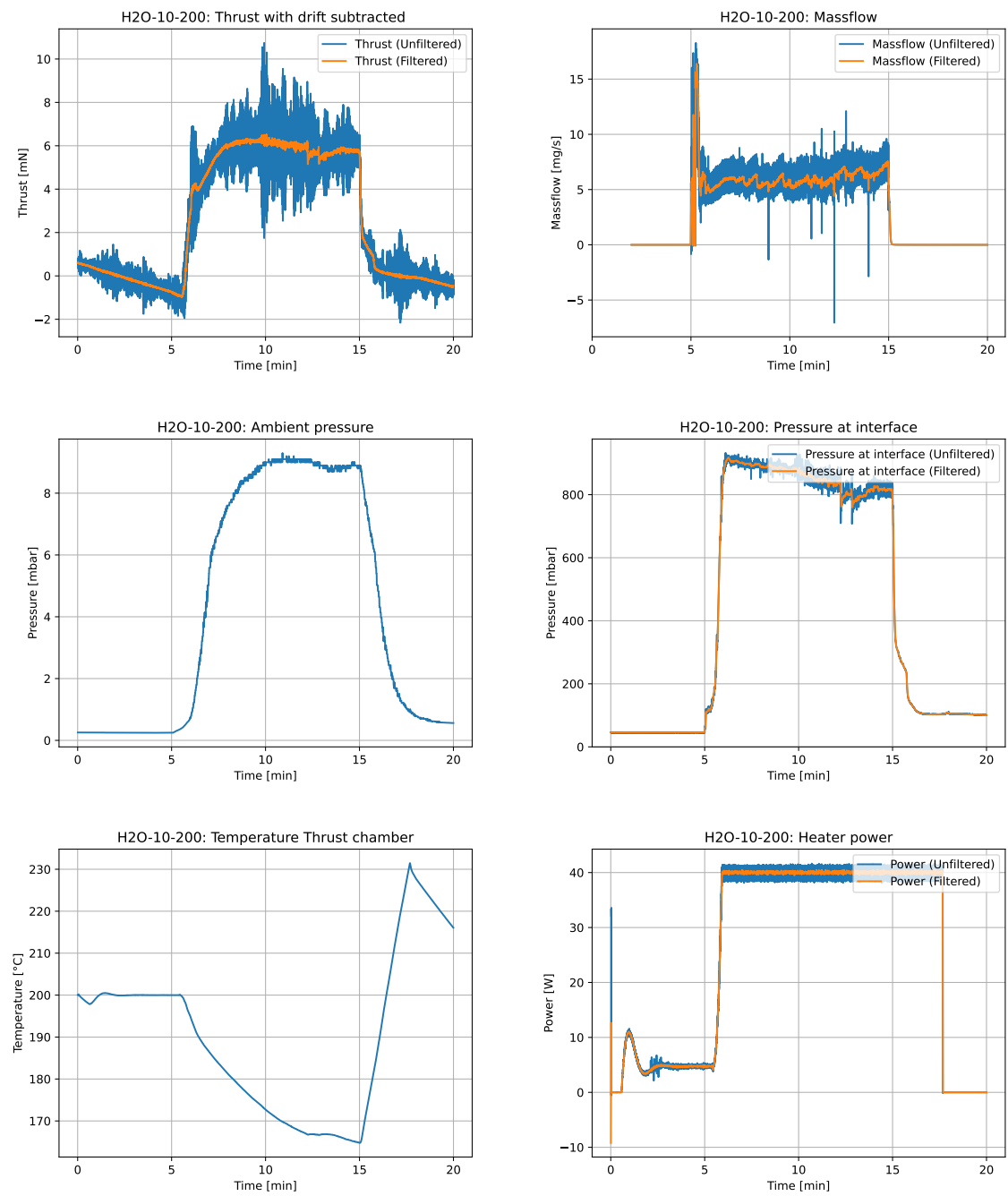


Figure B.15: Measured parameters of the water test at 200 °C and 1.0 bar (H2O-10-200).

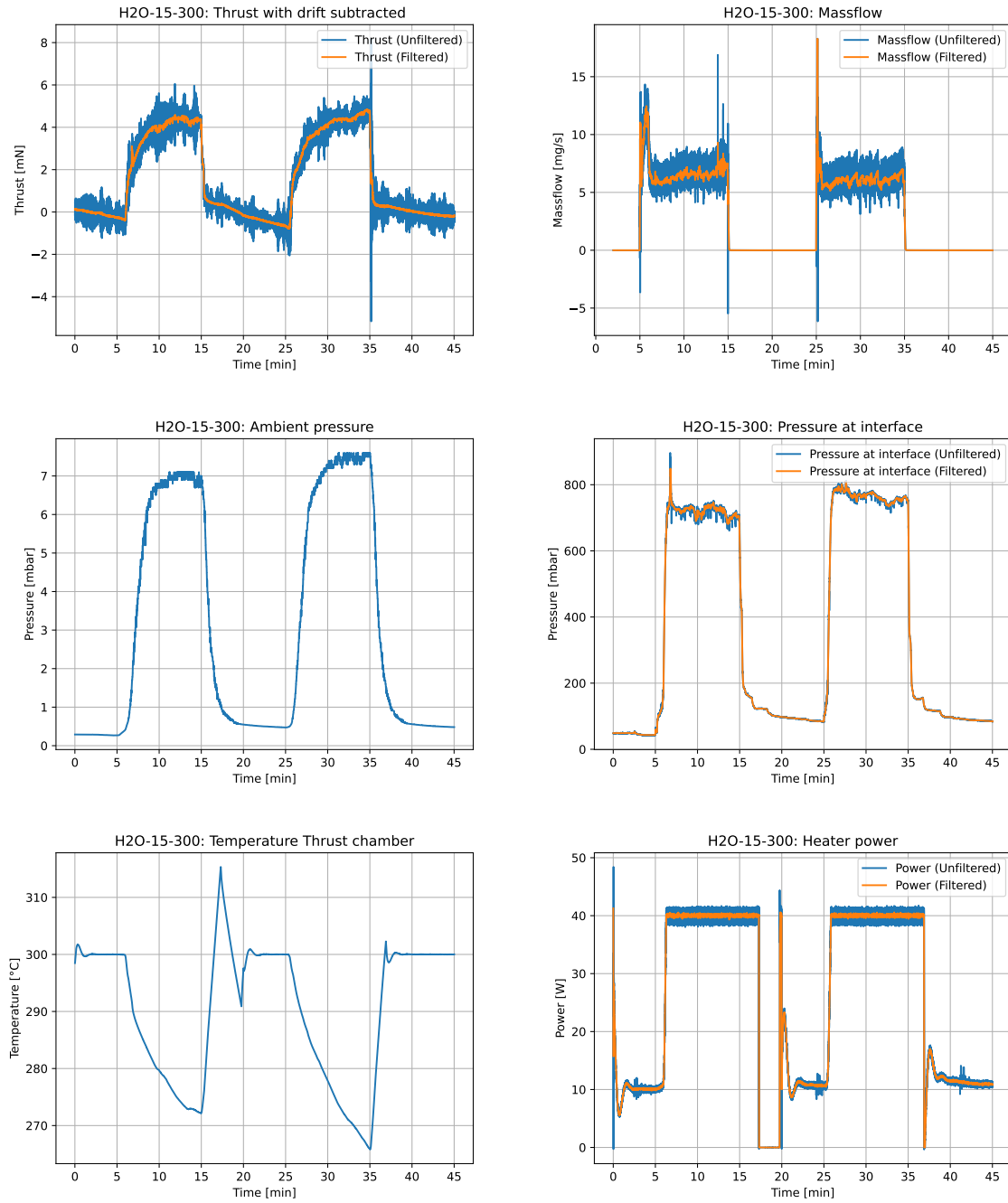


Figure B.16: Measured parameters of the water test at 300 °C and 1.5 bar (H2O-15-300).

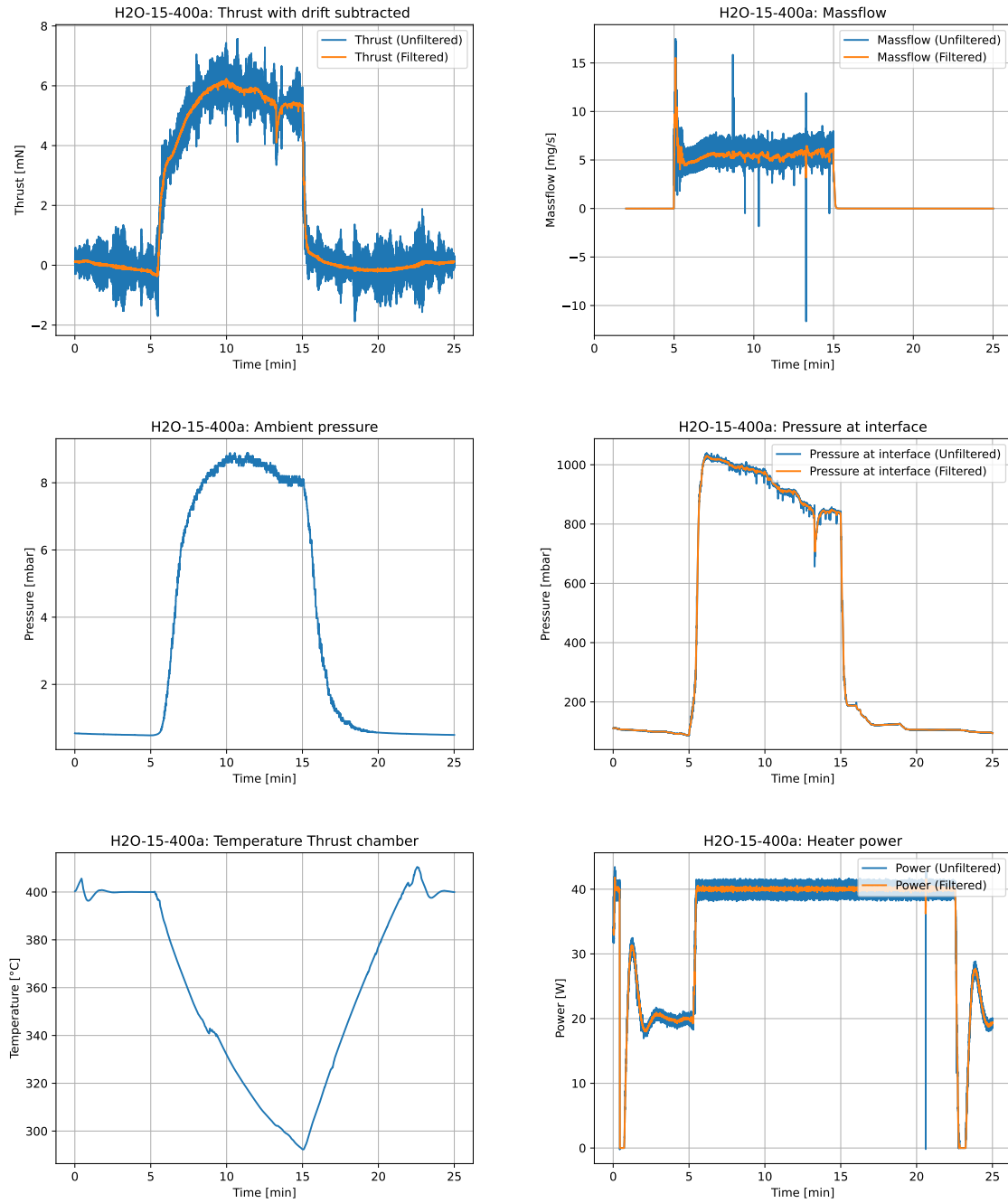


Figure B.17: Measured parameters of the water test at 400 °C and 1.5 bar (H2O-15-400).

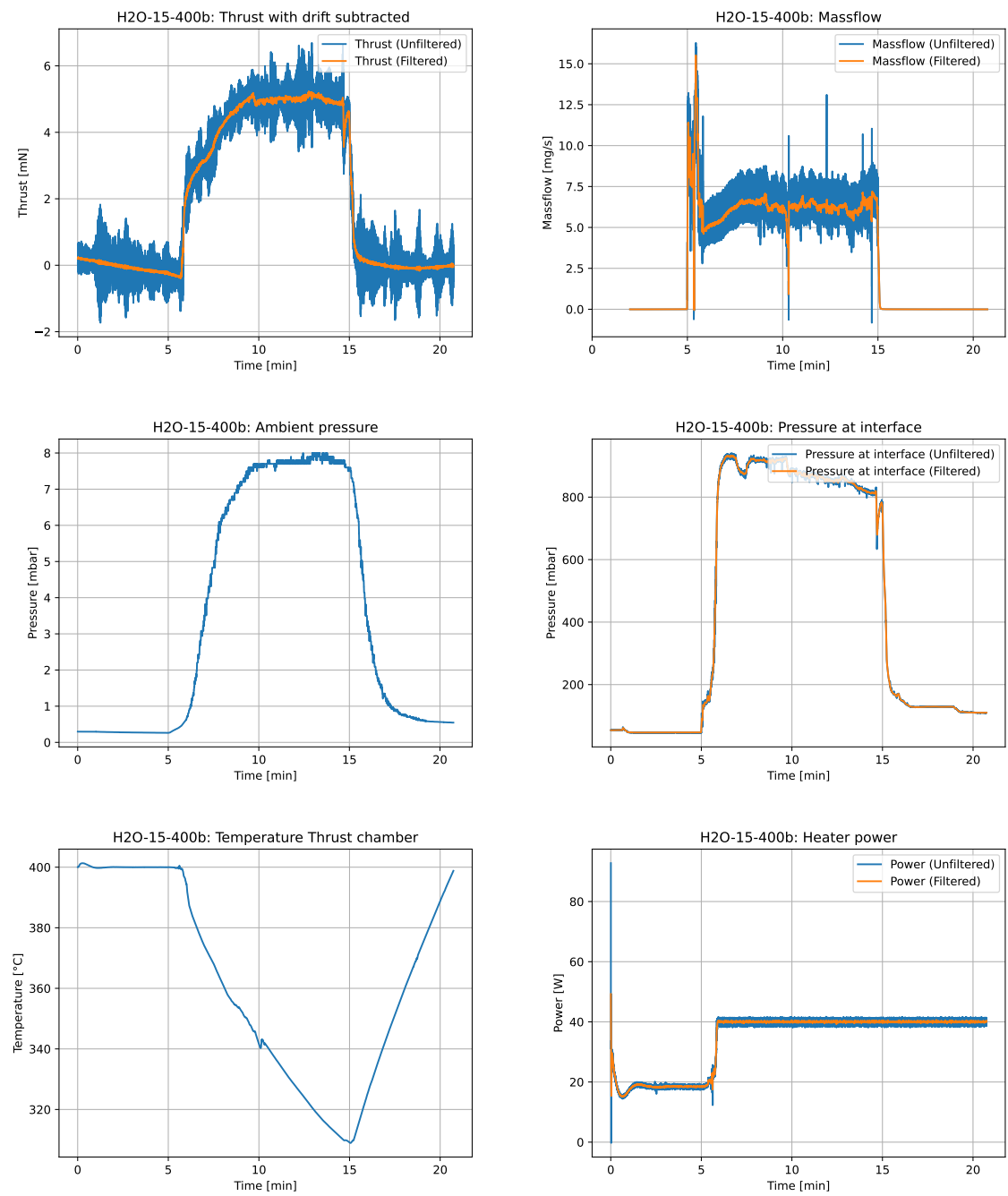


Figure B.18: Measured parameters of the water test at 400 °C and 1.5 bar (H2O-15-400).

B.6. Validation & Verification

This section is structured similarly to [chapter 9](#). It is split into a validation part ([subsection B.6.1](#)) and a verification part ([subsection B.6.2](#)). The first section includes all relevant tables for comparing the output of the Modified Rocket Theory of [chapter 4](#) to the test results of [chapter 7](#) and [8](#). The second section includes relevant tables for comparing the test results of previous works to the test results of this work.

B.6.1. Validation of the Analytical Model

The tables below compare the different tests to the modelled output. The results of this comparison for N2-10-300 ([Table B.11](#)) and H2O-15-300 ([Table B.14](#)) are discussed in [chapter 9](#).

Parameter	Model (MRT)	Test	Difference [%]
\dot{m} [mg/s]	27.24 ± 8.9%	19.25 ± 0.7%	-29.3
F [mN]	14.19 ± 9.5%	6.77 ± 1.9%	-52.3
ξ_F [-]	0.75 ± 1.3%	0.36 ± 2.3%	-52.3
Re_t [-]	4354 ± 9.4%	3313 ± 14.5%	-23.9
I_{sp} [s]	53.13 ± 1.2%	35.86 ± 2.1%	-32.5
$\xi_{I_{sp}}$ [-]	0.79 ± 1.1%	0.52 ± 3.6%	-34.2
C_d [-]	0.96 ± 0.2%	0.69 ± 9.3%	-28.1

Table B.8: Comparison of the modelled and measured parameters for the nitrogen test at 20 °C and 1.0 bar (N2-10-020).

Parameter	Model (MRT)	Test	Difference [%]
\dot{m} [mg/s]	21.12 ± 9.1%	15.38 ± 0.7%	-27.2
F [mN]	12.77 ± 10.3%	5.29 ± 1.9%	-58.6
ξ_F [-]	0.68 ± 2.0%	0.28 ± 2.8%	-58.6
Re_t [-]	2397 ± 9.3%	1939 ± 14.0%	-19.1
I_{sp} [s]	61.63 ± 1.5%	35.07 ± 2.0%	-43.1
$\xi_{I_{sp}}$ [-]	0.72 ± 1.7%	0.41 ± 2.2%	-43.1
C_d [-]	0.94 ± 0.3%	0.69 ± 8.5%	-26.6

Table B.9: Comparison of the modelled and measured parameters for the nitrogen test at 200 °C and 1.0 bar (N2-10-200).

Parameter	Model (MRT)	Test	Difference [%]
\dot{m} [mg/s]	31.99 ± 8.0%	23.93 ± 0.9%	-25.2
F [mN]	20.78 ± 8.6%	8.59 ± 1.9%	-58.7
ξ_F [-]	0.73 ± 1.3%	0.30 ± 2.3%	-58.7
Re_t [-]	3596 ± 8.5%	2965 ± 13.3%	-17.5
I_{sp} [s]	66.26 ± 0.9%	36.60 ± 2.1%	-44.8
$\xi_{I_{sp}}$ [-]	0.77 ± 1.1%	0.43 ± 2.3%	-44.2
C_d [-]	0.95 ± 0.2%	0.72 ± 7.4%	-24.2

Table B.10: Comparison of the modelled and measured parameters for the nitrogen test at 200 °C and 1.5 bar (N2-15-200).

Parameter	Model (MRT)	Test	Difference [%]
\dot{m} [mg/s]	19.03 ± 8.8%	13.36 ± 0.7%	-29.8
F [mN]	12.11 ± 10.3%	4.79 ± 1.7%	-60.4
ξ_F [-]	0.64 ± 2.2%	0.25 ± 2.8%	-60.4
Re_t [-]	1900 ± 9.1%	1498 ± 14.2%	-21.2
I_{sp} [s]	64.9 ± 1.7%	36.56 ± 1.8%	-43.7
$\xi_{I_{sp}}$ [-]	0.68 ± 1.9%	0.39 ± 2.0%	-42.6
C_d [-]	0.94 ± 0.3%	0.66 ± 8.8%	-29.8

Table B.11: Comparison of the modelled and measured parameters for the nitrogen test at 300 °C and 1.0 bar (N2-10-300).

Parameter	Model (MRT)	Test	Difference [%]
\dot{m} [mg/s]	17.41 ± 8.8%	12.43 ± 1.1%	-28.6
F [mN]	11.52 ± 10.6%	4.12 ± 2.7%	-64.2
ξ_F [-]	0.61 ± 2.5%	0.22 ± 3.7%	-64.2
Re_t [-]	1567 ± 8.8%	1243 ± 14.3%	-20.7
I_{sp} [s]	67.48 ± 2.0%	33.80 ± 2.9%	-49.9
$\xi_{I_{sp}}$ [-]	0.65 ± 2.2%	0.33 ± 3.0%	-49.2
C_d [-]	0.93 ± 0.3%	0.67 ± 9.0%	-28.0

Table B.12: Comparison of the modelled and measured parameters for the nitrogen test at 400 °C and 1.0 bar (N2-10-400).

Parameter	Model (MRT)	Test	Difference [%]
\dot{m} [mg/s]	16.72 ± 8.8%	5.99 ± 24.7%	-64.2
F [mN]	13.68 ± 9.6%	5.94 ± 12.3%	-56.6
ξ_F [-]	0.72 ± 1.6%	0.31 ± 12.4%	-56.6
Re_t [-]	2917 ± 9.3%	1564 ± 33.9%	-46.4
I_{sp} [s]	83.45 ± 1.3%	101.1 ± 27.9%	21.1
$\xi_{I_{sp}}$ [-]	0.75 ± 1.3%	0.95 ± 28.2%	26.7
C_d [-]	0.95 ± 0.2%	0.39 ± 30.2%	-58.9

Table B.13: Comparison of the modelled and measured parameters for the water test at 200 °C and 1.0 bar (H2O-10-200).

Parameter	Model (MRT)	Test	Difference [%]
\dot{m} [mg/s]	15.01 ± 9.0%	6.30 ± 10.3%	-58.0
F [mN]	12.88 ± 10.2%	4.15 ± 4.8%	-67.8
ξ_F [-]	0.67 ± 1.9%	0.22 ± 5.2%	-67.8
Re_t [-]	2106 ± 9.1%	1144 ± 21.4%	-45.7
I_{sp} [s]	87.52 ± 1.6%	67.17 ± 12.5%	-23.2
$\xi_{I_{sp}}$ [-]	0.71 ± 1.7%	0.56 ± 12.6%	-21.1
C_d [-]	0.94 ± 0.3%	0.52 ± 17.3%	-44.7

Table B.14: Comparison of the modelled and measured parameters for the water test at 300 °C and 1.5 bar (H2O-15-300).

Parameter	Model (MRT)	Test	Difference [%]
\dot{m} [mg/s]	13.70 ± 9.0%	5.87 ± 17.0%	-57.2
F [mN]	12.12 ± 10.5%	5.25 ± 23.8%	-56.7
ξ_F [-]	0.63 ± 2.3%	0.27 ± 23.9%	-56.7
Re_t [-]	1608 ± 9.2%	1030 ± 25.8%	-35.9
I_{sp} [s]	90.19 ± 1.9%	91.20 ± 29.7%	1.1
$\xi_{I_{sp}}$ [-]	0.68 ± 2.0%	0.73 ± 29.8%	7.4
C_d [-]	0.94 ± 0.3%	0.42 ± 22.0%	-55.3

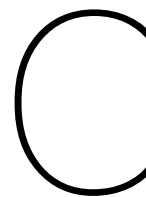
Table B.15: Comparison of the modelled and measured parameters for the water test at 400 °C and 1.5 bar (H2O-15-400).

B.6.2. Verification of the test results

The table below compares the nitrogen test at ambient temperature and 1.0 bar (N2-10-020) with previous works. The results of this comparison for N2-15-200 (Table 9.4) and H2O-15-300 (Table 9.5) are discussed in chapter 9.

Input							
Parameter	Versteeg		Hutten		Cramer		Vaes
T_c [K]	294	± 1.5	293	± 7.0	294	± 6.0	310 ± 17.4
P_c [mbar]	1107	± 50	985	± 50	987	± 50	1013 ± 57
P_a [mbar]	1.79	± 0.28	6.7	± 1.28	8.66	± 1.30	9.17 ± 1.38
A_t [$10^3 \mu m^2$]	76.5	± 8.4	75.3	± 7.0	104.5	± 15.3	122.6 ± 8.7
A_e [$10^3 \mu m^2$]	537.6	± 8.6	580	± 12.9	359	± 14.0	488 ± 15.0
H_t [μm]	496	± 4	538	± 8	522	± 34.3	499 ± 11.7
W_t [μm]	154	± 17	140	± 11	200.1	± 16.2	245.6 ± 11.7
ϵ [-]	7.03	± 0.68	7.70	± 0.89	3.44	± 0.64	3.98 ± 0.40
Output							
F [mN]	10.43	± 0.07	9.21	± 0.11	5.86	± 0.20	6.77 ± 0.13
\dot{m}_{N_2} [mg/s]	16.69	± 0.12	14.9	± 0.13	16.5	± 0.12	19.25 ± 0.14
$Re_{t,real}$ [-]	2208	± 25	2586	± 460	2993	± 348	3313 ± 482
I_{sp} [s]	63.77	± 0.61	63.5	± 0.89	36.23	± 1.23	35.86 ± 0.74
$\xi_{I_{sp}}$ [-]	0.90	± 0.01	0.91	± 0.02	0.54	± 0.05	0.52 ± 0.02
C_d [-]	0.85	± 0.10	0.86	± 0.08	0.69	± 0.05	0.69 ± 0.06

Table B.16: Comparison of the results for N2-10-020 with different authors.



Datasheets

This appendix contains some datasheets that have been consulted throughout this work, as well as a technical drawing made for manufacturing the sealing gasket.

C.1. Sealing gasket

This section shows the material the sealing gasket is made of (subsection C.1.1) and the technical drawing of its design (subsection C.1.2). See chapter 3 for more information.

C.1.1. Sigraflex® APX pure graphite foil

Datasheet of the graphite sealing gasket provided by *Wagner Gaskets & Seals*. The material combines resistance to high temperatures, impermeability to gases and liquids, and manufacturability.



SIGRAFLEX®

Flexible graphite foil for industrial sealing (metric)

SIGRAFLEX flexible graphite foil is manufactured from high quality expanded natural graphite free of adhesives and binders. Inhibitors can be added to enhance the performance. Advanced grades like SIGRAFLEX APX2® foil offer maximum protection against oxidation for greater reliability and longer service life.

Properties

- Soft and flexible, inert and highly impermeable to gases and liquids, fire safe
- Asbestos-free, no associated health risks
- Free of any polymers or organic binders
- No aging or fatigue under dynamic load even at elevated temperatures

- Even in long term services, no noticeable changes in properties
- No measurable cold or warm flow characteristics up to the maximum permissible gasket stress
- Electrically conductive, no static charge
- Excellent chemical resistance and high thermal shock capability
- Operating temperatures range from -250°C up to 550°C depending on chemical resistance. Life time might be limited at high temperatures. Consult the manufacturer when application temperatures exceed 450°C. Please refer to our technical guideline regarding thermal stability.
- Easy handling and processability during assembly or punching

Material data of SIGRAFLEX® Foil¹⁾

Typical properties	Units	APX2	APX	E	C	Z
Bulk density	g/cm ³	Standard 1.0	Standard 1.0	Standard 1.0	Standard 1.0	Standard 1.0
Ash content (DIN 51903)	%	≤ 2.0	≤ 2.0	≤ 1.0	≤ 2.0	≤ 0.15
Carbon content	%	≥ 98	≥ 98	≥ 99	≥ 98	≥ 99.85
Total chloride content	ppm	≤ 25	≤ 25	≤ 10	≤ 25	≤ 10
Total fluoride content	ppm	≤ 10 ²⁾	≤ 10	≤ 10	≤ 25	≤ 10
Total halogen content	ppm	≤ 70	≤ 70	≤ 40	≤ 100	≤ 40
Total sulfur content	ppm	≤ 300	≤ 300	≤ 300	≤ 300	≤ 300
Oxidation rate in air at 670 °C (TGA) ³⁾	%/hour	≤ 1	≤ 3	≤ 4	≤ 5	≤ 4
Oxidation inhibitor	yes	yes	yes	yes	yes	yes
Passive corrosion inhibitor (ASTM F 2168-13)	yes	yes	yes	yes	yes	yes
Material thickness (supplied as sheets, 1000 × 1000 mm, bulk density 1.0 g/cm ³) under the label SIGRAFLEX BASIS	mm	0.2 - 1	0.35 - 1	0.35 - 1	0.35 - 1	0.15 - 1
Material thickness (supplied on rolls)	mm	750/1500	500/1000/1500	500/1000/1500	500/1000/1500	500/1000/1500
Roll width	mm	≥ 4	≥ 4	≥ 4	≥ 4	≥ 4
Standard roll length	m	50	50	50	50	50

¹⁾ Data are valid for the bigger part of the product range. Other values or dimensions on request.

²⁾ On request

³⁾ Based on a thickness of ≥ 0.5 mm and a density of ≥ 1.0 g/cm³

**Material data of SIGRAFLEX® grade Z
with bulk density of 1.0 g/cm³**

Typical properties	Units	Values
Thermal conductivity at 20 °C	in plane	220
	through plane	5
Resistivity at 20 °C	in plane	11
	through plane	700
Coefficient of thermal expansion (20 – 1000 °C)	in plane	approx. 1
	through plane	approx. 50
Permeability coefficient for air	through plane	$< 2 \times 10^{-5}$
Shore hardness (D)		30
Tensile strength	N/mm²	≥ 4
Elongation at break	%	≥ 1
Compression factors (DIN 28090-2)		
Compressibility	ϵ_{KSW}	45
Recovery at 20 °C	ϵ_{KRW}	5
Hot creep	ϵ_{WSW}	< 3
Recovery at 300 °C	ϵ_{WRW}	4
Young's modulus at 20 N/mm² (DIN 28090-1)	N/mm²	700
ASTM	"m"-factor	2
	"y"-factor	1000
Compressibility (ASTM F36)		45
Recovery (ASTM F36)	%	11
Residual stress (DIN 52913) $\sigma_{0.16h, 300^\circ C, 50 N/mm^2}$	N/mm²	48
Coefficient of friction against steel, roughness ≤ 10 µm		0.1


Different types of SIGRAFLEX flexible graphite

E, C, Z, APX, APX2: Homogeneous flexible graphite grades
CS, ZS: Pressure sensitive adhesive backing
TF¹⁾: PTFE-coated for stuffing box packing (maximum 300 °C)
ZX¹⁾: Highly effective corrosion inhibitor (maximum 350 °C)

¹⁾ See separate technical informations

Applications

- Sheet products such as SIGRAFLEX HOCHDRUCK
- Metallic gaskets such as spiral wound gaskets, corrugated metal gaskets and kammprofile gaskets
- Compression packing for stuffing boxes

Approvals/Test reports

Please see www.sigraflex.com/downloads for details.

- BAM oxygen
- DVGW (DIN 3535-6)
- Proof of drinking water hygiene suitability (former KTW) (HY)
- WRAS
- Evaluation for compliance with food legislation requirements (TÜV Rheinland and Fraunhofer IVV)

Compressive strength of SIGRAFLEX® grade Z with bulk density of 1 g/cm³ and material width 20 mm (DIN 28090-1)

Material thickness	mm	0.35	0.5	1	1.5	2	3
20 °C (σ_{v0})	N/mm²	> 300	300	180	140	120	70
300 °C (σ_{80})	N/mm²	> 300	250	160	120	100	70




Graphite Materials & Systems | SGL CARBON GmbH | SGL Technic LLC
 Sales Europe/Middle East/Africa | sigraflex-europe@sglcarbon.com
 Sales Americas | sigraflex-americas@sglcarbon.com
 Sales Asia/Pacific | sigraflex-asia@sglcarbon.com
www.sigraflex.com | www.sglcarbon.com

TDS APX2_APX_E_C_Z_Foil.00
 05 2019/0 1NA Printed in Germany
 *registered trademarks of SGL Carbon SE

This information is based on our present state of knowledge and is intended to provide general notes on our products and their uses. It should therefore not be construed as guaranteeing specific properties of the products described or their suitability for a particular application. Any existing industrial property rights must be observed. The quality of our products is guaranteed under our "General Conditions of Sale".

C.2. Futek LSB200

Datasheet of the Futek LSB200 load cell [19]. It is used in combination with the Scaime CPJ Amplifier to measure the loads exerted on it via the thrust bench. See chapter 5 for more information.



FEATURES

- Up to 10 times the overload protection
- Overload is available in Tension and Compression
- Light weight
- Notable nonlinearity
- Miniature size
- Ultra Low Capacity and High Sensitivity
- Vibration and shock resistance
- High flex silicone cable

Non-loading surface, do not contact

Active End

Fixed End

+ Output (tension)

- Output (compression)

FUTEK Label

SPECIFICATIONS

PERFORMANCE	
Nonlinearity	±0.1% of RO
Hysteresis	±0.1% of RO
Nonrepeatability	±0.05% of RO
ELECTRICAL	
Rated Output (RO)	See chart on third page
Excitation (VDC or VAC)	10 max
Bridge Resistance	1000 Ohm nom.
Insulation Resistance	≥500 MOhm @ 50 VDC
Connection	#29 AWG, 4 conductor, spiral shielded silicone cable, 5 ft [1.5 m] long
Wiring Code	WC1
MECHANICAL	
Weight (approximate)	0.7 oz [19.3 g] (10–250 g)
Safe Overload	1000% of RO
Material	Aluminum (10–250 g)
IP Rating	IP40
Vibration Resistance	20-2000 Hz, 0.01g²/Hz per MIL-STD-810E
Shock Resistance	500 g per IEC60068-2-27
TEMPERATURE	
Operating Temperature	-60 to 200°F [-50 to 93°C]
Compensated Temperature	60 to 160°F [15 to 72°C]
Temperature Shift Zero	±0.01% of RO/°F [0.018% of RO/°C]
Temperature Shift Span	±0.02% of Load/°F [0.036% of Load/°C]
CALIBRATION	
Calibration Test Excitation	5 VDC
Calibration (standard)	5-pt Tension
Calibration (available)	5-pt Tension and Compression
Shunt Calibration Value	301 kOhm (10–20 g) 150 kOhm (50–250 g)
CONFORMITY	
RoHS	EU 2015/863
CE	EN55011; EN61326-1

Sensor Solution Source

Load · Torque · Pressure · Multi-Axis · Calibration · Instruments · Software

www.futek.com

CE

RoHS

ANSI

Z540-1

ISO

17025

ISO

9001

ISO

13485

U.S. Manufacturer

C.3. Scaime CPJ Amplifier

Datasheet of the Scaime CPJ Amplifier used in combination with the load cell [57]. See [chapter 5](#) for more information.

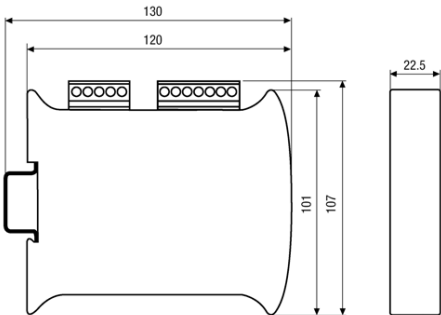
§1. Introduction – Introduction

Le CPJ est un conditionneur analogique de capteurs. Il est principalement destiné aux capteurs à pont de jauges tels que capteurs de pesage, force, couple ou pression. La version CPJ2S intègre la gestion de 2 seuils réglables.

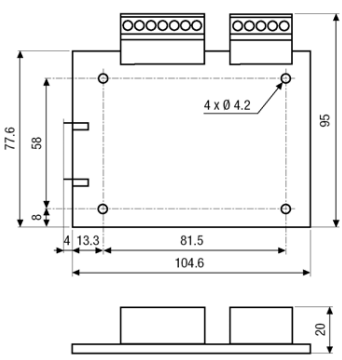
The CPJ device is a sensor analog conditioner. It is mainly used with strain gauges sensors as load cells, torque sensors or pressure sensors. The CPJ2S version includes management of 2 adjustable set points.

§2. Présentation – presentation

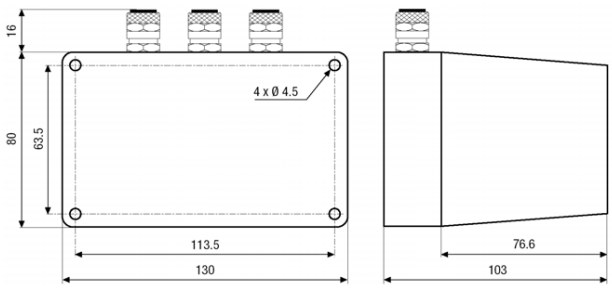
CPJ Version Rail DIN – CPJ, DIN rail model



CPJ Version Carte – CPJ, Board model



CPJ Version boîtier IP65 CPJ, IP65 Housing model



§3. Caractéristiques générales – General specifications

Alimentation	Power supply	24+/-4	VDC
Classe de précision	accuracy class	0.05	%
Dérive thermique de zéro	Zero temperature drift	<0.035	%/°C (FS*)
Dérive thermique de gain	Span temperature drift	<0.02	%/°C (FS*)
Plage de température de fonctionnement	Operating temperature range	0...+70	°C
Alimentation capteur (commutable par cavalier)	Sensor supply voltage (jumper selection)	3, 5, 10	V
Impédance min. capteur - alimentation 3, 5V - alimentation 10V	Min. sensor impedance - voltage 3, 5V - voltage 10V	80	Ω
		160	
Réglage du gain	Span adjustment	0.15 ... 12	mV/V
Consommation max. CPJ/CPJ2S	Max. supply current CPJ/CPJ2S	120/170	mA
Sortie tension	Voltage output	+/-10, 0-10	V
Sortie courant	Current output	4-20	mA
Impédance de charge en sortie tension	Load impedance (Voltage output)	>2000	Ω
Impédance de charge en sortie courant	Load impedance (Current output)	<500	Ω
Charge capacitive en sortie	Output capacitive load	<1	nF
Filtre (commutable par cavalier)	Filter (jumper selection)	10	Hz
Bande passante (jusqu'à)	Bandwidth (up to)	20	KHz

*FS = Pleine Echelle
*FS = Full Scale

D

Procedures

To conduct successfully tests with the EDM-based VLM discussed in this work, it is important to properly execute a number of preparatory steps. A couple of procedures have been established to aid the test conductor run successfully tests. Some procedures were already established by previous iterations, of which Cramer [15] is the most recent. Please refer to appendix C of her work for the leak and nitrogen testing procedures. These were also adhered to in this thesis. This appendix will feature some newly added procedures (disassembly, polishing, and water tests), as well as a modified assembly procedure. The procedures are constructed in such a way that they help maintain consistency throughout various works and are easily reproducible.

D.1. Disassembly Procedure

This procedure outlines the steps required to properly disassemble the EDM-based VLM while preserving all parts for inspection and storage. Follow these instructions carefully to ensure that each component is handled appropriately, maintaining overview, and the risk of damage is minimised. Measure the important nozzle profile dimensions afterwards. Note that, before disassembling the VLM, it is recommended to perform both an optical characterisation and leak test. In this way, the effect of the disassembly on the thruster's performance can be quantified.

Author: J.J.A. Vaes

Version: 1.0

Date: 14-11-2024

D.1.1. Required equipment

- Assembled EDM-based VLM components
- (Optional) Plier
- Tape
- M4 wrench
- M4 Torx screwdriver
- Storage box
- Camera
- Fine cloth
- Isopropyl Alcohol cleaner
- Micrometer
- Microscope (for optical characterisation)

D.1.2. Disassembly procedure

1. Conduct an optical characterisation and leak test before disassembly.
2. Remove the cartridge heaters by unscrewing them. They might be hard to unscrew them after a while, so pliers can be used to aid this process.
3. Clean the residual thermal paste of the cartridge heaters and block the heater holes using a piece of tape. This prevents the thermal paste that is still inside the holes from spilling.
4. Loosen the M4 bolts and remove their nuts. Do this in a diagonal manner (top-left to bottom-right and top-right to bottom-left, for example).
5. Remove the M4 bolts in a diagonal manner.
6. Remove the thermocouple.
7. Carefully separate the copper blocks, whilst making sure the components between them (i.e. nozzle profile, metal foam block and mesh) do not fall.
8. Separate all components and store them in an ordered manner.
9. Inspect and photograph each component for later reference. This helps in tracking their degradation over time.
10. Perform an optical characterisation on the copper blocks and nozzle profile. This aids in understanding the changing nozzle geometry over time.
11. Clean the components with a fine cloth and Isopropyl Alcohol Cleaner and store them.
12. Measure the important dimensions of the nozzle profile (thickness and throat/exit widths and heights) using a combination of a micrometer and microscopes (see [chapter 6](#) for more information).

D.2. Assembly Procedure

This procedure outlines the steps required to properly assemble the EDM-based VLM while ensuring proper alignment between the separate parts. Follow these instructions carefully to ensure that each component is handled appropriately, maintaining overview, and the risk of damage is minimised. Measure the important nozzle profile dimensions beforehand. Note that, after assembling the VLM, it is recommended to perform both an optical characterisation and leak test. In this way, proper VLM assembly (alignment) can be checked. Moreover, the effect of the assembly (and possible design modifications) on the thruster's performance can be quantified.

Author: L.J.M. Cramer
Modified by: J.J.A. Vaes
Version: 1.1
Date: 14-11-2024

D.2.1. Required equipment

- Disassembled EDM-based VLM components
- Fine cloth
- Isopropyl Alcohol cleaner
- Micrometer
- Microscope (for optical characterisation)
- 2x Shoulder bolts (ISO 7379 M3-04x20)
- 1x Metal foam block
- 1x Metal Mesh (RVS 304)
- (Optional) Sealing gasket (Graphite)
- Nozzle profile (0.5 mm)

- K-type thermocouple
- 6x M4 bolts (Torx head)
- 6x M4 nuts
- 6x M4 washers
- 36x Disk springs (S4214 DIN2093)
- M4 wrench
- M4 Torque wrench (FACOM A.402 0.5-2.5 Nm)
- 2x Cartridge heaters (Frd. 2077-1380 Ø1/8"x1")
- Thermal paste (Gallium-Indium-tin alloy)

D.2.2. Assembly procedure

1. Clean the components with a fine cloth and Isopropyl Alcohol Cleaner.
2. Measure the important dimensions of the nozzle profile (thickness and throat/exit widths and heights) using a combination of a micrometer and microscopes.
3. Implement two shoulder bolts in the back most holes of the bottom copper block (furthest from the nozzle).
4. Place the metal foam block and mesh inside the bottom block cavity. The mesh should be placed closest to the nozzle.
5. Consecutively place the first sealing gasket, the nozzle profile, the thermocouple (near the nozzle), the second sealing gasket, and the top block on top of the bottom block.
6. Insert the shoulder bolts a few millimetres into the top block to assure alignment.
7. Insert M4 bolts with springs (bottom) and washers (top) in the remaining four holes.
8. Tighten the bolts until the layers can no longer move (hand tight). Do this in a diagonal manner (top-left to bottom-right and top-right to bottom-left, for example).
9. Exchange the two shoulder bolts for M4 bolts.
10. Tighten with an initial value of 0.5 Nm with a torque wrench.
11. Further tightening depends on the measured leak rate and should thus be determined in conjunction with a leak test. See appendix C of Cramer [15] for the leak testing procedures.
12. Coat the cartridge heaters and fill the heater holes with the thermal paste. Ensure there is enough paste to fill the space between the heaters and the copper. Carefully insert the cartridge heaters and screw them in place. Remove excessive thermal paste.
13. Conduct an optical characterisation and leak test, after assembly. Ensure proper alignment of the copper blocks and nozzle profile [81]. If these preliminary tests are not satisfactory (nozzle deformations greater than 10% and leak rates higher than 5%, for example), repeat the disassembly and assembly procedures.

D.3. Water test procedures

This procedure outlines the steps required to properly execute water tests with the EDM-based VLM and feed system developed in this work (see [Figure D.1a](#)). The procedure is similar to the nitrogen procedure in Cramer's work, except for a few key differences that are explained in [chapter 3](#) and [8](#). Follow these instructions carefully to ensure that each component is handled appropriately, tests are executed safely, and the risk of damage is minimised. Note that, shortly before and after executing the water tests, it is recommended to perform both an optical characterisation and leak test. In this way, the effect of the tests on the VLM can be quantified (see [chapter 6](#) for more details). An important addition to this procedure is the power supply check. Since changed power supply settings (current control instead of voltage control) resulted in noticeable damage to the test equipment (see [chapter 3](#)), this check is essential to avoid future issues. Note that the required equipment subsection ([D.3.1](#)) only details important new additions to the equipment.

Author: H.S.E. Versteeg
Modified by: L.J.M. Cramer
 J.J.A. Vaes
Version: 3.0
Date: 19-11-2024

D.3.1. Required equipment

- Assembled EDM-based VLM components
- Assembled (nitrogen) test bench (TB-50m)
- Syringe
- Demineralised water
- MINSTAC VHS type solenoid (venting valve)
- Swagelok 304L HDF4 150 tank
- Sensirion SLI-1000

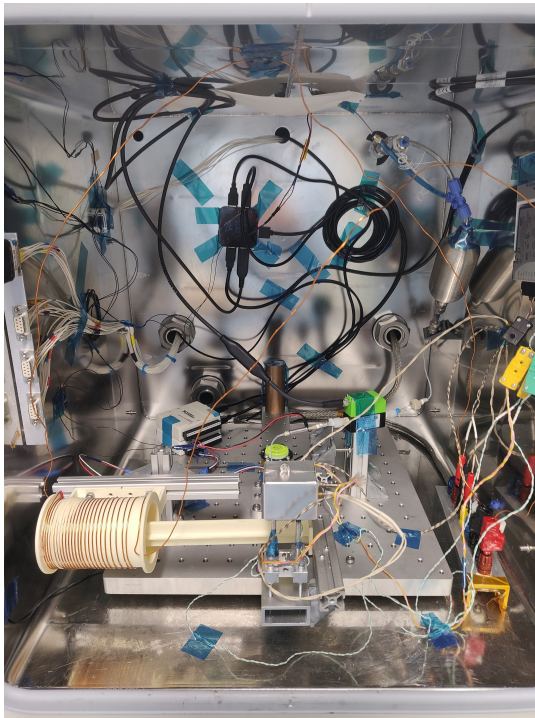
D.3.2. Preparation

Conduct an optical characterisation and leak test before testing. If these preliminary tests are not satisfactory (nozzle deformations greater than 10% and leak rates higher than 5%, for example), it is not advised to continue with the tests.

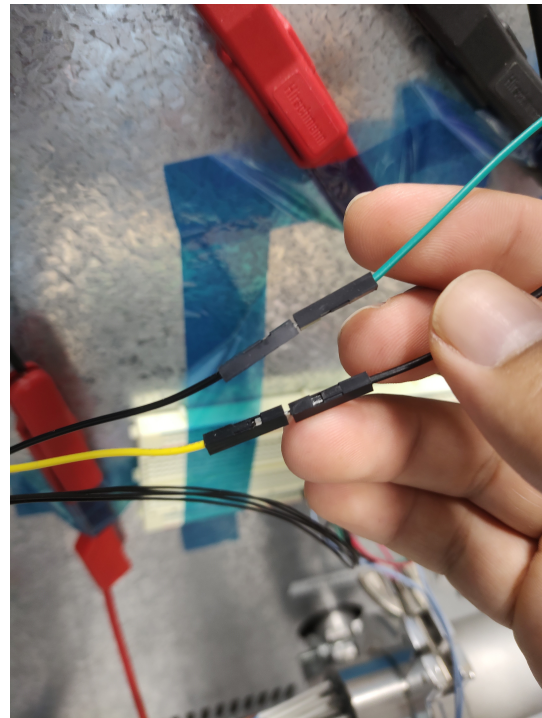
1. Turn on and/or plug in the components requiring warm-up or start-up time:
 - (a) Turn on the SM-7020-D, SM-7020, ES-030-10, E-030-1 and D-030-1 power supplies (60 min warm-up time).
 - (b) Ensure that both heater power supplies (Delta Elektronika ES-030-10 and SM-7020) are set to voltage control and not current control. This is done by turning the voltage knob fully clockwise. Carefully test this, before attaching the heaters.
 - (c) Make sure that the Brooks 5850S mass flow meter is plugged in (45 min).
 - (d) Turn on the cleanroom computer next to the vacuum chamber, and start LabVIEW and the Sensirion Sensor Viewer software, which are found on the desktop (5 min).
2. While the previous devices are warming up, install the thruster on the thrust bench, outside of the vacuum chamber:
 - (a) Connect the heat shield, taking care of all cables coming from the thruster.
 - (b) Connect the MINSTAC connector (at the end of the MINSTAC tube that is attached to the VLM) to the Lee valve. Use the MINSTAC torque wrench together with a 5/32 inch wrench for tightening the connections. The minimum torque is achieved by pressing the shorter torque arm clockwise until it just contacts the longer arm. Instruction can be found in the Lee company manual L12 [75].
 - (c) Connect the Lee valve to the outlet port of the Sensirion SLI-1000 and place the sensor horizontally on the thrust bench. Make sure it is secured and stable using some vacuum tape, if necessary.
 - (d) Use 4 long M4 screws with washers to attach the thruster securely to the end of the torsional beam. Use self-locking nuts to raise the VLM to allow for enough room for the propellant tube.
 - (e) Take distance measurements to determine the force conversion factor between the magnetic actuator force (d_{VTDC}), thrust force (d_{VLM}), and load cell (d_{LSB200}).
 - (f) Attach thermocouples with small pieces of vacuum tape to interesting locations (e.g. pressure sensing tube, VTDC, etc.).

- (g) Route cables for the P - T sensor, valve, thermocouples, heaters, and the propellant tubing over the torsional beam, from the thruster to the pivot in the middle to minimise added stiffness.
 - (h) Secure cables and tubing using small pieces of vacuum tape.
 - (i) Centre the magnet arm to the coil and align its end to 7.1 ± 0.1 cm from the high coil density side of the actuator.
3. Move the thrust bench inside the vacuum chamber, with the magnetic actuator facing to the side:
- (a) Ensure the power patch-through panel is at the opposite side of the vacuum chamber relative to the magnetic actuator.
 - (b) (If not already present:) Plug in the two NI DAQs (NI USB-6008 and NI USB-8451) to the USB dock in the vacuum chamber.
 - (c) Attach the I²C cable from the P - T sensor to the NI USB-6008 and NI USB-8451 DAQs through the colour-coded interface cable.
 - (d) Plug in the Sensirion SLI-1000 to the USB dock in the vacuum chamber.
 - (e) Connect the inlet port of the Sensirion SLI-1000 the MINSTAC connection leading to the bottom of the Swagelok 304L HDF4 150 tank.
 - (f) Attach the tank to the rear right corner of the vacuum chamber using an M6 nut.
 - (g) Fill the water tank with demineralised water using the syringe. The required volume depends on the test duration.
 - (h) Connect the T-junction the top of the propellant tank.
 - (i) Plug in one side of the T-junction to the propellant feed tube quick-connect at the rear top-right corner of the vacuum chamber.
 - (j) Connect the venting valve to the other side.
 - (k) Connect two pairs of red and black cables coming from the 9-pin connector at the rear top-left corner of the vacuum chamber to the propellant and venting valves. When looking at the valve with the pins facing towards you, and the direction of flow pointing upwards, the red wire should be on the right. Secure the cables with vacuum tape.
 - (l) Verify which pair of cables corresponds to which valve by checking the connection at the back of the vacuum chamber (see [Figure D.1b](#)). Make sure the venting valve is connected for now.
 - (m) Plug in the thermocouples to NI-9211. Write down which sensor location corresponds to what port.
 - (n) Run the magnetic actuator cables to be primarily perpendicular to the coil length axis at first and in a wide loop later and plug these into ports 6 and 7 on the power patch-through panel (colour coded for + and -). Secure them using small pieces of vacuum tape.
 - (o) Twist the heater cables around each other, this blocks the magnetic field it generates and prevents interference.
 - (p) Plug in the heaters to port 1-4 on the power patch-through panel, one heater occupies port 1-2 (colour coded for + and -), the other 3 (Red) and 4 (Black).
4. Test if all sensors and actuators are working:
- (a) Open `thrust_test_heated_N2.vi` with LabVIEW.
 - (b) Specify the desired test name and folder to save the data in, then run the program. Also run the Sensirion Software Viewer.
 - (c) Open and close the MINSTAC venting valve and verify that its functioning. A distinct 'tick' should be audible.
 - (d) Turn on one of the heaters at 10 Watt and verify that the temperature of the thruster is going up. Turn the heater off. Repeat this step for the other heater.

- (e) Verify that the remaining sensor and actuator data being recorded makes sense, fix possible issues that come up. (P - T sensor, thermocouples, liquid mass flow, and load cell)
 - (f) Stop `thrust_test_heated_N2.vi` and the Sensirion software.
5. Open up the feed system:
- (a) Verify that all connections are hand tight.
 - (b) Verify that the high-pressure shut-off valve at the bottom of the feed system board is closed.
 - (c) Verify that all manual valves are closed, they should be orientated perpendicular to the flow direction, indicating that it is blocked.
 - (d) Verify that the pressure regulator is fully closed by turning until a physical stop is reached and the thread is visible.
 - (e) Wear protective glasses.
 - (f) Clear away any cluttering items and make sure there is a clear path to the exit.
 - (g) Inform any other people working in the cleanroom that you will be working with a pressurised system.
 - (h) Turn the handle on top of the N_2 cylinder $\sim 180^\circ$ counterclockwise to open its main valve.
 - (i) Listen whether there is a leak.
 - (j) Open the high-pressure shut-off valve.
 - (k) Check that the cylinder pressure, as indicated on the high-pressure gauge, is still above the desired test pressure; otherwise, abort the test and have the N_2 cylinder replaced according to the instructions on the feed system board (see [subsection 5.1.2](#)).
 - (l) Open the red low-pressure shut-off valve and yellow selection valve toward the mass flow sensor in use, by aligning the handles with the tubing.
 - (m) Slowly open the pressure regulator valve (clockwise) until the indicator for the downstream pressure indicates a pressure of roughly 1.5 bar, the small gas burst going through can also be heard.



(a) Overview of the assembled water feed system.



(b) The valve connection at the back of the vacuum chamber.

Figure D.1: The water feed system required for the water tests.

D.3.3. Environment set-up

This section describes the steps to turn on the vacuum chamber and heat up the thruster.

1. Turn on the vacuum chamber:
 - (a) Specify a folder and test name and click run to start thrust_test_heated_N2.vi in LabVIEW.
 - (b) Make sure the heating power is set to 0 Watt and the temperature control setpoint to 0 °C.
 - (c) Make sure the venting valve is opened.
 - (d) Make sure the vacuum chamber door is properly closed.
 - (e) Turn the handle on the vacuum chamber such that the connection to the vacuum pump is open.
 - (f) Rotate the black knob on the vacuum chamber such that the vacuum chamber is closed off from the outside air.
 - (g) Turn on the vacuum pump (O/I switch)
 - (h) Make sure the pressure sensors in the LabVIEW program show that the pressure is decreasing.
2. Preheat thruster to desired temperature:
 - (a) Wait for the vacuum chamber to have reached a vacuum pressure of 50 mbar or lower.
 - (b) Turn on the heaters by setting the power level of the individual heaters to max 20 Watt and selecting Power Control by clicking the heating control selector button.
 - (c) Continue heating until the thrust chamber temperature has reached a temperature of 10 °C below the desired temperature. Set the heating power to 0 Watt.
 - (d) Set the input of the temperature controller to the desired temperature and click the heating control selector button to select Temperature Control. The temperature will now automatically rise to the desired temperature.
 - (e) Wait up to 5 minutes for the temperature oscillation to stabilise to an acceptable range (± 1 °C) and for the pressure inside the vacuum chamber to reach 5 mbar or lower.
 - (f) Close the venting valve.
 - (g) Switch the connecting to the propellant valve at the back of the vacuum chamber. Do not open the valve yet.
3. Stop thrust_test_heated_N2.vi in LabVIEW.
4. **Immediately** continue with the calibration of the test bench:
 - (a) Open 'Calibration for testing (attempt 1).vi' in LabVIEW
 - (b) Specify a folder and test name and click run to start the LabVIEW program.
 - (c) Specify temperature setting
 - (d) Note any offsets
5. Specify a folder and test name and click run to start thrust_test_heated_N2.vi in LabVIEW.
6. Wait up to 5 minutes for the temperature oscillation to stabilise to an acceptable range (± 1 °C) and for the pressure inside the vacuum chamber to reach 5 mbar or lower.

Note: Do not stop the LabVIEW program yet! Stopping the LabVIEW program will stop the control of the chamber temperature. The time between stopping this test and starting the thrust measurements should not be much longer than 10 seconds to keep the chamber temperature stable.

D.3.4. Thrust testing

1. Restart thrust_test_heated_N2.vi in LabVIEW and the Sensirion Sensor Viewer (click run and do not forget to start logging):
 - (a) Specify a folder and test name to save the upcoming thrust measurement.

- (b) Click the STOP TEST button to stop the LabVIEW program started for the environment set-up.
 - (c) Click on the Abort Execution button to stop the LabVIEW program.
 - (d) Click on Run to start the LabVIEW program to start recording for the thrust measurement.
2. Perform the test:
- (a) Perform the actions from [Table D.1](#) at the given times.
 - (b) During the experiment, make sure the variables shown in the LabVIEW and Sensirion interfaces are within the expected values.
 - i. If items are distinctly off, abort the test and assess the situation before continuing.
3. Stop the test:
- (a) At the end of the experiment, stop recording using the STOP TEST buttons.
 - (b) Press the Abort Execution button to stop the LabVIEW program.
 - (c) In case more tests take place:
 - i. Specify a folder and test name and click run to start thrust_test_heated_N2.vi in LabVIEW.
 - ii. Return to [subsection D.3.3](#).

Time	Actions
0:00	Start recording (LabVIEW and Sensirion)
5:00	Open the propellant valve
15:00	Close the propellant valve
25:00	Open the propellant valve
35:00	Close the propellant valve
45:00	Stop recording

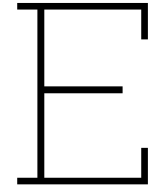
Table D.1: Actions to undertake during the water thrust measurements.

D.3.5. Shutdown

1. Turning off equipment and allowing the thruster to cool:
- (a) Close the valve between the chamber and the pump (handle left of the door).
 - (b) Turn off the vacuum pump.
 - (c) Do not open the pressure equalization valve yet, to avoid oxidation.
 - (d) Close the main valve on top of the N_2 cylinder.
 - (e) Close the high-pressure shut-off valve.
 - (f) Turn the pressure regulator fully counterclockwise, so that it will start at zero outlet pressure for subsequent tests, and gas in the high-pressure line between the cylinder and the regulator is not wasted.
 - (g) Bleed off excess gas in the low-pressure part of the feed system to ambient.
 - (h) Close the low-pressure shut-off and selection valves.
 - (i) Turn off the SM-7020, SM-7020-D, ES-030-10, E-030-1 and D-030-1 power supplies.
 - (j) Unplug the D-sub15 cable from the Brooks 5850S mass flow sensor.
 - (k) Wait for the thruster to cool down to ≤ 100 °C to avoid oxidation. Depending on the temperature tested at, doing this overnight may be preferable as, especially for lower temperatures, this can be very slow. Monitor the initial temperature behaviour from LabVIEW to estimate the time needed.
 - (l) Close LabVIEW, copy the acquired data to a USB-drive and turn off the computer.

2. Thruster hardware removal, after the thruster has cooled down sufficiently for safe handling (≤ 40 °C):
 - (a) Open the pressure-equalization port on the front of the chamber to allow air to enter.
 - (b) Wait for pressure inside chamber to return to ambient, then open the door.
3. Optional in case the vacuum oven has to be left empty, and no subsequent tests are executed:
 - (a) Uncouple the propellant quick connect at the back inside the chamber.
 - (b) Uncouple the propellant tank and liquid mass flow meter.
 - (c) Unplug the load cell.
 - (d) Unplug the USB DAQs from the USB hub.
 - (e) Unplug the heater and actuator electrical power cables.
 - (f) Unplug the sensors and valves electrical cables.
 - (g) Remove the DAQs from the vacuum chamber.
 - (h) Remove the thrust bench from the vacuum chamber.
 - (i) Disconnect the thruster from the thrust bench.
 - (j) Uncouple the MINSTAC tubing from the valve (can be done by hand).
 - (k) Remove heat shield from the thruster.

Conduct an optical characterisation and leak test, after testing. If these preliminary tests are not satisfactory (nozzle deformations greater than 10% and leak rates higher than 5%, for example), it is advised to address the issues and repeat the tests.



MATLAB Resistojet Performance Tool

The analytical model developed in this work, which is based on the Resistojet Performance Tool of Hutten [28], can be found below. Hutten's model is developed in Python and can be found on his GitHub page via this link: [Resistojet Performance Tool](#). The model presented here is named the MATLAB Resistojet Performance Tool (M-RPT) and is compatible with MATLAB. For more information about this model, please refer to [chapter 4](#).

```
1 %% MATLAB Resistojet Performance Tool (M-RPT)
2 % Author: J.J.A. Vaes
3 % Version: 1.0
4 % Date: 27-11-2024
5 % Tool developed to quickly estimate the performance of the EDM-based VLM
6 % presented in the work of Vaes (2024).
7
8 clear; close all; clc
9
10 %% Constants
11 g0      = 9.80665;                % Gravitational acceleration      [m/s^2]
12 R_A     = 8.31446261815324;       % Universal Gas Constant          [J/(mol-K)]
13
14 %% Engine Parameters (VLM-JV2)
15 % Fill in the measured engine parameters
16 Ht      = 499.1e-6;               % Nozzle throat height           [m]
17 Wt      = 232.8e-6;               % Nozzle throat width            [m]
18 rtc     = 260e-6;                 % Throat radius of curvature     [m]
19
20 He      = 471.9e-6;               % Nozzle exit height             [m]
21 We      = 1179.1e-6;              % Nozzle exit width              [m]
22 a_div   = deg2rad(20);            % Divergent half angle           [°]
23 a_con   = deg2rad(35);            % Convergent half angle          [°]
24
25 At      = 1.162e-7;               % Nozzle throat area             [m^2]
26 Ae      = 5.552e-7;               % Nozzle exit area               [m^2]
27 Ae_At   = Ae / At;                % Nozzle area ratio              [-]
28
29 %% Test Plan
30 % Fill in the parameters for the envisioned tests
31 Ta      = 293.14;                 % Ambient temperature            [K]
32 Pa      = 500;                    % Atmospheric pressure           [Pa]
33
34 % N2-10-020
35 % Tc     = 293;                    % Chamber temperature            [K]
36 % Pc     = 1.000e5;                % Chamber pressure               [Pa]
37
38 % N2-10-200
39 % Tc     = 473;                    % Chamber temperature            [K]
40 % Pc     = 1.000e5;                % Chamber pressure               [Pa]
41
42 % N2-15-200
```

```

43 % Tc      = 473;                                % Chamber temperature [K]
44 % Pc      = 1.500e5;                             % Chamber pressure [Pa]
45
46 % N2-10-300
47 % Tc      = 573;                                % Chamber temperature [K]
48 % Pc      = 1.000e5;                             % Chamber pressure [Pa]
49
50 % N2-10-400
51 Tc      = 673;                                % Chamber temperature [K]
52 Pc      = 1.000e5;                             % Chamber pressure [Pa]
53
54 Pa_Pc    = Pa / Pc;                             % Pressure ratio [-]
55
56 % Experimentally found values (optional)
57 F_EXP    = 4.12e-3;                             % Measured Thrust [N]
58 F_EXP2   = F_EXP .* 1e3;                         % Measured Thrust [mN]
59 m_EXP    = 12.42e-6;                             % Measured Mass flow rate [kg/s]
60 Isp_EXP  = F_EXP ./ (m_EXP * g0);                 % Measured Specific Impulse [s]
61 CF_EXP   = F_EXP ./ (Pc * At);                   % Measured Thrust Coefficient [-]
62
63 %% Propellant parameters
64 % Choose the right propellant ('Nitrogen' or 'Water') [Bell et al. (2014)]
65 Propellant = 'Nitrogen';
66
67 % Propellant properties in the heating chamber
68 Prop_chamber = py.CoolProp.CoolProp.AbstractState("HEOS", Propellant);
69 Prop_chamber.update(py.CoolProp.CoolProp.PT_INPUTS, Pc, Tc);
70
71 Mm      = Prop_chamber.molar_mass();              % Molar mass [kg/mol]
72 y      = Prop_chamber.cpmass() / ...              % Specific heat ratio [-]
73         Prop_chamber.cvmass();
74 Mu_c    = Prop_chamber.viscosity();               % Chamber viscosity [Pa-s]
75
76 % Calculate the throat emperature and pressure using IRT
77 Tt      = Tc .* (2 ./ (y + 1));                   % Ideal throat temperature [K]
78 Pt      = Pc .* (2 ./ (y + 1)) ...
79         .^(y ./ (y - 1));                           % Ideal throat pressure [Pa]
80
81 % Propellant properties in the nozzle throat
82 Prop_throat = py.CoolProp.CoolProp.AbstractState("HEOS", Propellant);
83 Prop_throat.update(py.CoolProp.CoolProp.PT_INPUTS, Pt, Tt);
84 Mu_t    = Prop_throat.viscosity();                % Throat viscosity [Pa-s]
85
86 %% Ideal Rocket Theory (IRT) [Zandbergen (2022)]
87 Y      = sqrt(y*(2/(y+1))^(...                    % Vandekerckhove function [-]
88         ((y+1)/(2*(y-1))));
89 R      = R_A / Mm;                                % Specific gas constant [J/(kg-K)]
90
91 % Determine the pressure ratio (Pe/Pc)
92 Pe_Pc   = 0.0001;                                % Nozzle pressure ratio (estimate) [-]
93 f      = @(x) ep(x, y, Y) - Ae_At;                % Define function handle for f(x)
94 Pe_Pc   = fsolve(f, Pe_Pc);                       % Solve equation using fsolve
95 Pe      = Pe_Pc * Pc;                             % Exit pressure [Pa]
96
97 % Find the pressure ratio (Pe/Pc) using a nonlinear system solver
98 function e = ep(Pe_Pc, y, Y)
99 e = Y ./ sqrt(((2.*y)./(y-1)).*Pe_Pc.^(2./y).*(1-Pe_Pc.^((y-1)./y)));
100 end
101
102 % Ideal Rocket Theory (IRT) values
103 c_IRT   = sqrt(R .* Tc) ./ Y;                     % Ideal Characteristic Velocity [m/s]
104 m_IRT   = (Pc .* At) ./ c_IRT                     % Ideal Mass flow rate [kg/s]
105 CF_IRT  = Y .* sqrt((2.*y./((y-1)...              % Ideal Thrust Coefficient [-]
106         * (1-(Pe_Pc).^((y-1)./y)))...
107         + (Pe_Pc - Pa_Pc) .* Ae_At);               % Ideal Thrust Coefficient [-]
108 F_IRT   = m_IRT .* CF_IRT .* c_IRT;                % Ideal Thrust [N]
109 F_IRT2  = F_IRT * 1000                             % Ideal Thrust [mN]
110 w_IRT   = F_IRT ./ m_IRT;                          % Ideal Exhaust Velocity [m/s]
111 Isp_IRT = w_IRT ./ g0                              % Ideal Specific Impulse [s]
112
113 %% Modified Rocket Theory (MRT)

```



```

114 % Modified Discharge Coefficient [Kuluva and Hosack (1971)]
115 Dht      = (2 * At) / (Wt + Ht);           % Hydraulic diameter throat      [m]
116 rt       = Dht / 2;                       % Throat cross sectional radius      [m]
117 Re_t_id  = (m_IRT * Dht) / (Mu_c * At)     % Throat Reynolds number             [-]
118 Q_d_KH   = ((rtc + 0.05 .* rt) ./...       % Discharge Coefficient (KH)        [-]
119           (rtc + 0.75 .* rt)).^0.019 .*...
120           (1 - ((rtc + 0.10 .* rt) ./ rt).^0.21...
121           .* (1./sqrt(Re_t_id)) .* (0.97 + 0.86 .* y))
122
123 % Modified Thrust Coefficient
124 % Thrust Coefficient Loss [Spisz, Brinich, and Jack (1965)]
125 CF_loss   = (17.6 .* exp(0.0032 .* Ae_At))...
126           ./ (sqrt((Q_d_KH .* Mu_c ./ Mu_t)...
127           .* Re_t_id) .* (2 / (y + 1)) .^ (5 / 6));
128 % Flow divergence loss [Berton (1991)]
129 C_a_div   = sin(a_div) / a_div;             % Correction factor                  [-]
130 CF_MRT    = C_a_div .* CF_IRT -...          % Modelled Thrust Coefficient        [-]
131           CF_loss;
132
133 % Modified Rocket Theory (MRT) values
134 Q_s_MRT   = CF_MRT ./ CF_IRT                % Modelled Isp Quality               [-]
135 m_MRT     = m_IRT .* Q_d_KH .* 1e6          % Modelled Mass flow rate            [mg/s]
136 F_MRT     = Q_d_KH .* Q_s_MRT .* F_IRT;     % Modelled Thrust                    [N]
137 F_MRT2    = F_MRT * 1e3                    % Modelled Thrust                    [mN]
138 Isp_MRT   = Isp_IRT .* Q_s_MRT              % Modelled Specific Impulse          [s]
139
140 %% Quality factors
141 % Determine the quality factors based on the modelled (or experimental
142 % results)
143
144 % Quality Factors of the Modified Rocket Theory (MRT)
145 Q_n_MRT   = CF_MRT ./ CF_IRT;               % Nozzle Quality                     [-]
146 Q_s_MRT   = Q_s_MRT;                       % Isp Quality                        [-]
147 Q_F_MRT   = F_MRT ./ F_IRT;                 % Thrust Quality                     [-]
148 Q_d_MRT   = Q_d_KH;                         % Discharge Coefficient (KH)        [-]
149
150 % Quality Factors of the experimental results (optional)
151 Q_n_EXP   = CF_EXP ./ CF_IRT;               % Nozzle Quality                     [-]
152 Q_s_EXP   = Isp_EXP ./ Isp_IRT;             % Isp Quality                        [-]
153 Q_F_EXP   = F_EXP ./ F_IRT;                 % Thrust Quality                     [-]
154 Q_d_EXP   = m_EXP ./ m_IRT;                 % Discharge Coefficient              [-]

```